Microstructural and geochemical processes in long-lived reactivated crustal-scale fault zones: A case study from the Median Tectonic Line, SW Japan.

Sharon P. Jefferies

Microstructural and geochemical processes in long-lived reactivated crustal-scale fault zones: A case study from the Median Tectonic Line, SW Japan.

Sharon P. Jefferies

A thesis submitted for the degree of

Doctor of Philosophy

Department of Earth Sciences

University of Durham

2006

DECLARATION

No part of this thesis has previously been submitted for a degree at this or any other university. The work described in this thesis is entirely that of the author, except where reference is made to previously published or unpublished work.

Sharon P. Jefferies

University of Durham

Department of Earth Sciences
June 2006

Abstract

The Median Tectonic Line (MTL) is a major, crustal-scale fault in Japan that separates the low-P/high-T Ryoke metamorphic belt of mainly subduction related granitoids from the high-P/low-T Sambagawa Belt of accretionary complex metasedimentary rocks. Like many large, crustal-scale faults, the MTL has a long history of movement having been active predominantly as a strike-slip fault since the mid-Cretaceous. Fault rock exposures in the core of the MTL preserve a history of deformation at a range of mid- to shallow-crustal depths. Ryoke mylonites 1-5 km north of the main contact record deeper level, Cretaceous top-to-the-south sinistral movements. The remainder of the fault zone core is surprisingly narrow (<50 m) exhibiting a wide variety of fault rocks that illustrate both the passage and interaction of syn-tectonic fluid influx over a range of deformation conditions. Exposures of the fault core at Miyamae, Mie Prefecture display a progressive sequence in fault rock evolution from ultramylonite → cataclasite → foliated cataclasite → phyllonite → breccia/gouge. This sequence occurs because cataclasis in the vicinity of the fault core creates permeable pathways for the ingress of chemically active fluids into the fault zone. This leads to the replacement of load-bearing phases such as feldspar by fine-grained, foliated aggregates of intrinsically weaker phyllosilicates and the onset of fluid associated diffusive mass transfer (DMT) in finest grained regions of the cataclastically deformed fault zone. Comparison with the findings of recent experimental studies suggest that the fault zone processes observed in the core of the MTL will lead to long-term weakening.

An integrated field, microstructural and geochemical study at Miyamae and Tsukide, Mie Prefecture, has highlighted two distinctive domains: 1) the narrow fine-grained foliated fault core where strain is localised; and 2) a wider damage zone of variably fractured mylonites to the north of the fault core that progressively grade into Ryoke protolith mylonite at distances over ~400 m north of the MTL central slip zone. The fine-grained foliated fault rocks within the core have experienced the most intense deformation, but show the apparently least altered geochemical signature. A model for the presence of a damage zone experiencing pervasive fluid flow and a fault core experiencing high fluid fluxes of channellized fluid flow structurally linked to a Ryoke protolith fluid reservoir is presented. A central slip zone 'seal' is inferred to retard mixing with Sambagawa-derived fluids. The phyllonitic fault rocks in the core of the MTL posses a strong permeability anisotropy where transverse fluid flow is inhibited and focused fault-parallel fluid flow occurs.

Foliated cataclasites are exceptionally well exposed in the MTL fault core at Anko, Nagano Prefecture. Processes of brittle fracture and cataclasis have led to the development of cm- to sub-mm spaced fracture systems defining a crude fabric. This fracture system established an initial architectural hierarchy that influenced the subsequent development of foliated cataclasite and gouge. Fluid influx at the onset of grain-scale brittle deformation led to precipitation of fibrous chlorite within the finest-grained sections of the fault core. This ultimately led to the development of a foliation within the ultra-cataclasite defined by an interconnected network of aligned phyllosilicate aggregates. The brittle reduction of grain-size and the ingress of a chemically active fluid phase promoted the operation of diffusive mass transfer mechanisms ('frictional-viscous creep') and reaction softening. Field and microstructural observations at Anko suggest that the foliated cataclasites are a shallower equivalent to the phyllonites found along the more deeply exhumed parts of the MTL at Miyamae.

Acknowledgements

Wow, there are so many people to thank. First and foremost I would like to thank my supervisor Bob Holdsworth, I really would never have got to this stage with out him. He has always given me tremendous support and guidance throughout the project, but he has also gone far beyond the call of duty to help me get through some difficult times over the past few years, picking me up when I was down. I also extend this thanks to Bob's wife Michelle and their sons Christopher, Thomas, Callum and Daniel, who have welcomed me into their home and allowed me to take up much of their husband/fathers very valuable time. Thanks also to my supervisors elsewhere, Toshi Shimamoto at Kyoto, Chris Wibberley at Nice and Geoff Lloyd at Leeds Universities for the helpful and enthusiastic work discussions and guidance during the project. Here I would also like to say a great big thanks to Jonny Imber, who has been like an additional supervisor, he has spared me his very busy time for enthusiastic discussions of ideas and reading of thesis drafts. Thanks to Toshi and the lads in his research group at Kyoto who welcomed us and looked after Bob and myself during our time in Japan, and thanks for introducing Bob to the joy of communal bathing – hee hee hee.

I have a huge thank you to say to my Japanese friends in Haze village, Ryuji, Yoko, Etsuko, Junko, Master and Mr Yuki – my 'Sanrinsha Family Crowd' – I would never have been able to complete the fieldwork for this PhD had they not been there to help and nurse me back onto my feet after a delusional moment out in the field where I thought I could catch a car –it turned out I couldn't!

There are lots of people to thank from Durham. A big thanks to all the RRG boys – Jonny, Phil, Ken, Bob, Adam, Bones and especially Woody and Nic. Cheers for enduring all my practise talks, supporting me through poster printing disasters and providing the friendly supportive faces at numerous conferences, and for making those conferences a lot of fun. I hope that Woody and Nic have forgiven me for making them share a bed at the Adelphi. Thanks also to Gary, my knight in shining armour during times of computer related crisis, Karen, Janice and Carol have been amazing points of reference for any questions or queries, about anything and everything that I could come up with. Thanks to Dave Sales for supplying my huge demand of thin sections and being really great and understanding during saw-related disasters. Thanks to Nick Marsh and Rob Kelly at Leicester for giving me free reign of their lab during XRF analysis and to Teresa, the technician at Durham who helped with the ICP-MS lab work. It was a real joy to work at Leeds University with Eric Condliffe during SEM and Microprobe analysis, thanks for the all the discussions and assistance during my time at Leeds.

Thanks for the great and lasting friendships that I have made during my time in Durham. Thank you especially to Deano, Fozzard, Bryant, Big Stu, H, Ozzy, Hammo, Dr Fox, Rich, Woody and Nic for the good times, the beers, the wine, the food, the laughs, the bumps, the bruises, the scars, the tears and the great great memories. During the final push, two weeks before submission, thanks to James for putting a roof over my head and letting me take over the living room of his house, thanks to H for looking after me and thanks to John for the moral support and the chocolate.

Almost there, thanks to Mum, Dad and Mark, who have always, and continue to do so, supported me in what ever I have chosen to do and thanks for never doubting and believing that I could do it.

Last, but my no means least, thanks to Ernie. Thanks for living with me, thanks for looking after me and thanks for loving me whilst writing up.

P.S. thank you the manufacturers of HP brown sauce.

This thesis is dedicated

in loving memory

to

Mary Teresa Collins

Know the true value of time; snatch, seize, and enjoy every moment of it. No idleness; no laziness; no procrastination; never put off till tomorrow what you can do today.

Lord Chesterfield
(1694-1773)

Miyamae outcrop April 2003

Because you never know what tomorrow may bring.....

Miyamae outcrop June 2005

Microstructural and geochemical processes in long-lived reactivated crustal-scale fault zones: a case study from the Median Tectonic Line, SW Japan.

1. INTRODUCTION.....1
1.1. THE WEAK FAULT PROBLEM.....1
1.2. STRENGTH OF THE CONTINENTAL LITHOSPHERE.....2
1.3. FAULT ZONE REACTIVATION.....6
1.4. DEFORMATION MECHANISMS.....6
1.4.1. Frictional deformation mechanisms.....9
1.4.2. Viscous creep deformation mechanisms.....13
1.5. ROCK CHARACTERISTICS AND THEIR INFLUENCE ON FAULT ROCK DEFORMATION.....15
1.5.1. Mineral strength.....15
1.5.2. Rock aggregate strength.....16
1.6. FAULT ROCK NOMENCLATURE.....19
1.7 METAMORPHISM AND DEFORMATION-INDUCED FLUID FLOW IN FAULT ZONES.....21
1.7.1. Closed versus open rock-fluid systems.....24
1.7.2. Channellized fluid flow.....24
1.7.3. Pervasive fluid flow.....24
1.8 LONG-TERM FAULT ZONE WEAKENING.....25
1.8.1 Reaction softening.....25
1.8.2 Fabric softening.....26
1.8.3 Grain size reduction.....28
1.8.4 Fluid assisted diffusive mass transfer.....29
1.9 THESIS OUTLINE.....29

2. THE NATURE AND RHEOLOGICAL CONSEQUENCES OF PHYLLONITE DEVELOPMENT IN THE CORES OF CRUSTAL-SCALE FAULTS: AN EXAMPLE FROM THE MEDIAN TECTONIC LINE, SW JAPAN.....31
2.1. INTRODUCTION.....31
2.2. GEOLOGICAL SETTING AND STRUCTURE OF THE MEDIAN TECTONIC LINE.....35
2.2.1. Geological setting.....35
2.2.2. Structural history and protoliths.....36
2.3. FAULT ZOEN STRUCTURE AND FAULT ROCKS OF THE MEDIAN TECTONIC LINE, MIE PREFECTURE.....37
2.3.1. MTL fault zone structure in the Miyamae village area.....37
2.3.2. Fault rocks of the MTL core: the Fukaya River Section.....41
2.3.2.1. Faults.....41
2.3.2.2. Ultramylonite.....42
2.3.2.3. Cataclasite.....42
2.3.2.4. Foliated cataclasite.....42
2.3.2.5. Phyllonite.....44
2.3.2.6. Orange-stained cataclasite.....46
2.3.3. Mineralogy and microstructures.....47
2.3.3.1. Ultramylonite.....47
2.3.3.2. Cataclasite.....47

2.3.3.3. Foliated cataclasite.....49
2.3.3.4. Phyllonite.....50
2.3.3.5. Orange-stained cataclasite.....54
2.3.4. Major element geochemistry.....54
2.4. DISCUSSION.....55
2.4.1. Fault rock sequence, cataclasis and fluid flow.....55
2.4.2. The onset of diffusive mass transfer deformation mechanisms and metamorphic processes.....58
2.4.3. Summary and rheological implications.....61
2.4.4. The textures and rheology of phyllonites: insights from deformation experiments.....62
2.4.5. The importance of phyllonites to the MTL past and present.....65
2.5. CONCLUSIONS.....66

3. GEOCHEMICAL INSIGHTS INTO FAULT ROCK DEVELOPMENT AND FAULT ZONE PROCESSES IN CRUSTAL-SCALE STRUCTURES: A CASE STUDY FROM THE MEDIAN TECTONIC LINE, SW JAPAN.....68
3.1. INTRODUCTION.....69
3.2. FAULT ROCK PROTOLITH.....70
3.3. STUDY AREAS AND FAULT ZONE STRUCTURE.....75
3.3.1. Miyamae field area.....75
3.3.2. Tsukide field area.....80
3.4. XRF WHOLE-ELEMENT ANALYSIS.....88
3.4.1. Major and trace element composition of fault rocks from the Miyamae transect.....88
3.4.2. Major and trace element composition of fault rocks from the Tsukide transect.....96
3.4.3. Discussion of geochemical processes identified from XRF whole-rock element data.....104
3.5. ICP-MS WHOLE-ROCK TRACE ELEMENT ANALYSIS.....111
3.5.1. Miyamae transect multi-element spiderdiagams.....112
3.5.2. Tsukide transect multi-element spiderdiagrams.....112
3.5.3. Discussion of geochemical processes identified from multi-element spiderdiagrams.....115
3.6. RARE EARTH ELEMENTS.....117
3.6.1. REE data – Miyamae transect fault rocks.....117
3.6.2. REE data – Tsukide transect fault rocks.....119
3.6.3. Discussion of geochemical processes identified from REE data.....121
3.7. FAULT ZONE VOLUME CHANGES.....122
3.8. DISCUSSION.....128
3.8.1. Coupled geochemical and microstructural analysis.....128
3.8.2. Fluid pathways and fault zone permeability structure within the MTL crustal-scale fault zone.....129
3.9. CONCLUSIONS.....136

4. THE DEVELOPMENT AND SIGNIFICANCE OF FOLIATED CATACLASITE AND GOUGE IN THE CORES OF CRUSTAL-SCALE FAULT CORES: EXAMPLES FROM THE MEDIAN TECTONIC LINE, SW JAPAN 138
4.1. INTRODUCTION 139
4.2. GEOLOGICAL AND STRUCTURAL SETTING 140
4.2.1. Regional setting 140
4.2.2. Local setting, Nagano Prefecture 142
4.3. THE MTL FAULT CORE, ANKO SECTION 144
4.3.1. Fault rocks of the MTL core 144
4.3.2. Field relationships and mesostructures 147
4.3.2.1. Faults 147
4.3.2.2. Ryoke mylonites 147
4.3.2.3. Quartzo-feldspathic cataclasite 149
4.3.2.4. Quartzo-feldspathic foliated cataclasite with clasts of fractured mylonite 150
4.3.2.5. Orange-black quartzose foliated cataclasite and gouge 152
4.3.2.6. Grey-green and orange-stained cataclasites 155
4.3.2.7. Fault rock sequence 156
4.3.3. Mineralogy and microstructures 157
4.3.3.1. Ryoke mylonites 157
4.3.3.2. Quartzo-feldspathic cataclasite and foliated cataclasite 159
4.3.3.3. Orange-black quartzose foliated cataclasite and gouge 163
4.3.3.4. grey-green and orange-stained cataclasite 165
4.3.4. Major element geochemistry 166
4.4. DISCUSSION 168
4.4.1. Brittle deformation, fluid flow and development of foliated cataclasites 168
4.4.2. Rheological implications 171
4.4.3. Comparison with other natural and experimental foliated cataclasites/gouges 174
4.4.4. How are foliated cataclasites/gouges related to phyllonites? 175
4.5. CONCLUSIONS 176

5. CONCLUSIONS & SUGGESTIONS FOR FURTHER RESEARCH 179
5.1. CONCLUSIONS 179
5.2. SUGGESTIONS FOR FURTHER RESEARCH 184

APPENDIX A: GEOCHEMICAL PROCEDURES AND RAW DATA 186

REFERENCES 205

Chapter 1
Introduction.

1.1. The weak fault problem.

Many crustal-scale fault and shear zones repeatedly localise deformation events on various timescales, implying that they are weak relative to adjacent regions of 'intact' crust (Holdsworth et al., 1997). Geophysical measurements of surface heat flow and stress orientations associated with faults such as the San Andreas Fault suggest that it moves under very low shear stresses suggesting it has an anomalously low frictional strength (e.g. Zoback et al., 1987). However, other authors have argued that such faults are in fact strong (e.g. Scholz, 2000). A major problem is that the geophysical techniques used to address these problems lack sufficient spatial resolution to identify the possible causes of weakening along principal displacement surfaces within such faults (Holdsworth, 2004).

Operative deformation mechanisms along long-lived reactivated fault zones, and in particular deformation mechanisms within fault rocks formed at depths close to the frictional-viscous (or brittle-ductile) transition where faults cut the main load-bearing region of the continental crust, will have a major influence on overall strength and subsequent deformation experienced by the crust as a whole (Stewart et al., 1999, 2000; Holdsworth et al., 2001; Imber et al., 2001). Therefore, the solution to the problem of weak faults lies in the study of exhumed crustal-scale fault zones. In particular, exhumed fault zones exposing deeper parts of the crust, e.g. between 5 and 15 km depth, are central to understanding the factors that control fault zone strength and reactivation over long geological time periods. Recent field-based research (e.g. Imber et al., 1997, 2001; Stewart et al., 2000; Gueydan et al., 2003; Collettini & Holdsworth, 2004; Wibberley, 2005; Jefferies et al., 2006) has focused on major

faults exhuming fault rocks formed at depths close to the frictional-viscous transition and have suggested that the development of foliated phyllosilicate-rich fault rocks – especially phyllonites - may be fundamentally important. This is supported by a growing body of experimental data (e.g. Shea & Kronenberg, 1993; Bos & Spiers, 2002) that has demonstrated the potential weakness of such phyllonites.

In light of this, the principal aim of this thesis is to investigate the occurrence and development of phyllosilicate-rich fault rocks along a long-lived crustal-scale reactivated fault zone: the Median Tectonic Line, SW Japan. The microstructural, mineralogical and geochemical processes involved in the formation of phyllosilicate-rich fault rocks are investigated and discussed in relation to fluid flow within crustal-scale fault zones and implications for strength reduction and long-term weakening.

1.2. Strength of the continental lithosphere.

Thickness of the continental lithosphere typically varies between 100-150 km, with an upper zone of quartzo-feldspathic crust (~30-40 km thick) overlying a dense, thick, olivine-rich mantle. The relative low density and buoyancy keeps the continental crust from being re-cycled or subducted back into the mantle (Sutton and Wilson, 1986). Therefore, the continental lithosphere is old in both absolute terms and relative to the oceanic crust. Consequently, it preserves numerous mechanical anisotropies, such as faults and shear zones, which have great longevity and often-complex displacement histories involving repeated episodes of reactivation. These ancient faults and shear zones divide the lithosphere into a series of 'blocks', which to some extent can deform independently to one another resulting in heterogeneous

patterns of deformation characteristic of the continental crust and lithosphere resulting in localisation of strain along long-lived faults and shear zones (Dewey et al., 1986).

Over the past two decades many people have held the view that the continental lithosphere comprises three rheologically different layers: a seismogenic upper crust; an aseismic lower crust; and a strong, mainly aseismic uppermost mantle (Fig. 1.1a). Frictional processes dominate deformation of the upper seismogenic layer of the crust. Both temperature and frictional strength of the upper crust increase with depth (Fig. 1.1a) to a critical temperature where viscous creep mechanisms begin to operate. The lower crust deforms in an essentially aseismic, ductile manner (Sibson, 1983). This produces a strength decrease with increasing temperature (Fig. 1.1a). Separating the quartzo-feldspathic continental crust from the olivine-rich upper mantle beneath is the Moho. This boundary corresponds to a sharp increase in strength (Fig. 1.1a) due to the fact that at any given temperature olivine is stronger than both quartz and feldspar according to the results of rock deformation experiments (Evans and Goetze, 1979).

For 'normal' continental lithosphere the upper mantle strength maximum should correspond to the primary load-bearing region in the lithosphere as a whole, while a strength maximum (or secondary load-bearing region) in the overlying continental crust corresponds with the frictional-viscous ("brittle-ductile") transition. This implies that lithosphere deformation will be controlled by the development of shear zones in the upper mantle. These displacements will be transferred up into the overlying crust and will be localised by weakening processes affecting faults/shear zones cutting through the frictional-viscous (brittle-ductile) transition (Holdsworth et al., 2001). Consequently, deformation mechanisms operating around the frictional-viscous transition have important implications in controlling the overall strength of the continental crust.

A recent alternative to the above model has been proposed by Jackson (2002). He proposed a model in which the mantle is weak and the upper crust is strong (Fig. 1.1b). He based his model on observations of earthquake depth distributions and gravity anomalies in the continents (Maggi et al., 2000a), which suggest that earthquakes in the continents are restricted to a single seismogenic layer in the upper brittle part of the crust and are either rare or absent in the underlying mantle. If this is the case it has the implication that patterns of surface faulting on the 100s of km scale are most likely controlled by the anisotropic strength of crustal blocks and their intervening faults (Jackson, 2002).

Within a model where all the strength of the continental lithosphere resides in the crustal seismogenic layer another effect, in addition to temperature, must play a part in allowing the lower continental crust to be seismic in some areas and not in others and to distinguish continental from oceanic mantle. Maggi et al. (2000b) suggested this effect was the presence of water, which is known to reduce creep strength dramatically, even if present in only a few parts per million in nominally anhydrous minerals (Hirth and Kohlstedt, 1996; Mackwell et al., 1998). Figure 1.1b is a theoretical strength-depth profile based on laboratory experiments (adapted from Mackwell et al., 1998) for continental conditions comprising a wet lower crust and wet upper mantle, neither of which has significant strength. Nearly all the strength resides in the seismogenic upper crust, and may, according to Jackson (2002) represent conditions in most continental settings. This profile should not be taken literally but it does illustrate the effect of small amounts of water on creep strength (Jackson, 2002).

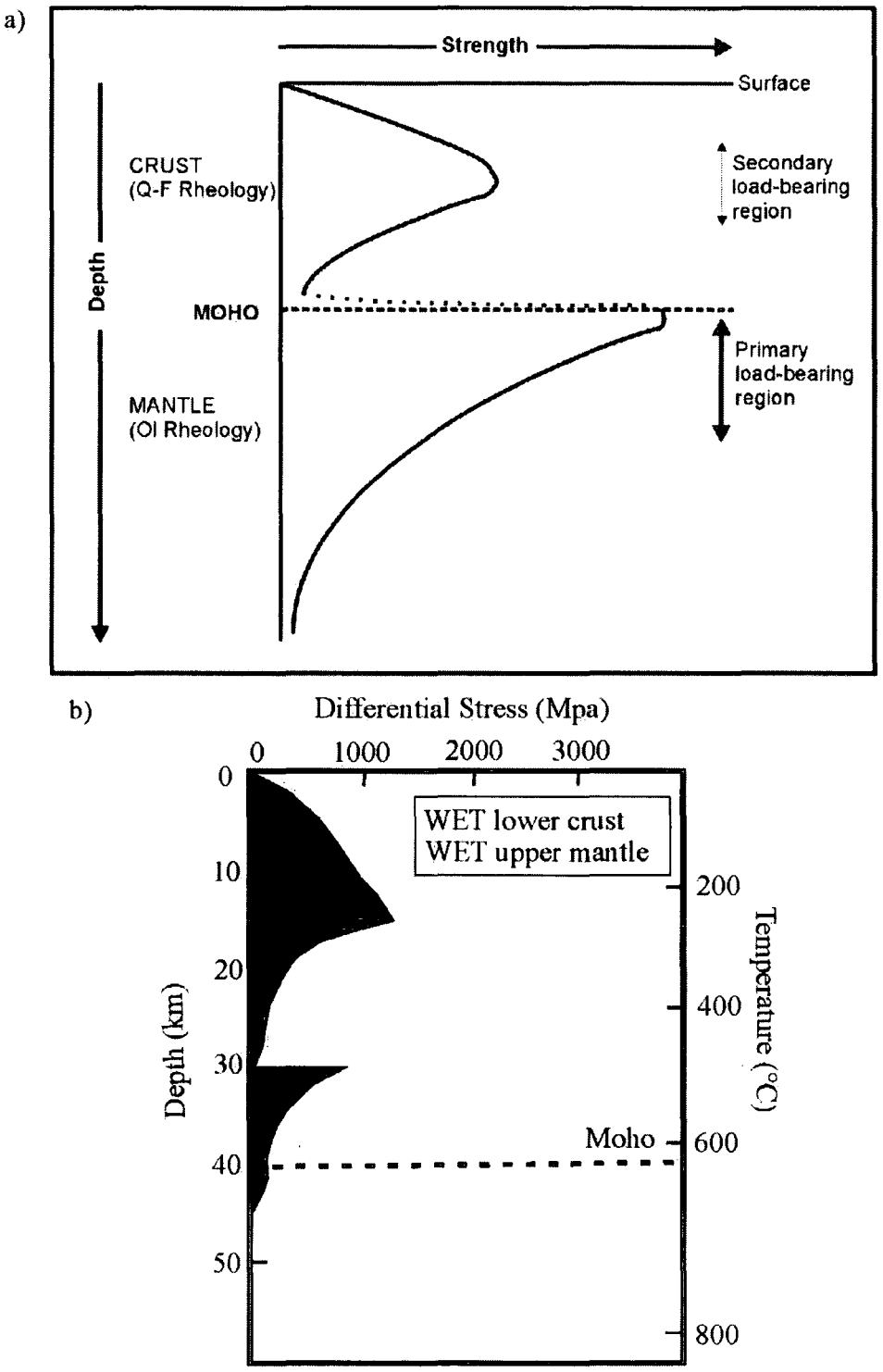

Figure 1.1. a) Not to scale. Schematic strength versus depth profile for average continental lithosphere showing the main load-bearing regions in the upper mantle and the mid- crust (after Molnar 1988). b) Theoretical strength versus depth profile based on laboratory experiments (adapted from Mackwell et al., 1998) showing continental conditions involving a wet lower crust and wet upper mantle, with strength residing in the seismogenic upper crust.

1.3. Fault zone reactivation.

Holdsworth et al. (1997) defined reactivation as *'the accommodation of geologically separable displacement events (at intervals >1 Ma) along pre-existing structures'*. Two distinct types of reactivation were recognised: those where reactivated faults display different senses of relative displacement during successive events are said to have undergone geometric reactivation (Fig. 1.2a); and those displaying similar senses of relative displacement for successive events have experienced kinematic reactivation (Fig. 1.2b).

Holdsworth et al. (1997) identified four main groups of generally reliable criteria to recognise reactivation along faults and shear zones: stratigraphic, structural, geochronological and neotectonic (summarised in Fig. 1.3). In order to recognise reactivation with certainty, wherever possible, several criteria and evidence for repeated displacement and associated deformation using absolute or relative time markers are required.

1.4. Deformation mechanisms.

The determination of operative deformation mechanisms, prior to, during and after reactivation is paramount to understanding the rheological evolution and identifying weakening processes of long-lived crustal-scale fault zones (White et al., 1986; Holdsworth et al., 2001). Lithological controls imposed by the characteristics of the rock (grain size, mineralogy, microcrack population, porosity and permeability) and environmental controls (temperature, pressure, stress, strain rate, fluid pressure

a)

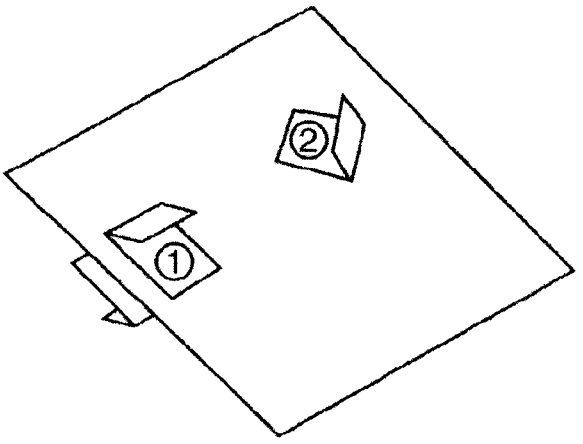

b)

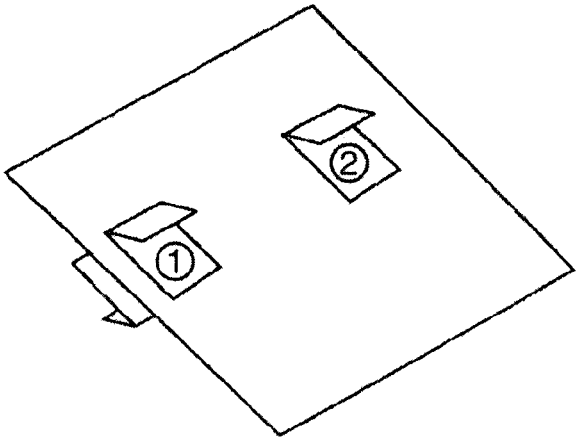

Figure 1.2. a) Geometric reactivation; reactivated structures display *different* senses of relative displacement for successive events. b) Kinematic reactivation, reactivated structures display *similar* senses of relative displacement for successive events (after Holdsworth et al. 1997).

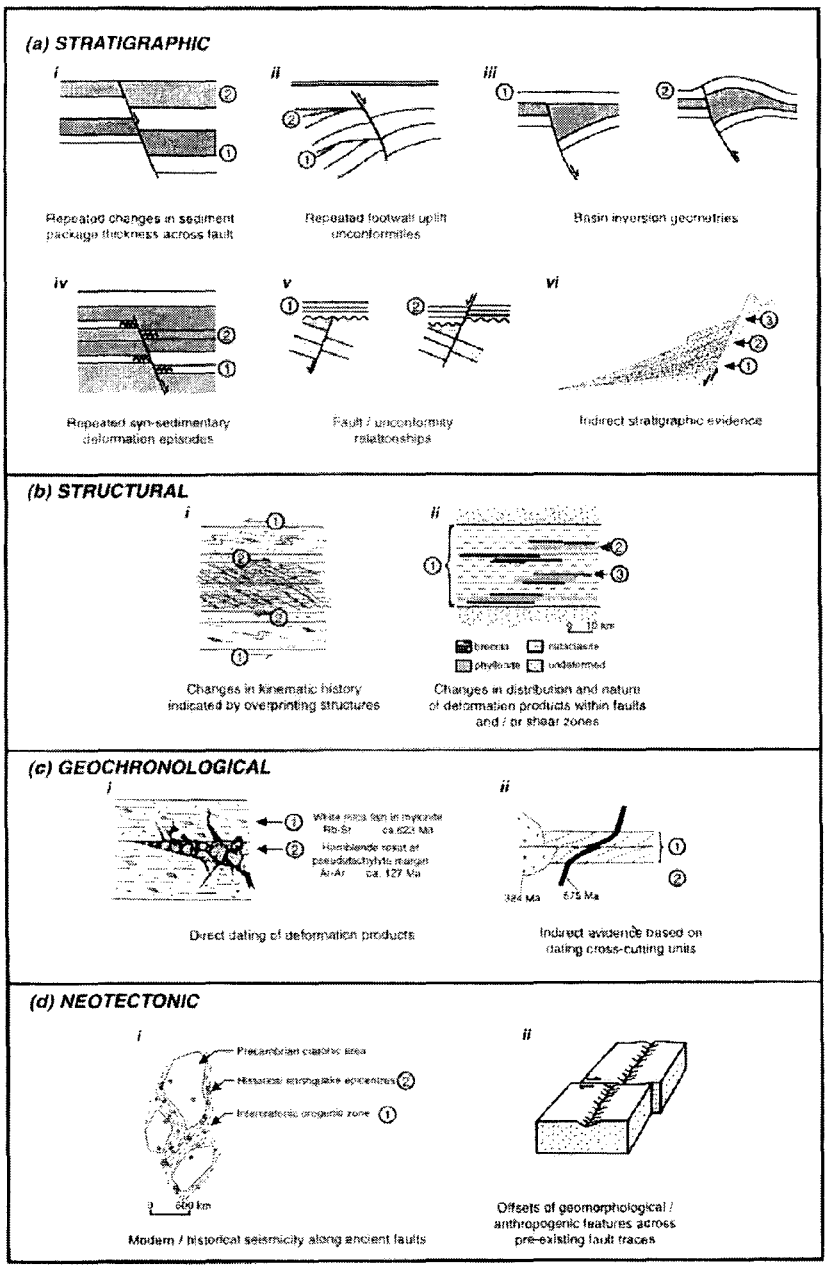

Figure 1.3. The criteria considered reliable for recognising reactivation: stratigraphic, structural, geochronological and neotectonic (after Holdsworth et al. 1997).

and fluid composition) act together to create the conditions under which deformation occurs (Fig. 1.4; Knipe, 1989); Rutter et al., 2001).

The following section briefly outlines the two main groups of deformation mechanisms known to occur within the continental crust: 1) pressure-sensitive *frictional* mechanisms and 2) pressure insensitive, thermally activated *viscous creep* mechanisms (Fig. 1.5; Schmid and Handy, 1991). Figure 1.6 presents a theoretical, vertical, crustal-scale fault zone showing the relationship between strength, deformation mechanisms and fault rock types with depth.

1.4.1. Frictional deformation mechanisms.

Frictional deformation mechanisms include such processes as fracture, frictional grain-boundary sliding, cataclasis and frictional melting and dominate in the upper ~10 km of the continental crust (Fig. 1.5; Sibson, 1977; Knipe, 1989). The frictional strength of rocks increases proportionally to effective normal stress and depth (Fig. 1.5). Fracture mechanisms involve the nucleation and crack propagation along which displacement occurs as deformation progresses, (see Lloyd and Knipe (1992) and references therein for a detailed review of mechanisms of fracture nucleation and propagation). Frictional grain boundary sliding takes place when frictional resistance between grains is overcome and cohesion between grains is lost so that grains slide and roll past one another (Knipe, 1989). Generally grains do not show evidence for intragranular deformation. Deformation depends on the amount and strength of intergranular cement and typically occurs at low effective stress due to a low confining pressure and/or high pore-fluid pressure. Grain-boundary sliding is known to occur without fracturing in fault breccias and gouges where pore-fluid pressures are high due to the presence of clay minerals.

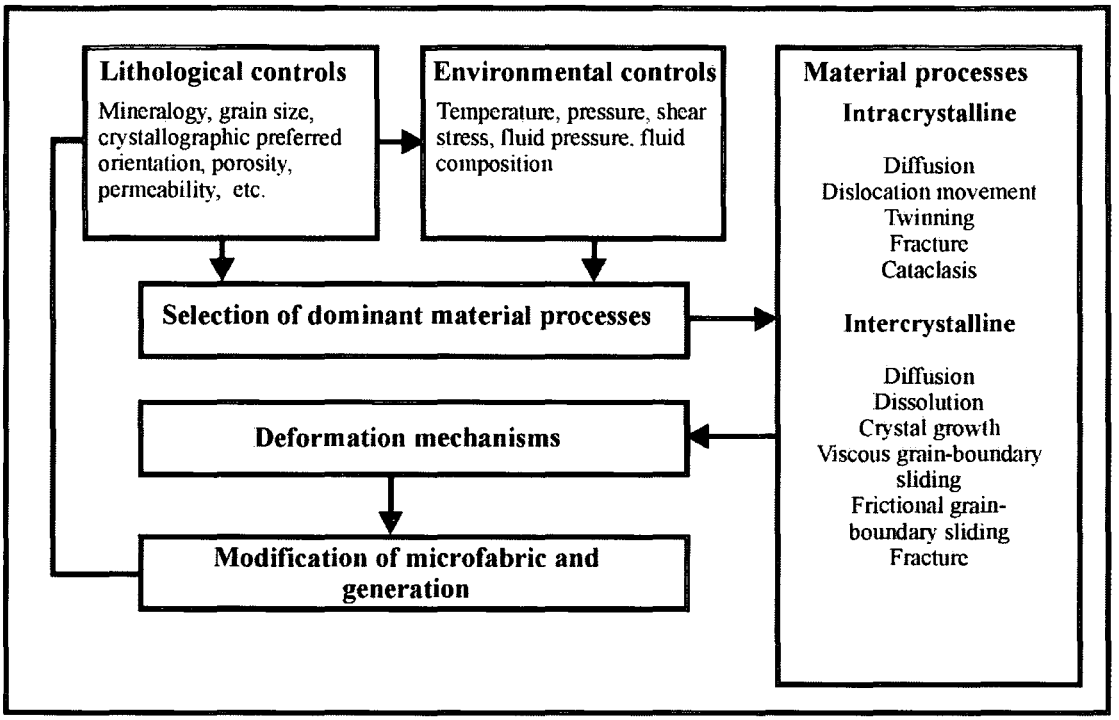

Figure 1.4. Flow chart to show the variables affecting the material behaviour of a deforming rock mass. Note the feedback between deformation processes and microstructural evolution of the rock (after Knipe 1989).

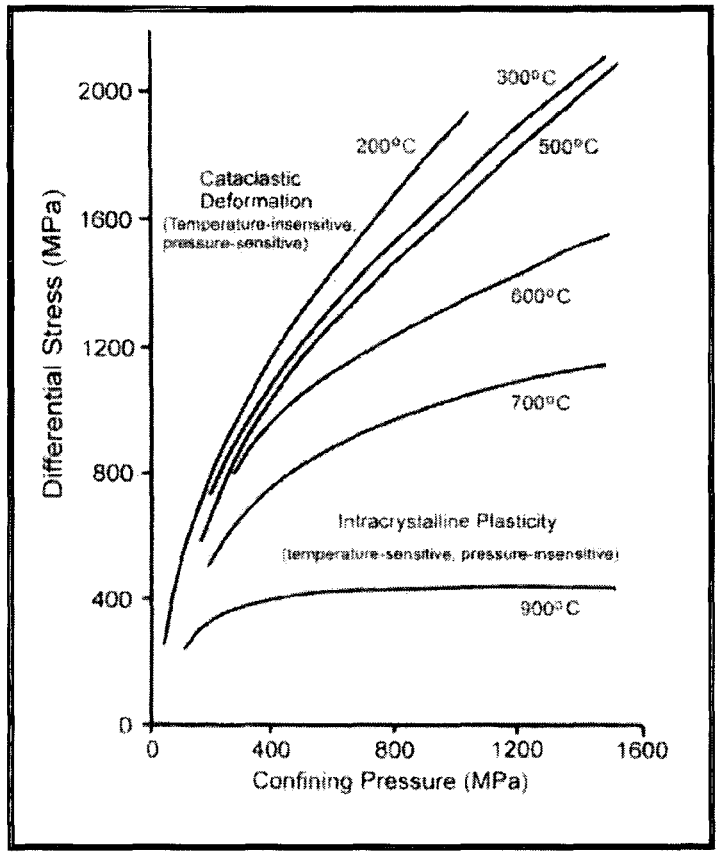

Figure 1.5. A simplified representation of the data of Tullis and Yund (1977) for the ultimate strength of the Westerly granite at a strain rate of 0.00001/second. Strength in the brittle regime (up to 300°C) is insensitive to temperature, but sensitive to confining pressure. At higher temperatures, deformation is increasingly sensitive to temperature and a reduction in pressure sensitivity as intracrystalline plastic processes begin to dominate.

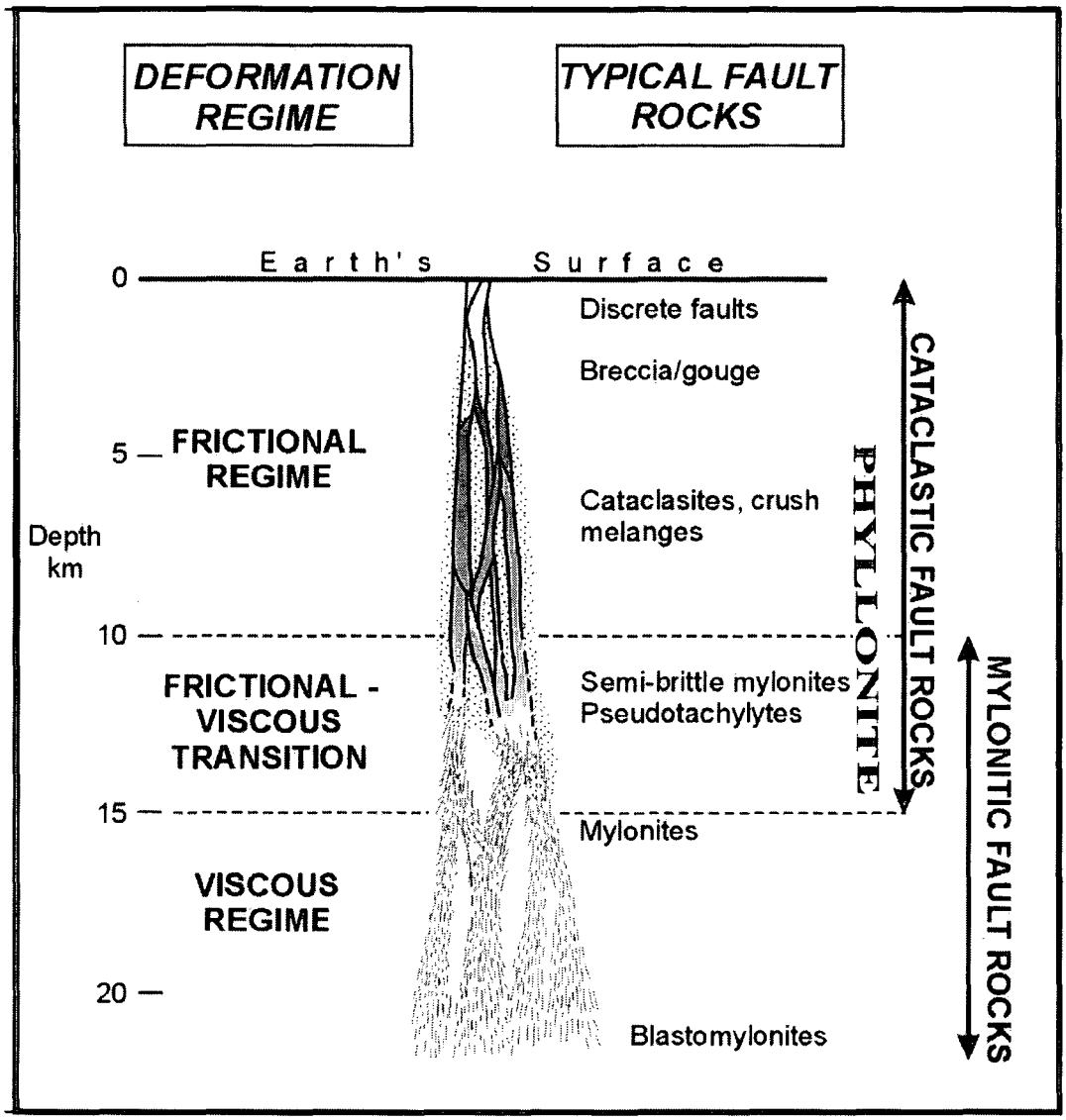

Figure 1.6. Conceptual model of a theoretically vertical, crustal-scale fault zone. Narrow brittle-frictional faults with a range of cataclastic fault-rock products pass with increasing depth into foliated mylonitic rocks in which intracrystalline plastic and diffusion-accommodated viscous flow processes progressively dominate (after Holdsworth et al. 2001).

Cataclasis and cataclastic flow comprises grain-scale fracturing, frictional sliding along fracture surfaces, frictional grain-boundary sliding and grain rotation (Knipe, 1989). Cataclasis is an important deformation mechanism within the uppermost 5-10 km of the continental crust occurring at moderate confining pressures and relatively high pore-fluid pressures (Sibson, 1983; Knipe, 1989). Cataclastically deformed fault rocks characteristically comprise randomly oriented, angular to rounded clasts within a fine-grained cataclastic matrix and their formation may involve significant dilatancy (i.e. volume change) having implications for fluid transport properties (Knipe, 1989; Oliver, 1996).

At high strain rates (10^{-2}-1 ms^{-1}), frictional sliding may result in localised frictional melting of the wall rocks along fault planes (Spray, 1995). Friction-generated melts (>1000°C) rapidly cool to crystallise as pseudotachylite and their formation is generally thought to be promoted in dry, fluid-absent environments (Sibson, 1977). However, a more recent study (Magloughlin, 1992) suggested some frictional melts might be generated in fluid-rich environments.

1.4.2. Viscous creep deformation mechanisms.

Viscous creep mechanisms comprise two groups of deformation mechanisms: 1) grain size sensitive diffusive mass transfer and 2) grain size insensitive crystal plasticity. Both are pressure insensitive and thermally activated (Fig. 1.5; Knipe, 1989). Diffusive mass transfer involves the transport of material away from sites of high intergranular normal stress to areas of relatively low intergranular normal stress through the process of diffusion (Rutter, 1983; Knipe, 1989). In the crust diffusive mass transfer processes are typically fluid-assisted, and include pressure solution and mass transport, which are driven by the presence of a chemical potential gradient,

which can be induced by stress variations (Wheeler, 1987) or fluid pressure gradients (McCaig and Knipe, 1990). The operation of diffusive mass transfer processes is promoted by elevated temperatures that increase solid-state diffusion rates, fine grain sizes with increased grain boundary area and shorter diffusion pathways, low strain rates and/or the presence of a chemically active fluid phase to allow easy transportation of dissolved material.

Knipe (1989) described fluid-assisted diffusive mass transfer as a 3-stage process involving source, diffusion and sink mechanisms. Source mechanisms control how material enters a diffusion pathway, the most important being pressure solution. Pressure solution is the chemical dissolution of material leading to the formation of characteristic stylolites, dissolution seams, truncated grains, slaty and crenulation cleavages (Passchier and Trouw, 1996). The way in which material is transported form source to sink regions is controlled by diffusion mechanisms. Material is either transported along grain boundaries (e.g. pressure solution creep, Rutter, 1983) or carried in a bulk fluid flow through the rock (e.g. mass transport, McCaig and Knipe, 1990). Characteristic features indicative of diffusion mechanisms include localised growth of retrograde minerals, fluid inclusions along grain boundaries and the occurrence of veins (Passchier and Trouw, 1996). Regions of localised dilation provide the sites for sink mechanisms to operate. Such sites comprise veins and strain shadows of fibrous beard development adjacent to relatively more rigid porphyroclasts. New mineral precipitates can be of a different composition from that of the minerals undergoing dissolution at source sites; this is termed incongruent pressure solution (Beach, 1979).

Grain size insensitive crystal plastic deformation at relatively low temperatures involves dislocation glide during which deformation is accommodated by the

movement of dislocations (linear defects) along slip planes (Knipe, 1989). Build up of dislocations (or dislocation tangles) can lead to a situation where further movement of dislocations through the crystal lattice is restricted resulting in work hardening. This is commonly observed as the precursor state to brittle fracturing and frictional sliding (Lloyd and Knipe, 1992). Patchy undulose extinction and the development of crystallographic fabrics are characteristic microstructures of dislocation glide. At higher temperatures and/or strain rates, recovery processes become increasingly active counteracting the process of work hardening. Recovery processes are predominantly achieved by dislocation climb, where defects are rearranged to lower the internal strain energy of a crystal via diffusive movement of defects to higher or lower slip planes (Knipe, 1989; Williams et al., 1994). Indicative recovery microstructures include sweeping, undulose extinction, deformation lamellae and presence of subgrains (Passchier and Trouw, 1996).

Dynamic recrystallization may operate in addition to recovery to further reduce dislocation density or internal strain energy of crystals during deformation. Evidence for dynamic recrystallization includes the replacement of old highly strained, work hardened grains with new, relatively strain free grains. Dynamic recrystallization is recognised to involve two mechanisms: grain boundary migration recrystallization and subgrain rotation recrystallization (Drury and Urai, 1990).

1.5. Rock characteristics and their influence on fault rock deformation.

1.5.1. Mineral strength.

Although operative deformation mechanisms have an important role to play in how a rock responds to deformation, characteristics such as the mineral composition

of the rock, including crystal structure and melting temperature of individual constituent minerals, leads to differences in strength. Therefore, a minerals response to an applied deformation is largely dictated by prevailing physical conditions, such as pressure and temperature. Table 1.1, after Stewart (1997), summarises the operative deformation mechanisms and resultant microstructures of quartz, feldspar and mica at varying temperatures. Note, however, that other environmental factors (i.e. lower strain rate, higher finite strain and fluid composition; see Fig. 1.5) can have the same effect as an increase in temperature.

1.5.2. Rock aggregate strength.

Rocks are polymineralic consisting of aggregates of different minerals, all of which at the same physical conditions will respond to deformation in different ways. The ratio of 'strong' to 'weak' minerals will determine the overall strength of the rock during deformation. Handy (1990), based on ratios of strong to weak minerals and the proportion of weak minerals present in polymineralic rocks, characterised three types of microstructural and mechanical behaviour, which he termed 'domains' (Fig. 1.7).

Domain 1 represents a load-bearing framework. The strong phase dominates and provides a load-bearing framework that separates isolated pockets of the weaker phase. The overall strength of the rock aggregate is controlled by the grain size, shape and distribution of the weak phase. Domain 2, the boudin-matrix field, is characterised by elongate grains of the stronger phase within a weaker matrix. The relative strength of each phase is low; both are rheologically active representing a matrix-controlled interconnected weak layer rheology. Domain 3, represents a clast-matrix field, where higher mineral strength ratios are >20% the volume of the weak phase. Relatively undeformed clasts of the strong phase are surrounded by the weak

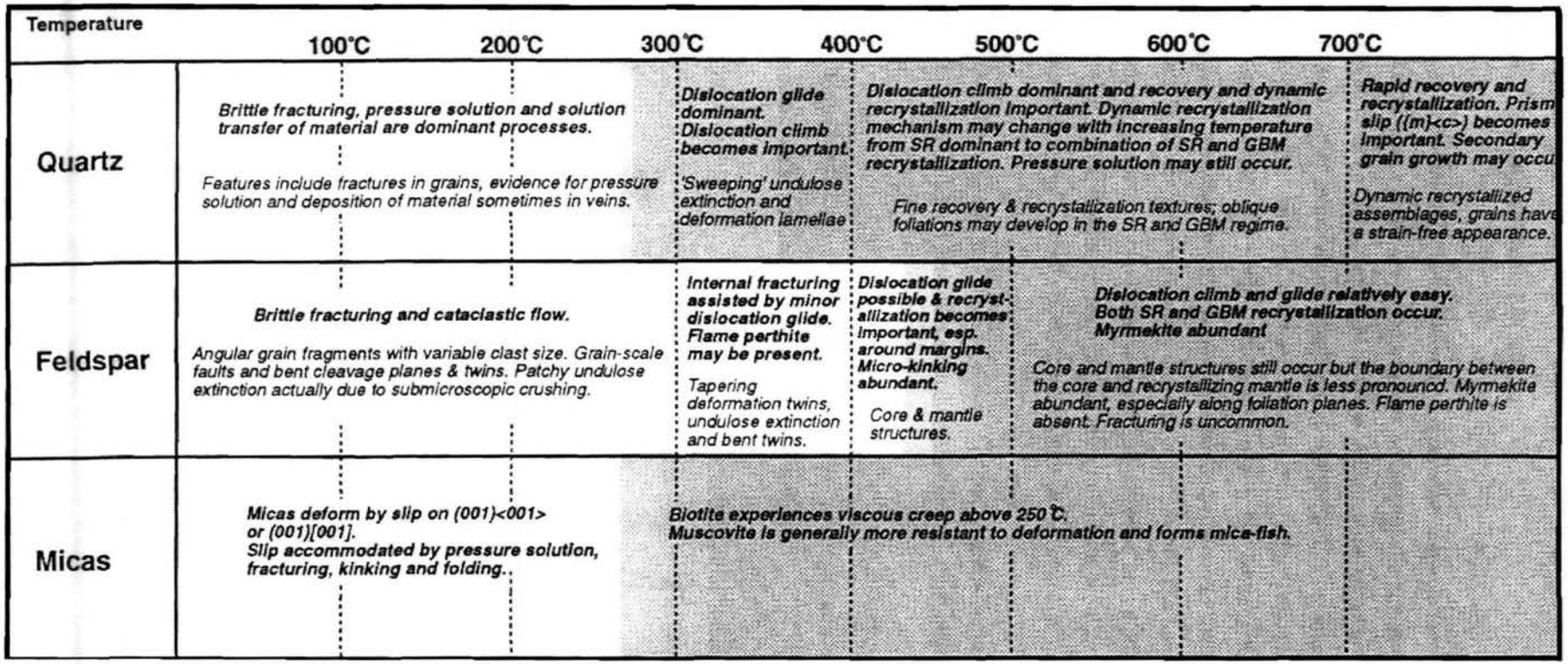

Table 1.1. The mechanical behaviour of quartz, feldspar and mica in response to deformation at different temperatures (after Stewart 1997, compiled from Passchier and Trouw 1996). Note that an increase in the fluid content and a decrease in strain rate will have the same effect as increasing temperature. Grey shading - crystal plastic and DMT processes (viscous creep).

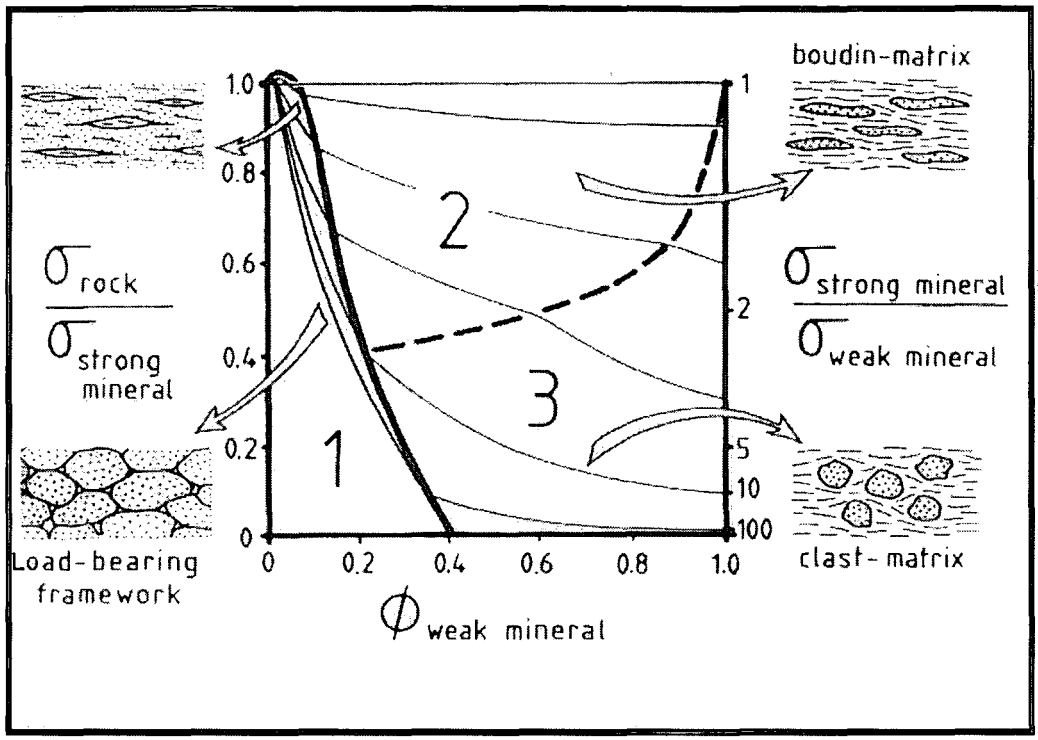

Figure 1.7. The characterisation of polyphase aggregate behaviour in solid-state deformation (after Handy 1990). Ø- volume proportion, σ-strength.

phase, leading to a matrix-controlled interconnected weak-layer rheology. Processes of deformation and metamorphism tend to break down the load-bearing framework of Domain 1 to generate an interconnected weak-layer rheology. If the weaker phase forms an interconnected layer along a fault zone you only require a very small percentage of the weak material to result in profound weakening of the entire fault (e.g. Holdsworth et al., 2001).

1.6. Fault rock nomenclature.

Table 1.2 (after Stewart, 1997) presents the fault-rock classification used in this thesis. The terminology used is predominantly based upon that of Schmid and Handy (1991) where fault rocks are classified according to the behaviour of the aggregate on a grain-scale. Hence, fault rocks formed predominantly by frictional or 'brittle' processes are termed cataclasites, whilst those that have experienced significant viscous modes of deformation, such as crystal-plastic deformation or diffusive mass transfer processes, are classed as mylonites. The more detailed definition of 'foliated cataclasite' provided by Chester et al. (1985) is referred to in the current study. Phyllonite is placed at the boundary between frictional and viscous modes of deformation (see Table 1.1) because although little to no evidence of dynamic recrystallization, or recovery, was seen within the phyllonites studied, evidence for the operation of diffusive mass transfer processes was widespread. Recent experimental studies using halite and kaolinite mixtures as analogues for quartz- and mica-rich fault rocks (Bos and Spiers, 2000, 2002; Bos et al., 2000a and b) produced *apparently* mylonitic textures through processes of frictional sliding along phyllosilicate foliae and diffusive mass transfer, with no crystal plasticity.

INCOHESIVE FAULT ROCKS		***Fault breccia***	Unconsolidated breccia (visible fragments >30% of total rock mass)
		Fault gouge	Unconsolidated matrix-dominated fault rock (visible fragments <30% of total rock mass
COHESIVE FAULT ROCKS	**Frictional modes of deformation dominant**	***Cataclasite***	Cohesive fault rock composed predominantly of mechanically disaggregated minerals. Clasts (angular and rounded) have subsequently suffered frictional grain-boundary sliding and rotation. Cataclasites are usually unfoliated. The cataclasite series comprises **Microbreccia** (0-10% matrix), **Protocataclasite** (10-50% matrix), **cataclasite** (50-90% matrix) and **ultracataclasite** (90-100% matrix).
		Foliated cataclasite	Cataclasite containing a foliation defined by either bands of fine and coarse comminuted clasts, fine grained material localises along parallel arrangement of fractures, or bands of syn-tectonic alteration product (e.g. white mica or chlorite) (Chester et al., 1985).
	Viscous modes of deformation dominant	***Phyllonite***	A phyllosilicate-rich fault rock with *'apparently'* mylonitic textures. It is a highly foliated mica-rich (chlorite dominated, plus white mica) brittle fault rock developed after cataclasis and extensive fluid influx. There is little to no evidence for significant amounts of dynamic recrystallization or recovery. Deformation occurs through processes of frictional slip and diffusive mass transfer, most importantly pressure solution (Bos and Spiers, 2000, 2002; Bos et al., 2000a and b).
		Mylonite	Mylonite contain a fabric in which crystal plastic and diffusive mass transfer processes are dominant. It comprises a matrix of crystal-plastically deformed or dynamically recrystallized material in which porphyroclasts occur. Mylonitic foliation may be defined by a grain-shape fabric (dynamic recrystallization of aa mineral), mineral segregation, flattened porphyroclasts/quartz ribbons or preferential alignment of elongate minerals and porphyroclasts. The mylonite series comprises **protomylonite** (10-50% matrix), **mylonite** (50-90% matrix) and **ultramylonite** (90-100% matrix).

Table 1.2. Fault rock classification used in this thesis, predominantly based on terminology of Schmid and Handy (1991) unless stated.

1.7. Metamorphism and deformation-induced fluid flow in fault zones.

Reactivated faults and shear zones are often zones of intense and localised retrograde (e.g. Imber et al., 1997) or prograde metamorphism (e.g. Holdsworth, 1994). Retrograde metamorphism occurs in most fault zones affecting fault rocks at mid to upper crustal depths in the presence of fluids. It often involves the breakdown and alteration of anhydrous minerals (e.g. feldspar) to low-grade assemblages of hydrous minerals (e.g. phyllosilicates).

Fault zones can act as barriers, conduits, or mixed conduit/barrier systems and form important components of fluid flow regimes operating within the upper crust (Caine et al., 1996). Potential sources for fluids at shallow to moderate depths (up to ~10 km) include meteoric, metamorphically derived, connate, basin and hydrothermal fluids (Engelder, 1984; Kerrich, 1986; Reynolds and Lister, 1987; McCaig, 1988; Forster & Evans, 1991). Deformation of rocks within fault zones causes substantial fluid migration in a range of metamorphic settings (Oliver, 1996 and references therein). Dilatancy (a volume change produced by deformation of rock bodies) is dependant on deformation conditions and rock and fluid properties, and is a key requirement for fluid movement at a range of scales (Etheridge et al., 1983). Deformation-induced dilatancy in the upper crust associated with earthquake faulting can cause km-scale fluid migration (Sibson et al., 1975; Sibson, 1985), and may include substantial components of lateral and downwards fluid flow to depths of 15 km, approximately the depth of the seismogenic layer on the San Andreas fault system (Sibson, 1981).

In the upper most crust, the three most important mechanisms for driving fluid flow around fault zones are seismic pumping (Sibson et al., 1975), involving pre-failure fluid flow into rocks dilating around a fault, dilatancy pumping (Sibson, 1986),

where sudden failure opens spaces along an irregular fault plane causing rapid fluid movement due to the sudden change in fluid pressure, and fault valve behaviour (Sibson, 1990), where faulting is controlled by cyclic changes in fluid pressure during the seismic cycle. Fault valve behaviour requires constant fluid input and a regional permeability barrier to maintain the high pore-fluid pressures within the fault zone. Sibsons (1990) fault valve model consists of five distinct phases, 1) input of fluid increases fluid pressure along sealed fault zones, 2) fluid pressure (hydrostatic) locally exceeds lithostatic pressure leading to tensile fracturing, 3) shear hydraulic fracturing occurs along the fault zone, 4) fluid is released along shear fractures within the fault zone, 5) fluid pressure decreases and mineralisation occurs along fault and fracture surfaces sealing the fault and the cycle begins again. Sibson (1990) suggested that fault valving was the most important mechanism for driving fluid flow around the frictional-viscous transition.

Hydraulic fracturing can also develop in response to fluid overpressure due to devolatilization reactions (e.g. Etheridge, 1983), but also occurs because deformation of fluid-saturated rocks causes changes in rock porosity. Deformation-driven fluid flow can be transient and potentially multidirectional resulting in either regular or irregular cycles of fluid flow or fluid retardation (Oliver, 1996).

Oliver (1996) presents a classification of types of behaviour for fault zone fluid flow based on inferences from geochemistry/petrology, field relations, and the results of experiments and numerical modelling. He discusses closed and open systems, channellized and pervasive flow (Fig. 1.8).

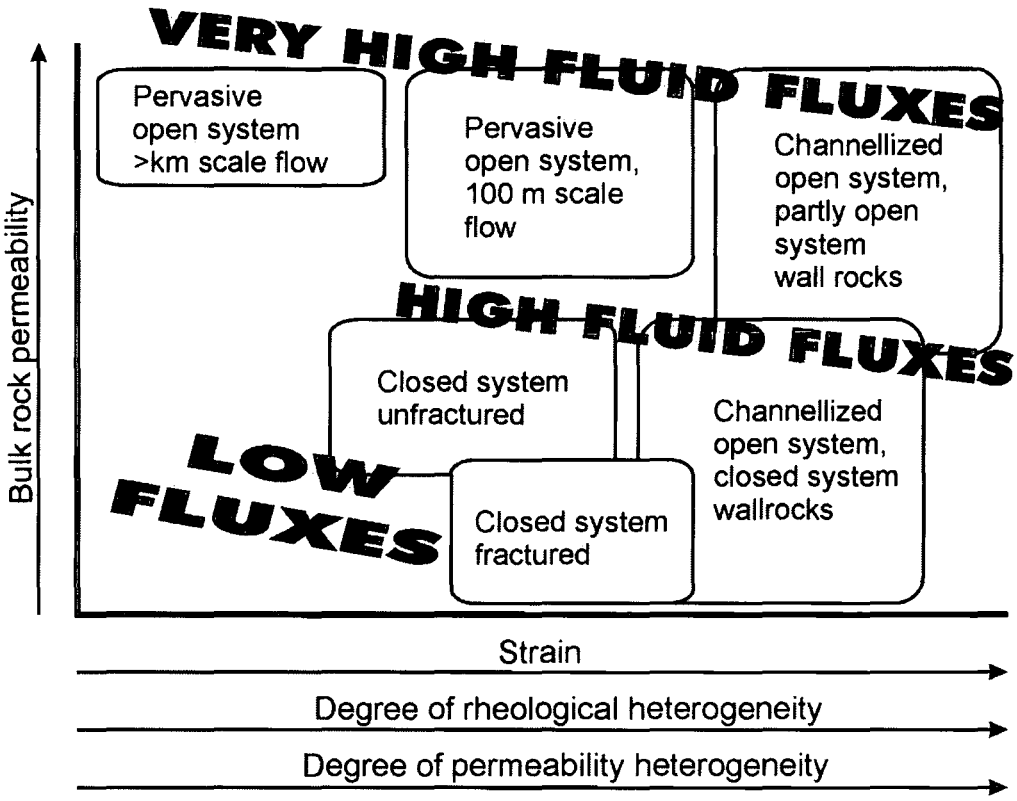

Figure 1.8. Categorization of different types of fluid flow with respect to permeability, deformation and fluid flux, after Oliver (1996).

1.7.1. Closed versus open rock-fluid systems.

A closed rock-fluid system is essentially characterised by a situation where the rock does not record 'significant' interaction with an externally derived fluid. An open system is one in which fluid composition is predominantly externally controlled, where rocks record the influx of large fluid volumes and where major-element metasomatism occurs (Oliver, 1996).

1.7.2. Channellized fluid flow.

Channellized flow at macroscopic scales refers to the tendency for fluid localisation through particular mesoscopic locations (open system behaviour), where other locations remain relatively untouched by fluids (closed system behaviour). At mesoscopic scales it refers to localization of fluid through particular fractures or layers, due to a structurally related permeability contrast (e.g. parts of one outcrop, or set of outcrops, could record 'closed' system behaviour while others record 'open'). At microscopic scales fluid flow is predominantly channellized through microcracks or grain boundaries where diffusion dominates. Enrichment or depletion of chemical components does not usually occur during microscale channellization because the rate and scale of diffusion normally allows equilibrium between these small fluid channels and the surrounding mineral assemblage to occur (see Oliver, 1996 and references therein).

1.7.3. Pervasive fluid flow.

In contrast, macroscopic pervasive flow (e.g. Ferry, 1992) requires all mesoscopic scale rock-fluid systems to record significant interaction with an infiltrating fluid, the magnitude of fluid fluxes may vary due to permeability

variations, but all rocks effectively form part of an open system. Figure 1.8 attempts to categorize the different types of fluid flow with respect to changes in permeability, deformation and fluid flux (after Oliver, 1996).

1.8. Long-term fault zone weakening.

Two fundamentally different groups of fault-zone weakening mechanisms are identified: 1) transient, syn-tectonic and 2) long term (Holdsworth et al., 1997). Transient, syn-tectonic mechanisms only refer to those operative during active deformation (i.e. high pore-fluid pressure), whereas long-term weakening methods are both syn-tectonic and semi-permanent resulting in weakening over long geological timescales. In terms of long-lived reactivated fault zones, we are most interested in mechanisms that result in a long-term state of weakening, therefore the following section presents just some of those weakening mechanisms likely to influence long-term crustal-scale fault zone strength. For more detailed reviews of fault zone weakening mechanisms see Rubie (1990) and Wintsch et al. (1995).

1.8.1. Reaction softening.

Reaction softening is a process that operates during syn-tectonic metamorphism and results in the replacement of relatively 'strong' mineral phases (e.g. feldspar) by intrinsically weaker mineral phases (e.g. phyllosilicates) (Wintsch et al., 1995; Imber et al., 1997). Experimental studies reveal that muscovite grains accommodate strain by dislocation glide over a wide range of temperature and pressure conditions and are likely to be weak over a wide range of crustal depths (Mares and Kronenberg, 1993). In addition, experimental studies reveal that foliated phyllosilicate-rich rocks appear

to be significantly weaker than massive quartzo-feldspathic rocks when deformed under comparable pressure, temperature and strain conditions (Shea and Kronenberg, 1993; Niemeijer and Spiers, 2005). Therefore, the syn-tectonic, reaction softening process involving chemical breakdown and alteration of such minerals as feldspar to white mica, and hornblende to chlorite, leads to a permanent change in mineralogy with considerable rheological consequences.

1.8.2. Fabric softening.

Two main processes are involved in fabric softening, foliation weakening (Jordan, 1987) and the development of crystallographic fabrics (White et al., 1986). As rock starts to deform, strong minerals (e.g. feldspar) remain rigid and deform predominantly by fracturing (Handy, 1990), whilst the relatively weaker phases (e.g. quartz and mica) deform in a crystal-plastic manner. With increasing strain stretching and elongation of the weaker minerals occurs so that they become interconnected, wrapping around isolated, rigid porphyroclasts producing an interconnected weak-layer microstructure (Fig. 1.9). The rheology of these rocks as a whole is then controlled by the rheology of the weak phase. This process is known as foliation weakening (Handy, 1992), and will typically develop if the weak phase constitutes 20% or more volume of the protolith (Fig. 1.7; Schmid and Handy, 1991). This means that the development of an interconnected weak-layer microstructure will weaken fault rocks relative to the protolith of the same composition. Reaction softening with the production of aligned aggregates of phyllosilicate minerals will markedly enhance this process of foliation weakening (Jordan, 1987; Handy, 1990; Imber et al., 1997, 2001).

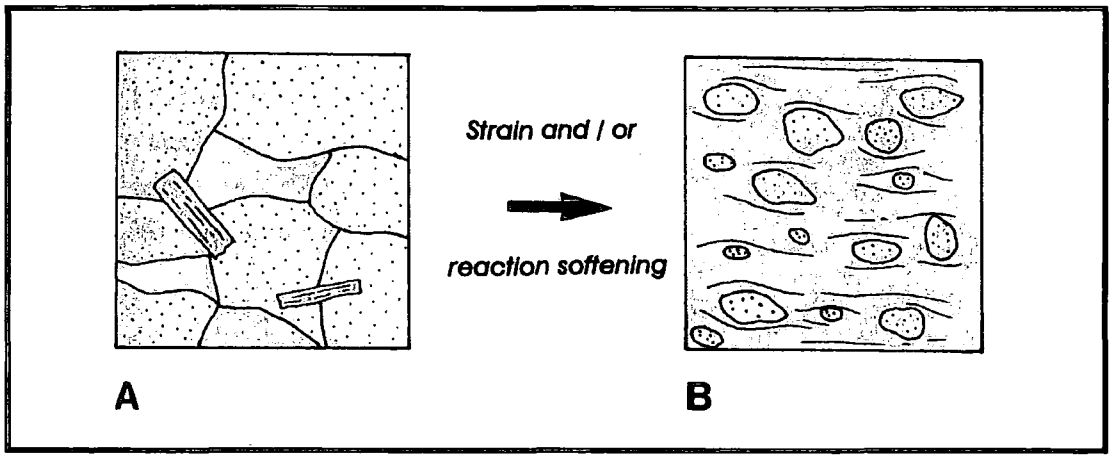

Figure 1.9. Schematic diagram illustrating foliation weakening. (A) Load-bearing framework microstructure (LBF). Stipple - interlocking strong phase, plane and dashed ornament - weak phase. (B) Interconnected weak layer microstructure (IWL). Stipple-strong phase (forming isolated, rigid porphyroclasts), dashed ornament - weak phase. (compiled by Imber 1998 from Handy 1990).

With continued crystal-plastic deformation, a preferred crystallographic fabric develops with alignment of crystallographic axes of a particular phase. Development of a crystallographic fabric depends on the minerals involved, and the operation of their intracrystalline slip systems, and the kinematics and movement direction along the fault (Law, 1990). In the case of phyllosilicates, minerals grains often align parallel to the mylonitic foliation, conveniently oriented for grain-boundary sliding (White et al., 1986). However, if fault zone reactivation is of the geometric type (see section 1.3; Fig. 1.2a), slip systems within previously deformed grains may not be ideally oriented for easy intracrystalline deformation, and therefore a strong crystallographic fabric is unlikely to weaken the fault (White et al., 1986).

1.8.3. Grain size reduction.

Within fault or shear zones a reduction in grain size can be achieved by either cataclasis or dynamic recrystallization. Finer grain sizes will promote the onset of grain size sensitive deformation mechanisms such as diffusive mass transfer (see sections 1.4.2. and 1.7.4.). Finer grain sizes, due to an increase in grain boundary surface area, are more susceptible to reaction softening (see section 1.8.1.) in comparison to coarser grained rocks of the same composition (Brodie and Rutter, 1985). The reduction in grain size leads to a change in the operative deformation mechanisms. This produces a marked weakening effect, but for such a grain size reduction to lead to a long-term weakening, temperatures within the fault zone need to remain sufficiently low to suppress grain growth during static recrystallization between deformation events (Imber, 1998).

1.8.4. Fluid-assisted diffusive mass transfer.

Localised grain size reduction accompanied with fluid influx into a fault zone may promote the onset of grain size sensitive, fluid-assisted diffusive mass transfer mechanisms (Imber et al., 1997, 2001; Imber, 1998; Stewart et al., 1999, 2000; Holdsworth et al., 2001; Holdsworth, 2004; see section 1.4.2.). Fine-grained fault rocks that deform by diffusion-dominated creep will deform under much lower stresses than rocks deforming by crystal-plastic mechanisms at the same strain rate (Handy, 1989 and references therein). As a result, fine-grained fluid rich fault zones are expected to be weak.

1.9. Thesis outline.

Following this introductory chapter, the thesis outline is as follows,

- **Chapter 2** – describes the development of phyllonite within the core of the Median Tectonic Line in Mie Prefecture, SW Japan. The microstructural and textural development of phyllonite is presented in detail and compared to the finding of recent experimental studies. A discussion of the rheological consequences of phyllonite formation is included.
- **Chapter 3** – presents the findings of an integrated field based, microstructural and geochemical study along two transects across the fault zone in Mie Prefecture (Miyamae and Tsukide). Key chemical changes are highlighted, and reflect geochemical/metamorphic processes and key mineralogical changes across the fault zone. Models

for porosity, permeability and fluid flow, with particular reference to the formation of phyllosilicate-rich fault rocks, within the Median Tectonic Line are discussed.

- **Chapter 4** – the development of foliated cataclasite and gouge in the core of the Median Tectonic Line in Nagano Prefecture, SW Japan are documented. The role of brittle deformation and fluid flow during foliated cataclasite formation are discussed in relation to their rheological significance. The relationship between phyllonite and foliated cataclasite along the Median Tectonic Line is explored
- **Chapter 5** – discusses the findings and general conclusions of the current study with suggestions for further research.

Chapter 2

The nature and rheological consequences of phyllonite development in the cores of crustal-scale faults: an example from the Median Tectonic Line, SW Japan.

This chapter in modified form was accepted for publication in the Journal of Structural Geology.

Abstract

Like many large, crustal-scale faults, the Median Tectonic Line (MTL) in SW Japan has a long history of movement having been active predominantly as a strike-slip fault since the mid-Cretaceous. Fault rock exposures in the core of the MTL preserve a history of deformation at a range of mid- to shallow-crustal depths. Ryoke mylonites 1-5 km north of the main contact record deeper level, Cretaceous top-to-the-south sinistral movements. The remainder of the fault zone core is surprisingly narrow exhibiting a wide variety of fault rocks that illustrate both the interaction and effects of syn-tectonic fluid influx over a range of deformation conditions. Exposures within 50 m of the central slip zone display a progressive sequence in fault rock evolution from ultramylonite → cataclasite → foliated cataclasite → phyllonite → breccia/gouge. This sequence occurs because cataclasis in the vicinity of the fault core creates permeable pathways for the ingress of chemically active fluids into the fault zone. This leads to the replacement of load-bearing phases such as feldspar by fine-grained, foliated aggregates of intrinsically weaker phyllosilicates such as white mica and chlorite. The grain size reduction associated with both cataclasis and mineral alteration creates conditions ideal for the operation of fluid-assisted, stress-induced diffusive mass transfer mechanisms. Comparison with the findings of recent experimental studies suggest that the fault zone processes observed in the core of the MTL will lead to long-term weakening, provided the network of phyllosilicate-rich fault rocks are able to form an interconnected thin layer of weak material on kilometre- to tens of kilometre-length scales.

2.1. Introduction

Many crustal-scale fault and shear zones repeatedly localise displacements on various timescales, but the mechanical significance of such heterogeneous deformation is controversial, especially for the frictional regime in the upper crust (e.g. see Rutter et

al., 2001 and references therein). It is generally believed that such faults must be weak relative to adjacent regions of intact rock, with many authors arguing that geophysical measurements of surface heat flow and stress orientations associated with faults such as the San Andreas Fault indicate a more fundamental fault weakening in an absolute sense, i.e. these faults are characterised by anomalously low frictional strengths (e.g. Lachenbruch & Sass, 1980; Zoback et al., 1987; Zoback & Beroza, 1993; Zoback, 2000). There is a lack of consensus, however, and others have argued that such faults are in fact strong (e.g. Scholz, 2000). Part of the problem is that most of the geophysical techniques used to address these problems lack sufficient spatial resolution to identify the possible causes of weakening along the principal displacement surfaces/zones that lie within fault zones that are typically < 1 km across (Holdsworth, 2004).

Geological studies of fault rock microstructures give an insight into the evolution of deformation mechanisms and rheological behaviour of fault zones at different depths (e.g. Schmid & Handy, 1991; Snoke et al., 1998 and references therein). Studies that have focused on fault rocks formed in the upper crust (< 5 km depth) (e.g. Zoback & Lachenbruch, 1992 and references therein) have proposed that weakening may be caused by several mechanisms. These include the presence of anomalously low-friction clay gouges (e.g. Wang, 1984; Morrow et al., 1992), the development of high fluid overpressures (e.g. Byerlee, 1990; Rice, 1992; Chester et al., 1993) or dynamic mechanisms such as thermal pressurization of fluids or frictional melting (e.g. Hickman et al., 1995). However, there is often a paucity of direct geological evidence to support these theories (Scholz, 1990) and it seems unlikely that they can account for long-term weakening and reactivation of basement faults in continental settings (e.g. Holdsworth et al., 2001).

More recently, field-based research (e.g. Imber et al., 1997, 2001; Stewart et al., 2000; Gueydan et al., 2003; Collettini & Holdsworth, 2004; Wibberley, 2005) has focused on major faults where exhumation has exposed fault rocks formed at depths closer to the frictional-viscous (or brittle-ductile) transition. In this depth range rocks potentially preserve evidence of the weakening mechanisms that operate where faults cut the main load-bearing region of the crust, e.g. between 5 and 15 km. These studies, together with others of shear zone localisation and development in granitoid rocks deformed under low greenschist facies conditions (e.g. Janecke & Evans, 1988; Shea & Kronenberg, 1992; Mitra, 1984; Chester et al., 1993; Goodwin & Wenk, 1995; Wintsch et al., 1995; Hippertt, 1998; Wibberley, 1999) have suggested that the development of cohesive foliated phyllosilicate-rich fault rocks – or phyllonites – which overprint early cataclastic fault assemblages may be fundamentally important. There is an increasing body of experimental data (e.g. Shea & Kronenberg, 1993; Bos & Spiers, 2002) demonstrating that such phyllonites are potentially very weak.

The present study focuses on the development of phyllonites in the core region of the Median Tectonic Line (MTL), SW Japan (Fig. 2.1a) and presents both geological field-based and microstructural observations. The MTL in this location was chosen for study because it has been exhumed to expose good outcrops of the central regions of the fault deformed close to the frictional-viscous transition. A diverse assemblage of fault rocks formed over progressively shallower crustal conditions is preserved. Later movements have tended to overprint and dismember fault rocks formed earlier and at greater depths so that in some sections through the MTL – such as the Tsukide area (Wibberley and Shimamoto, 2003) for example – phyllonites are absent.

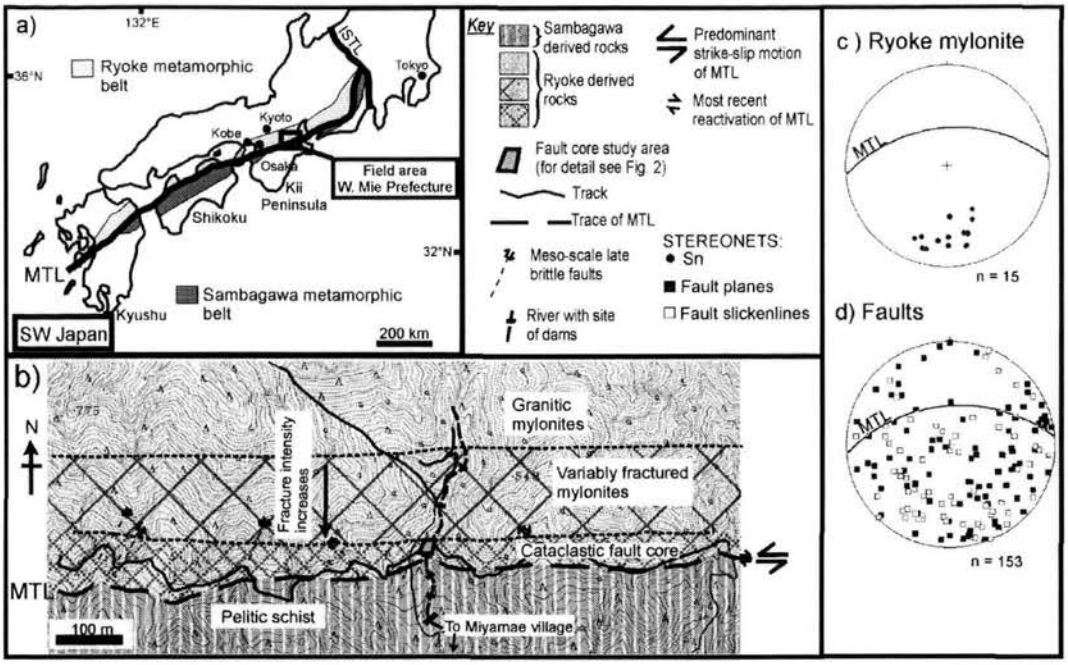

Figure 2.1. a) The Median Tectonic Line (MTL) in SW Japan showing adjacent metamorphic belts. ISTL = Itoigawa-Shizuoka Tectonic Line. b) Geological map of the MTL near Miyamae village, western Mie Prefecture. c) Stereonet showing Ryoke mylonite foliation (Sn). d) Stereonet showing meso-scale fault planes and fault slickenlines. The stereograms are lower-hemisphere equal-area stereographic projections, all data collected 350-60 m N of MTL central slip zone (CSZ).

2.2. Geological setting and structure of the Median Tectonic Line

2.2.1 Geological setting

The Median Tectonic Line is a major, crustal-scale fault in Japan that separates the low-P/high-T Ryoke metamorphic belt of subduction related granitoids with subordinate metasedimentary rocks from the high-P/low-T Sambagawa Belt of accretionary complex metasedimentary rocks (Fig. 2.1a). It has an onshore along-strike length of > 1000 km, with a displacement history reaching back at least to the early Cretaceous. Displacement estimates are uncertain and range between 200-1000 km (e.g. Ichikawa, 1980). The granitic Ryoke Belt rocks are variably mylonitized in a zone up to 5 km wide north of the MTL and formed during late Cretaceous to early-Tertiary sinistral movements. Exhumation during continued activity and reactivation of the fault has resulted in the current exposure of the fault zone displaying a wide variety of fault rocks generated at different levels in the mid- to upper-crust. Deformation associated with these sinistral displacements becomes increasingly brittle as the central part (hereafter referred to as the 'core') of the fault is approached with the development of cataclasites, breccias and gouges, many of which are foliated (e.g. Takagi, 1985, 1986; Wibberley & Shimamoto, 2003).

The MTL at the surface has a dip of around 60° N but geophysical evidence suggests that the fault shallows to around 35° from the surface to about 5 km depth (Ito et al., 1996). Previous studies in Mie Prefecture have suggested that the fault has primarily undergone sinistral strike-slip displacements (e.g. Hara et al. 1982; Ichikawa, 1980; Takagi et al., 1989; Ohtomo, 1993; Shimada et al., 1998). However, the MTL has recently been reactivated as a dextral strike-slip fault (Sugiyama, 1992), with displacements localized into incohesive fault rocks typically within a couple of

metres of the central slip zone (Okada, 1980; Research Group for Active Faults of Japan, 1991; Wibberley & Shimamoto, 2003).

2.2.2 Structural history and protoliths

In SW Japan, two contrasting protoliths occur either side of the MTL – Ryoke Belt granitoids to the north and Sambagawa Belt semi-pelitic schist to the south. Formation of the high-angle MTL and sinistral strike-slip displacements occurred during the early Tertiary (e.g. Ichikawa, 1980; Hara et al., 1980; Ohtomo, 1993 and references therein). Outside of this region of sinistral shear, the Ryoke granitoids in a zone up to 5 km wide are thought to preserve evidence of mylonitisation that occurred during an earlier late Cretaceous to earliest Tertiary sinistral top-to-south, sub-horizontal shearing event that pre-dates the formation of the high-angle MTL (Ohtomo, 1993; Yamamoto & Masuda, 1987; Sakakibara et al., 1989; Michibayashi & Masuda, 1993). From measurements of grain size for recrystallized quartz grains, Ito (1978) concluded that the effects of the late Cretaceous to earliest Tertiary mylonitisation in the Ryoke granitic rocks are recognised in a 5 km wide zone north of the MTL. The granitic mylonites have a mean grain size of ~1 mm and are composed of quartz, K-feldspar, plagioclase, hornblende and biotite. Quartz veins are common, are often discontinuous and range in size from the cm to metre-scale. Detailed studies of the Ryoke mylonitic rocks are presented by Hayama & Yamada (1980), Takagi (1985), Sakakibara (1995), Shimada et al. (1998) and references therein.

The Sambagawa protolith to the south of the MTL is typically a semi-pelitic schist composed primarily of quartz, white mica and feldspar (albite). The schist is very fine-grained, with albite forming primarily as porphyroblasts set within a fine-

grained quartz-mica matrix, with a grainsize of < 0.2 mm. The petrology (e.g. Enami et al., 1994) geochronology (e.g. Dallmeyer et al., 1995) and structure and tectonic evolution (e.g. Hara et al., 1980; Wallis et al., 1992) of the Sambagawa Belt are all well characterised.

The MTL *fault core* in the Mie Prefecture is defined by the zone of intense brittle deformation and alteration related to the formation of cataclasite and phyllosilicate-rich fault rocks during steeply dipping strike-slip motion along the faulted contact between the Ryoke and Sambagawa belts. The cataclastic deformation overprints earlier mylonites and is interpreted as having formed during continuous strike-slip deformation at progressively shallower crustal conditions (Takagi, 1986). The distribution of deformation in the core is highly asymmetric in the wall-rock protoliths. On the northern side of the MTL, the fault core is ~50 metres wide and a zone of variably fractured and faulted granitic mylonites continues for a further 200-250 m northwards (Fig. 2.1b). Within the Sambagawa rocks, however, foliated cataclastic fault rocks occur in a poorly exposed zone < 15 m wide.

2.3. Fault zone structure and fault rocks of the Median Tectonic Line, Mie Prefecture

2.3.1 MTL fault zone structure in the Miyamae Village area

The present study focuses on the well-exposed fault rocks on the northern side of the MTL, which are derived from Ryoke protoliths in the region above Miyamae village, Iitaka-cho, Matsusaka-shi, Mie Prefecture (Fig. 2.1b). Ryoke granitic mylonites exposed at distances > 300 m north of the central slip zone (Fig. 2.1b) have a mean grain size of ~0.45 mm and contain both K-feldspar and plagioclase (albite after andesine-oligoclase) porphyroclasts, set in a matrix of feldspars, quartz,

hornblende and biotite. There is some alteration of the feldspars to white mica, and hornblende and biotite to chlorite. The mylonitic foliation trends east-west (086), with an average dip of 61°N (Fig. 2.1c), and a mineral lineation is occasionally seen moderately plunging toward the east (Takagi, 1985, Shimada et al., 1999). Ductile microstructures including asymmetrically wrapped feldspar porphyroclasts and oblique foliations developed in recrystallized quartz aggregates elsewhere suggest sinistral reverse senses of shear (Shimada et al., 1999).

At distances less than 300 m north of the central slip zone, the earlier mylonitic textures are progressively overprinted by cataclastic deformation (see Table 2.1). From a distance of 100 m, faults are widespread and have a wide array of orientations (Fig. 2.1d) and are mutually cross-cutting so that no specific generations of faulting can be defined. The highly faulted core begins ~50 m north of the central slip zone and is well exposed in the north-south trending Fukaya River sections (Fig. 2.2a-b). Cataclastic fault rocks derived from ultramylonite are predominant, but foliated cataclasites and phyllonites are also present. Located 2 m north of the central slip zone, a distinctive orange-stained cataclasite occurs that is extremely altered with no original mylonitic features or textures preserved. Within the fault core, epidote veins are no longer visible, but cm-scale carbonate veining becomes extensive (Table 2.1).

The central slip zone, or plane of most recent slip, is a 1 cm wide gouge that cross cuts all other structures. The plane strikes east-west (085) and dips 59° toward the north. The gouge is extremely fine grained with SEM studies revealing a quartz, feldspar, kaolinite, chlorite, smectite and occasionally illite mineralogy (Takagi 2005, personal communication). Orange- and black-coloured incohesive foliated cataclasites and gouges occur for approximately 2 m either side of the central slip zone and are

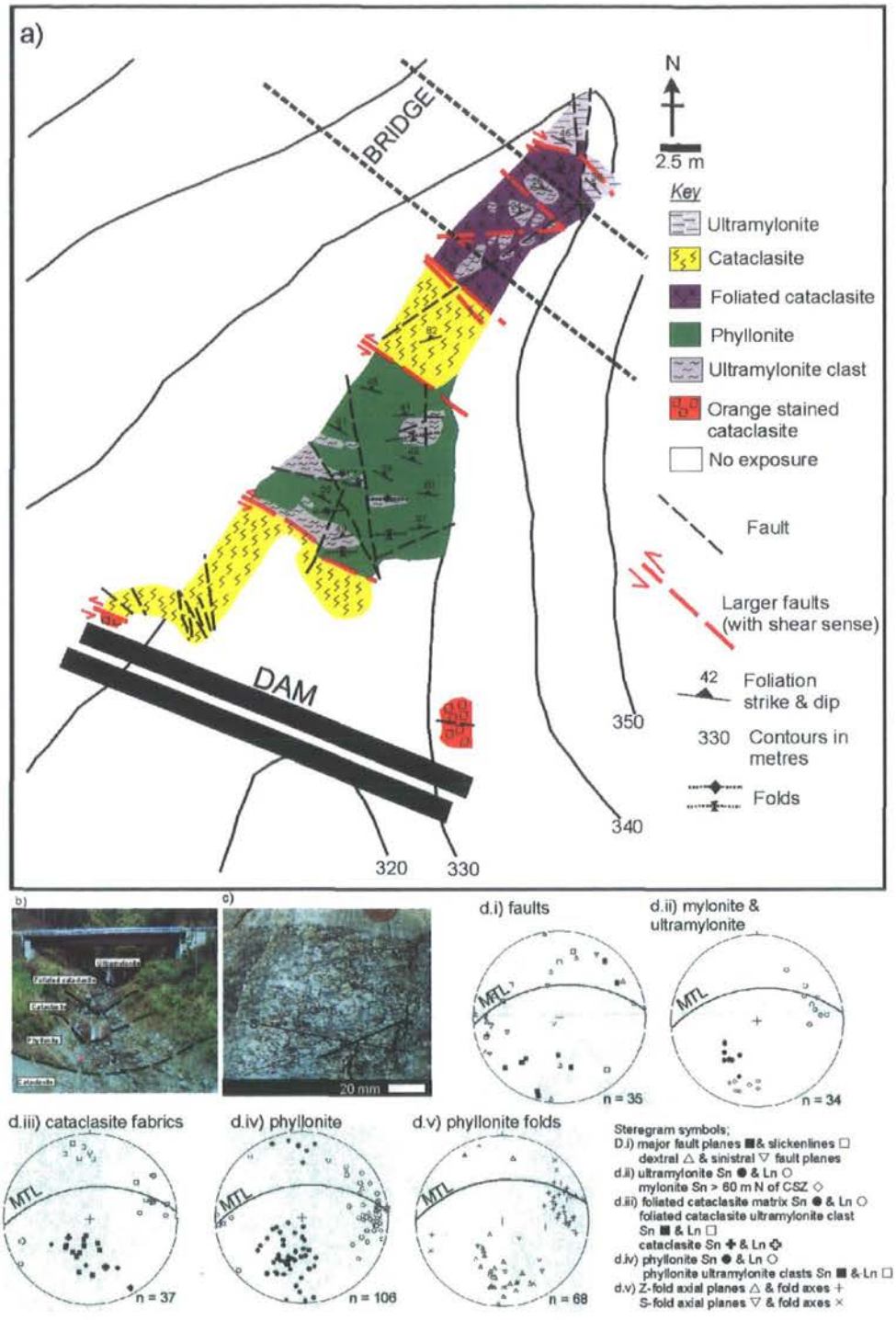

Figure 2.2. a) Simplified geological map of the MTL fault core. For further explanation see text. b) Photograph of the river section, taken from the top of the dam looking toward the north; the orange stained cataclasite in southern most part of map in (a) is out of view. c) Photograph of Ryoke granitic mylonite. d) Stereograms showing structural data on faults and fault rock deformation fabrics, Sn = foliation, Ln = mineral lineation, CSZ = central slip zone.

		VARIABLY FRACTURED MYLONITES					FAULT CORE	
Distance N of CSZ	350 m	300 m	250 m	200 m	150 m	100 m	50 m UM ⟵ P ⟶	0
Grainsize mm	0.45	0.4		0.12		0.8	0.03	0.01 <1.5
Hornblende + biotite %	5%	2.5%		<2%		<1.5%	0%	Absent
White mica %	2%	3-4%		4%		7%	30%	*8%
Chlorite %	5%	5%		6%		8%	10%	30%
K-feldspar : albite ratio	50:50	45:55		42:58		40:60	No K-feld'	
Veining	cm-scale epidote veins extensive			cm-scale epidote & calcite			Extensive cm-scale calcite veins	
Lineation	Weak elongated quartz			Weak elongated quartz			Very strong chlorite lineation	
Foliation	Weak	Good flattening & elongation of grains		Strong flattening of grains			Very strong grain flattening &chlorite alighnment	
Intensity of feldspar cataclasis	Mild	Mild with alteration of K-feld' to white mica		Extensive			Less fracturing of remaining albite, more alteration to white mica	
Intensity of faulting/ cataclasis	Weak fracturing	Weak fracturing		Widespread		Fracture & fault intensity increases	Strong intensive cataclasis	

Table 2.1. Showing textural and mineralogical changes with decreasing distance to the MTL central slip zone (CSZ). Compiled from field observations, optical microscopy, SEM and whole-rock XRF analyses. UM = indicates location of ultramylonite on the northern edge of the fault core, ⇦ P ⇨ = indicates location of phyllonitic overprint within the fault core. ✱ = note that the white mica content partly appears to decrease from ultramylonite to phyllonite due to the large increase in precipitated chlorite in the latter unit.

composed of quartz, calcite, white mica and chlorite. All these fault rocks locally preserve evidence for dextral Riedel shears and asymmetrical tails deflected around larger clasts (cf. Wibberley & Shimamoto, 2003).

The Sambagawa-derived rocks to the south of the MTL are poorly exposed and comprise a narrow, < 15 m wide zone of foliated gouge and cataclasite composed primarily of quartz, white mica and opaques.

2.3.2 Fault rocks of the MTL core: the Fukaya River Section

The north-south trending Fukaya River preserves a 50 m wide, almost completely exposed across-strike section of the Ryoke-derived fault rocks in the MTL core region north of the central slip zone (Fig. 2.2a -b). The exposure lies to the north and up-stream from a dam and extends northward beneath a logging road bridge, for approximately 50 m before reaching a waterfall where it becomes no longer passable (Fig. 2.2b).

2.3.2.1. Faults

Brittle faults often form the boundaries between different fault rock units exposed in the stream section and in some cases are marked by steep scarps and waterfalls (Fig. 2.2a-b). Most of the larger faults strike ESE, oriented at a low angle to the MTL central slip zone with moderate to steep northward dips. Where visible, slickenlines consistently indicate oblique sinistral motion with downthrows to the north (Fig. 2.2di). Collectively these faults appear to cause considerable lateral variations in fault rock distributions along strike (see also Wibberley and Shimamoto, 2003). Smaller faults appear to be mutually cross-cutting and show an array of

orientations and senses of shear, oriented at both high and low angles to the central slip zone of the MTL (Fig. 2.2di).

2.3.2.2. Ultramylonite

More-or-less intact ultramylonites crop out at the northern end of the section, and are contained as relict clasts in all the other fault rock units. Hence, they are thought to form the protolith for most of the other fault rocks preserved in the section (Fig. 2.2a-b). The ultramylonites typically weather to a grey-dark green colour and fracturing gives the rock a blocky appearance, with little or no veining visible. Other outcrop-scale features such as shear criteria are difficult to distinguish due to the very fine-grained nature of the rock (grain size ~0.01 mm), but a strong ultramylonitic foliation (mean 126/45N) defined by quartz-rich and quartz-poor domains and mineral lineation (mean 32/071) defined by alignment of white mica and chlorite are recorded (Fig. 2.2dii).

2.3.2.3. Cataclasite

Pale grey-green, unfoliated cataclasites (Fig, 2.3d) are derived from ultramylonite and are strictly proto-cataclasites as they have < 50% cataclasite matrix (Schmid and Handy, 1991). Two units occur either side of the phyllonite exposed in the river section (Fig. 2.2a-b), both being bounded by sinistral-oblique faults.

2.3.2.4. Foliated cataclasite

The foliated cataclasite forms a fault-bounded unit 13 m wide sandwiched between ultramylonite and cataclasite (Fig. 2.2a). The foliated cataclasite (~40% clast, 60% matrix) contains numerous clasts of fractured ultramylonite up to 3.5 m across,

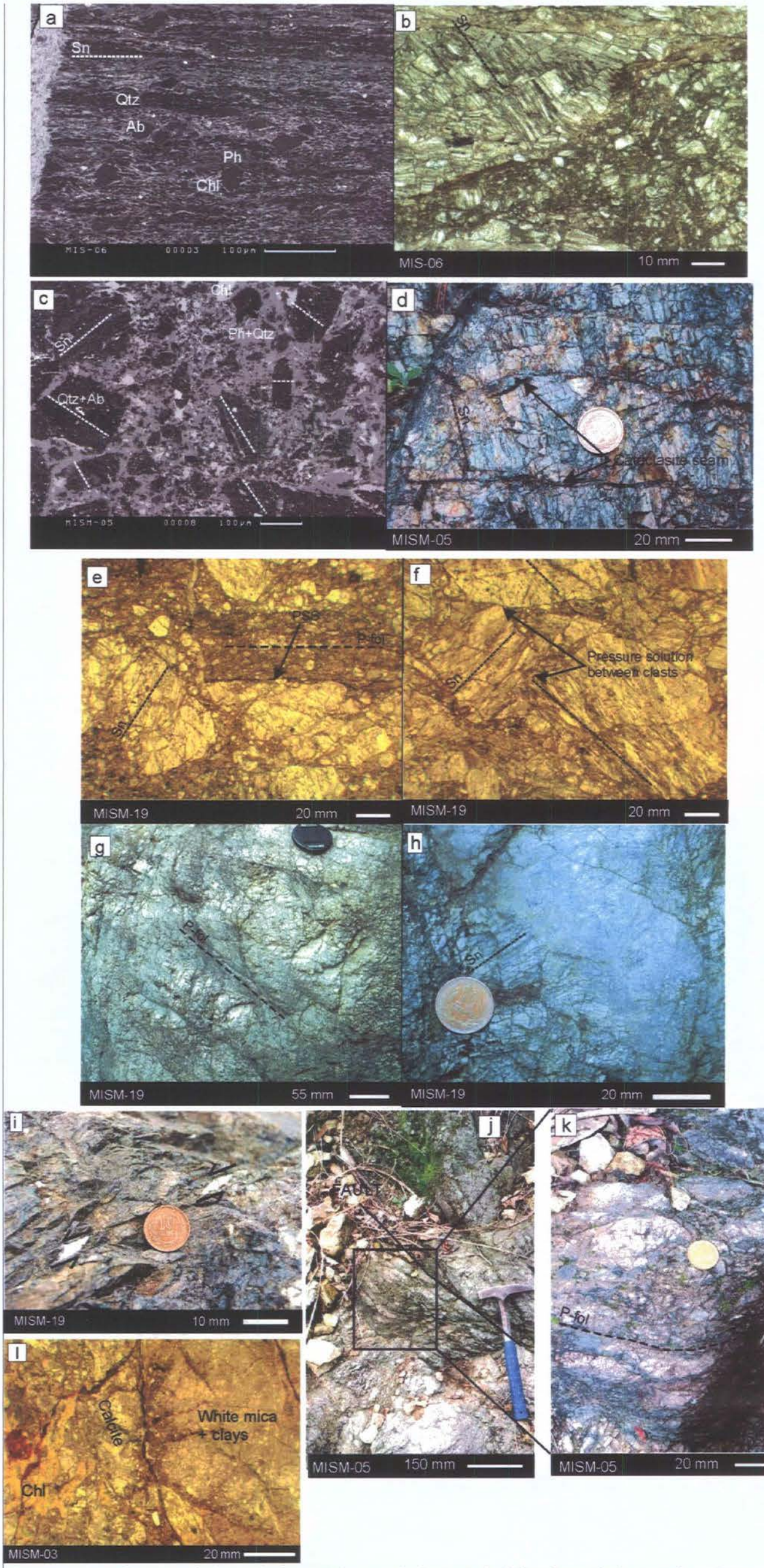

Figure 2.3. Key features of ultramylonite (a & b), cataclasite (c & d), foliated cataclasite (e to k) and orange stained cataclasite (l) within the MTL fault core. a & c SEM backscatter images. b, e, f & l plane polarised light thin section images. d, g, h, i, j & k field photographs. PSS = pressure solution seams, P-fol = phyllosilicate foliation, Sn = foliation, Qtz = quartz, Ab = albite, Ph = phengite, Chl = chlorite.

set in a fine-grained cataclasite matrix (mean grain size <0.5mm). Larger clasts have been individually mapped (Fig. 2.2a). The foliated cataclasite matrix is dark green and clasts have a milky white colour (Fig. 2.3g-h). Within the matrix, a weak foliation has begun to develop and clasts are often elongated parallel to this weak foliation with typical aspect ratios of 2:1. The foliations in the ultramylonite clasts (mean 105/32N) and cataclasite matrix (mean 101/34N) have a similar orientation (Fig. 2.2diii). A mineral lineation defined by phyllosilicates (white mica, chlorite) is locally preserved in the foliated cataclasite (mean 17/094), whilst relict mineral lineations in ultramylonite clasts plot as two clusters plunging shallowly north (23/354) and east (22/074) (Fig. 2.2diii). Within the foliated cataclasite cm-scale sinistral pull-apart structures infilled with calcite are observed (Fig. 2.3i). Together with the shallowly plunging lineation, these features are taken to indicate that the foliated cataclasite formed during sinistral top-to-the-south shearing along the MTL.

2.3.2.5. Phyllonite

In outcrop, the phyllonite has a distinctive dark green colouration due to high chlorite content and a strong ESE-striking foliation (mean 107/45N). The foliation is defined by a fine mm-scale compositional banding of alternating phyllosilicate-rich layers and quartz-feldspathic microlithons of ultramylonite, with numerous sub-parallel discontinuous very fine grained quartz-rich layers up to ~10 cm thick (Fig. 2.2div). The latter units are thought to represent relict (i.e. pre-phyllonite formation) quartz veins (cf. the vein in Fig. 2.4d). Phyllonite grainsize is typically < 1.5 mm. A well-preserved, shallowly eastward plunging mineral lineation is defined by the alignment of chlorites (mean 18/083) (Fig. 2.2div). Shear criteria associated with these fabrics are consistently sinistral and include asymmetrically wrapped quartz

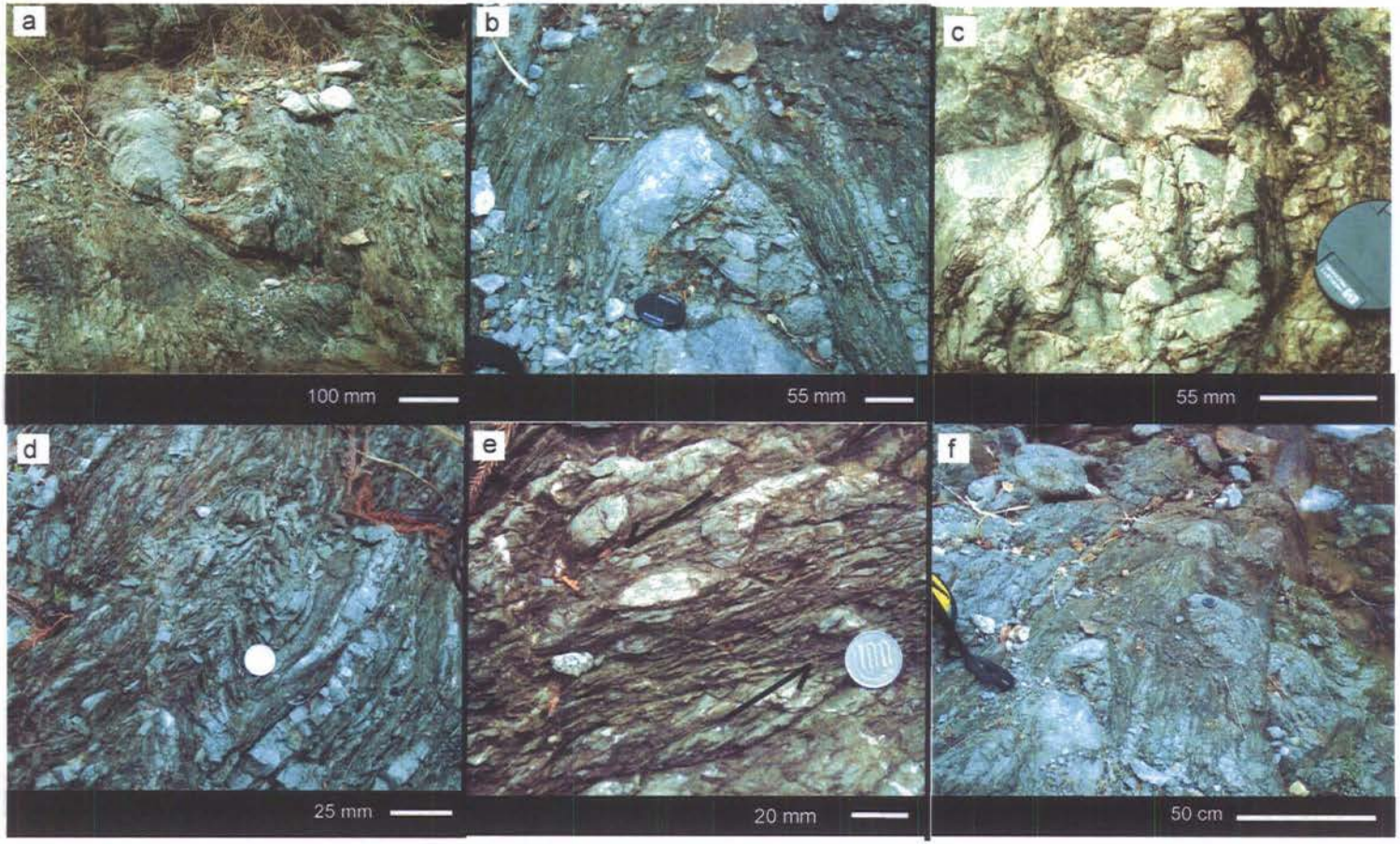

Figure 2.4. Field observations of phyllonite within MTL fault core. a & b) phyllonite enveloping ultramylonite lenses. c) phyllonitic fabric developing along fractures through an ultramylonite lens. d) cm-scale folds within the phyllonite. e) sinistral shear bands. f) metre-scale fold, looking down fold hinge.

segregations/veins and low-angle shear bands (Fig. 2.4e). Numerous augen and lenses of brittle fractured ultramylonite identical in appearance, composition and texture to the clasts found in the adjacent units of cataclasite occur within the phyllonite (Figs. 2.2a and 2.4a-b). The augen/lenses range in length from less than 1cm to over 1 metre and are strongly wrapped by and elongated within the main foliation, with typical aspect ratios of 11:1 (Fig. 2.4a-b). In general, ultramylonite foliations and lineations within the clasts have been reoriented so that they are now sub-parallel to those in the enveloping phyllonites (Fig. 2.2div). Within many clasts, a phyllonitic foliation is localised along the traces of cross-cutting pre-existing brittle fractures (Fig. 2.4c).

The phyllonite is highly folded by close to tight brittle-ductile fold structures on centimetre- to metre-scales. Dextral-verging folds dominate over sinistral-verging structures (Figs. 2.2dv and 2.4d). Dextral folds have moderately- to steeply-dipping northward axial planes (mean 091/60N), and gently to moderately (10-50°) eastward plunging fold hinges. Brittle-ductile dextral shear bands/Riedel shears with cm- to m-spacing are locally developed in areas unaffected by folding, whilst dextral faults possibly equivalent to P-shears locally offset dextrally-verging fold pairs. These late folds and brittle-ductile dextral shears (Fig. 2.4d and f) are absent elsewhere in the fault zone in Miyamae. However, similar dextral structures are present in incohesive foliated cataclasites/gouge at Tsukide (Wibberley and Shimamoto, 2003).

2.3.2.6. Orange-stained cataclasite

The orange-stained cataclasite crops out in isolated exposures next to the dam (Fig. 2.2a). Its age relative to the other fault rocks exposed in the section is uncertain. The distinctive orange colour appears to result from the weathering out of iron oxide

and it is relatively incohesive. Cataclasite and alteration are pervasive with few protolith features or textures recognisable.

2.3.3. Mineralogy and microstructures

2.3.3.1. Ultramylonite

These rocks are typically composed of quartz and albite porphyroclasts (~50 μm across) set in a matrix of very fine-grained (~10 μm) albite, quartz, phengitic white mica and chlorite. The phyllosilicate grains are strongly aligned defining the strong foliation that wraps around the porphyroclasts (Fig. 2.3a). Throughout many samples there are alternating chlorite-rich and white mica-rich domains. The ultramylonites are variably brecciated (e.g. Fig. 2.3b) with the local development of cataclasite identical in texture and composition to those found in the more internal regions of the fault core. Electron micro-probe analyses reveal that albite porphyroclasts are extensively altered to white mica of the same phengitic composition as that found within the matrix of both the ultramylonite and cataclasites. The ultramylonitic foliation is cross-cut by veins of little deformed carbonate (mainly calcite) in places intergrown with chlorite. Electron microprobe data show that the chlorite associated with the calcite veins is slightly enriched in Fe relative to the chlorite in the ultramylonite matrix.

2.3.3.2. Cataclasite

Mineralogically, the cataclasite and the ultramylonite are very similar. Microprobe analysis reveals that comparable varieties of Fe-rich chlorite, phengitic white mica (Fig. 2.5), albite, quartz and calcite occur throughout. However the albite is more extensively altered to phengite plus quartz in the cataclasites. In thin section,

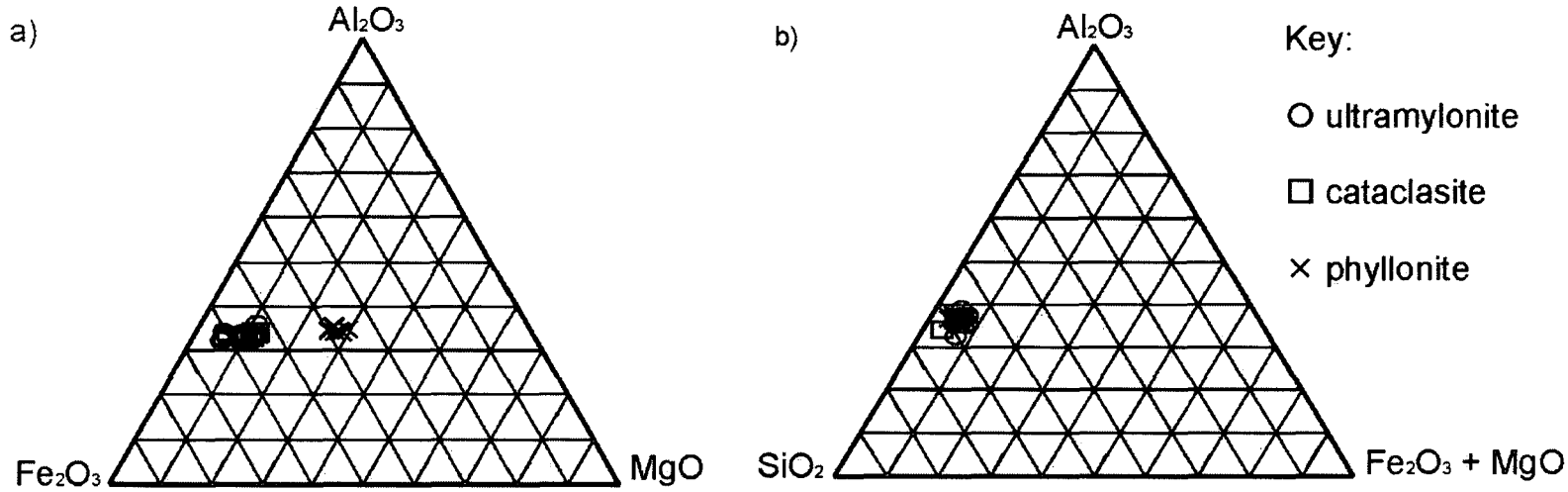

Figure 2.5. Ternary diagrams to show a) comparative Al_2O_3-Fe_2O_3-MgO content of chlorite and b) Al_2O_3-SiO_2-Fe_2O_3+MgO content of phengitic white mica within the MTL fault core ultramylonite, cataclasite and phyllonite. Data obtained from microprobe analysis.

the cataclasite is texturally distinct comprising angular fractured blocks of ultramylonite (ranging from ~50 μm upwards) within which small flecks of chlorite and white mica most prominently define the ultramylonitic foliation. The ultramylonite blocks typically sit within a very fine-grained (~3-10 μm) cataclasite, or locally 'ultracataclasite' matrix. Rotation of these blocks has occurred so that the ultramylonitic foliation is often randomly oriented (Fig. 2.3c). The matrix is primarily composed of phengitic white mica plus comminuted quartz. Fluid-assisted mineral reactions have resulted in extensive alteration of the original mineralogy to a fine-grained aggregate of phyllosilicate (white mica, chlorite) and quartz. Chlorite aggregates also occur as infills along the numerous fractures throughout the cataclasite. In hand specimen, these often appear as thin dark seams coating fracture surfaces (Fig. 2.3d). Fluid infiltration appears to have been greatest in the finest grained parts of the matrix based on the distribution of secondary alteration in thin section and SEM images.

2.3.3.3. Foliated Cataclasite

The angular and irregular shaped clasts of cataclastically-deformed ultramylonite within the foliated cataclasite are set in a fine-grained (~5 μm) matrix made up primarily of phyllosilicate (chlorite and white mica) plus some comminuted quartz. There is widespread textural evidence for the operation of pressure solution, particularly at the interfaces between clasts and matrix (e.g. Fig. 2.3e-f), where sub-parallel dissolution seams define the weak foliation seen in outcrop (Fig. 2.3g). On the cm-scale, the clasts are often slightly elongate parallel to the foliation due to a combination of mechanical rotation and the effects of distributed extensional microfaulting within clasts (Fig. 2.3g).

As the foliation in the cataclasites intensifies, the rocks become progressively more phyllonitic, i.e. rich in aligned chlorite and white mica. These regions of 'proto-phyllonite' initially localise adjacent to earlier brittle fractures that cut through the cataclasites (Fig. 2.3j-k). The foliation is also generally more intense in the finest grained areas of cataclasite matrix.

2.3.3.4. Phyllonite

The strong phyllonitic foliation is defined primarily by the alignment of grains of chlorite and phengitic white mica. Chlorite locally constitutes up to 30% of the phyllonite and its grain size (reaching ~30-40μm) is up to four times larger compared to the chlorite in fault rocks described previously. This gives the rock a distinctive green colour and a high sheen to foliation surfaces. White mica constitutes approximately 5-8% of the phyllonite, of which approximately half formed as an alteration product from albite, occurring both wrapped around albite grains and along feldspar cleavage planes. The remainder of the phyllonite is made up of varying proportions of quartz, albite, calcite (mainly occurring in veins) and opaques. The ultramylonite microlithons and quartz-rich layers (relict quartz veins) appear much brighter in thin section and have low proportions of phyllosilicate. They have undergone intense dynamic recrystallization presumably during the earlier development of the ultramylonite. During phyllonite development, these units appear to have undergone little internal deformation other than fracturing and cataclasis.

The ultramylonite lenses are internally cataclastically deformed (Fig. 2.6a) and this often helps to extend and break up the lenses along the phyllonitic foliation. Fractures are infilled with calcite and chlorite, and any areas of fine-grained cataclasite matrix are replaced by fine-grained chlorite (Fig. 2.6b).

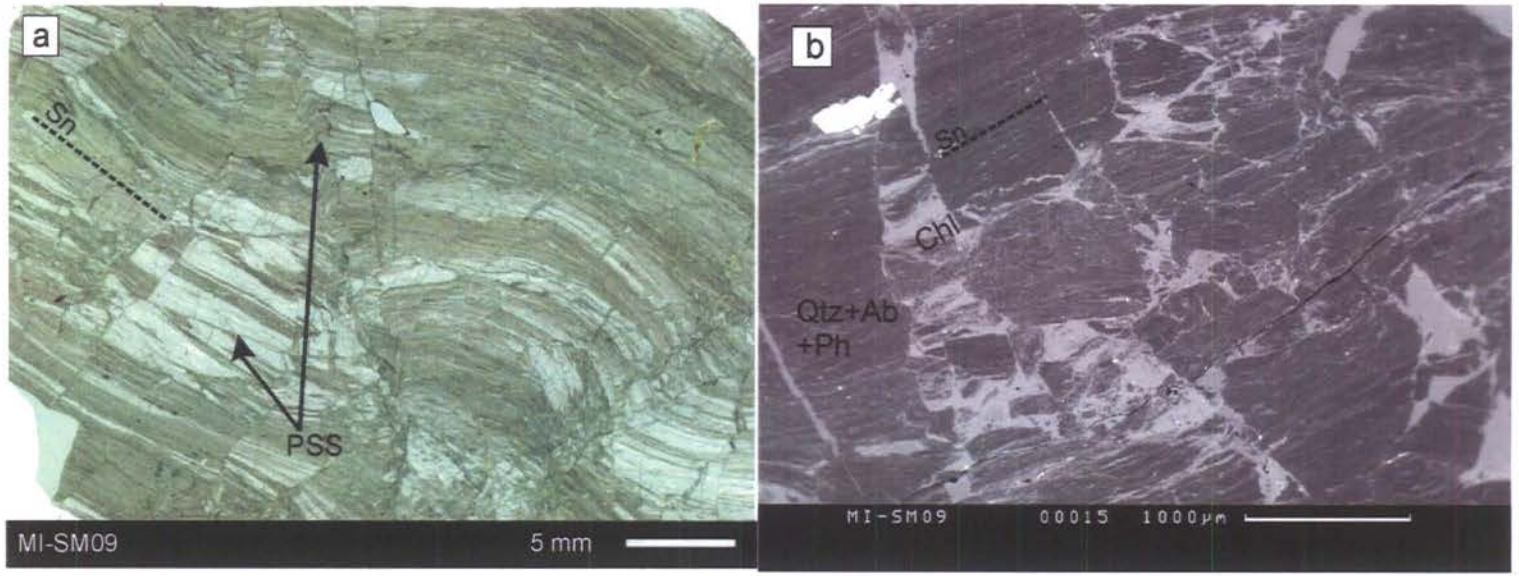

Figure 2.6. Images of an ultramylonite lens within the phyllonite. a) plane polarised light thin section image of ultramylonite lens. b) SEM back scatter image of fractured section of ultramylonite lens.

Compared to the fault rocks described previously, the phyllonites display much more evidence for pervasive fluid-assisted alteration and diffusive mass transfer. Albite porphyroclasts are typically brown and cloudy in appearance, as they have been partially altered to fine-grained aggregates of fibrous white mica (Fig. 2.7a). Microprobe analyses show that the white mica has a phengitic composition similar to that found in the ultramylonite and cataclasites (Fig. 2.5b). Pressure solution seams and fibrous overgrowths of white mica have developed widely adjacent to relatively more rigid porphyroclasts of albite (Fig. 2.7a-b). Significantly, the chlorite that defines the phyllonitic foliation contains less FeO and a much higher proportion of MgO compared to the chlorite that occurs within the ultramylonites, cataclasites and foliated cataclasites (Fig. 2.5a). This is consistent with the observation that the phyllonitic foliation overprints the previously formed fault rocks and suggests that a distinct, later phase of chlorite growth is associated with the phyllonite development. The highly altered albite porphyroclasts are increasingly flattened and elongated parallel to the network of chlorite grains that predominantly define the grain-scale foliation in the phyllonites. In addition, larger clasts of original ultramylonite occur, often with sub-angular shapes (Fig. 2.7c). These clasts are predominantly composed of phengitic white mica and quartz, at least some of which is derived from the breakdown of original albite. Viewed under higher magnifications, the white mica is often clearly seen to preferentially replace albite along cleavage planes (Fig. 2.7d).

Chlorite grains are inter-grown with lesser amounts of phengitic white mica (at an approximate ratio of 6:1) and form anastomosing, interconnected layers on mm- to μm-scales that bound and wrap porphyroclasts and fractured lenses of ultramylonite, mirroring what is seen on the outcrop-scale. The chlorite bounding these porphyroclasts and fractured lenses defines seams <0.5 mm in width running

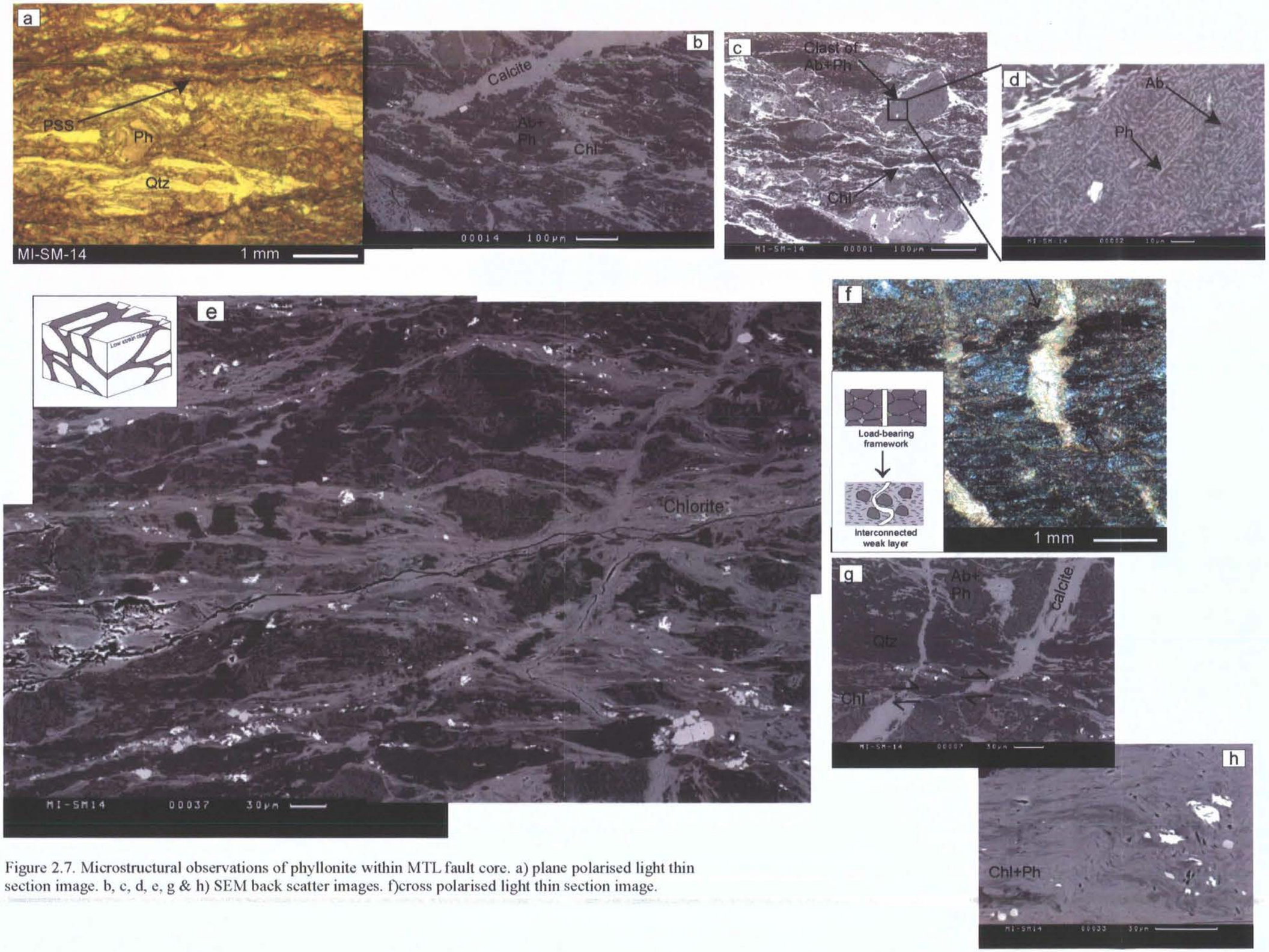

Figure 2.7. Microstructural observations of phyllonite within MTL fault core. a) plane polarised light thin section image. b, c, d, e, g & h) SEM back scatter images. f)cross polarised light thin section image.

through the phyllonite that form an interconnected network or layer (Fig. 2.7e). Within the phyllonite, calcite veins form at high angles (~90°) to the phyllonitic foliation, and are locally folded (Fig. 2.7f).

In thin section, many phyllonite samples show evidence for discrete fault-like offsets developed parallel to the main phyllosilicate foliation. Some calcite veins are offset with dextral senses of shear when crossing chlorite-rich bands (Fig. 2.7g). Shearing often leads to recrystallization of carbonate grains as the veins are progressively smeared out into the foliation. There are, however, examples of cross-cutting calcite veins unaffected by such processes. When viewed in SEM, thicker bands of intergrown chlorite and white mica have locally developed mm- to μm-scale, dextrally-verging folds (Fig. 2.7h). The fold hinges appear angular with kinking of individual phyllosilicate grains (Fig. 2.7h) suggesting semi-brittle conditions with frictional slip along phyllosilicate-foliae.

2.3.3.5. Orange-stained cataclasite

In thin section, few features are observed due to the extremely highly altered nature of the cataclasite (Fig. 2.3(l)), although a few relict ultramylonitic textures are locally preserved. The rock is heavily altered to very fine-grained (~5 μm) alteration products including white mica and clay minerals at the expense of albite. Carbonate and chlorite veining is observed on cm- to mm-scales.

2.3.4. Major element geochemistry

XRF whole-rock major-element analyses of selected fault rocks collected from the Fukaya River section were carried out to assess what changes in bulk geochemistry occur with fault rock evolution subsequent to the early mylonitisation

associated with the MTL (Fig. 2.8). These data illustrate a coherent series of chemical changes that are consistent with the observed changes in fault rock mineralogy as one passes from ultramylonite to cataclasite and ultimately phyllonite. There are significant gains in Fe_2O_3, MgO and LOI and decreases in Na_2O and SiO_2 that are likely related to the breakdown of anhydrous phases such as feldspar to hydrous minerals such as phengitic white mica and the widespread growth of chlorite, especially the relatively MgO-rich variety found exclusively in the phyllonites. All these changes are likely to be induced by the action of syn-tectonic fluids as they passed through the fault zone.

2.4. Discussion

2.4.1. Fault rock sequence, cataclasis and fluid flow

A complex fault sequence is associated with the development of the MTL reflecting the interplay of deformation mechanisms under changing P-T conditions, fluid influx, textural feedback processes and ongoing changes in mineralogy (Table 2.2) The earliest fault rocks associated with MTL deformation in the Ryoke belt are mylonites (Hayama & Yamada, 1980; Takagi, 1985; Sakakibara, 1995; Shimada *et al.*, 1998 and references therein). Lineations are generally shallowly plunging, suggesting that strike-slip movements are dominant and shear criteria are uniformly sinistral. Using quartz microstructures, lattice preferred orientations and geothermometry, Sakakibara (1995) concluded that mylonitisation of the Ryoke granitoids occurred over a temperature and pressure range of 470-350°C and 4-5 Kb, broadly equivalent to lowermost amphibolite to upper greenschist facies. He also proposed that, during their formation the mylonites were exhumed from approximately 18 to 11 km depth. The localised preservation of fibrous overgrowths

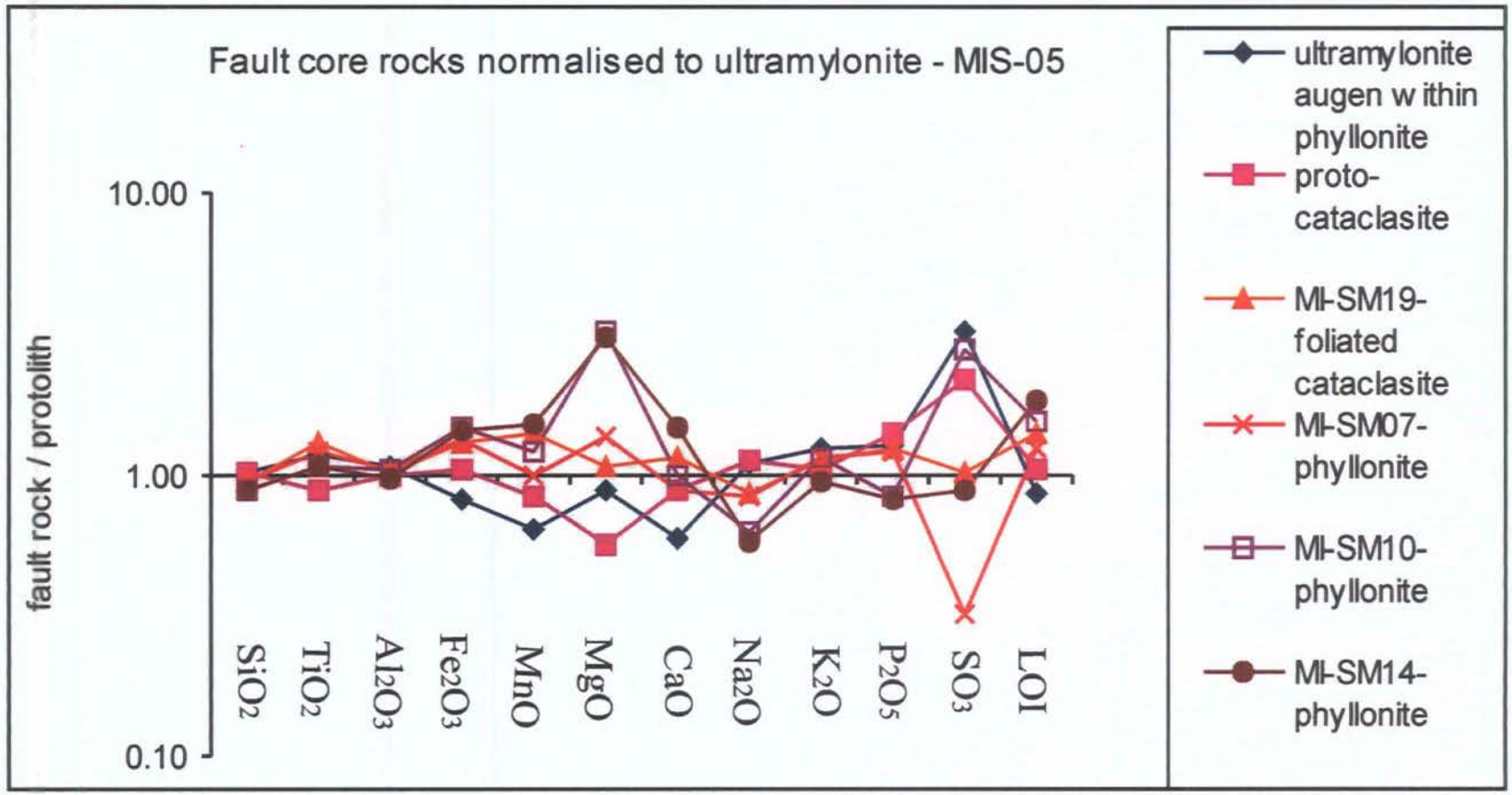

Figure 2.8. Plot showing XRF whole-rock major-element analyses for the main representative fault rock types from the MTL fault core normalised relative to ultramylonite, the earliest recognised rock in the fault core.

	MYLONITE	ULTRAMYLONITE	CATACLASITE	FOLIATED CATACLASITE	PHYLLONITE	MESO-SCALE FAULTING	CSZ & GOUGE
MOVEMENT SEQUENCE	1	2	3	4	5 & 8	3-7	8
KINEMATICS	← Sinistral shear →				Late dextral reactivation →		
DOMINANT DEFORMATION MECHANISMS	Crystal plasticity	Crystal plasticity & grain boundary sliding	Cataclasis	Cataclasis, DMT, cataclasis, fracture & frictional sliding μfn = 0.6-0.8	DMT & frictional sliding μfn = ~0.2	Fracture & frictional sliding μfn = 0.6-0.8 →	
METAMORPHIC PROCESSES		← Enhanced fluid influx →					
		← Breakdown of anhydrous phases i.e. Albite to white mica →				Dismembering fault rock units	
					← New growth of Mg-rich chlorite →		
RHEOLOGY				← Reaction softening & weakening due to onset of DMT - - - →			
				← - - - Frictional-viscous behaviour inferred →			

Table 2.2. Summary table to show the sequence of fault rock deformation within the MTL fault core, the associated deformation mechanisms, metamorphic processes and their rheological implications. μfn = coefficient of friction.

in some ultramylonite samples (Fig. 2.3a) may indicate that the onset of diffusion mechanisms was triggered by grainsize reduction due to dynamic recrystallization (cf. White *et* al., 1980; Schmid & Handy, 1991).

The ultramylonite developed close to the MTL fault core has subsequently undergone cataclasis, presumably at lower temperatures and pressures. The microstructural evidence from thin section and SEM studies, together with the observed major element geochemical trends suggest that focused influx of fluid into the fault core has occurred. This was presumably facilitated by fracturing and grain-scale dilatancy during cataclasis. This influx appears to have been greatest in the finest grained regions of cataclasite matrix, and in regions along and immediately adjacent to pre-existing brittle fractures. As a result, phyllosilicate precipitation and the development of phyllonitic fabrics initially localises within those sections of the fault core more affected by cataclastic deformation as illustrated on cm scales by the textures preserved in the foliated cataclasite of the MTL fault core. It is proposed that further fluid influx and phyllosilicate precipitation eventually converted the foliated cataclasite into phyllonite. Thus the observed fault rock alteration sequence is driven by the progressive and continuous influx of fluid into the fault zone on the northern side of the MTL, a process at least initially facilitated by fracturing and associated grain-scale dilatancy related to the onset of brittle faulting and cataclasis.

2.4.2. The onset of diffusive mass transfer deformation mechanisms and metamorphic processes

In parallel with the progressive alteration of fault rocks, fluid-assisted diffusive mass transfer increasingly begins to operate within the cataclasite as it evolves into phyllonite. Characteristic source microstructures, e.g. pressure solution seams and

grain dissolution features, and sink microstructures, e.g. fibrous mineral overgrowths, are widely preserved. Such stress-induced dissolution and precipitation processes are likely to have been triggered by the fine grain sizes in crushed-up cataclasites and by the presence of an active fluid phase. It is likely to have been enhanced still further by the growth of new secondary mineral phases during alteration. Importantly, the localisation of alteration and the onset of fluid-assisted diffusional mechanisms adjacent to pre-existing fractures and fine-grained zones of cataclasis allows rapid development of interconnected layers of phyllosilicate on all scales (e.g. Figs 2.4a and 2.7c, e).

A number of fluid-assisted retrograde metamorphic reactions are likely to have played an important role in the development of the MTL fault rock suite. Most significantly the Ryoke granitic mylonites 350-100 m north of the MTL central slip zone contain both K-feldspar and albite in approximately equal proportions. Combined optical mineralogical and SEM studies of samples collected in the fault core – including the ultramylonites - indicate that K-feldspar is no longer present and that all the feldspar remaining is of an albitic composition. This suggests either that the protolith has a more tonalitic composition close to the MTL core (Ito, 1978), or that albitisation of the K-feldspar occurred, along with phengite production (e.g. van Staal *et al.*, 2001), or that K-feldspar breakdown to phengite occurred directly. In the latter two cases, the reactions most likely began synchronous with the development of the ultramylonites close to and within the core region of the MTL due to the influx of fluids. However, microprobe and SEM studies within the cataclasites and phyllonites of the core show that phengitic white mica of essentially identical composition is *also* being formed due to the widespread retrograde breakdown of individual albite grains. This is consistent with a decrease in Na within the cataclasites and phyllonites of the

fault core relative to both the ultramylonite (Fig. 2.8) and the wall rock Ryoke protoliths (see Table 2.1).

The observed sequence of fault rock overprinting implies that the K-feldspar breakdown to phengite accompanying development of the ultramylonites is post-dated by albite alteration to phengite to generate the phyllonites. This sequence is strikingly similar to those described by Wibberley (1999) from granitoid thrust fault zones of the Pelvoux Massif, external Western Alps, and by Van Staal *et al.* (2001) from the shear zones of the Spruce Lake nappe in Canada. It may be a common feature of fluid-assisted retrograde metamorphism in collision/subduction-related tectonic settings. In addition, it has already been noted that the dominant chlorite in the phyllonites has a distinctly higher Mg composition compared to that in the adjacent ultramylonite and cataclasites. The observed changes in modes of retrograde metamorphism and chlorite composition likely reflect changes in fluid compositions or other environmental conditions such as temperature and pressure (e.g. Cathelineau, 1988; Wintsch *et al.*, 1995 and references therein).

Several studies have shown that the most recent displacements along the MTL are dextral (e.g. Sugiyama, 1980) and that these are associated mainly with incohesive fault rocks found within a couple of metres of the central slip zone (e.g. Wibberley & Shimamoto, 2003). In the Fukaya river section, however, there is clear evidence that the dextral shearing has also been preferentially localised into the phyllonites leading to the development of dextral-verging folds and brittle-ductile shear bands. Significantly, no other Ryoke-derived rock unit in close proximity to the MTL core – other than the central slip plane - is affected by this dextral shearing. Assuming that this late movement can be correlated with the late dextral slip recognised elsewhere along the MTL, then the observed focusing of strain exclusively within the

phyllosilicate-rich fault core is consistent with these rocks being weak on long timescales and under varying conditions in the upper crust.

2.4.3 Summary and rheological implications

A complex fault rock sequence is associated with the development of the MTL reflecting the interplay of deformation mechanisms under changing P-T conditions, fluid influx, textural feedback processes and ongoing changes in mineralogy (Table 2). An early phase of mylonitisation appears to have been associated with K-feldspar alteration in the Ryoke derived ultramylonites immediately to the north of the MTL. Strain appears to have localised increasingly into the MTL core at this stage, possibly due to weakening associated with the breakdown of load-bearing phases such as K-feldspar. The onset of fluid-assisted diffusional creep mechanisms triggered by strain-induced crystal plastic grainsize reduction in the ultramylonites at this time may also have further contributed to weakening.

Following exhumation to shallower depths and lower temperatures, the onset of fracturing and associated grain-scale dilatancy during the early stages of brittle faulting and cataclasis appears to have further localised fluid flow into the core region of the MTL. This eventually led to very substantial changes in mineralogy, chemistry and dominant grain-scale deformation mechanisms (Table 2). In the finest grained, most crushed-up sections of the fault core – often adjacent to larger pre-existing brittle faults - textures indicative of fluid-assisted diffusive mass transfer (e.g. fibrous overgrowths, solution seams) are widely preserved. They are also ubiquitous in the phyllonites. Such features are absent from less deformed sections of the brittle fault zone, and appear to indicate that the development of phyllonite from cataclasite is associated with the grain-size-controlled onset of diffusional viscous creep. In this

case, the change in deformation regime is controlled by a strain-induced, brittle reduction in grain-size and it is likely to lead to significant long-term weakening (Mitra, 1984; Wojtal & Mitra, 1986). This seems consistent with the observed localisation of high strain and later dextral reactivation into the MTL phyllonites. The fluid influx also led to the widespread retrograde replacement of strong mineral phases such as feldspar (albite) by fine-grained, aligned weak aggregates of phengite and new chlorite. This introduction of new phases and the consequent change in deformation mechanisms can lead to reaction-enhanced ductility (White & Knipe, 1978; Wintsch *et al.*, 1995). This is likely also to have caused a decrease in fault strength as the textural studies of the transition from foliated cataclasite to phyllonite clearly demonstrate that the weak phyllosilicate materials increasingly coalesce to form an interconnected layer on all scales (e.g. Figs. 4a, 7c & e). Ultimately, this leads to the collapse of the load-bearing framework, development of a highly foliated phyllonite and weakening of the entire fault zone.

2.4.4. The textures and rheology of phyllonites: insights from deformation experiments

The strongly developed foliation and lineation in the MTL phyllonites and the anastomosing and coalescing nature of the fabric surrounding variably flattened porphyroclasts gives the rocks a superficially mylonitic appearance. However, optical and SEM textural studies have found little evidence for significant amounts of dynamic recrystallization or recovery having occurred in these rocks. A possible solution to this apparent enigma comes from the findings of recent experimental work that use rock analogue mixtures to assess the rheological effects of fluid-assisted diffusional mechanisms in phyllosilicate-rich fault rocks.

In a series of experimental studies Bos & Spiers (2000; 2002) and Bos *et al.* (2000 a and b) and Niemeijer and Spiers (2005) performed ultra-high strain rotary shear experiments on simulated fault gouges consisting of halite and kaolinite mixtures as analogues for the deformation of quartz- and mica-rich fault rocks. The experiments were carried out under temperature conditions where pressure solution and cataclasis are known to dominate over dislocation creep in halite. In wet samples with > 10 wt% phyllosilicate, brittle failure was followed by strain weakening towards a steady-state shear strength that was dependent on both sliding rate and normal stress (so called 'frictional-viscous flow'). Significantly, although no crystal plasticity occurred during any of the experiments, the microstructures produced at lower sliding velocities are remarkably similar to the *apparently* mylonitic textures seen within the MTL phyllonites.

Bos & Spiers (2002) and Niemeijer & Spiers (2005) have proposed a microphysical model in which the shear strength of the gouge undergoing steady-state flow is determined by combined resistance to shear created by frictional sliding on the phyllosilicate foliae, pressure solution in the halite (=quartz) and dilation on the foliation. Figure 2.9 is a calculated strength profile produced using this microphysical model for a strike-slip scenario comparable to the MTL phyllonite. It was drawn for a quartz-mica phyllonite with an average grain size of 50 μm. The profile has been constructed using strain rates of 10^{-10} and 10^{-12} s^{-1}, equivalent to a fault zone of 10 to 1000 meters width sliding at 30 mm per year. The Byerlee's Law and dislocation creep for wet quartz curves used in Figure 2.9 represent a "classical" two-mechanism crustal strength profile, with the frictional-viscous transition located at ~12 km depth. The frictional viscous curve derived from the experimental data predicts that the dilatant or cataclastic portion of the crust is represented in the upper few km's (Fig.

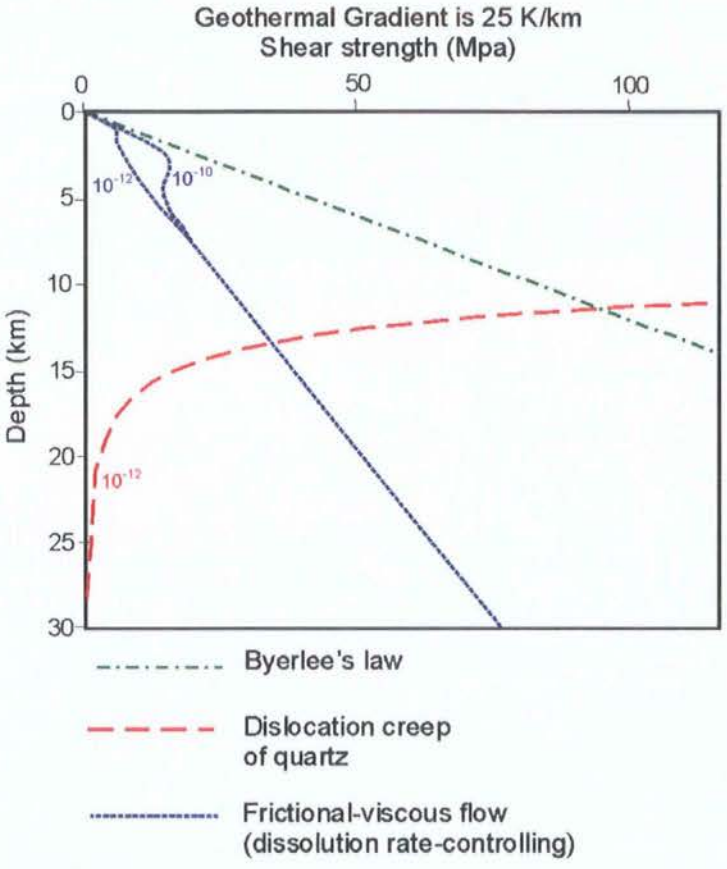

Figure 2.9. Calculated strength profile for the MTL phyllonites produced by Niemeijer & Spiers (2005). Profile drawn for quartz-mica phyllonite with a quartz "grain size" of 50 μm within a strike-slip fault.

2.9). For a strain rate of 10^{-10} s^{-1}, at around 3-4 km depth, pressure solution controls slip on the foliation and a negative slope is predicted because the operation of pressure solution becomes easier with depth due increasing temperature. Between 3 and 7 km, the strength accordingly falls away from the quasi-Byerlee line down toward the lower strength line representing stable-slip on the foliation with a reduced coefficient of sliding friction. Effectively this reduces the thickness of the seismogenic layer to less than 5 km. This predicted profile might even represent an upper boundary for the estimated strength of the phyllonites since if plastic deformation by dislocation creep of the phyllosilicate were in operation; the fault rock might be even weaker (see Kronenberg *et al.*, 1990; Shea & Kronenberg, 1992, 1993; Mares & Kronenberg, 1993; Niemeijer & Spiers 2005).

One potential limitation to the application of the strength profile to the MTL is that many of the phyllonites contain significant amounts of albite, often arranged in fine bands (Albers 2005). However, available data on the dissolution kinetics of albite suggest that its resistance to pressure solution would be similar to quartz (e.g. Hellman *et al.*, 1997). Further experimental work is needed, on real quartz-mica and quartz-albite-mica fault rocks under hydrothermal conditions in order to test the underlying microphysical model and predictions.

2.4.5. The importance of phyllonites to the MTL past and present

Phyllonites with apparently mylonitic textures that overprint cataclasites and localise subsequent displacements are increasingly being recognised in fault rock suites associated with crustal-scale faults where there is good independent evidence for long-term weakening, e.g. reactivated faults (Imber *et al.* 1997, 2001; Stewart *et al.* 2000), low angle normal faults (Collettini & Holdsworth 2004) and foreland

basement décollement thrusts (Wibberley, 2005). The development of such weak fault rocks could well explain the long-lived history of the MTL in SW Japan. Unfortunately, due to poor exposure, we do not know if significant amounts of phyllonitic fault rocks like those seen in the Fukaya River section are associated with the entire MTL fault zone. This is important, because any weakening effects will only be transmitted up-scale to affect the entire fault zone if a well-connected network of weak fault rock can form over length scales of 10s or 100s of kilometres (Holdsworth 2004). It appears that this was able to happen during the Tertiary sinistral displacement history along the MTL, and during the initial stages of Quaternary dextral reactivation – as evidenced by the localisation of dextral folds and shearing into the phyllonites.

By contrast, the patterns of most recent displacement and seismicity in this region of Japan suggest that the MTL is currently no longer behaving as a weak structure. Current seismic activity along the entire MTL across SW Japan is relatively low and, as a result, no linear distribution of microearthquakes is found along the fault trace (Okano and Kimura, 1996), and no creep motion has been detected (Onoue et al., 2002). Speculatively, it is possible that the relatively recent change to dextral motion has dismembered the previously mature, weak fault rock network established during millions of years of sinistral motion, leading to a general locking-up and strengthening of the MTL in SW Japan.

2.5. Conclusions

This paper provides the first detailed description of phyllonitic fault rocks from Japan's largest strike-slip fault zone, the Median Tectonic Line. These phyllonites were generated in the core zone of the MTL by syntectonic alteration of fractured

ultramylonites and cataclasites. Structural, mineralogical and geochemical studies show that early ultramylonites at the edge of the core zone provide the protolith to the other fault rocks in the core zone. Cataclasis and fluid-driven feldspar alteration to phengite and precipitation of chlorite resulted in the sequential generation of cataclasite, foliated cataclasite and ultimately phyllonite, with increasing localisation of deformation at each stage. Widespread microstructural evidence for the operation of DMT processes in these phyllonites suggests the importance of fluid-assisted viscous creep deformation mechanisms in these rocks.

The microphysical model of Bos & Spiers (2002) and Niemeijer and Spiers (2005) for combined frictional-viscous creep in quartz-mica phyllonites has been used to generate a strength profile for conditions appropriate to deformation along the MTL. This profile illustrates that very significant weakening is likely over long timescales illustrating that phyllonites potentially play a key role in facilitating long-term weakening along crustal-scale faults. The findings of the present study will also be extremely relevant to the San Andreas Fault should foliated, phyllosilicate-rich fault rocks be found when drilling in the SAFOD (San Andreas Fault Observatory at Depth) experiment penetrates the fault core at 4 km depth.

Chapter 3
Geochemical insights into fault rock development and fault zone processes in crustal-scale structures: a case study from the Median Tectonic Line, SW Japan.

Abstract

The Median Tectonic Line is a major, crustal-scale fault in Japan that separates the low-P/high-T Ryoke metamorphic belt of mainly subduction related granitoids from the high-P/low-T Sambagawa Belt of accretionary complex metasedimentary rocks. The current study presents an integrated field, microstructural and geochemical study of fault zone processes occurring within Ryoke derived fault rocks to the north of the MTL. Geochemical analytical techniques have been used in combination with field-based and microstructural observations to give an insight into the geochemical processes and fluid flow occurring within different portions of the MTL fault zone across two transects, near the villages of Miyamae and Tsukide, ~ 15 km along strike from one another in western Mie Prefecture, SW Japan. The study has highlighted two distinctive domains: 1) the narrow fine-grained foliated fault core where strain is localised; and 2) a wider damage zone of variably fractured mylonites to the north of the fault zone that progressively grades into Ryoke protolith mylonite at distances over ~ 400 m north of the MTL central slip zone. Whole-rock geochemical analyses suggests that variably fractured mylonites 50-350 m north of the MTL central slip zone within the Tsukide field area have undergone a more varied and extensive alteration in comparison to that experienced across the Miyamae field area. The fine-grained foliated fault rocks within the core of the MTL have experienced the most intense deformation, but show the apparently least altered geochemical signature, relative to other fault rocks as they show whole-rock major and trace element concentrations closest to protolith values. The geochemical signatures of fault rocks across the MTL support a model for the presence of a high permeability damage zone characterised by a crack geometry porosity network across the zone of variably fractured mylonites to the north of the MTL fault core. In contrast to this damage zone, the permeability and porosity network within the phyllonitic fault core at Miyamae is likely to be characterised by a strong permeability anisotropy where across-fault fluid flow is inhibited and focused fault-parallel fluid flow occurs through a connected network of tubular geometry porosity and permeability.

3.1. Introduction

The aim of the present study is to consider the hypothesis that processes of fault rock development and evolution observed during field and microstructural investigations can also be tracked using fault rock geochemistry. The coupled microstructural-geochemical approach will then provide a further informed insight into the processes operative within long-lived crustal-scale reactivated fault zones. In particular the study attempts to identify evidence within the geochemical signature of fault rocks for the operation of diffusive mass transfer processes associated with the formation of phyllonite and phyllosilicate-rich fault rocks within the MTL fault core. Within the phyllonites, the operation of fluid-assisted diffusive mass transfer mechanisms is recognised by the presence of characteristic source microstructures, e.g. pressure solution seams and grain dissolution features, and sink microstructures, e.g. fibrous mineral overgrowths, accompanied by the growth of new secondary mineral phases during alteration. Within the geochemical signature of the fault rocks a progressive increase in alteration relative to the protolith with closer proximity to the fault core (where field-based and microstructural observations suggest deformation and alteration has been most intense) is predicted. Dissolution and precipitation processes observed within the phyllonites are also expected to be recorded in the enrichment and depletion of mobile elements within these rocks relative to the protolith.

The study involved the collection of a series of samples from transects across the MTL fault zone in two field areas, Miyamae and Tsukide ~15 km along strike from one another located in Iitaka-cho, Matsusaka-shi, Mie Prefecture. The selection and description of fault rock protolith is presented along with a description of the fault zone structure within the two field areas. Whole-rock major, trace and rare earth

element concentrations determined from X-ray fluorescence (XRF) and inductively coupled mass spectrometry (ICP-MS) analysis of a representative suite of both protolith and fault rock samples across the two transects are documented. Volume changes, across both transects, relative to the protolith and volume changes relative to precursor fault rocks are calculated and discussed in relation to the processes inferred from the various geochemical techniques used.

3.2. Fault rock protolith and regional setting

The investigation of any geochemical variation in fault zones is founded on the comparison of the composition of the fault rock with an assumed protolith. Through this comparison, it can then be demonstrated whether or not any changes in rock composition have occurred during deformation. There are many potential difficulties associated with the geochemical investigation of fault and shear zones, and these include problems related to the scale of the fault zone and the inhomogeneous nature of the protolith and fault rock (McCaig, 1997). Two sampling strategies can be employed when comparing the chemistry of fault rocks with their protoliths (O'Hara, 1988). One method is to sample on a regional scale across a number of outcrops to deduce an average composition for comparison. Another method, which has been employed during the present study is to sample on an outcrop scale to carry out comparison of the chemical composition of individual samples. This allows progressive chemical changes across the fault zone to be studied. Individual chemical compositions can then also be directly related to microstructural and mineralogical observations within individual fault rock samples.

The Median Tectonic Line is a major, crustal-scale fault in Japan that separates the low-P/high-T Ryoke metamorphic belt of subduction related granitoids

from the high-P/low-T Sambagawa Belt of accretionary complex metasedimentary rocks (Fig. 3.1a). It has an onshore along-strike length of > 1000 km, with a displacement history reaching back at least to the early Cretaceous. Displacement estimates are uncertain and range between 200-1000 km (e.g. Ichikawa, 1980). The granitic Ryoke Belt rocks are variably mylonitized in a zone up to 5 km wide north of the MTL and formed during late Cretaceous to early-Tertiary sinistral movements. Exhumation during continued activity and reactivation of the fault has resulted in the current exposure of the fault zone displaying a wide variety of fault rocks generated at different levels in the mid- to upper-crust. Deformation associated with these sinistral displacements becomes increasingly brittle as the core of the fault is approached with the development of cataclasites, breccias and gouges, many of which are foliated (e.g. Takagi, 1985, 1986; Wibberley & Shimamoto, 2003; Jefferies et al., 2006). Previous studies in Mie Prefecture have suggested that the fault has primarily undergone sinistral strike-slip displacements (e.g. Hara et al. 1982; Ichikawa, 1980; Takagi et al., 1989; Ohtomo, 1993; Shimada et al., 1998). However, the MTL has recently been reactivated as a dextral strike-slip fault (Sugiyama, 1992), with displacements localized into incohesive fault rocks typically within a couple of metres of the central slip zone (Okada, 1980; Research Group for Active Faults of Japan, 1991; Wibberley & Shimamoto, 2003) and phyllonitic fault rocks exposed ~5 m north of the central slip zone near the village of Miyamae, Mie Prefecture (Jefferies et al., 2006).

Although the study focuses upon the deformation and geochemical processes of the Ryoke derived fault rocks, within the fault core localised to ~1 m of the central slip zone Sambagawa derived fault rocks also occur. Therefore, Ryoke and Sambagawa geochemical protoliths both needed to be determined. The precursor

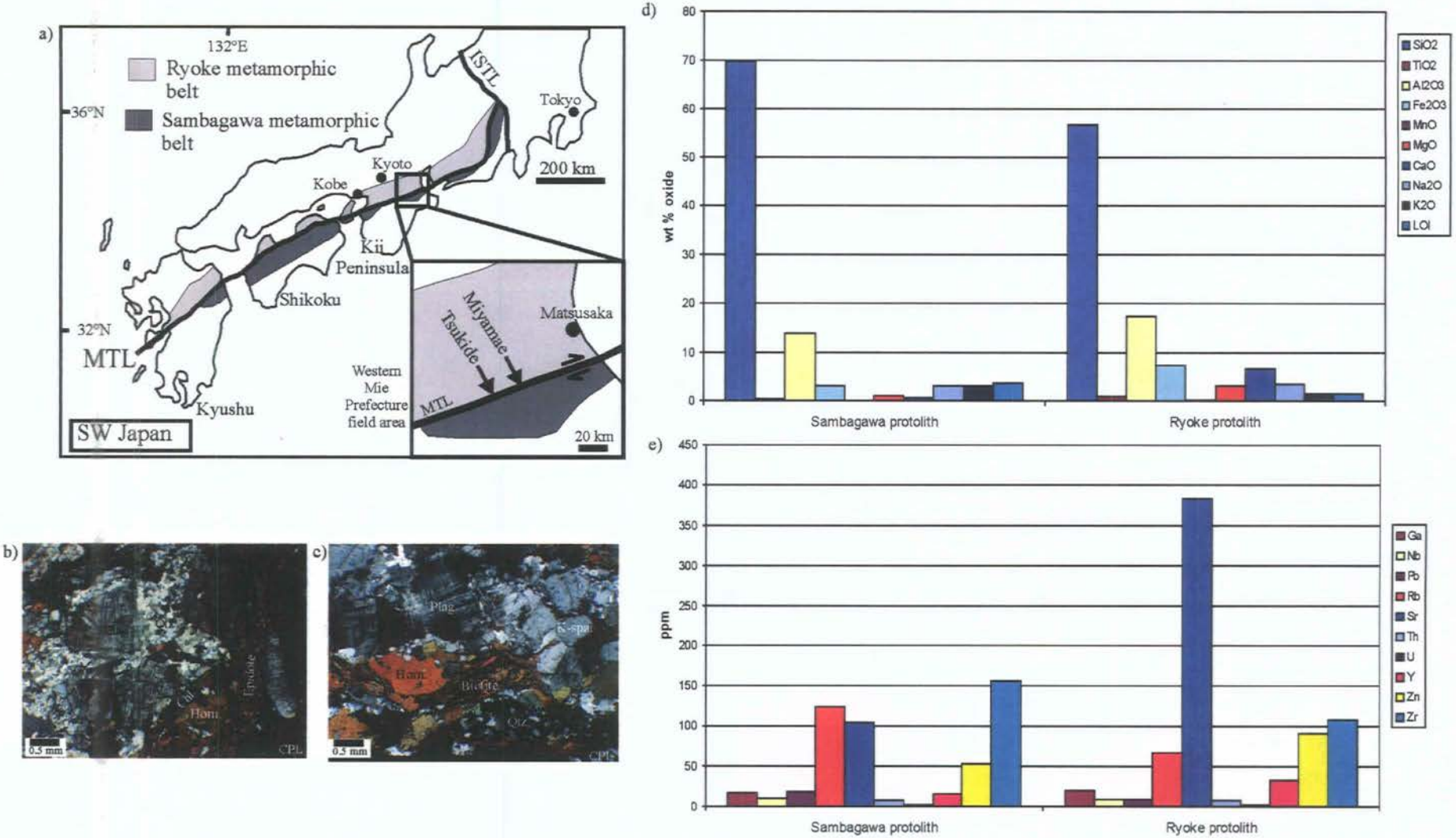

Figure. 3.1. a) The Median Tectonic Line (MTL) in SW Japan showing adjacent metamorphic belts and location of Mie Prefecture field area with approximate locations of the Miyamae and Tsukide transects. ISTL = Itoigawa-Shizuoka Tectonic Line. b) Cross polarised light (CPL) thin section view of Ryoke protolith mylonite MIS-19, showing plagioclase (Plag), quartz (Qtz), chlorite (Chl), hornblende (Horn) and epidote. c) CPL thin section view of Ryoke protolith mylonite MIS-18. d) Mean XRF whole-rock major element analyses and e) mean XRF whole-rock trace element analyses of Sambagawa and Ryoke protoliths.

rock, and therefore protolith, to the Ryoke-derived fault rocks produced during upright strike-slip related deformation are mylonites that developed during an earlier late Cretaceous to earliest Tertiary sinistral top-to-the-south, sub-horizontal shearing event (Yamamoto & Masuda, 1987; Sakakibara et al., 1989; Michibayashi & Masuda, 1993; Ohtomo, 1993; Jefferies et al., 2006). The effect of this mylonitisation in the Ryoke granitic rocks extends up to 5 km north of the MTL (Ito, 1978). Continued activity and reactivation of the MTL as an upright structure resulted in exhumation and the current exposure of the fault zone displaying a variety of increasingly brittle fault rocks (including cataclasites, breccias and gouges) generated at different levels in the mid- to upper-crust (Takagi, 1985; Jefferies et al., 2006).

The Ryoke metamorphic belt is heterogeneous in nature, comprising a series of large granitic plutonic bodies. The diversity in protolith varies on a scale larger than that of the region covering the two Miyamae and Tsukide field areas. Extensive mapping of the mylonitic rocks of the Ryoke Belt in western Mie Prefecture carried out by Takagi (1985) shows the spatial extent of protolith heterogeneity within the Ryoke Belt. A type locality for the Ryoke mylonite (identified by Shimada et al., 1999) unaffected by the later strike-slip deformation was sampled and compared to specimens collected from available exposures as far north of the MTL central slip zone as possible. Comparable Ryoke mylonites (samples MIS-19 and MIS-18) were found at exposures ~ 475 m north of the MTL along the Fukaya River within the Miyamae field area. These rocks have a grain size of ~1 mm and are composed of quartz, K-feldspar, plagioclase, hornblende and biotite (Fig. 3.1b and c). Quartz veins are common, are often discontinuous and range in size from the cm to metre-scale.

The two samples, MIS-19 and MIS-18, were thus used as representative samples of protolith material during geochemical analysis. The decision to designate these protolith rock samples is also supported by the work of Shimada et al. (1999). Based

upon analysis of quartz grain size they concluded that the rocks in the Miyamae region at distances >400 m north of the MTL were representative of the regional protolith.

Figure 3.1d and 3.1e present whole-rock major and trace element data obtained from analysis using XRF powder pellets and fusion beads. The mean major element composition of the Ryoke protolith is dominated by SiO_2 (57 wt%) and Al_2O_3 (17 wt%), reflecting the abundance of silicates such as quartz, feldspar and epidote. Fe_2O_3 (7.3 wt%) and CaO (6.8 wt%) are second in abundance to SiO_2 and Al_2O_3 and most likely reside within the biotite, hornblende and epidote present within the Ryoke mylonite. All other major elements are present in much lower proportions (typically <4 wt%). The Ryoke protolith whole-rock trace element data are dominated by Sr (containing 383 ppm). Sr is the daughter isotope of Rb, which is found in white mica, biotite and feldspar.

The same process adopted for the selection of a Ryoke protolith was applied in the selection of a Sambagawa protolith. A sample from a classic Sambagawa schist outcrop featured in Shimada et al. (1999) was compared to the Sambagawa schist found in outcrops to the south of the MTL. The Miyamae field area had virtually no outcrops of schist, but outcrops created by road cuts in the Tsukide field area allowed the sampling of protolith Sambagawa schist (sample TKR-32) located ~ 225 m south of the MTL central slip zone.

The Sambagawa protolith is composed primarily of quartz, white mica and feldspar. Figures 3.1d and 3.1e show that the Sambagawa protolith contains ~70 wt% SiO_2 reflecting the very high quartz content of the schist. Al_2O_3 is the second dominant major element (14 wt%) again representing the quartzo-feldspathic nature of the rock.

3.3. Study areas and fault zone structure

3.3.1. Miyamae field area

Figures 3.2a-c are maps and outcrop sketches of the Miyamae field area showing the location of the samples that constitute the geological and geochemical transect across the fault zone. Section 2.3.1. and Table 2.1 describe the textural and mineralogical changes that occur from Ryoke mylonite through the variably fractured mylonites with decreasing distance to the MTL central slip zone in the Miyamae area (see also Jefferies et al., 2006). To accompany this description of the fault zone structure Figure 3.3 presents a microstructural 'snap-shot' of each of the samples analysed across the Miyamae transect. The most notable features evident are the decrease in grain size, extensive alteration of feldspar and the increasing cataclastic nature of the mylonites with decreasing distance to the fault core (see also Table 2.1).

The MTL fault core in the Miyamae field area is exposed within two outcrops; a ~50 m wide almost completely exposed across-strike plan view river section (Fig. 3.2b; Jefferies et al., 2006) and a ~25 m long road-cut profile section, oriented ~45° to the strike of the MTL, that exposes the central slip zone gouge (see Fig. 3.2ci-iii). The fault rocks exposed within the fault core at Miyamae include ultramylonite, cataclasite, foliated cataclasite, phyllonite, orange-stained cataclasite and orange-black foliated cataclasite. Within the Fukaya river section (see Fig. 2.2 and Fig. 3.2b) a progressive sequence in fault rock evolution from ultramylonite → cataclasite → foliated cataclasite → phyllonite → breccia/gouge is observed. An orange-stained cataclasite is repeatedly found just to the north of the MTL central slip zone. It is highly altered and no evidence remains to draw conclusions upon the relative timing of its formation. An orange-black foliated cataclasite is always located within 1 metre

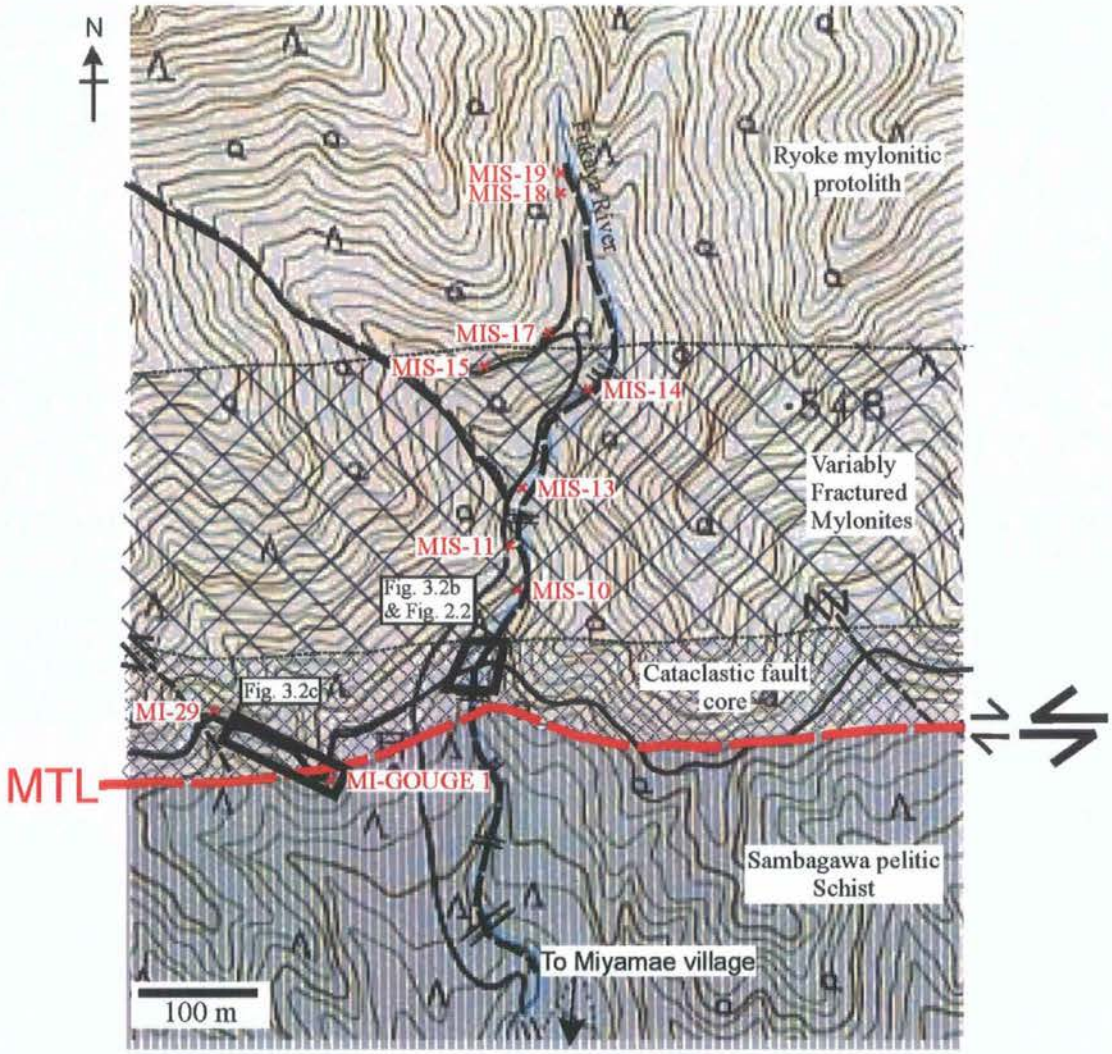

Figure 3.2a Map showing Miyamae field area and location of samples forming a transect across the fault zone. Exposures of the fault core are indicated by black boxes, small shear sense arrows indicate sinistral strike-slip displacements, large shear sense arrows indicate late dextral reactivation.

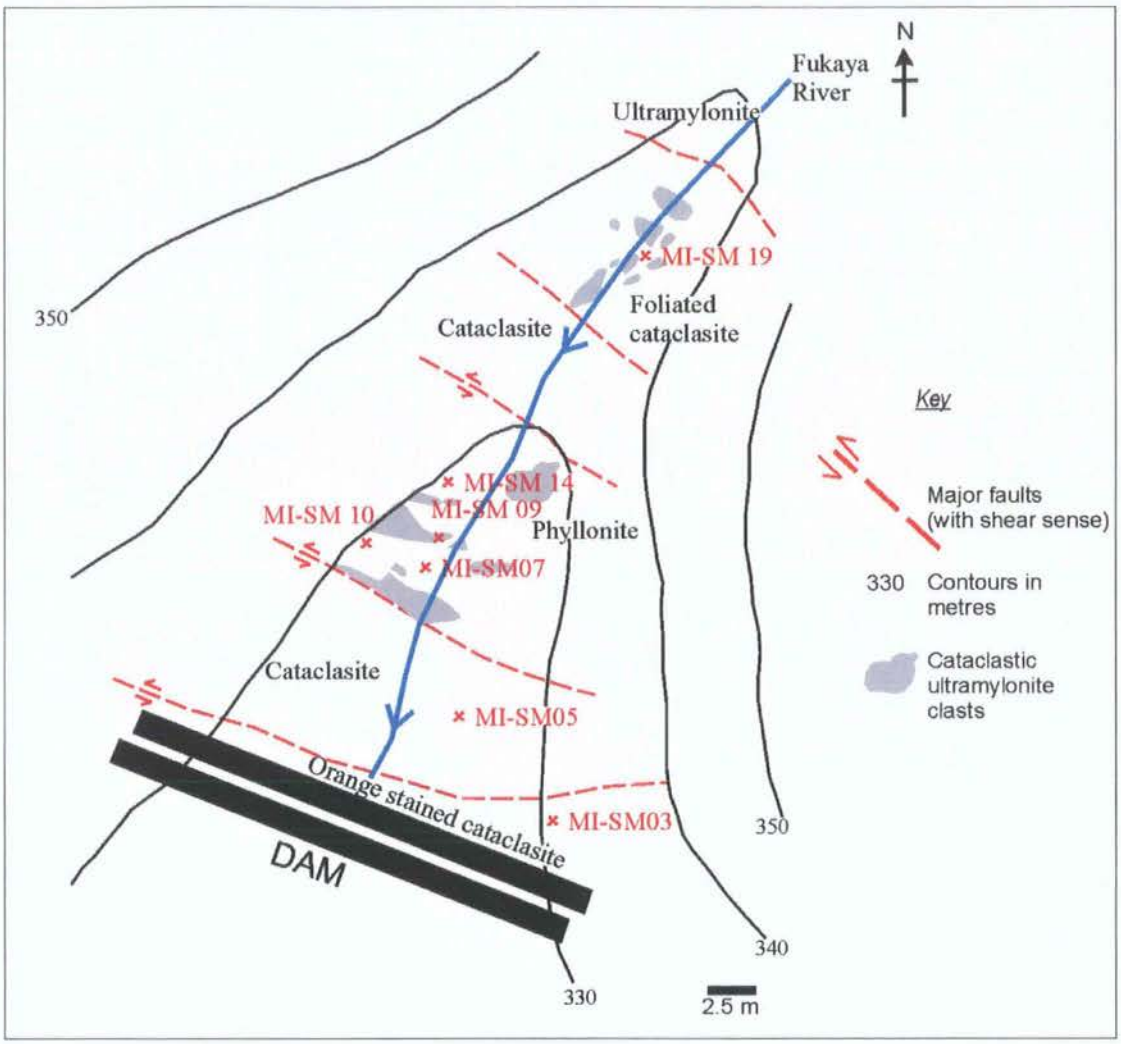

Figure 3.2b Simplified map of Fukaya River section exposure of the fault core, Miyamae field area, showing approximate positions of fault rocks and fault rock samples. For a more detailed geological map see Figure 2.2a and Figure 2.2d for structural data and Jefferies et al., 2006.

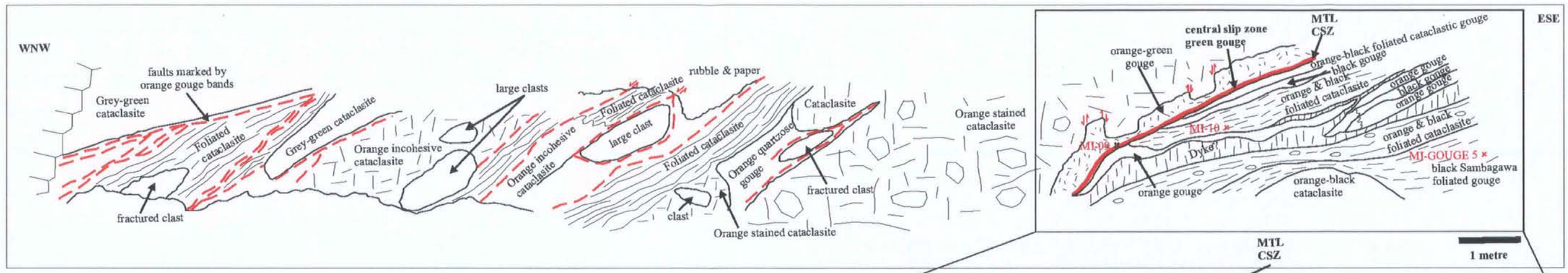

Figure 3.2c i) outcrop sketch of fault core exposure including central slip zone (CSZ) gouge. ii) Photograph of section of the fault core showing the variety and mixture of fault rocks localised to the CSZ. iii) Stereogram showing structural data and deformation fabrics of fault rocks, great circle represents central slip zone measured in the field (see Fig. 3.2ci-ii).

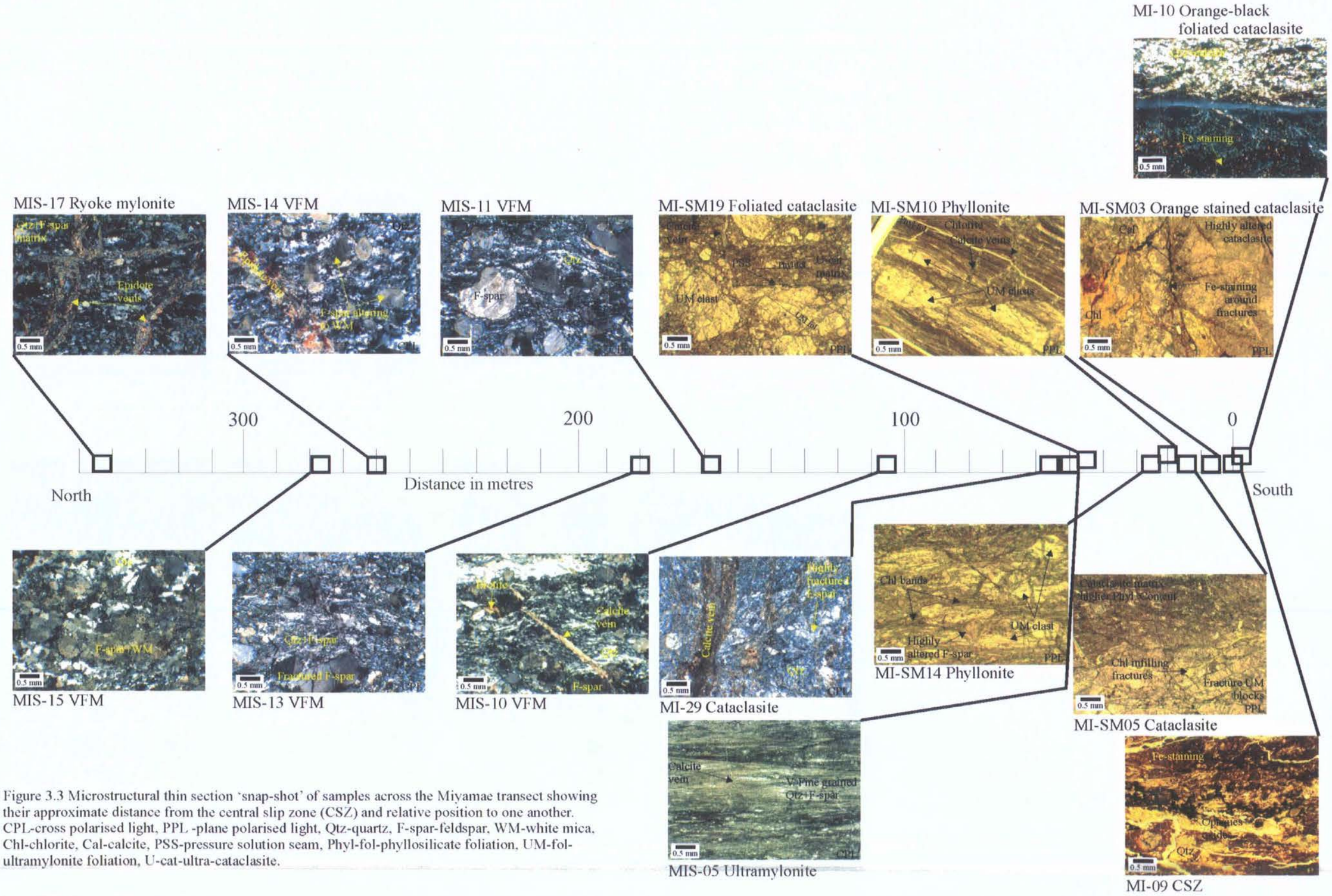

Figure 3.3 Microstructural thin section 'snap-shot' of samples across the Miyamae transect showing their approximate distance from the central slip zone (CSZ) and relative position to one another. CPL-cross polarised light, PPL -plane polarised light, Qtz-quartz, F-spar-feldspar, WM-white mica, Chl-chlorite, Cal-calcite, PSS-pressure solution seam, Phyl-fol-phyllosilicate foliation, UM-fol-ultramylonite foliation, U-cat-ultra-cataclasite.

of the central slip zone (Fig. 3.2ci-ii). It can be both cohesive and incohesive consisting of quartz-rich cataclasite and a finer grained, black, phyllosilicate-rich cataclasite derived from both Ryoke and Sambagawa derived material within a zone of mechanical mixing close to the central slip zone (Wibberley and Shimamoto, 2003). The central slip zone strikes E-W (085) and dips 59° north, it is defined by a cm-wide gouge that crosscuts all other fault rocks (Fig. 3.2ci-ii). It is extremely fine-grained with a quartz, feldspar, kaolinite, chlorite, smectite and illite mineralogy. Sections 2.3.2. and 2.3.3. describe all these fault rocks in detail. Table 3.1 presents a summary of textural and mineralogical changes and associated deformation mechanisms and metamorphic processes observed within the above fault core rocks of the Miyamae field area.

3.3.2. Tsukide field area

The Tsukide field area and sample localities are shown in Figure 3.4a-b, the fault zone structure is similar to that described from Miyamae. At distances over 350 m north of the central slip zone, Ryoke granitic mylonite is exposed, and with a grain size of ~0.7 mm and feldspar (K-feldspar and plagioclase) porphyroclasts up to 2 mm in length, set in matrix of quartz, feldspar plus small amounts of biotite and hornblende. Some alteration of feldspar to white mica, and hornblende and biotite to chlorite occurs. Centimetre-scale epidote veins are common throughout the mylonite (Fig. 3.5). The mylonitic foliation strikes east-west with a mainly sub-horizontal to gentle northwards dip (Fig. 3.4aii).

At distances less than 350 m north of the central slip zone, earlier mylonitic textures are progressively overprinted by cataclastic deformation (see Table 3.2 and Fig. 3.5). Across the zone of variably fractured mylonites 300-50 m north of the central slip zone (see Fig. 3.4a), grainsize decreases from ~0.45 to ~0.2 mm,

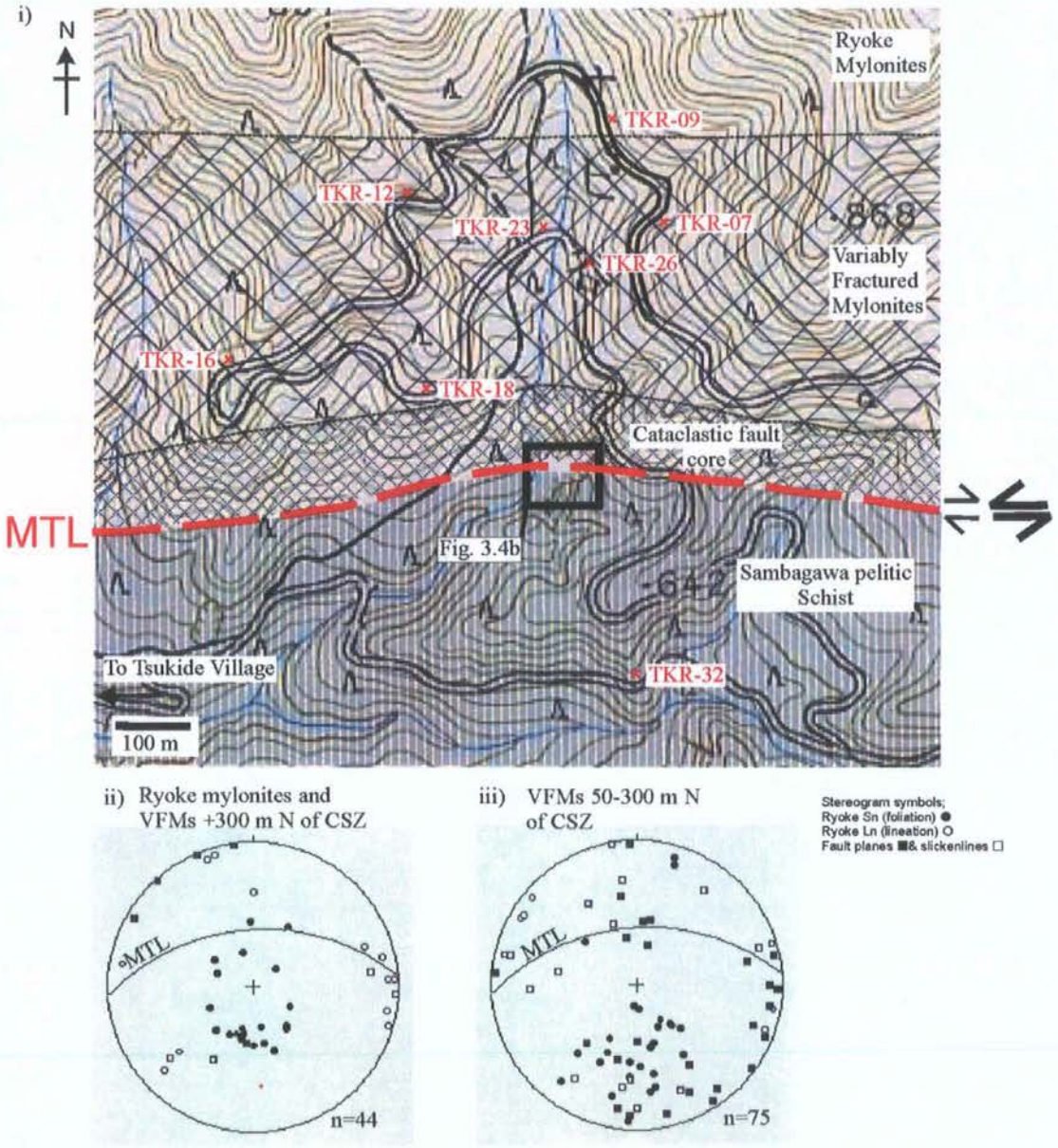

Figure 3.4a. i) Map showing Tsukide field area and location of samples forming a transect across the fault zone. Exposures of the fault core indicated by black boxes. ii) Stereogram showing structural data collected over 300 m north of the central slip zone. iii) Stereogram showing structural data collected 50-300 m north of the central slip zone. The great circle represents central slip zone measured in the field (see Fig. 3.4bi).

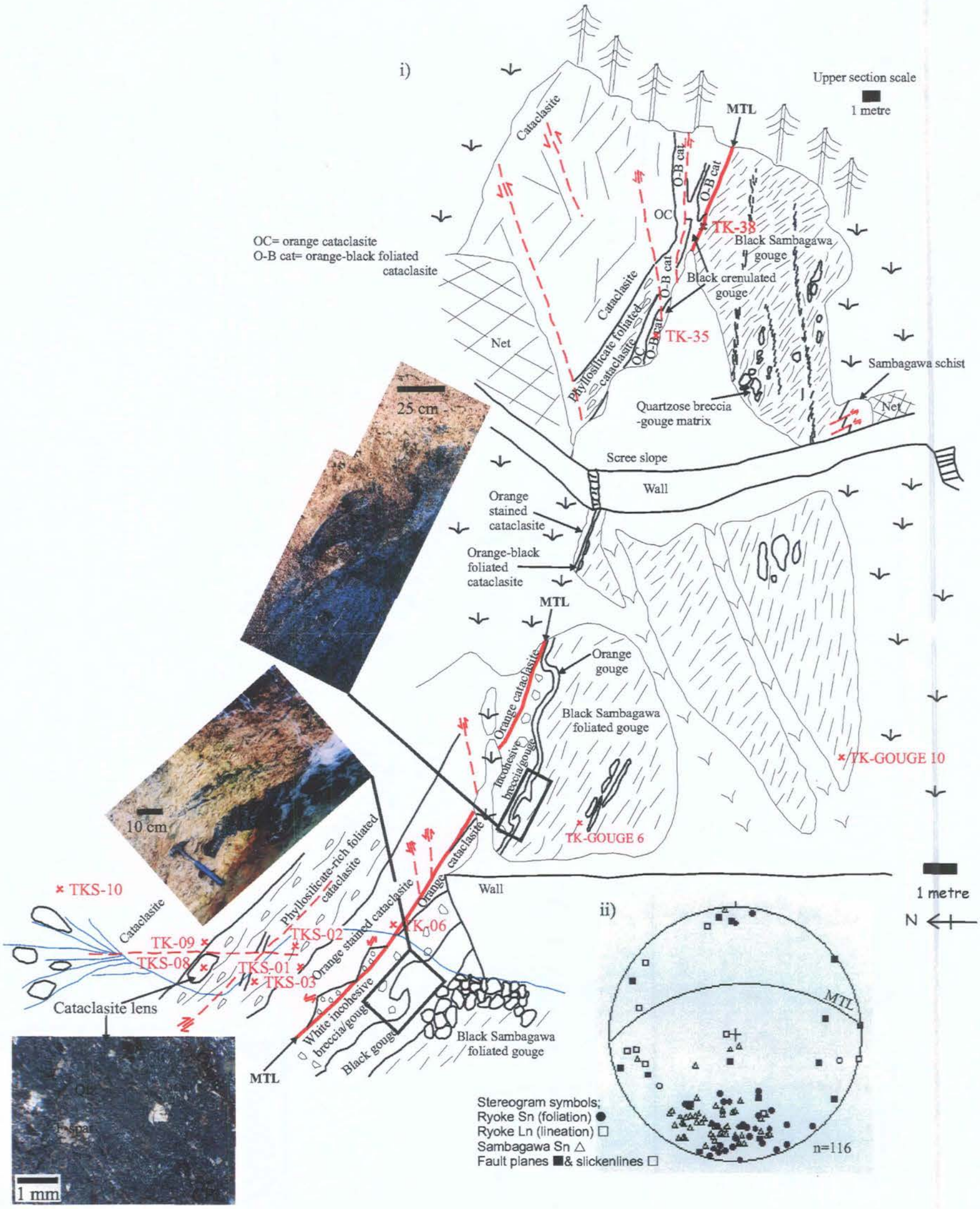

Figure 3.4b) i) Outcrop sketch of Tsukide fault core exposure showing central slip zone gouge, zoom in photos of intermixed zones of Ryoke and Sambagawa derived material, and cross polarised light (CPL) photomicrograph of cataclastic ultramylonite lens. Outcrop also featured in Wibberley and Shimamoto (2003). ii) Stereogram showing deformation fabrics of Ryoke and Sambagawa fault rocks, great circle represents central slip zone measured in the field (see Fig. 3.4bi).

	ULTRAMYLONITE	CATACLASITE	FOLIATED CATACLASITE	PHYLLONITE	ORANGE STAINED CATACLASITE	ORANGE-BLACK FOL. CATACLASITE
Grain size	~0.01 mm	~0.3 mm (<50% matrix	~0.5 mm 60% matrix	Up to 1.5 mm	<0.3 mm	~0.3 mm
White mica %	30%	~15%	~15%	~8%	~35%	~15%
Chlorite %	10%	~15%	~15%	~30%	~20%	~15%
Veining	Extensive cm-scale calcite veins		Calcite veins	Extensive sub-cm scale calcite veins	Calcite and chlorite veining on cm- to mm-scales	Extensive carbonate precipitation
Lineation	Strong white mica and chlorite	Not visible	Weak chlorite	Strong chlorite	Not visible	None visible
Foliation	Defined by quartz poor and quartz rich domains	Unfoliated	Weak phyllosilicate foliation within fine grained matrix	Very strong chlorite	Not visible	Foliation defined by interconnected fracture network
Dominant deformation mechanisms	Crystal plasticity and grain boundary sliding	Cataclasis	Cataclasis, DMT, fracture and frictional sliding	DMT and frictional sliding	Cataclasis	Cataclasis, fracture, frictional grain boundary sliding, cataclastic flow
Metamorphic processes	Enhanced fluid flow					
	Breakdown of anhydrous phases i.e. Feldspar to white mica					
				New growth of Mg-rich chlorite		
Microstructural "snap-shot"	MIS-05 Fig. 3.3.	MI-29 MI-SM05 Fig. 3.3.	MI-SM19 Fig. 3.3.	MI-SM10 MI-SM14 Fig. 3.3	MI-SM03 Fig. 3.3.	MI-10 Fig. 3.3.

Table 3.1. Summary table showing textural and mineralogical changes within the fault rocks of the Miyamae transect fault core and associated deformation mechanisms and metamorphic processes.

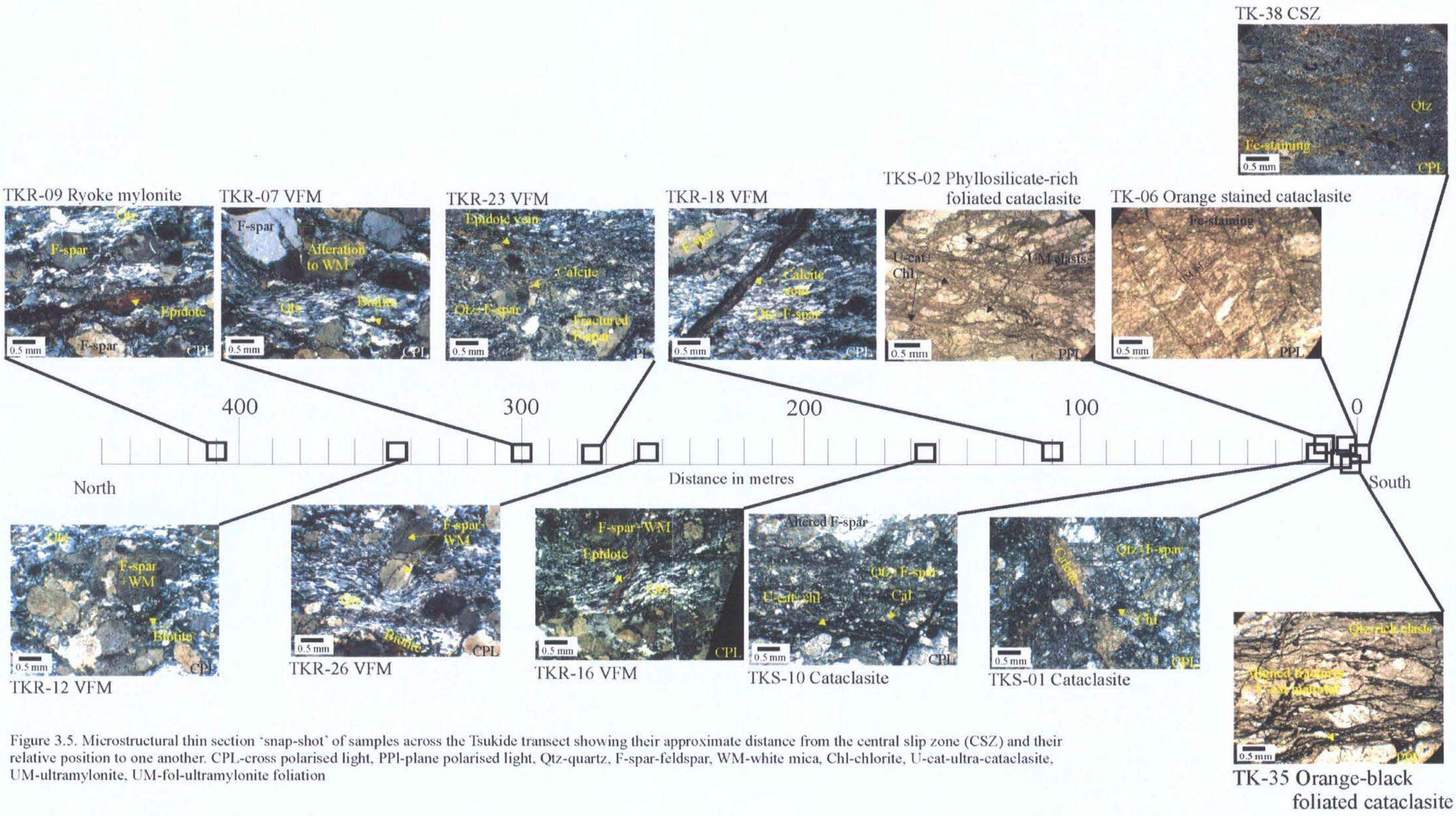

Figure 3.5. Microstructural thin section 'snap-shot' of samples across the Tsukide transect showing their approximate distance from the central slip zone (CSZ) and their relative position to one another. CPL-cross polarised light, PPl-plane polarised light, Qtz-quartz, F-spar-feldspar, WM-white mica, Chl-chlorite, U-cat-ultra-cataclasite, UM-ultramylonite, UM-fol-ultramylonite foliation

	VARIABLY FRACTURED MYLONITES						FAULT CORE	
Distance N of CSZ	400 m	350 m	300 m	250 m	200 m	150 m	100 m	50 m	0
Grainsize mm	~0.7 mm P. Clasts up to 2 mm	~0.45	~0.4 P. Clasts up to ~2 mm	<0.3		~0.2	<0.2	Clasts range ~0.1-1 mm	
Hornblende + biotite %	~5%	3%	~2%	<1%		<1%	<0.5%	Hornblende absent <0.25% biotite	
White mica %	<2%	~5-7%	~7%	~8%		~8%	~8%	~20%	
Chlorite %	~3%	~3.5%	~4%	~5%		~5%	~5%	~15%	
K-feldspar : albite ratio	50:50	45:55	42:58	40:60		40:60	40:60	No K-feldspar visible	
Veining	Extensive cm-scale epidote veins		Sub-cm scale quartz veins plus limited epidote veins			Limited epidote veins		Sub-cm scale calcite veins	
Lineation	← Weak quartz elongation →							Weak elongation of chlorite	
Foliation	← Good defined primarily by flattening of quartz →							Defined by alignment of chlorite	
Intensity of feldspar cataclasis	Very mild	Mild with extensive alteration of K-feldspar to white mica			Extensive fracturing and white mica alteration		Extensive	Less fracturing more extensive alteration to white mica + quartz	
Intensity of faulting/ cataclasis	Weak fracturing			Widespread	Fracture and faulting intensity increases			Intensive cataclasis	
Microstructural "snap-shot"	TKR-09 Fig. 3.5.	TKR-12 Fig. 3.5.	TKR-07 Fig. 3.5.	TKR-26 Fig. 3.5.		TKR-16 Fig. 3.5.	TKR-18 Fig. 3.5.	TKS-02 Fig. 3.5.	

Table 3.2. Showing textural and mineralogical changes with decreasing distance to the MTL central slip zone (CSZ) across the Tsukide transect. Compiled from field observations and optical microscopy.

hornblende and biotite percentages decrease, while white mica, chlorite and albite contents increase. With closer proximity to the fault core, fault and fracture intensity increases. Adjacent to many faults, breccia zones up to 1 m wide are developed with enhanced alteration and quartz mineralisation. Sub-cm scale quartz veins occur throughout the variably fractured mylonites (Table 3.2). Due to the progressive cataclastic overprint mylonite lineations are difficult to distinguish, but the mylonitic foliation strikes east-west with a gentle-moderate (40-70°) northward dip (Fig. 3.4aiii). Over this distance faults are widespread and have an array of orientations (Fig. 3.4aiii), they are mutually crosscutting so no specific generations of faulting can be defined.

Within the Tsukide field area, the cataclastic fault core is exposed in one outcrop (Fig. 3.4b), which provides a large cross-section of the fault core including the central slip zone. The cataclasite within the fault core appears to be derived from ultramylonite, with clast size ranges from ~0.1-1 mm. Extensive alteration of feldspar to white mica plus quartz occurs (Fig. 3.5); hornblende, biotite and epidote are no longer present. Sub-cm scale calcite net veining is extensive and chlorite growth is preferentially concentrated within fine-grained sections of the cataclasite. Bands of aligned chlorite grains begin to define a foliation within these sections (Fig. 3.5). With further cataclasis and chlorite growth, the cataclasite gradually develops into a phyllosilicate-rich foliated cataclasite (Fig. 3.4b and Fig. 3.5). Clasts of cataclastically deformed ultramylonite typically up to ~ 0.5 mm in size sit within the ultra-cataclasite matrix. Further feldspar breakdown to white mica occurs and chlorite growth (constituting up to ~ 20% of the foliated cataclasite) preferentially concentrates within the ultra-cataclasite defining the foliation visible in outcrop. The foliation strikes ENE and dips steeply (60-85°) toward the north, sub-parallel to the MTL central slip zone

exposed in the outcrop (086/58N with slickenlines plunging 43° toward 081). Elongation of clasts along this phyllosilicate foliation is also observed. A weak chlorite lineation plunging gently (~10-20°) toward both the east and west is visible in isolated patches (Fig. 3.4bii). There is evidence for limited pressure solution at clast boundaries (sample TKS-02 Fig. 3.5). Within the available exposures here at Tsukide, phyllosilicate development within the cataclasite does not progress to the extent of that viewed within the Miyamae area (Fukaya river section, Fig. 2.2 and Fig. 3.2b) to produce phyllonitic fault rocks.

As found within the Miyamae field area, the distinctive orange-stained cataclasite occurs just to the north of the central slip zone (Fig. 3.4b and sample TK-06 Fig. 3.5). Again it is extremely altered with extensive Fe-staining possibly due to infiltration of meteoric fluids at shallow crustal conditions. Calcite veining is extensive throughout the orange-stained cataclasite and precursor ultramylonite textures are still visible in places (sample TK-06 Fig. 3.5).

Orange-black foliated cataclasite and gouge occur within 1 m of the central slip zone and are composed of quartz, calcite, white mica and chlorite. Orange coloured bands are more quartzose with higher phyllosilicate contents within the black bands. The foliation within these cataclasites is in part defined by an interconnected fracture network and associated fine-grained ultra-cataclasite material (see sample TK-35 Fig. 3.5). Evidence for limited pressure solution is also seen within fine-grained sections of the cataclasite. The central slip zone is a ~1 cm wide extremely fine-grained gouge (sample TK-38 Fig. 3.5) that truncates all adjacent structures (Fig. 3.4b). Close to the central slip zone a series of Riedel-like slip surfaces occur (Fig. 3.4b). Oblique slip on these surfaces within the Ryoke derived cataclasites, combined with slip on the MTL-parallel central slip zone may have led to inter-fingering and mixing of Ryoke and

Sambagawa derived material to form the orange-black foliated cataclasites (Fig. 3.4b) (see Wibberley and Shimamtoto, 2003). Table 3.3 presents a summary of textural, mineralogical, operative deformation mechanisms and metamorphic processes within the cataclastic fault rocks within the MTL core at Tsukide.

3.4. XRF whole-rock element analysis

Chemical changes during deformation are commonly investigated using X-ray fluorescence (XRF) analyses of major and trace elements in a representative suite of both protolith and fault rock samples. Data from whole rock chemical analyses only show relative changes in bulk rock chemical composition (Gresens, 1967). For example, if a fault rock experiences SiO_2 enrichment during silicification it will show much lower concentrations of all other elements compared with its protolith (Streit and Cox, 1998). In order to eliminate this problem of 'relative abundance', the elemental concentrations in a fault rock have to be normalised to that within the protolith. As protolith and fault rocks in this study both contain high concentrations of SiO_2 and Al_2O_3, variations in the concentrations of less abundant elements may not be apparent (the 'constant sum effect' e.g. Rollinson, 1993). Normalisation of fault rock samples to the protolith also addresses this problem since the amount of enrichment or depletion of each element in each fault rock can be calculated relative to the protolith.

3.4.1. Major and trace element composition of fault rocks from the Miyamae Transect.

Fault rock composition – raw data.

Figure 3.6 presents mean raw data for each of the fault rock types across the MTL fault zone at Miyamae. SiO_2 and Al_2O_3 dominate in all other fault rocks

	CATACLASITE	PHYLLOSILICATE-RICH FOL. CATACLASITE	ORANGE STAINED CATACLASITE	ORANGE-BLACK FOL. CATACLASITE
Grain size	~0.4 mm	Clasts up to ~0.5 mm	<0.3 mm	~0.3 mm
White mica %	~15%	~15%	~15%	~15%
Chlorite %	~15%	~20%	~15%	~15%
Veining	Extensive calcite net veining		Calcite veining	
Lineation	None visible	Weak elongation of chlorite	Precurser ultramylonite textures visible	
Foliation	Within fine-grained sections defined by bands of aligned chlorite grains	Defined by chlorite bands and elongation of clasts	Precurser ultramylonite textures visible	Foliation defined by interconnected fracture network & associated fine-grained material
Dominant deformation mechanisms	Fracture and cataclasis	Cataclasis, limited pressure solution, fracture and frictional sliding	Cataclasis	Cataclasis, fracture, frictional grain boundary sliding, cataclastic flow, possible limited pressure solution
Metamorphic processes	Breakdown of anhydrous phases i.e. Feldspar to white mica			
		Enhanced fluid influx		
		Chlorite growth		
Microstructural "snap-shot"	TKS-10 TKS-01 Fig. 3.5.	TKS-02 Fig. 3.5.	TK-06 Fig. 3.5.	TK-35 Fig. 3.5.

Table 3.3. Summary table showing the textural and mineralogical changes within the fault rocks of the Tsukide transect fault core and the associated deformation mechanisms and metamorphic processes.

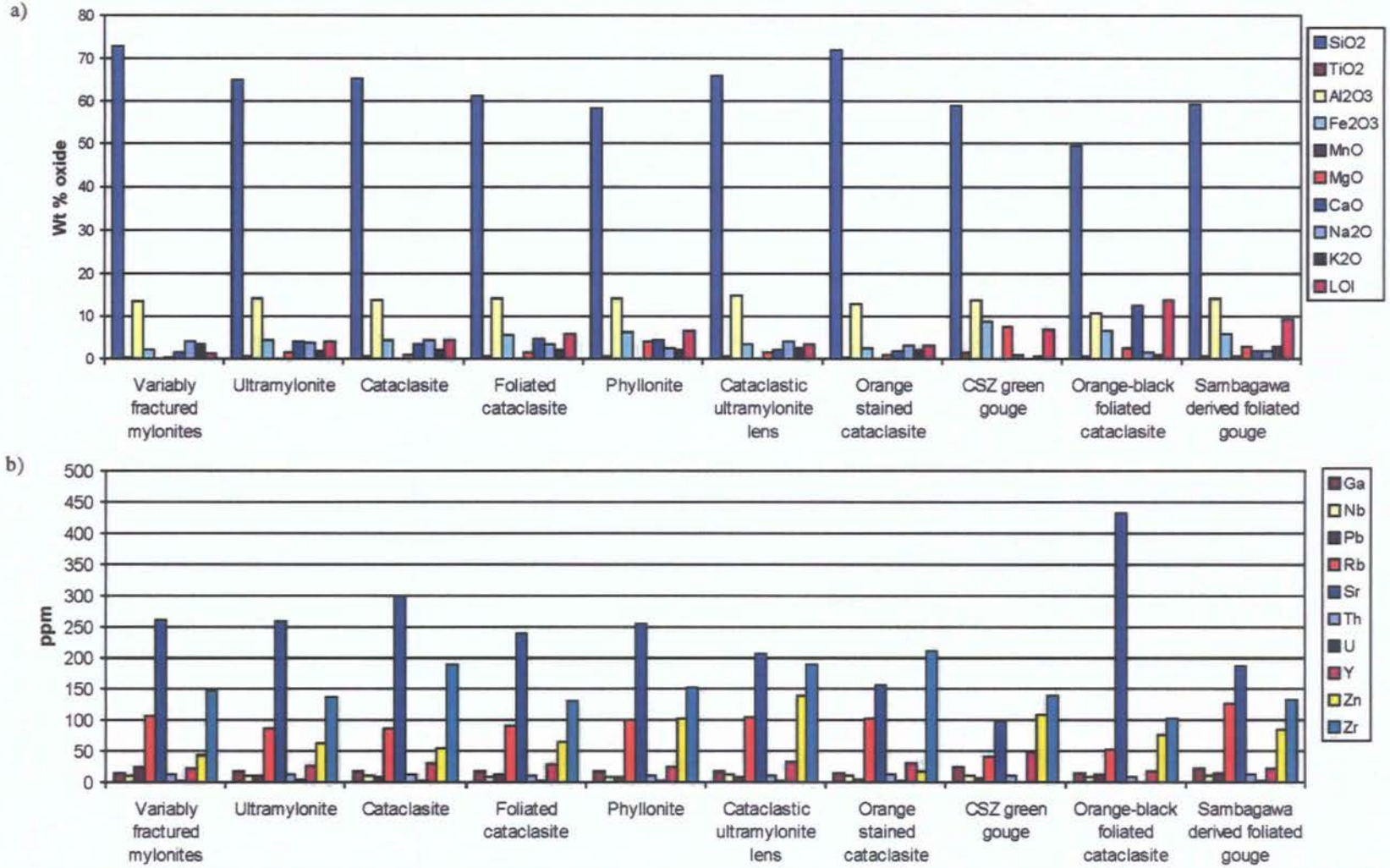

Figure 3.6. a) Mean XRF whole-rock major element data for fault rocks across the Miyamae transect. b) Mean XRF whole-rock trace element data for fault rocks across the Miyamae transect.

reflecting the abundance of silicates such as quartz, feldspar and white mica (as observed within the Ryoke protolith). There is some variation in SiO_2 concentrations (from 72 wt% in the variably fractured mylonites to 50 wt% in the orange-black foliated cataclasite), whilst Al_2O_3 remains fairly constant (~ 14wt%) (Fig. 3.6a). Fe_2O_3 and MgO are variable across the fault zone, with Fe_2O_3 present in higher proportions than MgO, but ratios of the two vary between each fault rock, with highest concentrations of both elements within the phyllonites and central slip zone gouge. Na_2O (~2.5-4.5 wt%) and K_2O (~2 wt%) concentration varies little across the Ryoke-derived fault rocks (Fig. 3.6a), but is highest in the variably fractured mylonite (4 wt% Na_2O and 3.5 wt% K_2O). CaO concentration is higher in fault rocks from the MTL fault core ranging between 1.7 wt% in the variably fractured mylonites to 12.5 wt% within the orange-black foliated cataclasite. CaO, Na_2O and K_2O concentrations are extremely low within the central slip zone gouge (<1 wt%) and the Sambagawa derived foliated gouge (<3 wt%). Loss on ignition (LOI) is very low within the variably fractured mylonites (1.3 wt%), but varies between 3.2-13.85 wt% in the cataclastic fault rocks from the MTL fault core. MnO concentrations in all rocks are negligible and TiO_2 concentration is highest in the central slip zone gouge, but still only accounts for ~1.5 wt%.

Figure 3.6b includes trace element data also obtained during XRF analysis. All fault rock trace element data are dominated by Sr, Rb, Zr and to a lesser extent Zn. The lowest concentrations of these four trace elements are observed within the central slip zone gouge (containing <150 ppm of each).

Protolith-normalised major and trace element data.

Figure 3.7a presents a protolith-normalised major-element geochemical transect across the MTL fault zone in the Miyamae field area, showing the fault rock type for each individual sample and an approximate indication of distance from the central slip zone. Together with the central slip zone gouge the variably fractured mylonites from the whole-rock major element data appear to have experienced the most amount of alteration showing the greatest divergence from the Ryoke protolith composition. The data show enrichment in SiO_2, Na_2O and K_2O and depletion in all other major elements relative to the protolith (Fig. 3.7a) producing a saw-tooth like pattern (most markedly for MgO and CaO). Al_2O_3 remains constant across the fault zone and close to protolith concentrations (Fig. 3.7a). The cataclasite MI-29 to the north of the ultramylonite MIS-05 at the edge of the MTL fault core experiences a decrease in K_2O (3.5 wt% in MIS-11 to 1.4 wt%) and an increase in Na_2O (4 wt% in MIS-11 to 5.2 wt%) relative to the variably fractured mylonites. CaO content increases within cataclasite MI-29 relative to the variably fractured mylonites, but appears to still be depleted relative to the Ryoke protolith.

Ultramylonite MIS-05 was collected at the northern edge of the fault core 50 m north of the central slip zone. The K_2O and Na_2O trend observed in cataclasite MI-29 is reversed (Fig. 3.7a), and now begin to increase and decrease respectively. Relative to the cataclasite and variably altered mylonites to the north, all major elements within ultramylonite MIS-05 either decrease in the degree of enrichment (Na_2O, SiO_2) or depletion (MgO, Fe_2O_3, MnO, CaO, TiO_2, K_2O) moving closer to protolith concentrations. This trend continues from ultramylonite MIS-05 to foliated cataclasite MI-SM19. The foliated cataclasite shows enrichment in Na_2O and a smaller degree of enrichment in K_2O, SiO_2 and TiO_2 relative to the protolith (Fig. 3.7a). MgO remains

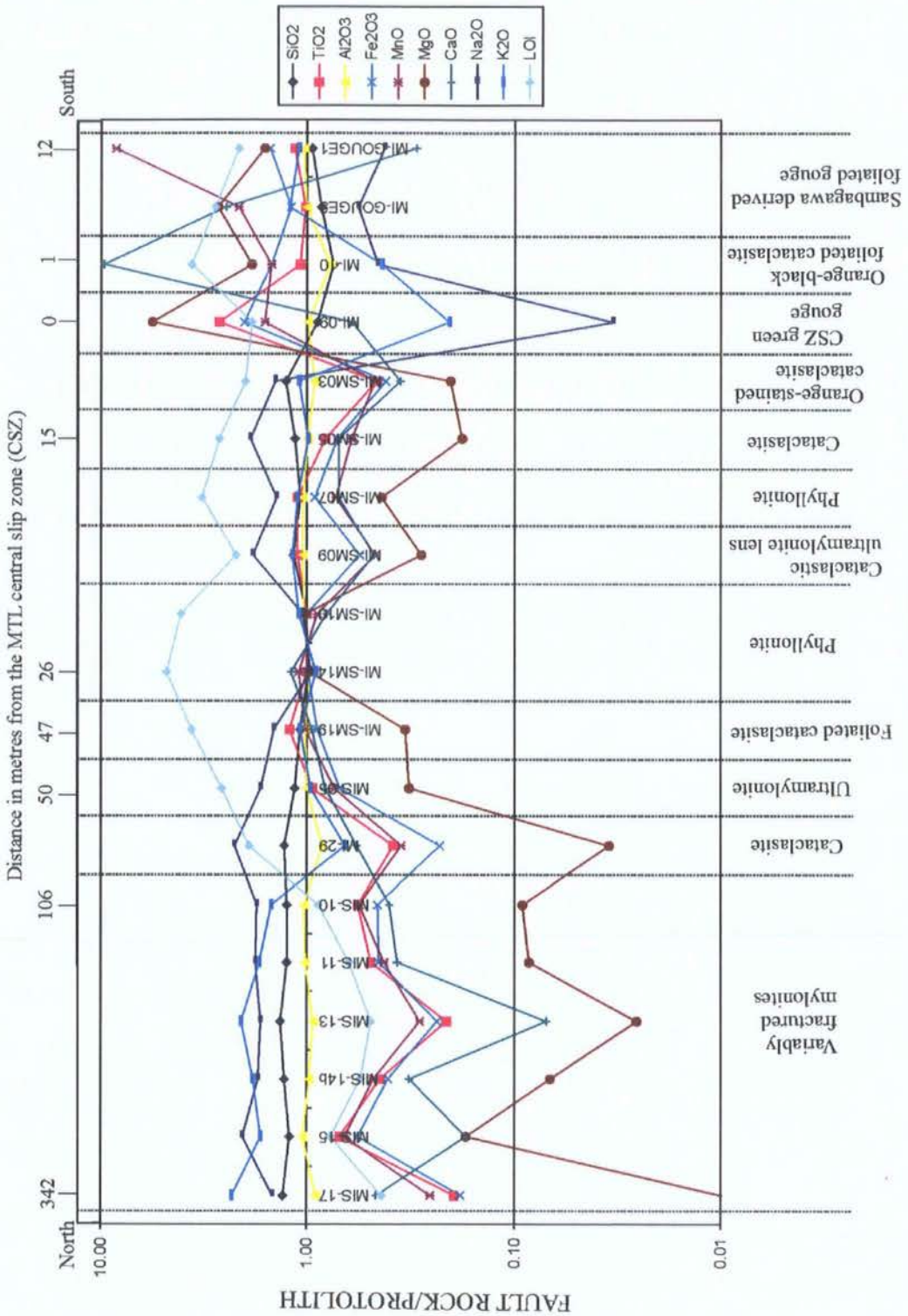

Figure 3.7a Protolith-normalised major-element geochemical transect across the MTL fault zone in the Miyamae field area, the fault rock type of each individual sample and an approximate indication of distance from the central slip zone is provided, note: distance is in a non-linear scale.

in significant depletion relative to the protolith, but only minor depletion of the other major elements (Fe_2O_3, CaO, MnO) is suggested.

Samples MI-SM14 and MI-SM10 are two of the most extensively developed phyllonites (containing highest phyllosilicate contents and abundant operation of DMT processes) from the Fukaya river section (Fig. 3.2b, see also Chapter 2). The noticeable feature of Figure 3.7a is that these two phyllonites mineralogically and texturally, are the most altered fault rocks within the MTL fault core, in terms of major element geochemistry show apparently the least amount of alteration and geochemical divergence from the protolith chemical composition. Phyllonite MI-SM07 contains a lower proportion of phyllosilicates and shows much less evidence for the operation of DMT processes in comparison to phyllonite samples MI-SM14 and MI-SM10. Significantly, phyllonite MI-SM07 shows a greater geochemical divergence away from protolith concentrations in comparison to MI-SM14 and MI-SM10 (Fig. 3.7a). An enrichment in Na_2O and slight enrichment in SiO_2, TiO_2 and K_2O relative to the protolith are observed, with depletions in Fe_2O_3, CaO, MnO and MgO.

The cataclastic ultramylonite lens MI-SM09 is a large lens enveloped within phyllonite (Fig. 3.2b). In comparison to the phyllonites (MI-SM14, MI-SM10, MI-SM07) that entirely enclose it, the ultramylonite lens has a greater enrichment of Na_2O, K_2O, SiO_2 and TiO_2 (Fig. 3.7a), and a greater depletion in Fe_2O_3, CaO, MnO and MgO. In geochemical terms it appears to have undergone a greater degree of alteration compared to the phyllonites measured relative to the protolith.

To the south of the phyllonites ~15 m north of the central slip zone more cataclasite occurs (Fig. 3.2b). Cataclasite MI-SM05 shows a divergence away from protolith geochemical composition comparable to that of the ultramylonite MIS-05

and cataclasite MI-29 further north (Fig. 3.7a). The orange-stained cataclasite MI-SM03 has a more geochemically altered appearance than the adjacent cataclasite MI-SM05, and there is correspondingly a greater depletion of TiO_2, MnO, Fe_2O_3, CaO and MgO, whilst Na_2O and K_2O are enriched relative to the protolith to approximately the same degree to that observed within the foliated cataclasite MI-SM19. SiO_2 enrichment in orange-stained cataclasite MI-SM03 is approximate to that observed in cataclasite MI-29 (Fig. 3.7a).

The central slip zone gouge MI-09 shows the greatest geochemical divergence from the Ryoke protolith that it has been normalised to, as does the orange-black foliated cataclasite MI-10 (Fig. 3.7a). The major elements that have generally shown depletion (MnO, Fe_2O_3, TiO_2, MgO) within Ryoke derived fault rocks to the north show enrichment within the central slip zone gouge, orange-black foliated cataclasite and Sambagawa derived foliated gouge (Fig. 3.7a), whilst major elements that have shown enrichment (SiO_2, Na_2O, K_2O) in the fault rocks to the north are depleted (Fig. 3.7a).

The Sambagawa-derived foliated gouge samples MI-GOUGE 5 and MI-GOUGE 1 (collected 3.5 and 12.45 m south of the central slip zone) have been normalised to the Sambagawa schist protolith. These two samples show significant geochemical divergence from the Sambagawa protolith (Fig. 3.7a).

LOI across the variably fractured mylonites is consistently less than that occurring within the Ryoke protolith ranging between 44-88% of that experienced by the protolith (Fig. 3.7a). Within the fault core, from MI-29 southward, there is a marked increase in LOI ranging from 192% of that occurring within the protolith in cataclasite MI-29 to 479% in phyllonite MI-SM14.

Figure 3.7b presents whole-rock trace element analyses for fault rocks across the fault zone in the Miyamae field area, presented in the same format as major element data in Figure 3.7a. Most trace elements produce a saw-tooth pattern across the fault zone, least so Nb and Zr. Similarly as observed with the major elements, the variably fractured mylonites show the greatest divergence away from protolith trace element concentrations. This divergence decreases in the ultramylonite (MIS-05) and cataclasites (MI-29, MI-SM19, MI-SM09, MI-SM05) of the fault core and is least in the phyllonites (MI-SM14, MI-SM10). A more varied saw-tooth pattern of trace element data returns in the fault rocks adjacent to the central slip zone gouge (MI-09, MI-10).

3.4.2. Major and trace element composition of fault rocks from the Tsukide Transect.

Fault rock composition – raw data.

Figure 3.8 presents mean raw data for each of the fault rock types across the MTL fault zone at Tsukide. The whole-rock major elemental compositions of the fault rocks across the Tsukide samples closely resemble those observed across the Miyamae transect. All fault rock compositions are again dominated by SiO_2 (varying between 75 wt% in the cataclastic ultramylonite lens and 55 wt% in the central slip zone gouge) and Al_2O_3 (remaining ~14 wt%). Fe_2O_3 concentration varies, but is highest (5.5 wt%) in the central slip zone gouge and orange-black foliated cataclasite, Fe_2O_3: MgO ratios vary between fault rocks, but MgO concentration is lower than that of Fe_2O_3 throughout all fault rocks. Na_2O (~1.3-5 wt%) and K_2O (~1-3 wt%) concentration varies little across the fault rocks (Fig. 3.8a), but the greatest difference between the two major elements occurs within the cataclastic ultramylonite lens. CaO concentration within the Tsukide transect fault rocks is generally lower than that

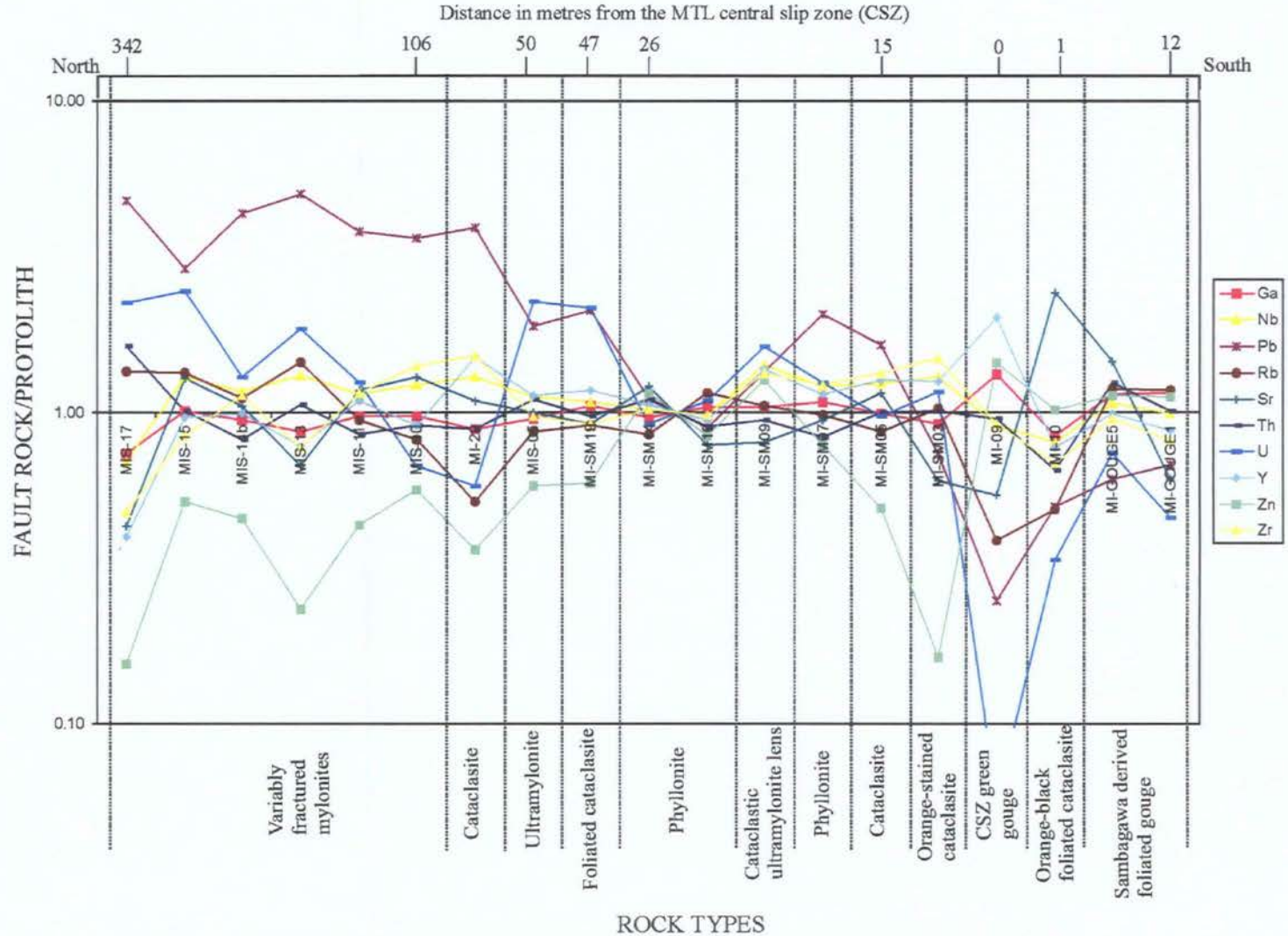

Figure 3.7b Protolith-normalised trace-element geochemical transect across the MTL fault zone in the Miyamae field area, the fault rock type of each individual sample and an approximate indication of distance from the central slip zone is provided, note: distance is in a non-linear scale.

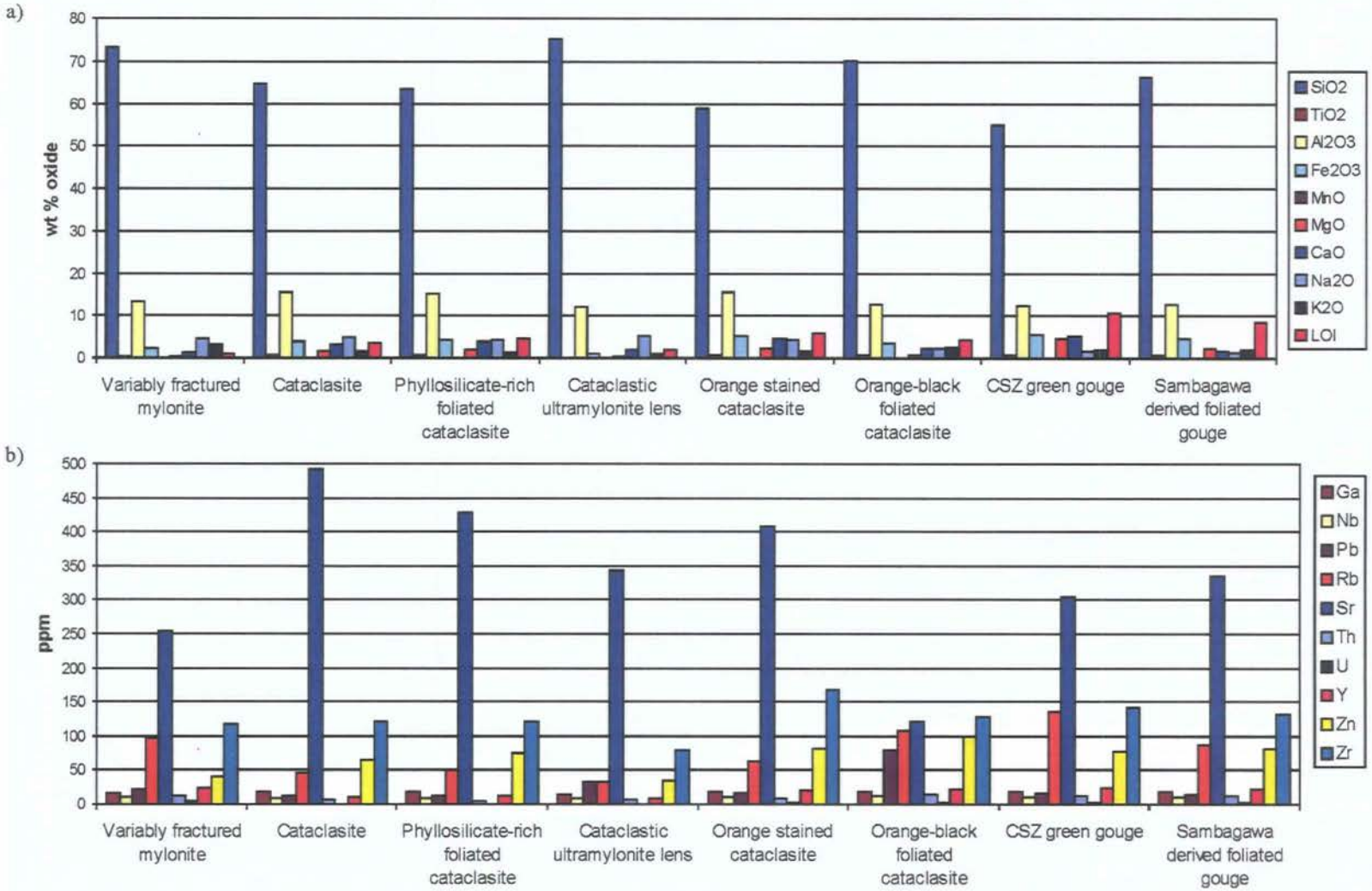

Figure 3.8. a) Mean XRF whole-rock major-element data for fault rocks across the Tsukide transect. b) Mean XRF whole-rock trace-element data for fault rocks across the Tsukide transect.

observed within the Miyamae fault rocks (see Fig. 3.6a and Fig. 3.8a). CaO increases from the variably fractured mylonite (1.3 wt%) to the phyllosilicate-rich foliated cataclasite (4 wt%), across all other fault rocks it constitutes <2.5 wt%. LOI is also very low within the variably fractured mylonites (~1 wt%), but varies between 2-11 wt% across the cataclastic fault rocks of the MTL fault core, with the lowest concentrations within the cataclastic ultramylonite lens and highest in the central slip zone gouge. MnO and TiO_2 concentrations in all rocks are again negligible (<1 wt%).

Figure 3.8b presents trace element data for the Tsukide fault rocks. Sr, Rb, Zr and Zn dominate each fault rock analysis, as observed within the Miyamae fault rocks, but Sr concentrations are higher within the Tsukide samples. Sr varies from 254 ppm within the variably fractured mylonites to 491 ppm in the Ryoke-derived cataclasite. Lowest concentrations are again observed within the central slip zone gouge (containing <128 ppm of each trace element analysed).

Protolith-normalised major and trace element data.

Figure 3.9a presents a protolith-normalised major-element geochemical transect across the MTL fault in the Tsukide field area. The variably fractured mylonites in the Tsukide field area show a very similar pattern of alteration and divergence from protolith geochemistry to that observed within the Miyamae variably fractured mylonites (compare Fig. 3.7a and Fig. 3.9a). Al_2O_3 remains constant. There is enrichment in SiO_2, Na_2O and K_2O to the same degree as that experienced by the Miyamae variably fractured mylonites and depletion in all other major elements relative to the protolith (Fig. 3.9a). There is ~95 m gap in available outcrop exposure between variably fractured mylonite TKR-18 and cataclasite TKS-10 within the fault core (Fig. 3.4a). The analysis of cataclasite TKS-10 shows a decrease in the depletion

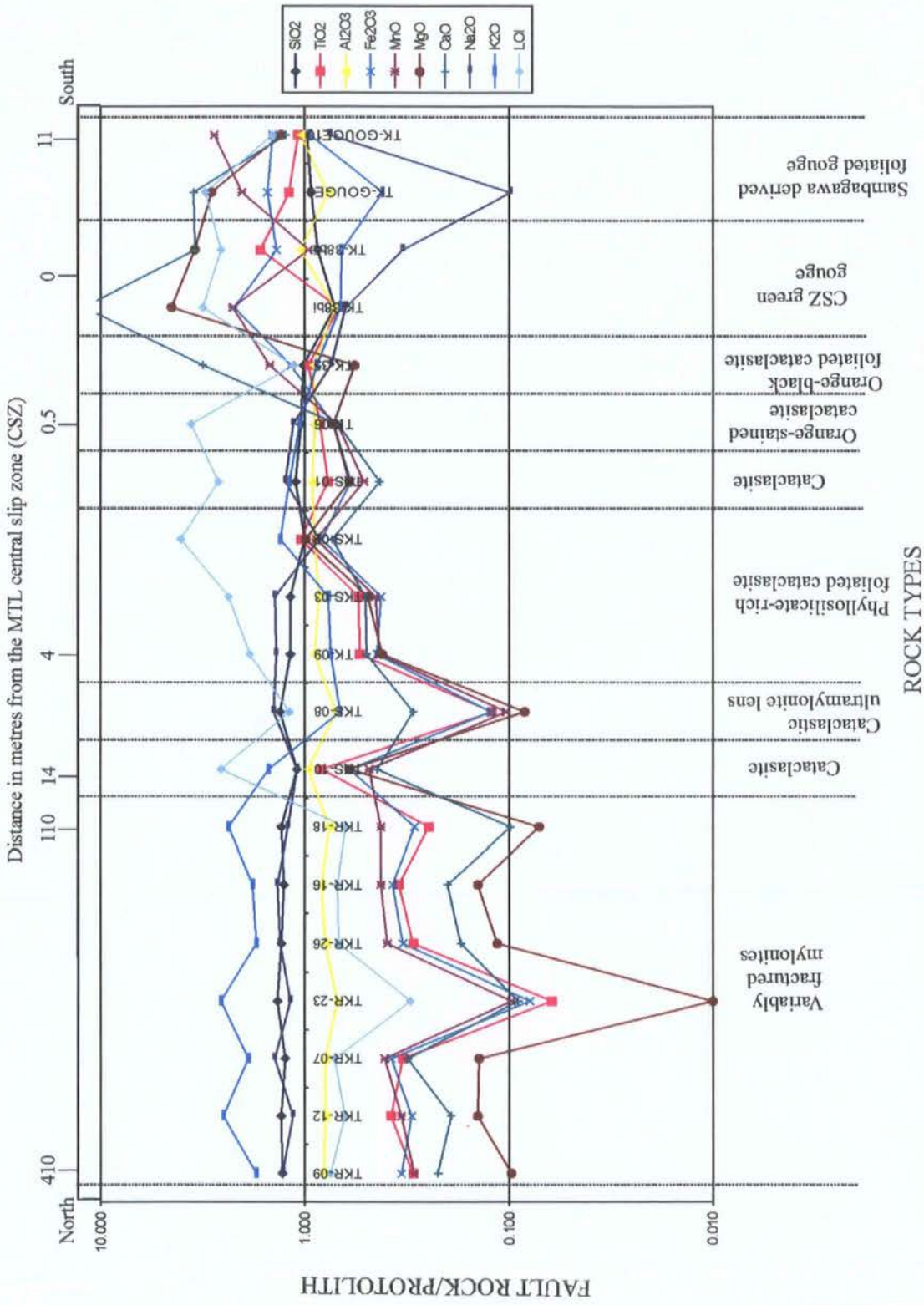

Figure 3.9a Protolith-normalised major-element geochemical transect across the MTL fault zone in the Tsukide field area, the fault rock type of each individual sample and an approximate indication of distance from the central slip zone is provided, note: distance presented in a non-linear scale.

of TiO_2, MgO, Fe_2O_3, MnO and CaO moving closer to concentrations analysed from the Ryoke protolith. Na_2O and K_2O still appear enriched (K_2O more so than Na_2O) relative to the protolith, but the amount of enrichment decreases in comparison to the variably fractured mylonites to the north (Fig. 3.9a). Na_2O decreases from 4.3 wt% in TKR-18 to 3.9 wt% in TKS-10, and K_2O decreases from 3.6 to 2.3 wt%.

Cataclasite TKS-10 to the south develops into phyllosilicate-rich foliated cataclasite, samples TK-09, TKS-03 and TKS-02. Within the phyllosilicate-rich foliated cataclasites each of the major-element data are more closely grouped in comparison to the fault rocks to the north (Fig. 3.9a). For the first time as we move south across the fault zone, Na_2O content is higher than K_2O in samples TK-09 and TKS-03. Na_2O is enriched 140% compared to the protolith whilst the samples contain only 76% of the K_2O. TKS-02 is a more extensively evolved phyllosilicate-rich foliated cataclasite, with a higher chlorite content and a more pervasively developed foliation. The major-element data in TKS-02 lies close to protolith concentrations (Fig. 3.9a), and the trend in Na_2O and K_2O reverses from that observed within the foliated cataclasites TK-09 and TKS-03. To the south of the phyllosilicate-rich foliated cataclasite is cataclasite TKS-01, located just 1.15 m north of the central slip zone and orange-stained cataclasite TK-06 0.5 m north, the pattern of their major-element analyses on Figure 3.9a mirrors that of cataclasite TKS-10 north of the foliated cataclasites. The only difference of note is that Na_2O and K_2O concentrations are of approximately equal proportions in the cataclasites to the south.

Sample TKS-08 is a cataclastic ultramylonite lens within the phyllosilicate-rich foliated cataclasite (Fig. 3.4b), and the major-element geochemistry shows a greater divergence from protolith concentrations in comparison to the phyllosilicate-rich foliated cataclasite that surrounds it. Relative to the protolith, TKS-08 shows

enrichment in SiO_2 and Na_2O, and depletion in CaO, Fe_2O_3, TiO_2, MnO and MgO and is comparable to the trends observed within the variably fractured mylonites to the north (Fig. 3.9a).

The orange-black foliated cataclasite TK-35 immediately adjacent to the central slip zone has been normalised to the Sambagawa protolith in this instance, and a spread of data diverging from the protolith composition again occurs (Fig. 3.9a). A noticeable enrichment in CaO relative to the Sambagawa protolith is observed. Two central slip zone gouge samples, TK-38bi and TK-38bii, show different concentrations of each major-element relative to the Sambagawa protolith (Fig. 3.9a). The same pattern is observed within the two Sambagawa derived foliated gouge samples, but TK-GOUGE 10 collected 11.5 m to the south appears to show major-element compositions closer to that of the Sambagawa protolith in comparison to the previous Sambagawa-derived fault rocks close to the central slip zone.

LOI across the variably fractured mylonites, like that observed across the Miyamae transect, is less than that occurring within the Ryoke protolith ranging between 30-74% of that experienced by the protolith (Fig. 3.9a). Within the fault core a marked increase in LOI is again observed ranging from 119% compared to the protolith in the cataclastic ultramylonite lens TKS-08 to 406% in the most extensively developed phyllosilicate-rich foliated cataclasite TKS-02.

Figure 3.9b presents whole-rock trace element analyses for the fault rocks across the Tsukide fault zone transect. The variably fractured mylonites from Tsukide show a greater divergence from protolith concentrations in comparison to variably fractured mylonites from Miyamae (Fig. 3.7b). Similarly whole-rock major and trace element data from foliated cataclasites within the fault core at Tsukide lie further from protolith concentrations in comparison to the Miyamae phyllonitic fault rocks. All

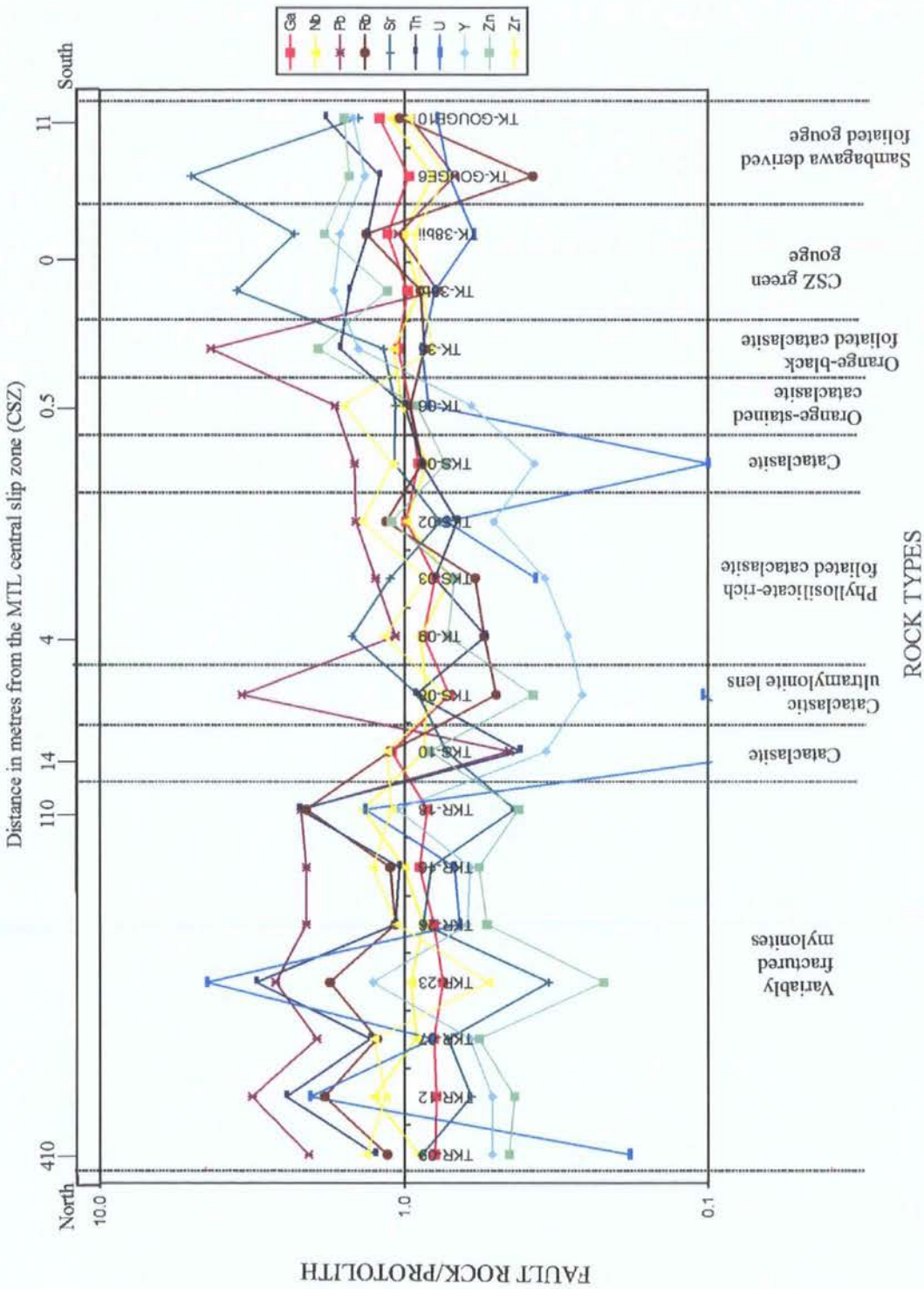

Figure 3.9b Protolith-normalised trace-element geochemical transect across the MTL fault zone in the Tsukide field area, the fault rock type of each individual sample and an approximate indication of distance from the central slip zone is provided, note: distance is a non-linear scale.

elements produce a saw-tooth pattern across the fault zone. Across the variably fractured mylonites, Rb, Pb, Th and U generally show enrichment while other trace elements analysed display depletion relative to the Ryoke protolith. Across the fault rocks within the core of the fault zone, the cataclasites (TKS-10, TKS-01, TKS-08, TK-06) show greatest divergence from protolith concentrations similar to the variably fractured mylonites. The phyllosilicate-rich foliated cataclasite samples (TK-09, TKS-03, TKS-02) show least divergence from protolith concentrations, but the data does not plot in such a tight cluster as that observed within the phyllonites from Miyamae (compare Fig. 3.7b and Fig. 3.9b). The fault rocks to the south of the fault zone (TK-35, TK-38bi, TK-38bii, TK-GOUGE 6, TK-GOUGE 10), normalised to the Sambagawa protolith, show a more general enrichment in most trace elements except for Pb and U which show depletion across all five samples.

3.4.3. Discussion of geochemical processes identified from XRF whole-rock element data.

As Al_2O_3 remains relatively constant across both transects and close to the protolith concentration, this suggests that Al_2O_3 behaved as an immobile element during the deformation and alteration that produced the MTL fault rocks. Several studies have confirmed the relative immobility of Al in rocks that have been subjected to alteration and deformation (e.g. Grant, 1986; Selverstone et al., 1991). Across both transects, approximately at the northern edge of the fault core, an increase in Na_2O and a decrease in K_2O is observed within the cataclasites (Figs. 3.7a and 3.9a; Tables 3.4 and 3.5). This Na-metasomatism reflects the progressive increase in the albitisation of K-feldspar across the MTL fault zone (see Table 2.1 and Table 3.2) (Van Staal et al., 2001; Jefferies et al., 2006). The variably fractured mylonites in

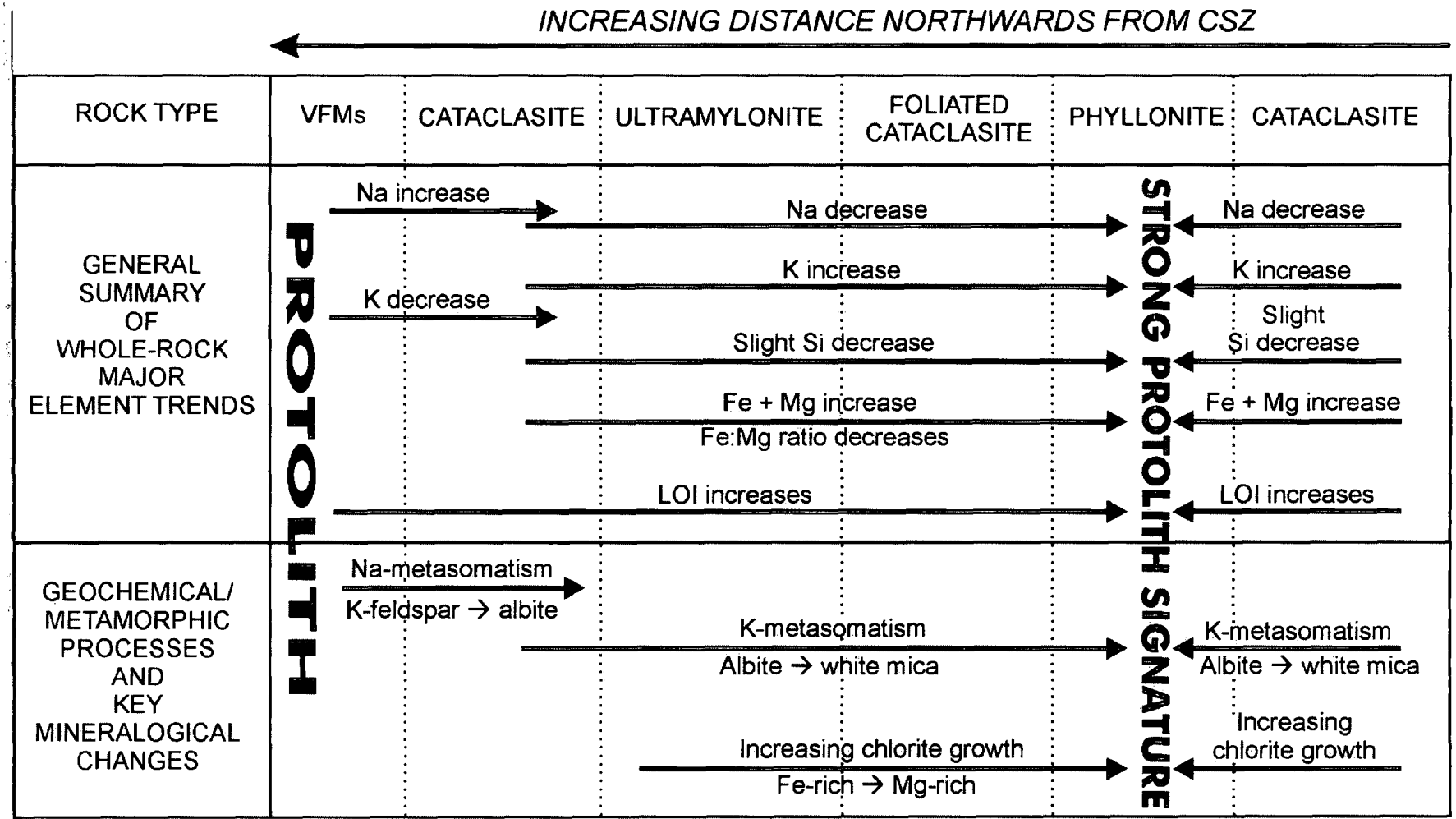

Table 3.4. Summary of XRF whole-rock major element data trends across Ryoke derived fault rocks within the Miyamae field area and the geochemical/metamorphic processes and mineralogical changes accounting for these trends.

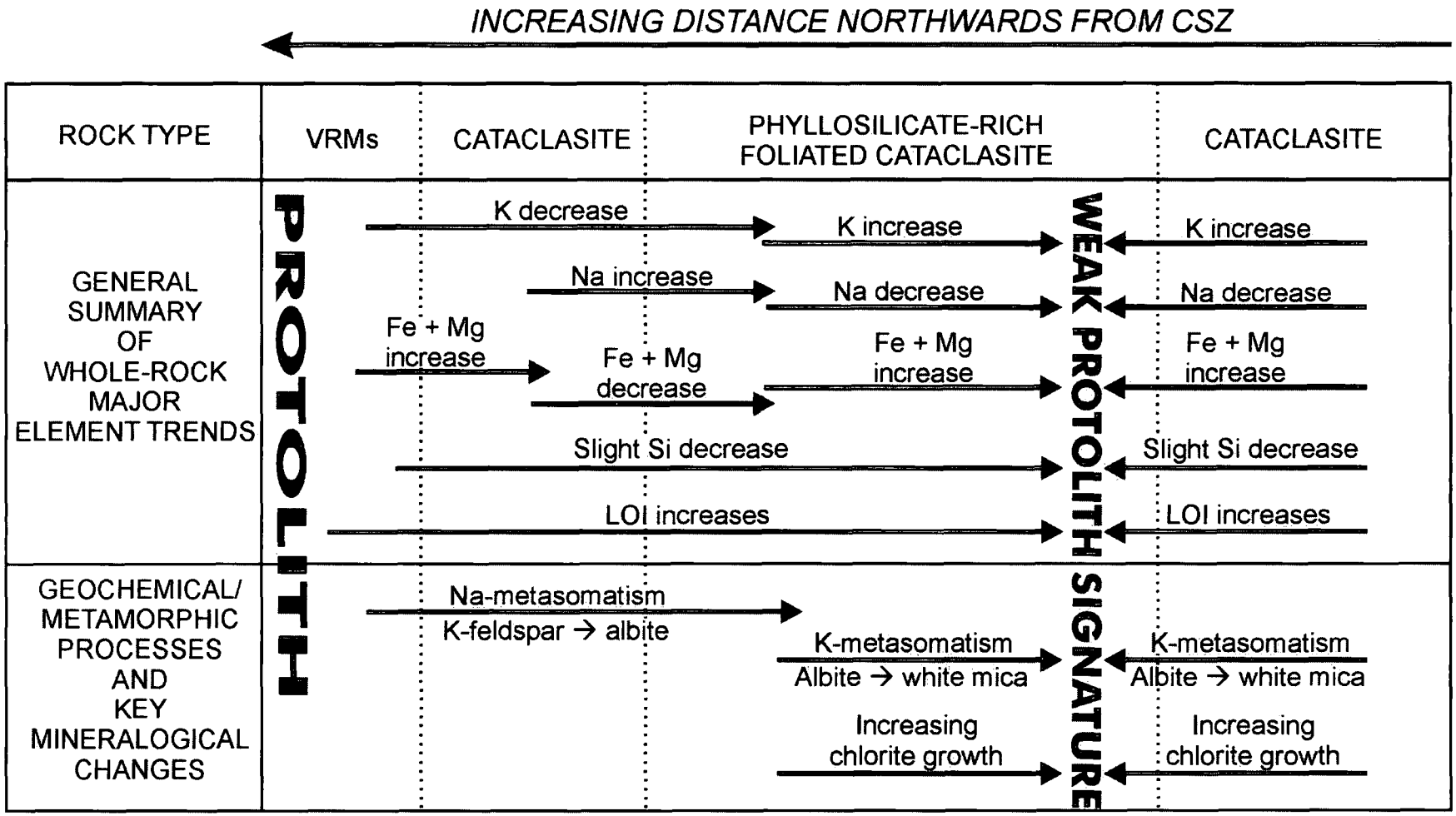

Table 3.5. Summary of XRF whole-rock major element data trends across Ryoke derived fault rocks within the Tsukide field area and the geochemical/metamorphic processes and mineralogical changes accounting for these trends.

Miyamae and Tsukide have a very similar geochemical profile and form a distinct zone enriched in SiO_2 relative to the Ryoke protolith (Figs. 3.7a and 3.9a). This may correspond to a zone of preferential quartz cementation. Quartz veins occur throughout the variably fractured mylonites, but are not widespread. The large reductions in MgO, Fe_2O_3 and CaO and increases in K_2O or Na_2O (Tables 3.4 and 3.5) may reflect alteration of mafic-type minerals, such as hornblende and biotite, coupled with breakdown of Ca-rich feldspar to albite and white mica. Across the variably fractured mylonites with decreasing distance to the fault core, microstructural observations show the progressive alteration of biotite and hornblende to chorite, and increasing proportions of albite and white mica (Table 2.1 and Table 3.2). The pervasive fracturing observed in the field and fluid infiltration within the fractured mylonites would have aided all of these processes.

Within the fault core along the Miyamae transect between cataclasite MI-29 and ultramylonite MIS-05 the trend in Na_2O and K_2O observed within the rocks to the north is reversed, i.e. Na_2O decreases and K_2O increases (Fig. 3.7a and Table 3.4). It appears that Na-metasomatism within the breakdown of K-feldspar to albite in the outer fault zone has given way to K-metasomatism with the breakdown of albite to white mica (phengite in this case, see Section 2.3.3; Table 3.4) (cf. Van Staal et al., 2001; Jefferies et al., 2006). This geochemical signature of K-metasomatism is also recognised along the Tsukide transect between the phyllosilicate-rich foliated cataclasites TKS-03 and TKS-02 (Fig. 3.9a; Table 3.5), reflecting the more extensive phyllosilicate development within TKS-02 (see Section 3.3.2 and Fig. 3.5).

The K-metasomatism geochemical trend continues from the ultramylonite MIS-05 to foliated cataclasite MI-SM19 along the Miyamae transect (Fig. 3.7a and Table 3.4). There is also a slight decrease in SiO_2 from cataclasite MI-29 southward to the

foliated cataclasite that also reflects the breakdown of feldspar (Table 3.4). During the breakdown of albite to white mica and quartz, Na is released (e.g. Hemley and Jones, 1964). The variably fractured mylonites to the north of the fault core may have provided a sink for some Na mobilising out of the fault core, thus also accounting for some of the enrichment in this element relative to the Ryoke protolith.

Thus, with closer proximity to the fault core, the change from Na-metasomatism to K-metasomatism does not necessarily reflect a major change in fluid composition with time. Aqueous fluids only have to provide a medium for cation exchange, and a decrease in temperature is sufficient to increase the stability field of muscovite relative to both K-feldspar and albite in the presence of a fluid (Simpson and Wintsch, 1989; Wintsch et al., 1995).

From MI-29 to MI-SM19, the degree of divergence of major elements from protolith concentrations decreases within the phyllonites MI-SM14 and MI-SM10 apparently showing very similar concentrations of all major elements to the protolith (Fig. 3.7a and Table 3.4). To the south of the phyllonites, cataclasite MI-SM05 and orange-stained cataclasite MI-SM03 show very similar geochemical profiles to the cataclasites and ultramylonite to the north. Chemical changes in the phyllonites are likely to be complex because, in part, the geochemical processes occurring overprint previously Na-metasomatised tectonites. Within phyllonites MI-SM14 and MI-SM10 evidence for the operation of DMT processes including pressure solution are widespread (see section 2.3.3.4). It appears that the solution transfer processes occurring within the phyllonite are effectively altering and removing the previous alteration signature within the ultramylonite and cataclasites. Thus evidence for Na-metasomatism is best preserved in less-altered 'protected' lenses within the phyllonite, and this is what we observe texturally and geochemically in the cataclastic

lens MI-SM09 enveloped within the phyllonite at Miyamae (see Fig. 2.6 and Fig. 3.7a). LOI values give a more realistic indication of which of the fault rocks have suffered most alteration relative to the Ryoke protolith. LOI increases across the fault zone into the fault core (Table 3.4) reaching a peak in the most extensively developed phyllonite MI-SM14, showing a LOI value 479% more than that of the Ryoke protolith (Fig.3.7a). This reflects the breakdown of anhydrous mineral phases to syn-tectonic, OH-bearing mineral phases, i.e. white mica from feldspar, and the introduction of chlorite and clays (kaolinite). The cataclastic ultramylonite lens shows a LOI dip again reflecting its relative isolation in geochemical terms from the surrounding phyllonites.

These processes are also reflected along the Tsukide transect (Fig. 3.9a and Table 3.5). The phyllosilicate-rich foliated cataclasites show the least amount of divergence from protolith composition, and TKS-02 with the highest phyllosilicate content shows the least divergence and highest LOI (406% of that within the protolith). The dip in LOI and greater apparent alteration (geochemical memory of a more altered state) is also recorded in the analysis of the cataclastic ultramylonite lens TKS-08 that lies within the phyllosilicate-rich foliated cataclasite. Microstructural and geochemical observations suggest that the phyllosilicate-rich foliated cataclasites may be a precursor or shallower equivalent to the phyllonites at Miyamae (see Chapter 4), and thus the geochemical data has not become so homogenised since phyllosilicate-growth and fluid-assisted reactions during DMT processes are not as extensively developed.

Given the advanced development of phyllonitic fabrics within the MTL fault core at Miyamae, it is also possible to consider the ultramylonite as the phyllonite protolith (see Fig. 2.8 and section 2.3.4.). By normalising major element whole-rock

analyses of the fault rocks within the MTL fault core to ultramylonite MIS-05, a progressive increase in Fe_2O_3 and MgO from ultramylonite through cataclasite and foliated cataclasite to phyllonite is observed reflecting the increasing precipitation of chlorite as the phyllonite develops (see Fig. 2.8; Table 3.4; Jefferies et al., 2006).

The 'saw-tooth' form and greater spread of normalised whole-rock trace element data along both Miyamae and Tsukide transects (Fig. 3.7b and 3.9b) where elements are enriched in some fault rocks and depleted in others suggests that transverse (across-strike) migration of components has taken place across the fault zone (Hippertt, 1998). This particularly applies to mobile elements such as Pb, Rb, Sr and U. However, as the other trace elements are largely considered to be insoluble and therefore immobile it may be that migration of major elements (Si, K, Na) between fault rocks (i.e. Na release during breakdown of albite to white mica and quartz) produced a 'relative abundance' effect resulting in the observed profile (Hippertt, 1998). This is in accordance with the previously discussed potential silica enrichment and Na mobilisation from reactions within the fault core. The Tsukide trace element data (Fig. 3.9b) show greater divergence from protolith concentrations in comparison to the Miyamae data (Fig. 3.7b). This may reflect a wider more prolonged circulation of fluids across the Tsukide transect. In Miyamae, once the phyllonites formed, it is possible that they acted as a channel for the through-flow of circulating fluids, and as a result, less fluid circulation and alteration occurred within fault rocks elsewhere across the fault zone. Permeability data from Wibberley and Shimamoto (2003) suggest that across the variably fractured mylonites in the Tsukide area, there are zones of very low permeability due to cementation. Therefore, at some time during deformation, a highly connected porosity must have existed in these rocks for fluid infiltration and cementation to occur. The variably fractured mylonites, although now

apparently cemented are geochemically preserving an earlier alteration event that became 'frozen in' as continued deformation became increasingly focused to within the MTL cataclastic fault core.

It is difficult to draw conclusions about the possible geochemical processes occurring within the central slip zone and orange-black foliated cataclasite along both Miyamae and Tsukide transects due to the fact that they are most likely derived from a mixture of both Ryoke and Sambagawa material. Thus the whole rock analysis will represent an average of both components.

3.5. ICP-MS whole-rock trace element analysis.

An inductively coupled plasma mass spectrometer (ICP-MS) was used in the analysis of whole-rock trace element data. This represents a more refined technique compared to the XRF analysis of low abundance trace elements. The trace element data are presented here in the form of multi-element spiderdiagrams (e.g. Thompson et al., 1984) with a representative suite of fault rocks across each transect being analysed. The elements are arranged according to their mobility in an aqueous environment, with mobile elements (Cs, Pb, Ba, Rb, Sr and U) plotted on the left of the spiderdiagram and relatively immobile elements (Th, Ta, La, Nb, Ce, Nd, Zr, Hf, Sm, Tb, Y, Tm and Tb) plotted to the right (Pearce, 1983; Rollinson, 1993).

Trace element and REE data are conventionally normalised to chondritic abundances (Rollinson, 1993). Here trace element data are presented in chondrite normalised plots, including the Ryoke protolith MIS-18, and protolith normalised plots used to determine the amount of trace element enrichment and/or depletion experienced by each of the fault rocks.

3.5.1. Miyamae transect multi-element spiderdiagrams.

The chondrite-normalised trace element plot (Fig. 3.10a) illustrates that the Ryoke protolith and all fault rocks show enriched trace element abundances relative to chondritic values. The mobile elements (to the left) have a 'saw-tooth' pattern compared to the immobile elements (to the right). Chondrite-normalised mobile element compositions are slightly more scattered than the immobile element compositions. Within both protoliths and fault rocks, the greatest enrichment is observed in Rb, U and Th (Fig. 3.10a). The immobile elements Sm to Yb have a slight negative slope, and generally all fault rocks contain higher concentrations of mobile over immobile elements.

Figure 3.10b presents protolith-normalised trace element data. There is a marked contrast between the more varied 'saw-tooth' pattern of the mobile trace elements (Cs to Ta) compared to the relatively smooth pattern of the immobile trace elements (La to Yb). There is an apparent enrichment in Zr and Hf in all fault rock samples relative to the protolith, with a progressive enrichment and divergence from protolith concentrations from variably fractured mylonite, through cataclasite, foliated cataclasite, phyllonite to orange-black foliated cataclasite and central slip zone gouge. Sm to Yb plot sub-parallel to the x-axis and are not significantly enriched or depleted with respect to the protolith.

3.5.2. Tsukide transect multi-element spiderdiagrams.

The Tsukide transect trace-element chondrite normalised plot (Fig. 3.11a) has a very similar form to the equivalent Miyamae transect data (Fig. 3.10a). All trace elements are enriched relative to chondrite concentrations and mobile elements have higher concentrations across all samples relative to immobile elements. The negative

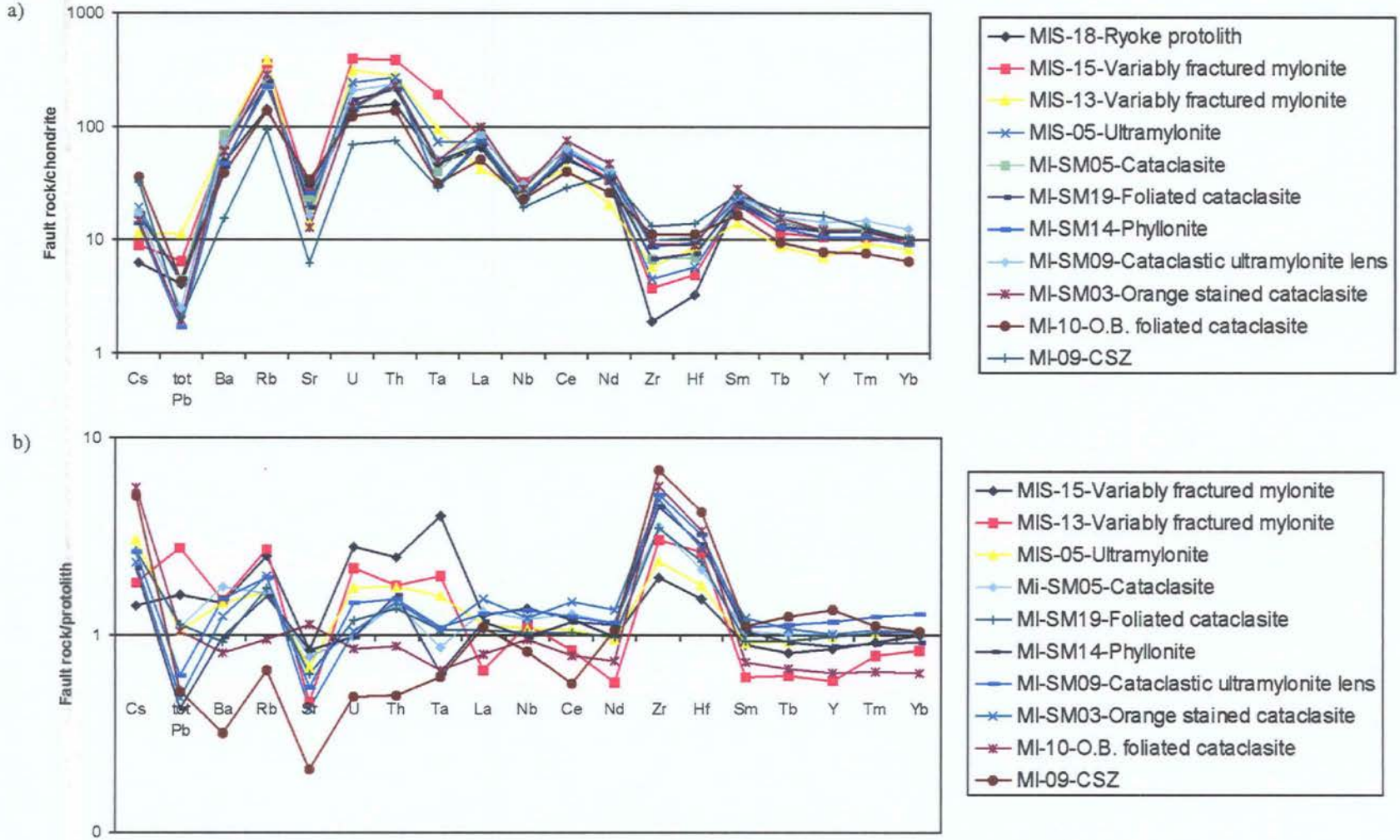

Figure 3.10. A) multi-element spiderdiagram of ICP-MS trace element data from a representative suite of fault rocks across the Miyamae transect normalised to chondritic abundances. B) multi-element spiderdiagram normalised to protolith concentrations.

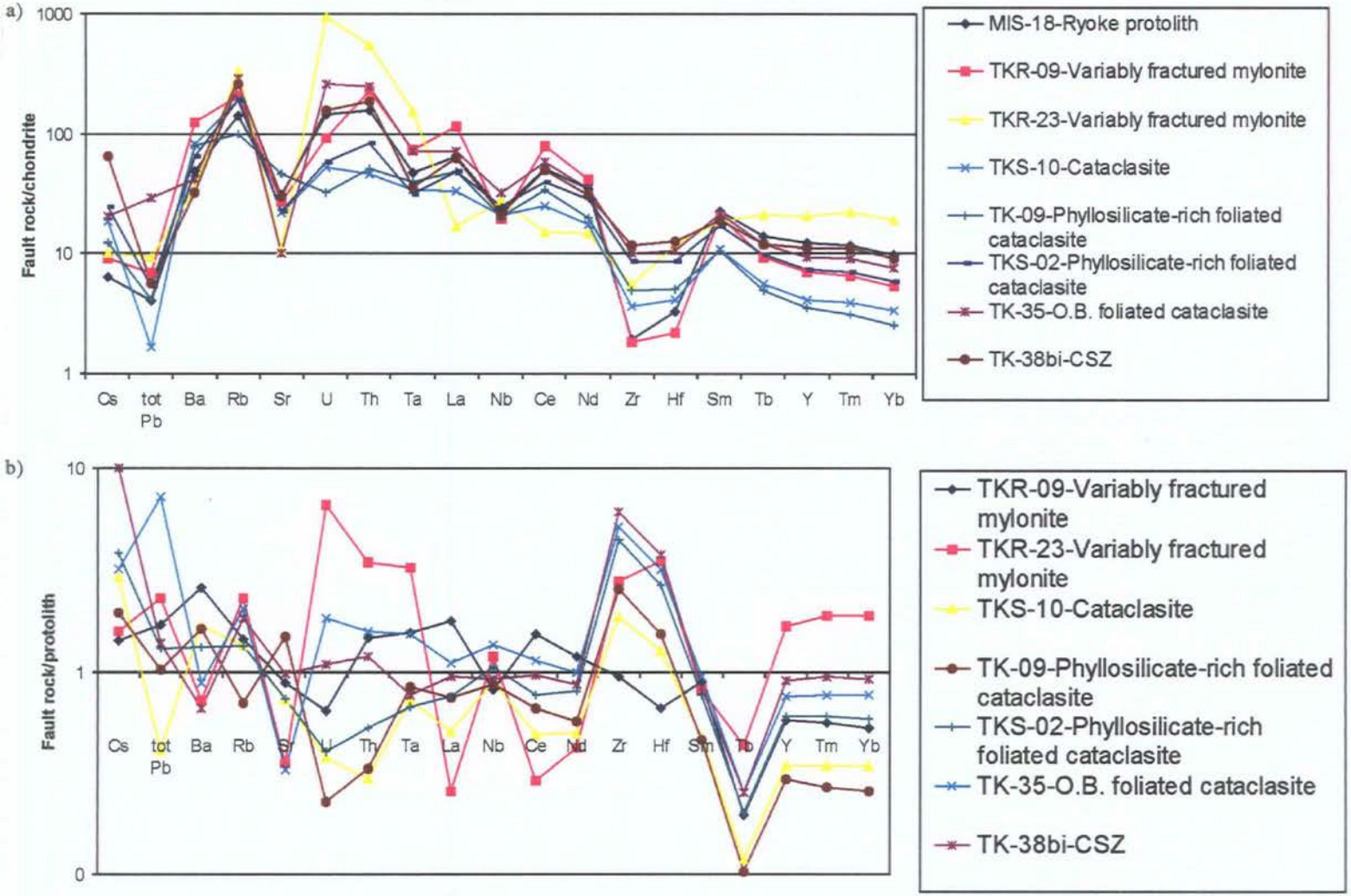

Figure 3.11. a) multi-element spiderdiagram of ICP-MS trace element data from a representative suite of fault rocks across the Tsukide transect normalised to chondritic abundances. b) multi-element spiderdiagram normalised to protolith concentrations.

slope from Sm to Yb is also present, but, as a whole, the Tsukide data shows a wider scatter of each trace element across all samples (Fig. 3.11a).

The protolith-normalised spiderdiagram (Fig. 3.11b) shows that the more mobile elements on the left of the plot (Cs to La) show a much more chaotic pattern within the Tsukide fault rocks in comparison to the Miyamae plot: Figure 3.10b. U and Th concentrations show the widest scatter, Nb the least. Enrichment in Zr and Hf is also noted, with a progressive enrichment from variably fractured mylonite, through cataclasite and phyllosilicate-rich foliated cataclasite to orange-black foliated cataclasite and central slip zone gouge (Fig. 3.11b). The Tsukide fault rocks show an apparent depletion in Tb compared to protolith concentration, but immobile elements Y, Tm and Yb plot sub-parallel to the x-axis like that observed within the Miyamae fault rocks (see Fig. 3.10b). However, the scatter of data is wider than within the Miyamae fault rocks. Variably fractured mylonite TKR-23 is enriched in Y, Tm and Yb relative to the protolith, whilst there is a progressive depletion in these elements from the central slip zone TK-38bi, through orange-black foliated cataclasite TK-35, phyllosilicate-rich foliated cataclasite TKS-02, variably fractured mylonite TKR-09 to cataclasite TKS-03 and phyllosilicate-rich foliated cataclasite TK-09.

3.5.3. Discussion of geochemical processes identified from multi-element spiderdiagrams.

The distinctive feature of protolith-normalised trace element spiderdiagrams from both Miyamae and Tsukide is the contrast between the more varied 'saw-tooth' pattern produced by the mobile elements (to the left) and the smoother curves of the immobile elements (to the right) (cf. Fig. 3.10b and 3.11b). The varied pattern of immobile elements support the suggestion that perhaps lateral migration of

components has taken place across the fault zone cataclasites and mylonites (Hippertt, 1998). But the spread and divergence away from protolith concentrations observed in the immobile elements is supporting evidence for the transverse migration of other major elements, producing an apparent dilution/enrichment of the immobile elements remaining in the fault rocks (Hippertt, 1998). Progressive alteration with deformation and the breakdown and removal of material (i.e. Na-metasomatism and K-metasomatism discussed in section 3.4.3.) created the apparent progressive enrichment observed in Zr and Hf across the fault rocks from both Miyamae and Tsukide transects.

The most immobile elements to the right of the spiderdiagram plot sub-horizontal to the x-axis because the initial concentration of each of these trace elements essentially does not change, but their proportion of the fault rock make-up does alter as more mobile elements are added or removed. This is reflected in the concentration of Y, Tm and Yb within variably fractured mylonite TKR-23, phyllosilicate-rich foliated cataclasite TK-09 and cataclasite TKS-10 that show the greatest divergence from protolith compositions. It is also these samples that show the greatest enrichment in major elements SiO_2, Na_2O and in particular K_2O (see Fig. 3.9a). Microstructural analysis has shown that the most extensively developed phyllosilicate-rich foliated cataclasite TKS-02 is one of the most altered Ryoke derived fault rocks along the Tsukide transect, displaying significant evidence for fluid assisted processes. This rock type has immobile trace element concentrations that plot closer to protolith concentrations than the other fault rocks listed above. The trace element data here also appear to be mirroring the homogenisation of elements through processes of diffusion and/or mechanical mixing discussed in section 3.4.3. Likewise the fault rocks from the fault core along the Miyamae transect show

immobile trace element concentrations very close to that of the Ryoke protolith (Fig. 3.10b).

The greater spread of data and more varied pattern produced by the Tsukide transect fault rocks in comparison to the Miyamae fault rocks may be produced by the wider circulation of fluids across the Tsukide transect in comparison to a more focused fluid flow within the phyllonites along the Miyamae transect (see also section 3.2.3.).

3.6. Rare earth elements.

Rare earth elements (REE) were analysed using ICP-MS. The atomic number of the REEs increases progressively from La (Z = 57) to Lu (Z = 71) and are often grouped into the 'light rare earth elements' (LREE) (La, Ce, Pr, Nd and Sm) and the 'heavy rare earth elements' (HREE) (Gd, Tb, Dy, Ho, Er, Tm, Yb and Lu). The REEs behave as a chemically coherent group and are believed to be relatively immobile during hydrothermal alteration. However, is has been reported that REEs may become increasingly mobile at metamorphic grades of greenschist facies and above, and/or in the presence of halogen- or carbonate-rich fluids (Humphries, 1984; Grauch, 1989).

3.6.1. REE data - Miyamae transect fault rocks.

The Miyamae chondrite-normalised REE plot shows a tight cluster of data across all fault rocks, with all fault rocks containing higher concentrations of all REE relative to chondritic concentrations (Fig. 3.12a). A slight Eu anomaly is observed, indicating the presence of feldspar. The LREE are present in higher concentrations than the HREE across all fault rocks.

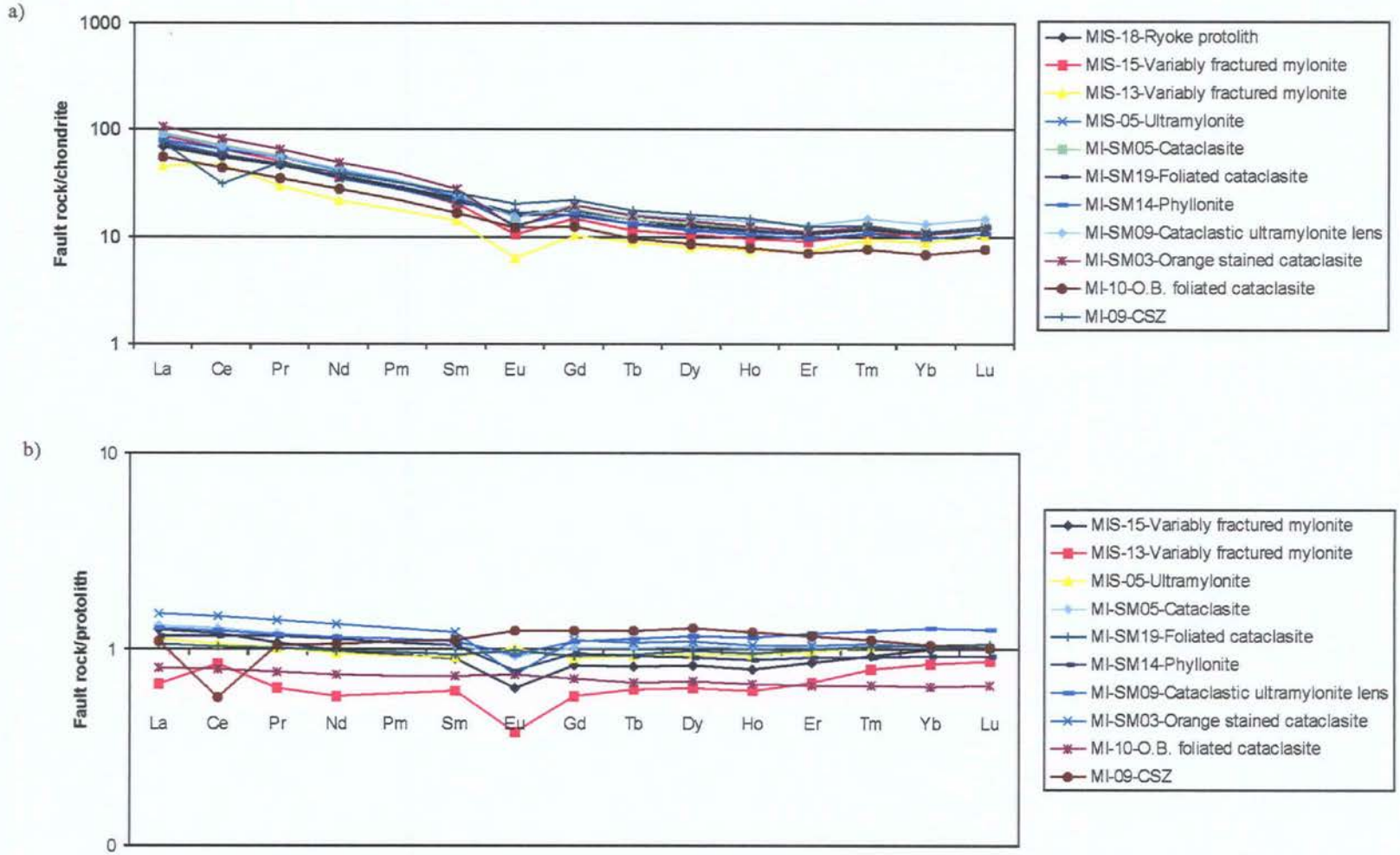

Figure 3.12. a) Rare earth element data from a representative suite of fault rocks across the Miyamae transect normalised to chondritic abundances and b) normalised to protolith concentrations.

When normalised to the protolith (Fig. 3.12b) the REE data plots are sub-parallel and show relatively little scatter from protolith concentrations. There is a progressive increase in LREE (La to Nd) concentration from variably fractured mylonite, through ultramylonite, cataclasite, phyllonite and orange-stained cataclasite (Fig. 3.12b). The HREE (Tm, Yb and Lu) in all fault rocks, except orange-black foliated cataclasite MI-10 and cataclastic ultramylonite lens MI-SM09, show concentrations almost identical to that of the protolith.

3.6.2. REE data – Tsukide transect fault rocks.

Figure 3.13a presents REE concentrations of Tsukide transect fault rocks normalised to chondritic concentrations, and displays a very similar pattern to that observed in the equivalent Miyamae plot (Fig. 3.12a); an ordered sub-parallel arrangement of REE concentrations across all fault rocks with a slight negative Eu anomaly and higher concentrations of LREE relative to the HREE across all fault rocks. The only significant difference is the slightly wider scatter of Tsukide data as observed in the trace element data between Tsukide and Miyamae fault rocks (compare Fig. 3.10 & 3.11 and 3.12 & 3.13). LREE (La to Nd) concentrations of Tsukide fault rocks normalised to protolith concentrations (Fig. 3.13b) also show a progressive increase from variably fractured mylonite TKR-23, through cataclasite TKS-10, phyllosilicate-rich foliated cataclasite TK-09 and TKS-02 to the central slip zone gouge TK-38bi and orange-black foliated cataclasite TK-35. Variably fractured mylonite TKR-09 is enriched in LREE relative to the Ryoke protolith. The wider scatter of data from the Tsukide transect means that this progression is more apparent. The HREE (Sm to Lu) are generally depleted across all fault rocks (except variably fractured mylonite TKR-23, see Fig. 3.13b) relative to

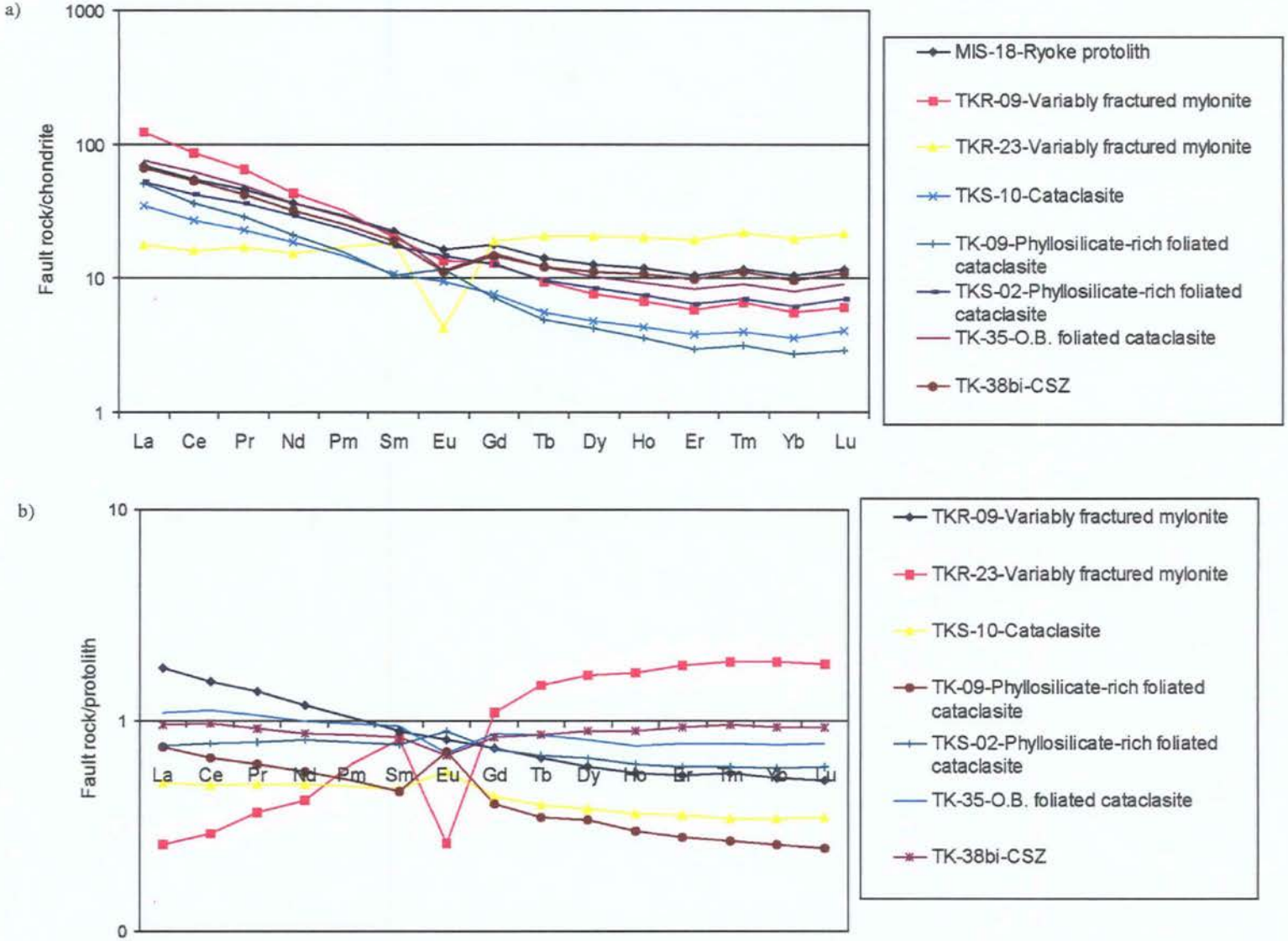

Figure 3.13. a) Rare earth element data from a representative suite of fault rocks across the Tsukide transect normalised to chondritic abundances and b) normalised to protolith concentrations.

Ryoke protolith concentrations. Variably fractured mylonite TKR-09 contains between 89-52% HREE concentration of that within the protolith. This HREE concentration decreases further within cataclasite TKS-10 and reaches a low of between 46-25% of protolith concentrations within phyllosilicate-rich foliated cataclasite TK-09. However, the most extensively developed phyllosilicate-rich foliated cataclasite TKS-02 reverses this trend and shows an increase in HREE relative to these fault rocks plotting closer to protolith concentrations (containing up to 89% HREE concentration of that within the protolith) (Fig. 3.13b). Cataclasite TKS-10, and phyllosilicate-rich foliated cataclasites TK-09 and TKS-02 show slight positive Eu anomalies while the other fault rocks show slight negative Eu anomalies (Fig. 3.13b).

3.6.3. Discussion of geochemical processes identified from REE data.

LREE abundances across both Miyamae and Tsukide fault rocks listed above appears to show a progressive increase across samples that have undergone more extensive deformation and alteration. From microstructural observations, the mineral phases forming during deformation in the MTL fault rocks are chlorite and white mica, it may be that these mineral phases preferentially accumulated the LREEs that were introduced via fluids (Vocke et al., 1987).

The Tsukide transect HREE data, in particular, appears to track the increasing degree of deformation from variably fractured mylonite to the cataclastic fault rocks within the core of the MTL. Variably fractured mylonite TKR-23 shows enrichment in HREE and a progressive depletion and divergence from protolith concentrations is observed from variably fractured mylonite TKR-09 through cataclasite TKS-10 to phyllosilicate-rich cataclasite TK-09, apparently reflecting an increase in deformation

and alteration. However, the most extensively developed phyllosilicate-rich cataclasite TKS-02 shows a reverse in this trend containing HREE concentrations closer to that of the protolith (see Fig. 3.13b). Within TKS-02 fluid assisted diffusive mass transfer processes and pressure solution begins to operate, thus starting the process of geochemical homogenisation by diffusion. The fault core at Miyamae exposes phyllonites where this homogenisation process has progressed to a more advanced stage. The onset of geochemical homogenisation is linked to appearance of typical diffusive mass transfer textures in thin section (i.e. pressure solution seams and fine-grained fibrous mineral growth). This would account for the closer cluster of the REE data, so that the geochemical signature we now see is a complex one where earlier geochemical processes operating during progressive deformation and alteration are masked.

3.7. Fault zone volume changes.

Inferences on the transfer of components in faults and shear zones are complex because the system is open to a number of elements with extremely variable mobilities, thus commonly leading to volume changes. To determine volume changes one must first determine which elements have been immobile in that particular fault zone. Once determined the immobile element then provides a reference frame to establish the amount of gain or loss of more mobile elements. The most popular and widely used method for this is the graphical, isocon plot of Grant (1986) adapted from the method of Gresens (1967). All elemental concentrations are plotted on diagrams of concentration of protolith versus altered fault rock. The points that plot on a straight line through the origin represent the immobile elements of equal chemical concentration ratios in the protolith and altered rock. Such a line is called an isocon and is given by the equation:

$$C^a = (M^p/M^a)C^p \quad \text{(Eq. 1)}$$

Where C^p and C^a are the elemental concentrations in the protolith and altered rocks respectively. M^a is the mass of the altered rock relative to the mass of the protolith M^p (Grant, 1986). Al was identified as the immobile reference frame within the MTL during this study.

Volume changes in each fault rock were determined using the simplified expression of Brimhall and Dietrich (1987):

$$\varepsilon = (C^p/C^a)(\rho^p/\rho^a)-1 \quad \text{(Eq. 2)}$$

Where C is the concentration of the immobile element used as reference, ρ is density, and superscripts ^{p} and ^{a} refer to protolith and altered rocks, respectively.

Figure 3.14 presents the percentage volume change of each fault rock relative to the Ryoke protolith across a) the Miyamae transect and b) the Tsukide transect. Across the whole of the Miyamae transect the fault rocks have experienced a volume gain relative to the Ryoke protolith (Fig. 3.14a). Volume gain in the variably fractured mylonites ranges between 17.5-50.2%; the highest volume gain is within the cataclasite MI-29 at the northern edge of the cataclastic fault core. Within the fault core volume gain is highest within the foliated cataclasite MI-SM19 (34.4%) and lowest within phyllonite MI-SM10 (13.6%).

Volume gain across the Tsukide transect is not only larger but is more variable than that experienced across the Miyamae transect (Fig. 3.14b). Across the Tsukide transect variably fractured mylonites volume gain varies between 17.2-122.5%. Cataclasite TKS-10 and cataclastic ultramylonite lens TKS-08 at the northern edge of the Tsukide fault core outcrop (Fig. 3.4bi) display volume gains of 60.6% and 68%, respectively. The

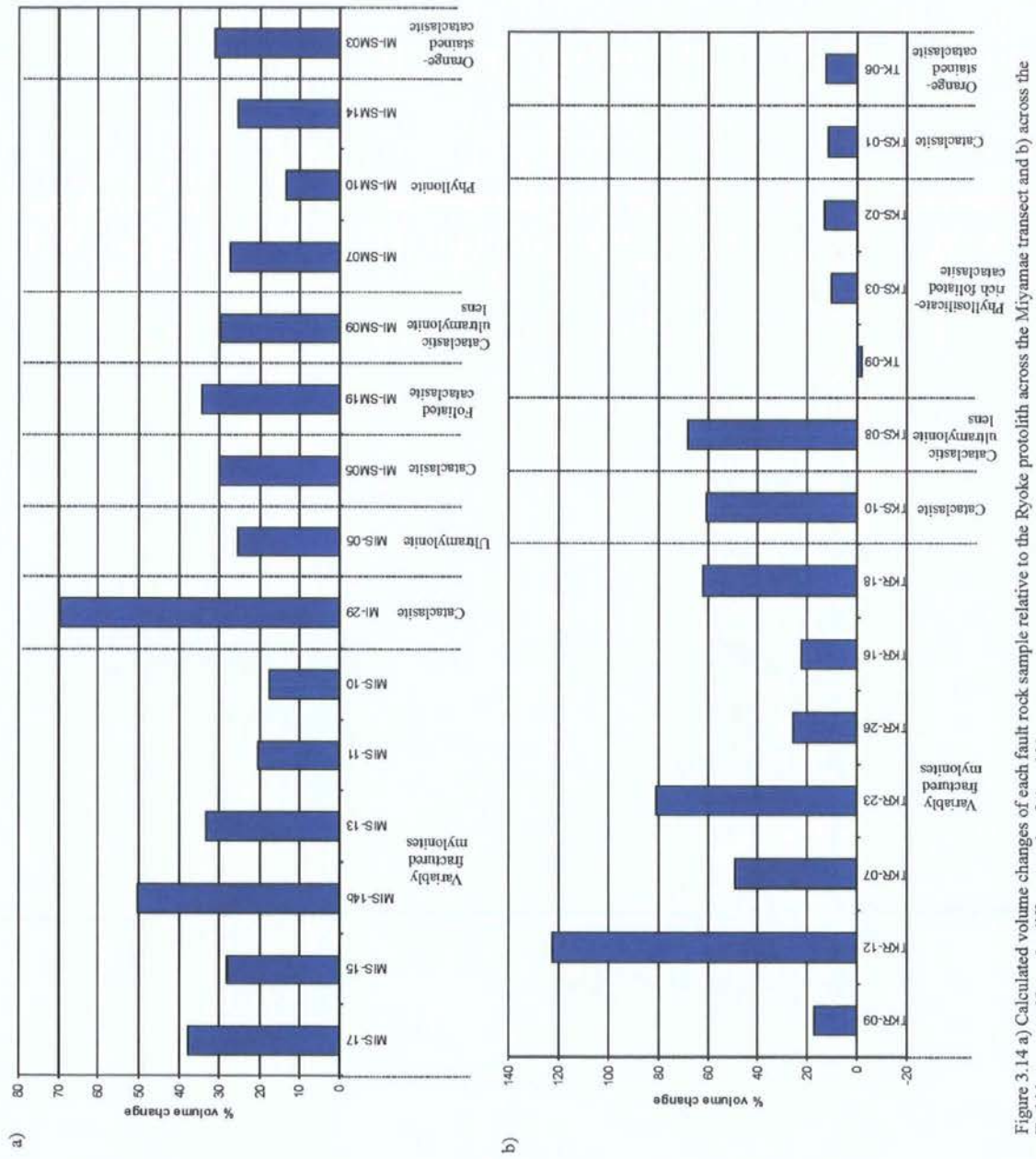

Figure 3.14 a) Calculated volume changes of each fault rock sample relative to the Ryoke protolith across the Miyamae transect and b) across the Tsukide transect. Note: the different scale of a) and b).

other fault rocks within the core show much smaller volume gains (up to 13.2% in phyllosilicate-rich foliated cataclasite TKS-02) and a volume loss of 1.8% relative to the Ryoke protolith is observed in phyllosilicate-rich foliated cataclasite TK-09.

Figure 3.15 presents volume changes of each fault rock type across the fault zone relative to its precursor fault rock in order to find out more about the volume changes associated with increasing degrees of deformation. At both Miyamae and Tsukide variably fractured mylonite volume changes relative to Ryoke protolith were calculated. Within the fault core at Miyamae volume changes in ultramylonite MIS-05 were deduced relative to mean variably fractured mylonite. Volume changes in cataclasites MI-SM05 and MI-SM09 relative to an ultramylonite sample (MIS-05) and foliated cataclasite (MI-SM19) relative to a cataclasite (MI-SM05) sample were determined. From phyllonite samples MI-SM07 through MI-SM10 to MI-SM14, phyllosilicate content increases and a stronger phyllonitic fabric develops with more widespread evidence for pressure solution and fluid assisted diffusive mass transfer (see MI-SM10 to MI-SM14 Fig. 3.3). In order to investigate volume changes associated with progressive phyllonite development MI-SM07 volume changes were calculated relative to foliated cataclasite MI-SM19, MI-SM10 relative to MI-SM07 and MI-SM14 relative to MI-SM10. Volume changes occurring in cataclasite TKS-10, TKS-01 and TK-08 were calculated relative to mean variably fractured mylonite, phyllosilicate-rich foliated cataclasite TK-09 relative to TKS-10. Phyllosilicate-rich foliated cataclasite TKS-02 volume change relative to TK-09 was calculated, again in order to show volume changes associated with increasing phyllosilicate growth and foliation development. The variably fractured mylonites from both the Miyamae transect (Fig. 3.15a) and Tsukide transect (Fig. 3.15b) show significant volume gains (9.9% and 47%, respectively relative to the Ryoke protolith). These significant gains

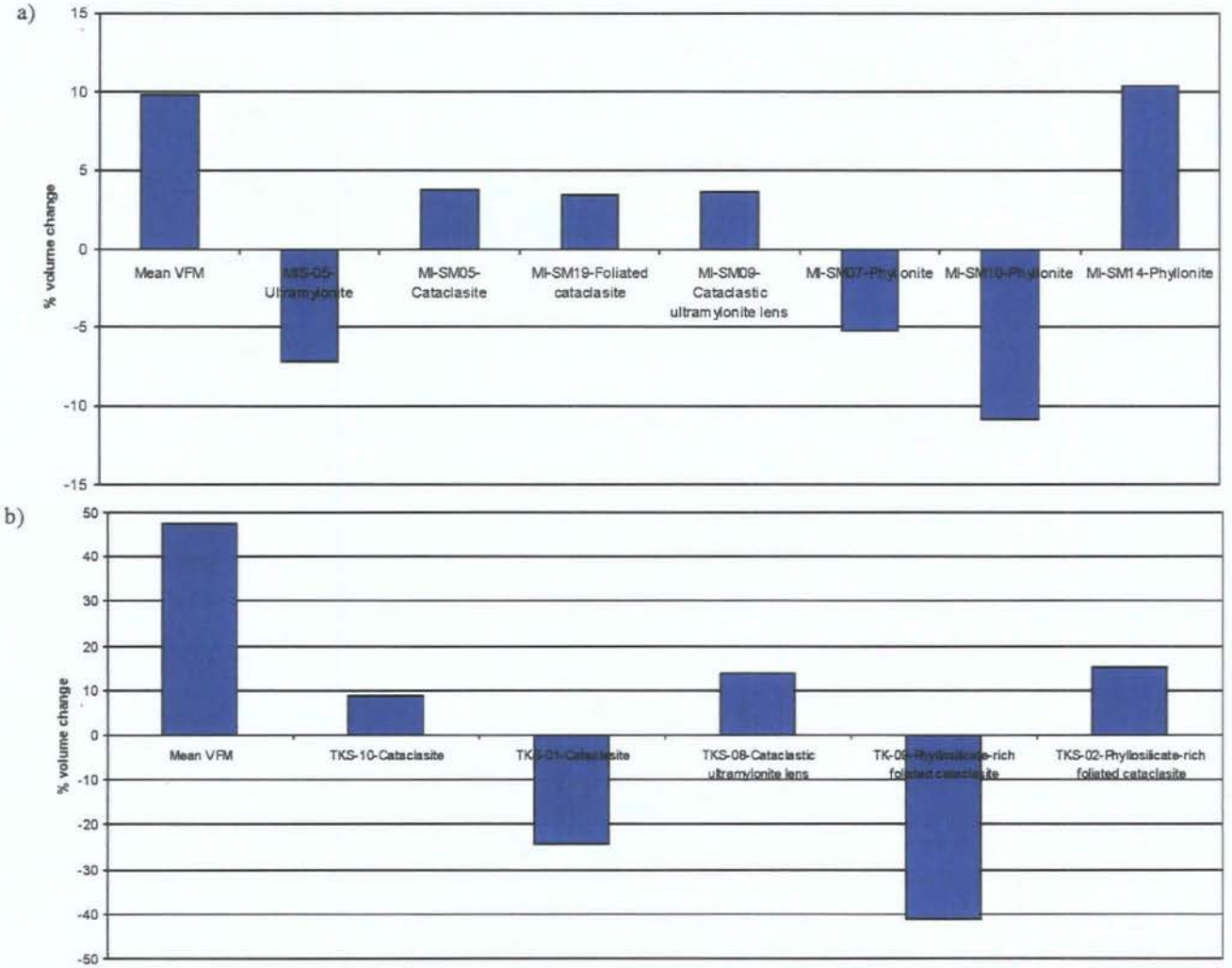

Figure 3.15 a) volume changes of fault rocks relative to the precurser fault rock across the Miyamae transect and b) across the Tsukide transect. For further explanation see text. Note: the different scale of a) and b).

may reflect volume increases reflected by cementation and epidote veining at Miyamae and quartz and epidote veining at Tsukide as observed in the field (see section 3.3.). The ultramylonite relative to the variably fractured mylonite at Miyamae shows a volume loss of 7.2%, possibly reflecting the influx of fluid into the MTL fault core leading to the breakdown of albite and the release of Na that was mobilised out of the fault core and into the adjacent variably fractured mylonites. The cataclasites within the fault core at Miyamae then show a volume gain of ~3% relative to the ultramylonite (Fig. 3.15a). This volume gain can be accounted for by the extensive development of calcite veining coupled with the onset of chlorite precipitation. Phyllonite MI-SM07 shows a volume decrease of 5%, and relative to MI-SM07, phyllonite MI-SM10 shows a volume decrease of 10.8%. This increasing volume loss with progressive phyllonite formation reflects the operation of solution transfer processes that are likely remove and mobilise components from the fault rock. Geochemical data also suggests loss of SiO_2, Na_2O and K_2O in these rock types (see section 2.3.3.). MI-SM14 is the most extensively developed phyllonite sample and relative to MI-SM10 shows a volume gain of 10.3%. It is proposed that this switch in volume change trend records the point at which the effects of solution transfer processes are effectively masked by the extensive precipitation of chlorite, accounting for the majority of this volume increase.

A very similar trend is observed within the cataclasites (TKS-10 and TKS-08) and phyllosilicate-rich foliated cataclasites (TK-09 and TKS-02) within the Tsukide fault core (Fig. 3.15b).

3.8. Discussion.

3.8.1. Coupled geochemical and microstructural analysis.

This study set out to test the hypothesis that processes of fault rock development and evolution observed during field and microstructural investigations can also be identified and tracked using whole-rock major and trace element geochemistry. Whole-rock major-element data have highlighted the progressive breakdown of load-bearing phases in the protolith due to Na- and K-metasomatism (e.g. K-feldspar to albite) and growth of new, weaker mineral phases (e.g. white mica and chlorite) at different stages during fault rock development (Tables 3.4 and 3.5). However, this is only reliable if one protolith is involved in fault zone deformation. A mixture of two different protoliths will give an average composition of both components and thus produce misleading results with regards to the degree of alteration.

Precise whole-rock trace element and REE data obtained from ICP-MS is not as useful as whole-rock major element data to investigate mineralogical changes between individual fault rock samples. The main reason for this is that it is difficult to know which minerals these low abundant trace elements and REEs reside in. It does however appear to be an effective technique for tracking the degree of overall alteration of each fault rock relative to the protolith. Trace-element and REE data were also able to track the overprint of different alteration processes as variably fractured mylonites were progressively altered and deformed into the cataclastic MTL fault core, followed by a phyllosilicate overprint imposed upon these cataclasites.

3.8.2. Fluid pathways and fault zone permeability structure within the MTL crustal-scale fault zone.

The fault rock evolution in both transects is characterised by the same metamorphic reactions and qualitatively similar geochemical changes (Tables 3.4. and 3.5). At Miyamae there is clear evidence that later dextral shearing has been preferentially localised into the phyllonitic core. This observation suggests that the development of phyllonitic fault rocks has resulted in long-term weakening of the MTL (see section 2.4.2.). Evidence for this late dextral reactivation within the Tsukide fault core occurs within the most incohesive faults rocks localised to within 1 metre of the central slip zone, but is not evident within the phyllosilicate-rich foliated cataclasites. The purpose of this section is to interpret the differences in degree of alteration and rheological evolution between the two transects in terms of likely fluid pathways through and along the MTL.

Alteration of the protolith mylonite and mineralisation along faults, fractures and breccias occurs across both field areas, although it is more heterogeneous at Tsukide than Miyamae. These observations suggest that the zone of variably fractured mylonites had facilitated fluid flow along the fault zone and is comparable to the enhanced permeability damage zones described in previous models of fault zone permeability structure (e.g. Caine et al., 1996; Evans et al., 1997). However, any fluid flow model must account for the greater heterogeneity of alteration within the Tsukide damage zone compared with that at Miyamae. It is therefore important to consider the nature and distribution of the porosity network within the MTL fault core and damage zone.

Géraud et al. (1995) carried out a study of oriented sections and core samples from a shear zone in granitoid host rocks from the Massif Central in France, which

were drilled along three reference axes parallel to the X, Y and Z axes of the finite strain ellipsoid. Nuclear magnetic resonance (NMR) and X-ray tomodensitometry (medical scanner) were used to image the distribution of water in core samples. Mercury injection measurements provided information on the size distribution of the connected voids whilst scanning electron microscopy showed the shape and orientation of the voids (Géraud et al., 1995). Such studies have illustrated that porosity varies with strain. Tabular cracks and fractures are more common in the less deformed fault rocks within the damage zone immediately adjacent the central fault core, whilst pore spaces in more strained foliated fault rocks within the fault core are tubular in geometry (Géraud et al., 1995). The tubular pore spaces are preferentially oriented in the foliation (XY) plane and are widespread along phyllosilicate strips. Assuming that this model can be applied to the phyllosilicate-rich MTL fault rocks, a porosity created by a series of connected tabular fractures is likely to exist across the variably fractured mylonites at both Miyamae and Tsukide (Fig. 3.16). By contrast, application of the Géraud et al. (1995) model would suggest that the porosity network within the phyllonites at Miyamae is likely to be tubular in geometry (Fig. 3.16), and the less foliated phyllosilicate-rich cataclasites within the fault core, especially at Tsukide, most likely will have a porosity network that consists of a mixture of tabular cracks and tubes. The progression from a porosity network dominated by cracks to one dominated by tubes reflects an increase in strain and deformation intensity (Géraud et al., 1995).

Permeability measurements carried out on phyllosilicate-rich foliated fault rock samples from thrust faults in Wyoming do reveal a distinct orientation dependence of permeability (Evans et al. 1997). These rocks are texturally and compositionally comparable to those of the MTL. Permeability measurements are much higher when

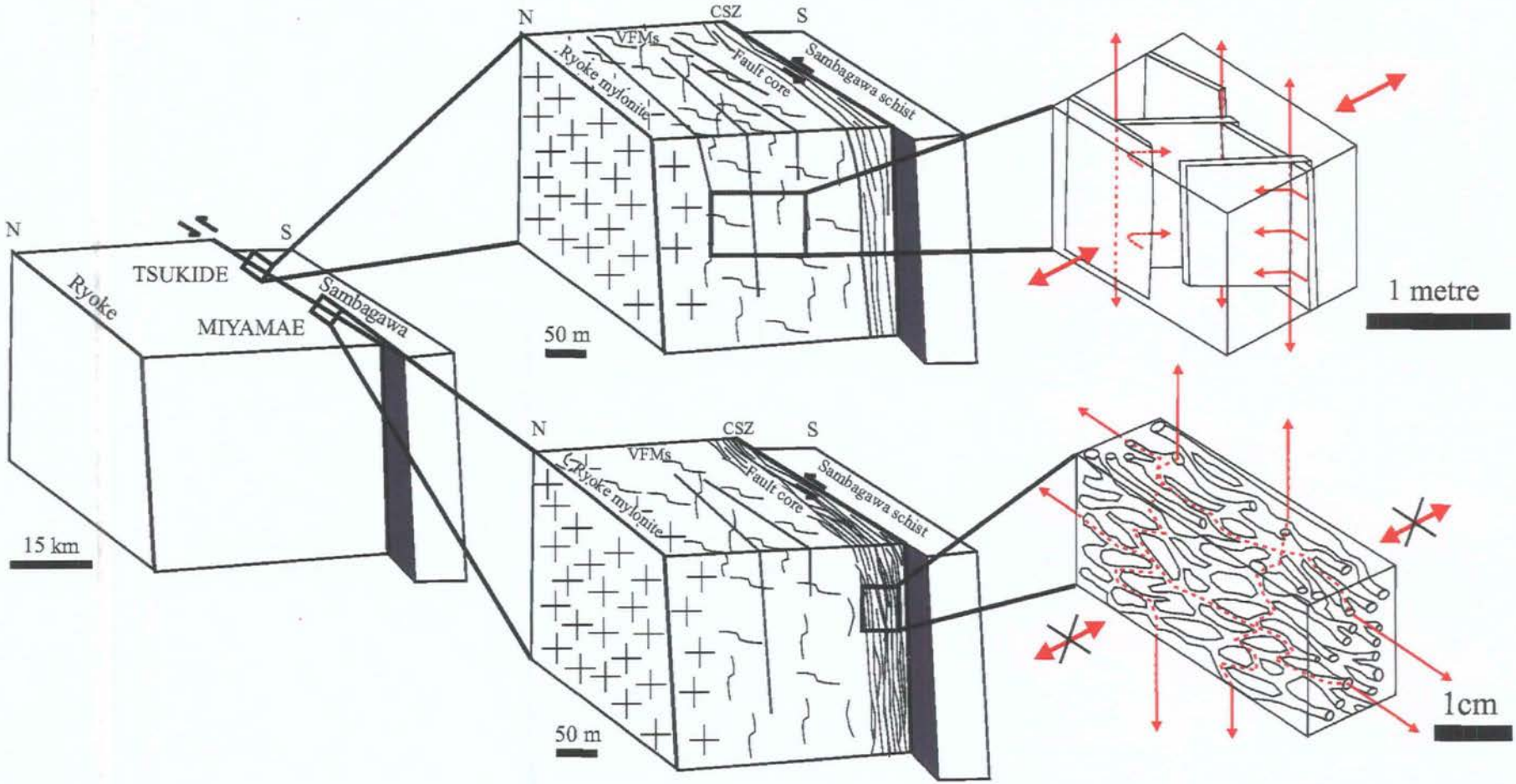

Figure. 3.16. Schematic block diagram showing relative location of the Miyamae and Tsukide transects with a summary model of permeability pathways across the crustal section exposed across each transect (CSZ= central slip zone, VFMs = variably fractured mylonites. On the right, sketches of the likely porosity network within the variably fractured mylonites from Tsukide, dominated by interconnected cracks and fractures, and the phyllonites from Miyamae dominated by tubular shaped pore spaces along phyllosilicate minerals (porosity network based upon model of Géraud et al., 1995), red arrows = principal fluid pathways.

measured parallel to the fault plane and samples perpendicular to the fault plane have much lower permeabilities. Although the phyllonites, once they had formed, at Miyamae could have restricted fluid flow transverse to the fault zone, there is much microstructural and geochemical evidence (fluid assisted diffusive mass transfer processes see section 2.3.3. and homogenisation of elements through processes of diffusion see sections 3.4.3. 3.5.3. and 3.6.3.) to suggest that they acted as effective conduits for large volumes of fault-parallel fluid flow (Fig. 3.16). At Miyamae, fluid flow pathways may have migrated over time from pervasive flow across the wider zone of variably fractured mylonites, becoming rapidly focused and channellized within the strongly foliated phyllonites of the fault core (Fig. 3.16). Once formed, the phyllonites would restrict fluid flow across the fault, which could account for the less altered nature of the Miyamae field area variably fractured mylonites in comparison to their equivalents at Tsukide.

Microstructural observations of foliated cataclasites from the Anko section of the MTL in Nagano Prefecture suggest that these fault rocks may have formed at shallower depths than the phyllonitic fault rocks exposed at Miyamae (see section 4.4.4.). If we assume that the foliated fault rocks at Tsukide formed at a similar depth to those at Anko, then the fault rocks at Miyamae are likely to have experienced higher mean stresses. With an increase in mean stress, there will be a closure of void space and porosity. According to Géraud et al. (1995) the crack geometry porosity within the variably fractured mylonites is likely to be highly pressure sensitive and therefore becomes markedly reduced at depth. However, tubular pore spaces in the phyllonites are less pressure sensitive compared to cracks so that permeability would be expected to decrease less rapidly with depth (Walsh, 1965). Consequently channelling of fluid flow along the fault zone would be more efficient at depth where

strongly foliated phyllosilicate-rich fault rocks occur (see also Géraud et al., 1995) and may have enhanced the suggested preferential channelling of fluid flow into the Miyamae phyllonites.

Simple numerical models involving two rock types with different rheologies (Oliver et al., 1990) have shown that strain partitioning also influences the distribution of fluid flow pathways, where fluid is channellized in some zones and restricted in others. In general, it was shown that an increase in strain leads to an increase in the degree of channellization of fluid flow within crustal rocks (Oliver, 1996). Thus, it is possible that focusing of fluid flow from the wider zone of variably fractured mylonites north of the fault core to within the Miyamae phyllonites accompanied a focusing of strain within the fault core during and after phyllonite formation. This concentration of strain within the fault core ultimately resulted in localisation of late dextral reactivation to within the phyllonites (see section 2.4.3.).

A key finding of this study has been to highlight the apparent convergence in the compositions of the phyllosilicate-rich rocks within the fault core with those of the wall rock protoliths. This contrasts sharply with the highly altered, compositionally heterogeneous rocks within the intervening damage zone that physically separates the fault core and the wall rocks (Tables 3.4 and 3.5; Fig. 3.17a). We propose that these differences in protolith-normalised geochemical compositions reflect the different intensities of fluid channellization and volumetric throughput within the fault core compared with the damage zone (Fig. 3.17b). In particular, fluid-rock ratios – hence the degree of fluid-rock interaction – are likely to have been higher at deeper crustal levels where fluid flow was strongly focussed within weak phyllonitic shear zones (e.g. Miyamae) compared to shallower depths within the MTL where fluid flow occurred through wider, more diffuse damage zones (e.g. Tsukide). We

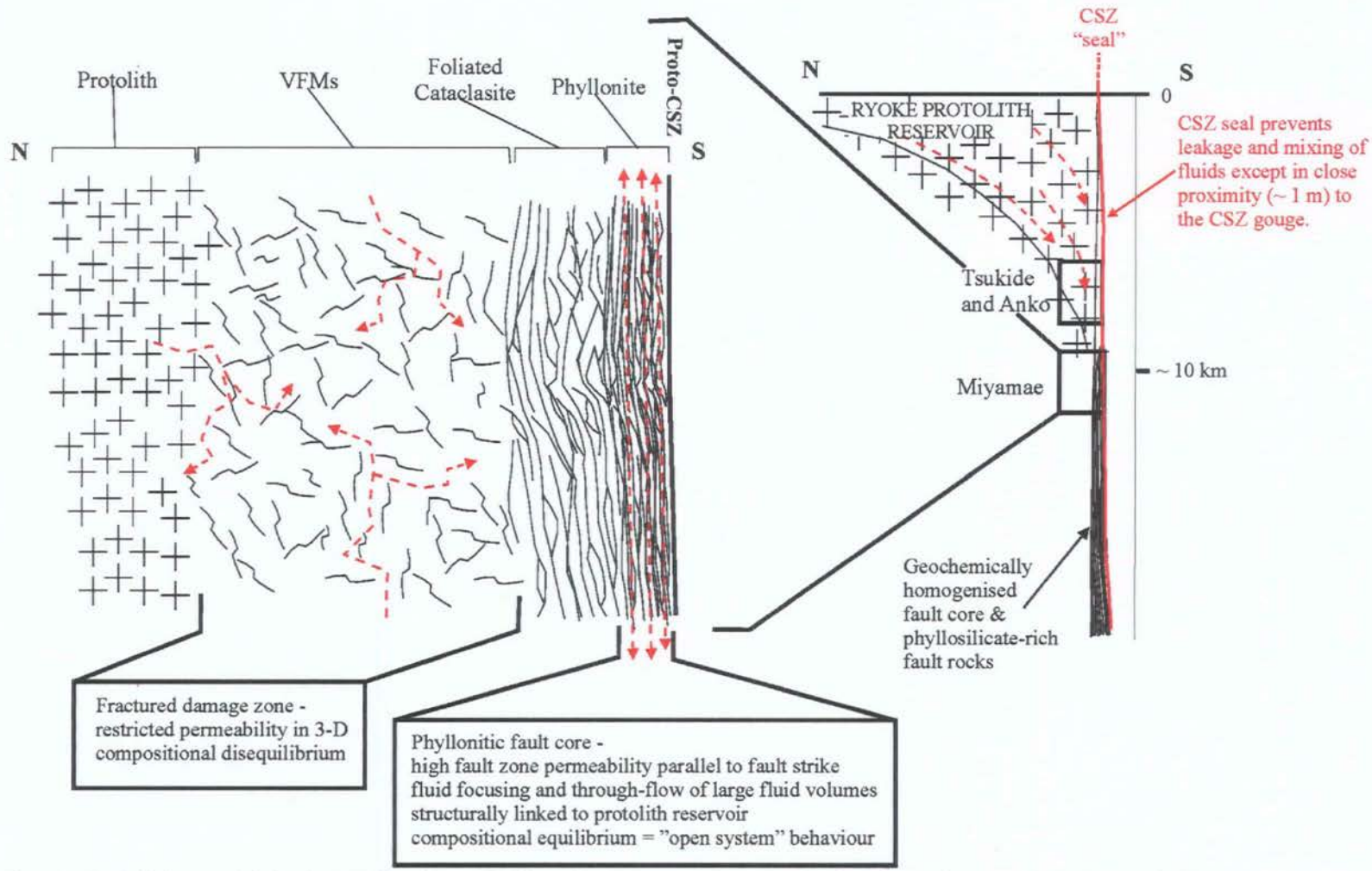

Figure 3.17. Fluid flow models for the MTL based upon field based, microstructural and geochemical observations. Red dashed arrows indicate fluid flow pathways. VFMs = variably fractured mylonites, CSZ = central slip zone. For discussion see text.

speculate that fluid channelling through the phyllonitic core resulted in geochemical homogenisation in which fault rock compositions were, in effect, reset by the composition of the incoming fluids (i.e. "open system" behaviour). According to our model (Fig. 3.17b), the degree of fluid channelling, hence the apparent intensity of geochemical alteration, is likely to change (decrease) as a particular section is exhumed, this could partially (bearing in mind the complications of a mixed-protolith composition, see section 3.8.1) account for the highly heterogeneous geochemical signature of the late gouges (Figs. 3.7a-b and 3.9a-b). Our model assumes that the fluids responsible for the alteration observed at Miyamae and Tsukide carried no significant geochemical imprint of their own other than that acquired from the Ryoke protolith. We therefore suggest that the fluids are likely to have had crustal or meteoric – as opposed to mantle – sources (Fig. 3.17b). Possible ways to test the hypothesis are discussed in Chapter 5.

This model requires a "central slip zone seal" to extend close to the surface to prevent fluid mixing and restrict geochemical 'leakage' between Sambagawa and Ryoke derived rocks. We infer from the nature of the most recently formed near-surface central slip zone at both Miyamae and Tsukide (Figs, 3.2c and 3.4b) that this seal is likely to be an extremely fine-grained clay-rich gouge. The experimental study of Wibberley and Shimamoto (2003) involving permeability measurements of samples from the Tsukide fault core outcrop (Fig. 3.4b) revealed that the central slip zone gouge has a permeability more than two orders of magnitude lower than adjacent Ryoke and Sambagawa derived foliated gouges. When measured perpendicular to the slip plane permeability decreased further having the lowest permeability of all fault rocks measured across the Tsukide field area. Therefore, the clay-rich gouge could very well provide an effective seal, preventing 'leakage' and mixing of Ryoke and

Sambagawa reservoir-derived fluids within the fault core, except possibly very close to the central slip zone (Fig. 3.17b).

In summary, the development of a phyllosilicate-rich fault core at Miyamae appears to have given rise to strongly anisotropic porosity and permeability (Fig. 3.16), with fault-parallel fluid flow further enhanced by strain localisation effects. Within the fault core at Miyamae, strain was strongly localised along weak phyllonitic fault rocks that developed in response to intense fluid channelling and fluid-rock interaction (Fig. 3.17). However, this does not account for what led to focusing of fluid flow *prior* to the onset of phyllonitisation in this transect, but not at Tsukide. The simplest explanation is that phyllonitisation occurred along a relatively well-developed, pre-existing, highly permeable brittle fault (i.e. a principal displacement surface) which was surrounded by a damage zone of lower fracture connectivity. In contrast, it is suggested that significantly less brittle strain localisation had occurred at Tsukide: a wider, more diffuse damage zone accommodated brittle deformation at this locality. If this interpretation is correct, it suggests that the geochemical evolution of long-lived weak phyllosilicate-bearing crustal-scale fault zones is inexorably linked to their pre-existing brittle architecture.

3.9. Conclusions.

An integrated field, microstructural and geochemical approach to the study of crustal-scale fault zones can provide a valuable insight into the fluid-related geochemical processes operating across the fault zone (Tables 3.1-3.5; Figs 3.16 and 3.17a-b). Whole-rock major elemental analysis of fault rocks normalised to protolith concentrations can track the points across the fault zone at which mineralogical

changes and the onset of metamorphic reactions occur. Precise whole-rock trace element and REE data provide a useful measure of the degree of overall alteration of fault rocks relative to the protolith, whilst also tracking the overprint of different alteration processes. The geochemical approach to the study of the MTL has illustrated that the fluid-assisted diffusive mass transfer processes involved in the formation of the phyllonites exposed in the Miyamae fault core, and to a lesser extent the phyllosilicate-rich foliated cataclasites exposed at Tsukide, led to a geochemical resetting and homogenisation relative to protolith compositions most likely through processes of fluid assisted diffusive mass transfer, where previous alteration signatures are themselves altered, overprinted and reset. Similar processes are likely to be recognised in other equivalent crustal-scale fault zones, suggesting that the models presented in Figures 3.16 and 3.17 have general and widespread application.

Chapter 4
The development and significance of foliated cataclasite and gouge in the cores of crustal-scale fault cores: examples from the Median Tectonic Line, SW Japan.

Abstract

The Median Tectonic Line (MTL) is Japan's largest onshore fault and has been active since the mid-Cretaceous. Foliated cataclastic fault rocks are known to occur at a number of localities along the MTL but are exceptionally well exposed in the fault core at Anko, Nagano Prefecture. Following an early phase of mylonitisation during left lateral shearing processes of brittle fracture and cataclasis occurred following exhumation leading to the development of cm- to sub-mm spaced fracture systems defining an initial crude foliation. This fracture system established an initial architectural hierarchy that influenced the subsequent development of the foliated cataclasite and gouge. Fracture systems coalesce to form interconnected zones of ultra fine-grained ultracataclasite. Fluid influx at the onset of grain-scale brittle deformation led to precipitation of fibrous chlorite within the finest-grained sections of the fault core. This ultimately led to the development of a foliation within the ultra-cataclasite defined by an interconnected network of aligned phyllosilicate aggregates. The brittle reduction of grain-size and the ingress of a chemically active fluid phase promoted the operation of diffusive mass transfer mechanisms ('frictional-viscous creep' at $\mu \leq 0.2$) and reaction softening. Significant weakening is indicated by the preferential localisation of subsequent movements within regions of foliated ultracataclasite. Extensive carbonate mineralisation and cementation events are recognised at several different stages in the fault rock evolutionary sequence and suggest episodic periods of fluid overpressuring. Field and microstructural observations at Anko suggest that the foliated cataclasites are a shallower crustal equivalent to phyllonitic fault rocks found along more deeply exhumed parts of the MTL. Although 95% of the exposed fault core experienced predominantly brittle deformation the overall rheology was likely controlled by the highly interconnected network of foliated ultracataclasite.

4.1. Introduction

It is generally believed that reactivated crustal-scale fault zones are likely to be weak relative to adjacent regions of intact rock. The textures preserved in exhumed fault rocks contain valuable information about structural setting and deformation mechanisms operating at depth along both ancient and modern fault zones (e.g. Sibson, 1977; Schmid and Handy, 1991; Snoke et al., 1998; Holdsworth et al. 2001). Recent field-based research along major faults (e.g. Imber et al., 1997, 2001; Stewart et al., 2000; Gueydan et al., 2003; Collettini and Holdsworth, 2004; Wibberley, 2005; Jefferies et al., 2006) has focused on the importance of foliated, fine-grained phyllosilicate-rich fault rocks known as *phyllonites* formed close to the main load-bearing region of the crust at the frictional-viscous (or brittle-ductile) transition at 8-15km depths. The textural sequences preserved in these rocks bear close comparison with those developed during analogue deformation experiments designed to examine the influence of phyllosilicates and pressure solution in fine grained fault rocks (e.g. Bos and Spiers, 2000, 2002; Bos et al., 2000 a & b). These experiments predict a profound and long-term weakening of faults that develop phyllonites and therefore provide a plausible explanation for the development of reactivated faults, low-angle normal faults and weak plate boundary structures such as the San Andreas Fault (Holdsworth, 2004).

Foliated brittle fault rocks such as cataclasite, breccia and gouge are also reported along many major crustal discontinuities such as the San Andreas Fault zone (e.g. Chester et al., 1985, 1993; Chester and Logan 1987; Snoke et al., 1998) and have been reproduced experimentally (e.g. Yund et al., 1990; Beeler et al., 1997). These rocks are generally thought to have formed at significantly less than 10 km depth. Deformation processes are considered to be predominantly brittle, although there is

good evidence for both grain-scale reaction softening and the operation of fluid-assisted diffusional mechanisms in many cases (e.g. Evans and Chester, 1995). The rheological significance of such foliated brittle fault rocks is rather poorly understood, although they are thought to be associated with fault zone weakening (e.g. Chester, 1995).

The present study focuses on the development of foliated cataclasite and gouge in the core of the Median Tectonic Line (MTL), Nagano Prefecture, SW Japan (Fig. 4.1) and presents both field-based and microstructural observations. The development of these rocks is compared with the development of phyllonites from another, more deeply exhumed section of the MTL. The comparison is used to test the hypothesis that the foliated cataclastic rocks at Nagano are shallower crustal equivalents to the phyllonitic sequences and the rheological implications are discussed.

4.2. Geological and structural setting

4.2.1. Regional setting

The Median Tectonic Line is a major, crustal-scale fault dividing SW Japan into Inner (northern) and Outer (southern) zones. The fault has a strike length of > 1000 km and a long displacement history reaching back to the early Cretaceous. Displacement estimates vary and are poorly constrained, ranging between 200-1000 km (Ichikawa, 1980). The MTL at present has a steep to sub-vertical dip and forms the boundary between the low-P/high-T Ryoke metamorphic belt of granitoids and metasedimentary rocks to the north from the high-P/low-T Sambagawa belt of accretionary complex metasedimentary rocks to the south (Fig. 4.1). Current exposures of the fault zone display a wide variety of fault rocks generated at different

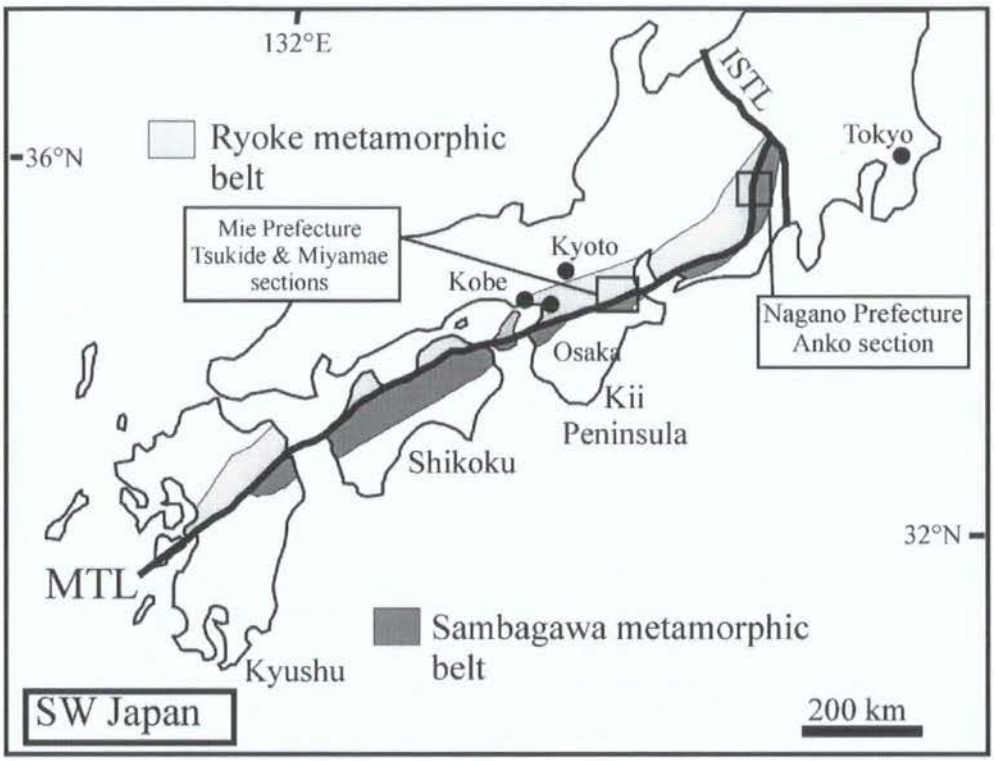

Figure 4.1. The Median Tectonic Line (MTL) in SW Japan showing adjacent metamorphic belts. ISTL = Itoigawa-Shizuoka Tectonic Line.

levels in the mid- to upper-crust, now exhumed as a consequence of continued activity and reactivation of the fault.

Within the Ryoke Belt, late Cretaceous to early-Tertiary sinistral motion along the MTL resulted in the formation of a variably mylonitized zone that reaches a thickness of up to 5 km (Ito, 1978). Two shearing events are inferred by most authors (Ohtomo, 1993: Yamamoto and Masuda, 1987; Sakakibara et al., 1989; Michibayashi and Masuda, 1993). A broad zone of mylonitisation that formed during an earlier phase of late Cretaceous to earliest Tertiary sinistral top-to-south shearing is thought to have developed when the MTL was a shallowly inclined structure. A later and narrower central region of sinistral strike-slip displacements is then proposed to have occurred along a steeply-dipping MTL during the early Tertiary (e.g. Ichikawa, 1980; Hara et al., 1980; Ohtomo, 1993 and references therein). The deformation associated with the latter phase of sinistral displacements becomes increasingly brittle as the central part, or 'core' of the fault is approached, with the development of cataclasites, breccias and gouges, many of which are foliated (e.g. Takagi, 1985, 1986; Wibberley and Shimamoto, 2003; Jefferies et al., 2006). In the more southwestern parts of the MTL (western Kii Peninsula, Shikoku and Kyushu; Fig. 4.1) a dextral strike-slip reactivation is also recognised, with displacements localized within incohesive and phyllosilicate-rich fault rocks typically found within 10 m of the central slip zone (Okada, 1980; Wibberley and Shimamoto, 2003; Jefferies et al., 2006).

4.2.2. Local setting, Nagano Prefecture

In Nagano Prefecture, the MTL runs approximately N-S (Fig. 4.1) with a sub-vertical dip and is cut out to the north of this area by the Itoigawa-Shizuoka Tectonic Line (ISTL) (Takagi, 1986). The Sambagawa belt in Nagano Prefecture is composed

mainly of greenschist-blueschist facies quartzose pelites (Takagi, 1986). The present paper focuses on fault rocks derived from the Ryoke belt. The metamorphic protoliths are composed of amphibolite-facies psammitic and pelitic schists, with variable mica content and subordinate units of tonalitic orthogneiss (Ohtomo, 1993; Yamamoto, 1994). The metamorphic rocks characteristically contain white mica, biotite, quartz, plagioclase, garnet, sillimanite and andalusite (Yamamoto, 1994). A mid-Cretaceous (90-110 Ma) age estimate for this regional metamorphism has been suggested using radiometric age data and geological evidence (Tanaka and Nozawa, 1977; Takagi, 1986).

The tonalitic gneiss body, known as the Hiji gneissose tonalite, is the oldest of the granitic rocks in the Ryoke Belt (Ryoke Research Group, 1972) with the age of emplacement considered to be mid-Cretaceous (ca. 100 Ma) (Takagi, 1986). Adjacent to the MTL in the Nagano Prefecture, the tonalitic gneiss has been deformed to form a zone of sub-vertical mylonites up to 1 km wide (Hayama et al., 1963; Hayama and Yamada, 1980, Takagi, 1986). Sinistral shear criteria, such as asymmetrically wrapped porphyroclasts, mica fish and oblique quartz fabrics are ubiquitous (Takagi 1986). The gneiss consists of quartz, plagioclase, K-feldspar, biotite and hornblende; the proportion of these minerals and grain size is very heterogeneous throughout. Banded gneiss is found toward the centre of the Hiji tonalite body, with gneissose banding trending sub-parallel to the MTL (010°-040°) with steeply west dipping to sub-vertical orientations (Takagi, 1986). The effects of brittle sinistral deformation are localised into a central core region within which cataclastic rocks form as subvertical intercalated belts locally up to 100 m wide.

4.3. The MTL fault core, Anko section

The present study was carried out along the Anko section of the MTL fault core along a small tributary of the Aokigawa River, Kashio region, Nagano Prefecture. This section was selected as it is particularly well-exposed and featured previously in a study of deformation, hydrothermal alteration and fault activity along the MTL carried out by Tanaka et al. (1996). The present study focuses on the Ryoke-derived cataclastic rocks and, more specifically, the formation of foliated cataclasites and gouges within the MTL fault core. The boundary between the cataclastic rocks in the fault core and the Ryoke-derived mylonites that lie to the west is not exposed. The Sambagawa rocks along this section are described by Tanaka et al. (1996) and are not discussed in the present paper.

4.3.1 Fault rocks of the MTL core

The NE-SW trending tributary of the Aokigawa River preserves an almost completely exposed ~240 m long section of generally N-S to NE-SW striking, steeply-dipping to subvertical faults and fault rocks within the core of the MTL (Fig. 4.2a-e). The Sambagawa rocks comprise black- and green-coloured semi-pelitic schists (see also Takagi, 1986; Tanaka et al., 1996). The Ryoke-derived rocks exposed in the section include mylonite developed from high-grade metamorphic psammitic to pelitic schist and tonalite, together with a variety of cataclasites, foliated cataclasites and gouges apparently derived from the pre-existing mylonites.

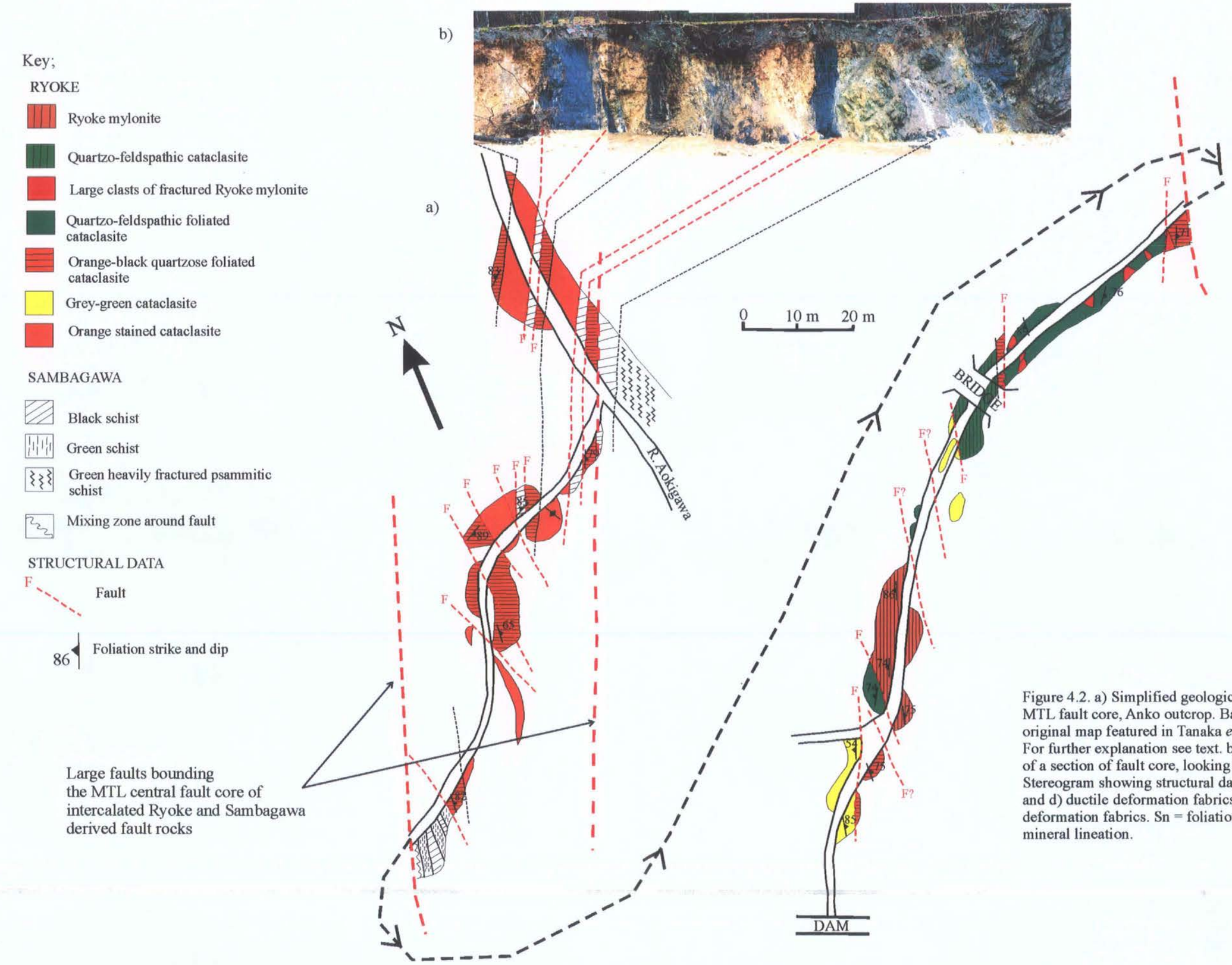

Figure 4.2. a) Simplified geological map of the MTL fault core, Anko outcrop. Based upon original map featured in Tanaka *et al.*, (1996). For further explanation see text. b) Photograph of a section of fault core, looking NE. c) Stereogram showing structural data on faults and d) ductile deformation fabrics, e) brittle deformation fabrics. Sn = foliation, Ln = mineral lineation.

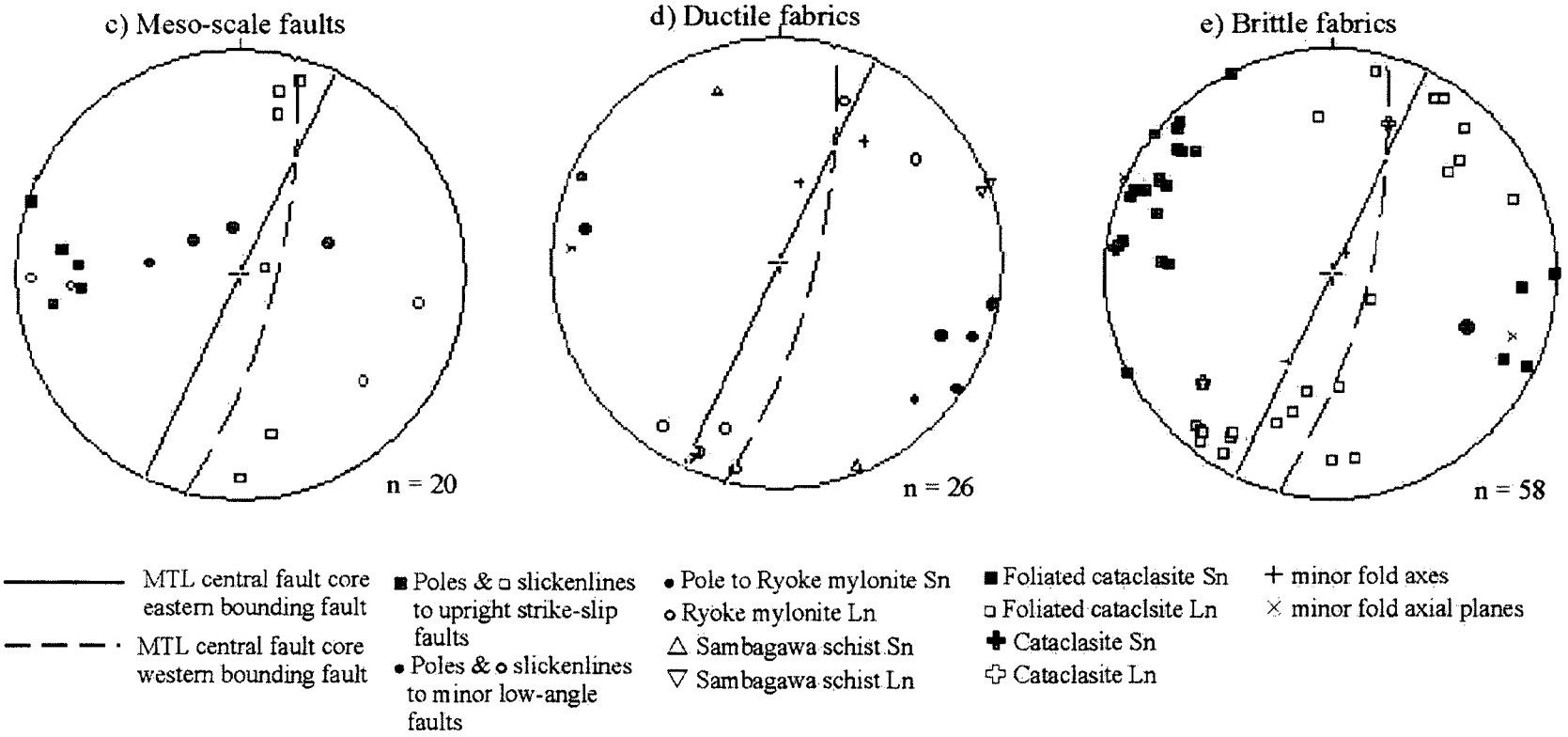
c) Meso-scale faults
n = 20
d) Ductile fabrics
n = 26
e) Brittle fabrics
n = 58
MTL central fault core eastern bounding fault
MTL central fault core western bounding fault
■ Poles & □ slickenlines to upright strike-slip faults
• Poles & o slickenlines to minor low-angle faults
• Pole to Ryoke mylonite Sn
o Ryoke mylonite Ln
△ Sambagawa schist Sn
▽ Sambagawa schist Ln
■ Foliated cataclasite Sn
□ Foliated cataclsite Ln
✚ Cataclasite Sn
✜ Cataclasite Ln
+ minor fold axes
× minor fold axial planes

4.3.2 Field relationships and mesostructures

4.3.2.1. Faults

The Anko section is cut by numerous brittle mesoscale faults that can be divided into at least two generations. These faults appear to post-date all other structures, including the deformation associated with the development of the foliation within the cataclasites throughout the fault core. An earlier generation of faults are probably more significant in terms of displacement as they intercalate fault rocks derived from both Ryoke and Sambagawa protoliths in a central region of the fault core 20-30m wide (Figs 4.2a and 4.3a). These faults strike N-S, at low angles to the regional orientation of the MTL; have steep dips and shallowly plunging slickenlines consistent with strike-slip movements (Fig. 4.2b-c). No unambiguous senses of shear could be determined where slickenlines are preserved in exposed fault surfaces. Associated with many of these late brittle faults is a zone of hydrothermal alteration up to 1 m wide where the fault rocks exhibit a 'bleached' appearance (Fig. 4.3a). Narrow (<10cm wide) carbonate-cemented, unfoliated gouges are developed along these faults (Fig. 4.3b) together with late Fe-staining and sulphide (pyrite) mineralisation.

A later generation of moderately dipping mostly reverse faults trending ENE and dipping south (Fig. 4.2c) crosscut all other structures, including the N-S-trending steep fault planes (see Tanaka et al., 1996). These faults are associated with minor sulphide mineralization.

4.3.2.2. Ryoke mylonites

Mylonitised Ryoke psammitic and pelitic rocks crop out toward the southwestern end of the tributary inter-sliced with units of foliated quartzo-feldspathic

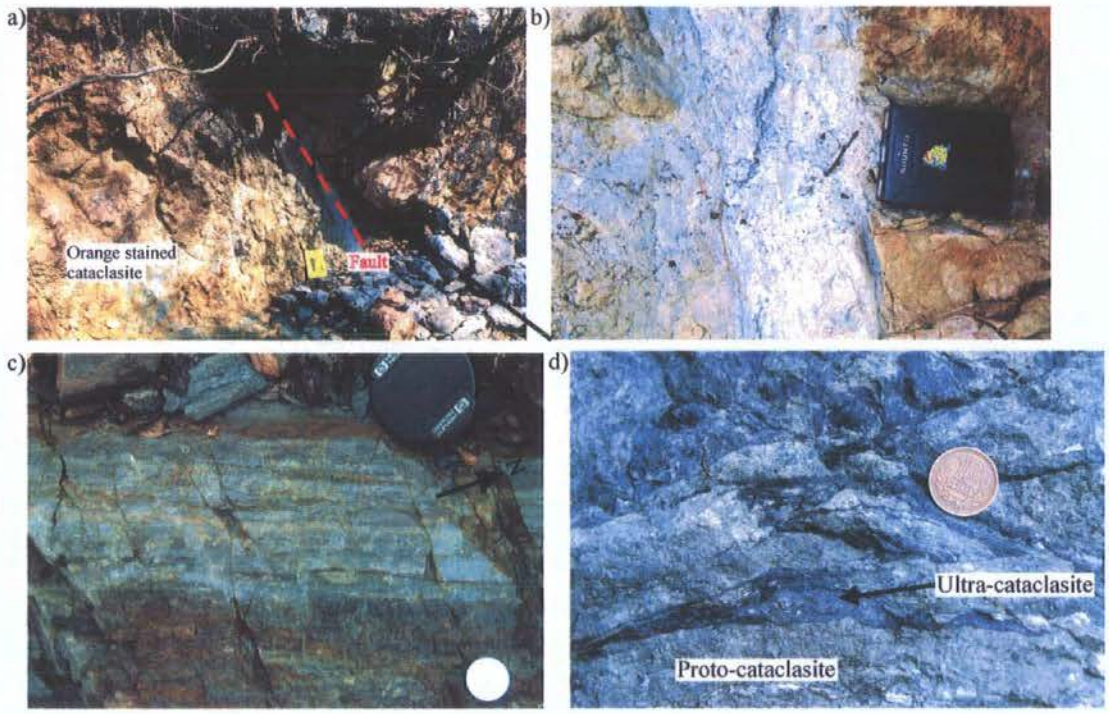

Figure 4.3. a) section view looking north of bleached carbonate rich gouge adjacent to fault cutting through orange stained cataclasite, b) close-up of gouge. c) plan view of Ryoke mylonite, d) section view looking south of quartzo-feldspathic cataclasite showing ultra-cataclasite seams developing along fractures

cataclasite (Fig. 4.2a). The mylonitic rocks are fine-grained (grainsize ~0.05-0.1 mm) and often have a distinctive orange and black coloured banded appearance. Fe-staining of the more quartzo-feldspathic psammitic layers (Fig. 4.3c) imparts the distinctive orange colouration, while the black pelitic layers are finer grained (<0.05 mm) and have a higher mica content. The inter-banding of orange and black units is developed on tens of cm- to sub-mm-scales and appears to be a relict compositional layering transposed almost entirely into concordance with the strong mylonitic foliation (Fig. 4.3c). The foliation has a uniform orientation (mean 019/78W) with a mineral lineation defined by mica and elongated quartz plunging shallowly toward either the NNE or SSW (Fig. 4.2d). Intrafolial isoclinal folds are locally present, but few hinge lines are actually exposed. Where they can be measured, folds are upright with moderate to steeply NNE-dipping hinges, oriented approximately parallel to the mineral lineation (Fig. 4.2d). These folds appear to have formed during intense ductile shearing associated with mylonitisation. Cross-cutting veins of calcite <1 cm wide are locally present and appear to entirely post-date mylonitisation.

4.3.2.3. Quartzo-feldspathic cataclasite

The quartzo-feldspathic cataclasite crops out in a ~10 m wide zone below the small bridge over the river tributary (Fig. 4.2a), and is derived from Ryoke tonalitic mylonite. In outcrop not many original features are visible due to the pervasive grain-scale crushing, but the rock is composed of a mixture of proto-cataclasite and variably foliated ultracataclasite (Fig. 4.3d). In the proto-cataclasite sections, feldspar grains reach up to ~1.2 mm and in isolated regions the relict mylonitic foliation is still visible to the naked eye. The ultra-cataclasites are dark grey-black and so fine grained that individual grains are undistinguishable in hand specimen.

4.3.2.4. Quartzo-feldspathic foliated cataclasite with clasts of fractured mylonite

This fault rock is continually exposed in a 40 m long section located immediately west of the central fault core (Fig. 4.2a). It is very similar in terms of composition and mineralogy to the quartzo-feldspathic cataclasite, but is finer grained and has been subjected to more intense deformation. Regions of light grey cataclasite derived from fractured quartzo-feldspathic mylonite are recognisable, surrounded by dark grey foliated ultracataclasite (Fig. 4.4a). The entire fault rock is highly fractured, but in finer grained regions displays a crude mesoscopic foliation defined in hand specimens primarily by the preferential alignment of an anastomosing and coalescing network of fracture surfaces with cm- to sub-mm-spacing (Fig. 4.4a-b). A weak to moderately strong ultra-fine foliation is also developed in many ultracataclasite seams oriented sub-parallel to the fracture foliation. Collectively, the foliations strike ~NNE-SSW with a steep to vertical dip. A fine mineral lineation is defined by aligned chlorite grains that plunge gently to moderately NNE or SSW (Fig. 4.2e). Clasts in the less deformed light grey cataclasites reach up to ~1 mm across, whilst individual grains in the ultra-cataclasites often cannot be distinguished using the naked eye. Thin (mm- to sub-mm thickness) seams of ultracataclasite lie along many fracture surfaces that define the mesoscale foliation (Fig. 4.4b), and also locally form crosscutting veins (Fig. 4.4a) consistent with injection of mobilised material into voids during deformation. In sections where the mesoscopic foliation is most intensely developed in the cataclasites, open to tight cm-scale folds are locally present. This suggests that the development of the foliation is at least locally associated with the onset of mesoscopic cataclastic flow, although no consistent orientation or sense of vergence is preserved in the available exposures.

Figure 4.4. a) section view looking south of tonalitic mylonite clasts within cataclasite, b) section view looking south of ultra-cataclasite injection along fractures through quartzo-feldspathic foliated cataclasite, c) view looking north of large metre-scale tonalitic mylonite clast, d) close up plan view of the previous tonalitic mylonite clast.

Lenticular clasts of relict grey mylonitic tonalite up to 3 m across and up to 5 m long are widely preserved and are wrapped by the foliation in the cataclasite (Fig. 4.2a and 4.4a, c). They are also internally disrupted by networks of brittle fractures, some of which are associated with well-developed seams of foliated ultracataclasite up to 10cm wide. Within the centre of some larger tonalitic clasts, cataclasis is limited and good mylonitic textures are preserved (Fig. 4.4d). Elongate feldspar porphyroclasts reaching up to 5 mm in length are aligned parallel to the mylonitic foliation in the fine-grained quartz-mica matrix. A compositional layering defined by alternating quartz-rich and quartz-poor bands lies parallel to the mylonitic foliation. Toward the edges of the large clasts, the intensity of cataclasis increases and mylonitic textures are progressively obliterated.

4.3.2.5. Orange-black quartzose foliated cataclasite and gouge

This unit of foliated cataclasite and gouge is very distinctive and crops out mainly in the central region of the fault core where it is intercalated with orange-stained cataclasite and units derived from Sambagawa schists (Fig. 4.2a). At first glance the m- to sub-mm-inter-banding of orange and black units (Fig. 4.2b) appears to resemble the Ryoke psammitic and pelitic mylonites that outcrop upstream along the tributary (Fig. 4.5a). However, the coarser (up to ~1 mm) grained bands of Fe-oxide-stained orange cataclasite contain no visible feldspar and appear to be composed almost entirely of quartz and subordinate carbonate. The black bands form a closely-spaced, anastomosing and coalescing network of extremely fine-grained foliated ultra-cataclasites (Fig. 4.5b). The textures and mineralogy of the latter units cannot be resolved with the naked eye. The foliation is consistently steeply dipping to sub-vertical, but varies in strike from N-S to NE-SW. An associated mineral lineation

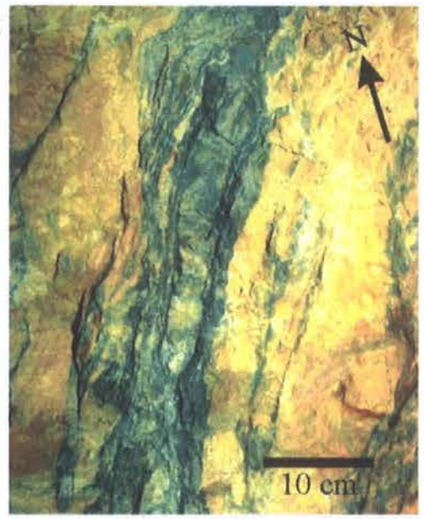

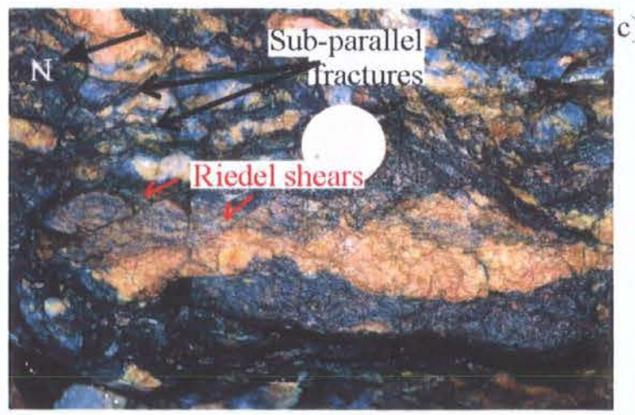

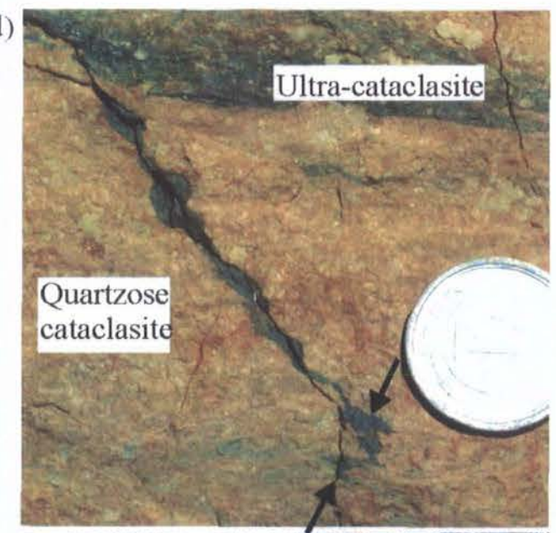

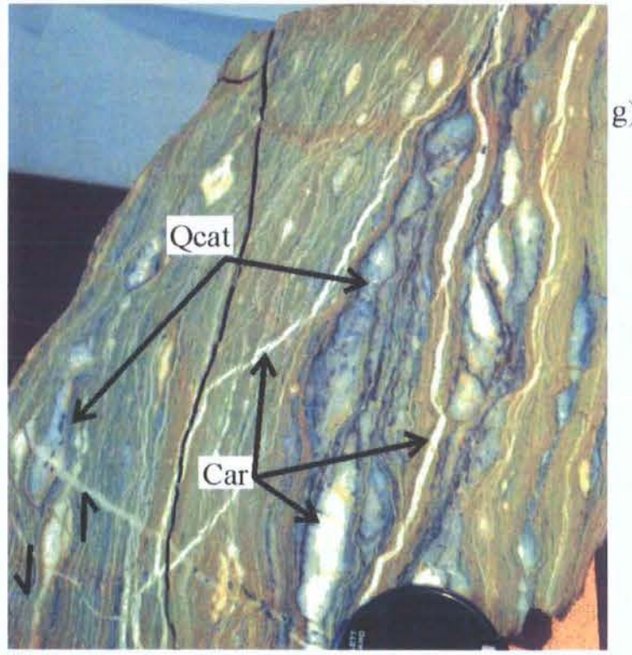

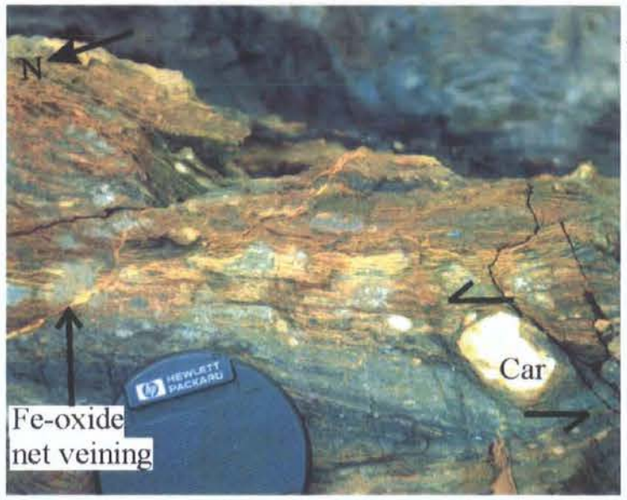

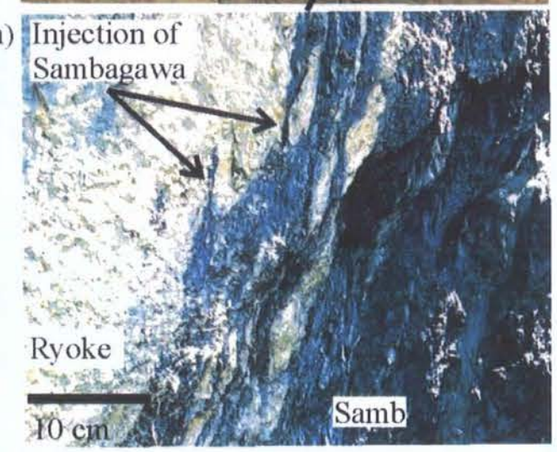

Figure 4.5. a) plan view of orange-black quartzose foliated cataclasite, b) plan view of black bands forming a closely spaced network of ultracataclasite localising along cm-spaced fractures, that with Riedel shears, break down the orange quartzose layers and clasts, c) plan view of cm-scale sinistral shear bands, d) folded injection seam of ultracataclasite across orange quartzose cataclasite,observed within loose block e) section view looking SW of cm-scale fold affecting ultracataclasite units, f) polished block of Anko gouge containing thin (<1 mm) carbonate veins, the gouge also contains clasts of quartzose cataclasite (Qcat) and carbonate (Car). Asymmetric wrapping of the foliation

defined by aligned chlorite grains plunges shallowly to moderately S-SW or N-NE (Fig. 4.2e). The swings in strike appear to reflect the development of sinistral shear band structures on cm- to m-scales, with regions of more NE-SW-trending foliation having undergone clockwise back-rotation between N-S-trending higher strain zones (e.g. see Fig. 4.5c).

There is ubiquitous field evidence to suggest that the formation of the dark ultracataclasite localises along fractures with cm to sub-mm-spacing (Fig. 4.5b). In many cases the foliation is defined by both the parallel alignment of grains and a dense, closely-spaced fracture network. The dark seams and associated fractures pervasively cross-cut the orange quartzose layers and clasts, and appear to be cataclastically breaking them down from the edges inward forming a crude 'core and mantle' structure (Fig. 4.5b). The quartzose clasts broken down in this manner are typically elongate within the foliation and appear to be being smeared out due to the effects of cataclastic flow. Injection seams of dark ultracataclasite cutting across orange quartzose cataclasites are common and are locally folded and flattened parallel to the foliation (Fig. 4.5d).

Centimetre-scale Riedel-type shears are widely developed lying anticlockwise to the crude foliation at angles of up to ~ 45° (Fig. 4.5b). These shears are consistent with sinistral shear and are coated with dark ultracataclasite. Locally, these shears and the foliated units of dark ultracataclasite are folded by irregular cm-scale open to tight folds (Fig. 4.5e) with variable orientations.

In areas up to several tens of cm wide adjacent to intercalated units of other fault bounded rock types, the orange black quartzose foliated cataclasite appear to lose coherence to form gouges with a pervasive flow foliation (Fig. 4.5c, f and g). Relict clasts of quartzose cataclasite and pale carbonate up to 10 cm across are locally

preserved strongly wrapped by the foliation. The wrapping is often slightly asymmetric and, together with the local development of cm-spaced shear bands oriented anticlockwise to the foliation, suggests sinistral senses of shear (Figs. 4.5b, f and g). The foliation is locally folded by cm-scale tight to isoclinal folds. Fold hinges have mainly sub-vertical plunges and most likely formed due to strike-slip motion of the adjacent fault, although a consistent sense of vergence could not be ascertained. Fold hinges are often thickened, with pinching and shearing out of fold limbs by numerous fractures and associated ultracataclasite seams.

The highly foliated gouges characteristically preserve interlinked networks of white and orange carbonate and Fe-oxide, with individual veins typically less than 1 mm wide. The veins anastomose and coalesce and are preferentially aligned sub-parallel to the foliation, although they locally crosscut – and therefore post-date – this fabric (Fig. 4.5f-g). Regions of foliated gouge adjacent to orange Ryoke – Sambagawa contacts appear to have been particularly incohesive, with evidence of cuspate-lobate boundaries between units of Ryoke- and Sambagawa-derived gouge (Fig. 4.5h). In some localities, black Sambagawa-derived gouge appears to have been injected into orange Ryoke-derived units.

4.3.2.6. Grey-green and orange-stained cataclasites

Both these fault rocks units are essentially unfoliated. The pale grey-green cataclasite crops out in two fault-bounded slices along the upper part of the river tributary (Fig. 4.2a). It appears to be derived from a Ryoke quartzo-feldspathic mylonite with the mylonitic foliation and feldspar porphyoclasts up to 0.6 mm across still visible is isolated patches. A few weakly foliated ultracataclasite bands have formed along some fractures and are extremely fine-grained.

The orange-stained cataclasite occurs primarily in the central region of the fault core intercalated with the orange-black quartzose foliated cataclasite (Fig. 4.2a). It is distinctive as it lacks any foliation. The orange colour appears to result from the weathering out of iron oxide and it is relatively incohesive. Cataclasis and alteration are pervasive and no features or textures are recognisable, with a grainsize generally <1 mm.

4.3.2.7. Fault rock sequence

The mylonitic rocks derived from Ryoke psammite, pelite and tonalite are consistently the earliest recognised fault rocks preserved. These rocks are heterogeneously overprinted by the effects of increasingly pervasive brittle fracturing and cataclasis leading to the development of cataclasite and foliated ultracataclasite assemblages. The latter units are initially localised along fracture systems preferentially aligned parallel to the MTL leading to the formation of a crude meso-scale foliation. A sub-parallel ultra fine-grained fabric additionally develops in the ultra-cataclasites. The development of injection veins and irregular folds points to the localised onset of cataclastic flow. With increased deformation, the ultra-cataclasites become dominant and lose cohesion, ultimately forming flow-banded units of foliated gouge. Carbonate mineralization and veining episodes initiate after the cessation of mylonitisation and are associated with, and reworked by, every stage of cataclastic deformation in the MTL core, culminating in the focusing of carbonate and Fe-oxide net veining in the most intensely deformed foliated gouges.

The units of essentially unfoliated orange and grey-green cataclasite are problematic in terms of their relative age. There is no clear evidence to suggest that they are derived from later reworking of the foliated cataclasites at shallower crustal

depths and the grey-green cataclasite preserves relicts of only mylonitic textures. The incipient development of ultra-cataclasite seams in the latter lithology seems to suggest that these units may represent regions of cataclasite effectively 'frozen in' and little affected by the later development and localisation of shearing into the adjacent units of foliated cataclasite.

Finally at least two later phases of brittle faulting are recognised. The more significant faulting event significantly disrupts and interslices the pre-existing fault rock units in the core of the MTL and is associated with late carbonate and local sulphide mineralization.

4.3.3 Mineralogy and microstructures.

4.3.3.1. Ryoke mylonites

The mylonites derived from metamorphosed Ryoke psammites and pelites are composed of alternating domains with differing quartz-mica contents. The orange coloured bands visible in outcrop are composed of a fine-grained (~0.05-0.1 mm) recrystallized quartz-rich matrix, with ~20% white mica plus chlorite (Fig. 4.6a). The white mica is coarser grained than the chlorite, with muscovite mica-fish up to 0.7 mm in length (Fig. 4.6b) preserved throughout. Plagioclase and K-feldspar porphyroclasts up to 1 mm in length, along with fractured garnet porphyroclasts ~0.5 mm in length are common within the quartz-rich layers (Fig. 4.6a). The feldspars show strained and sweeping extinction patterns and deformation twins and therefore appear to have undergone only limited ductile deformation. The slight asymmetry of feldspar porphyroclasts and mica-fish consistently indicate sinistral shear (Fig. 4.6a-b). Thin (<0.1mm wide) shear zones lined with very finely comminuted white mica run parallel or at low-angles to the foliation in the mylonites and are often localised

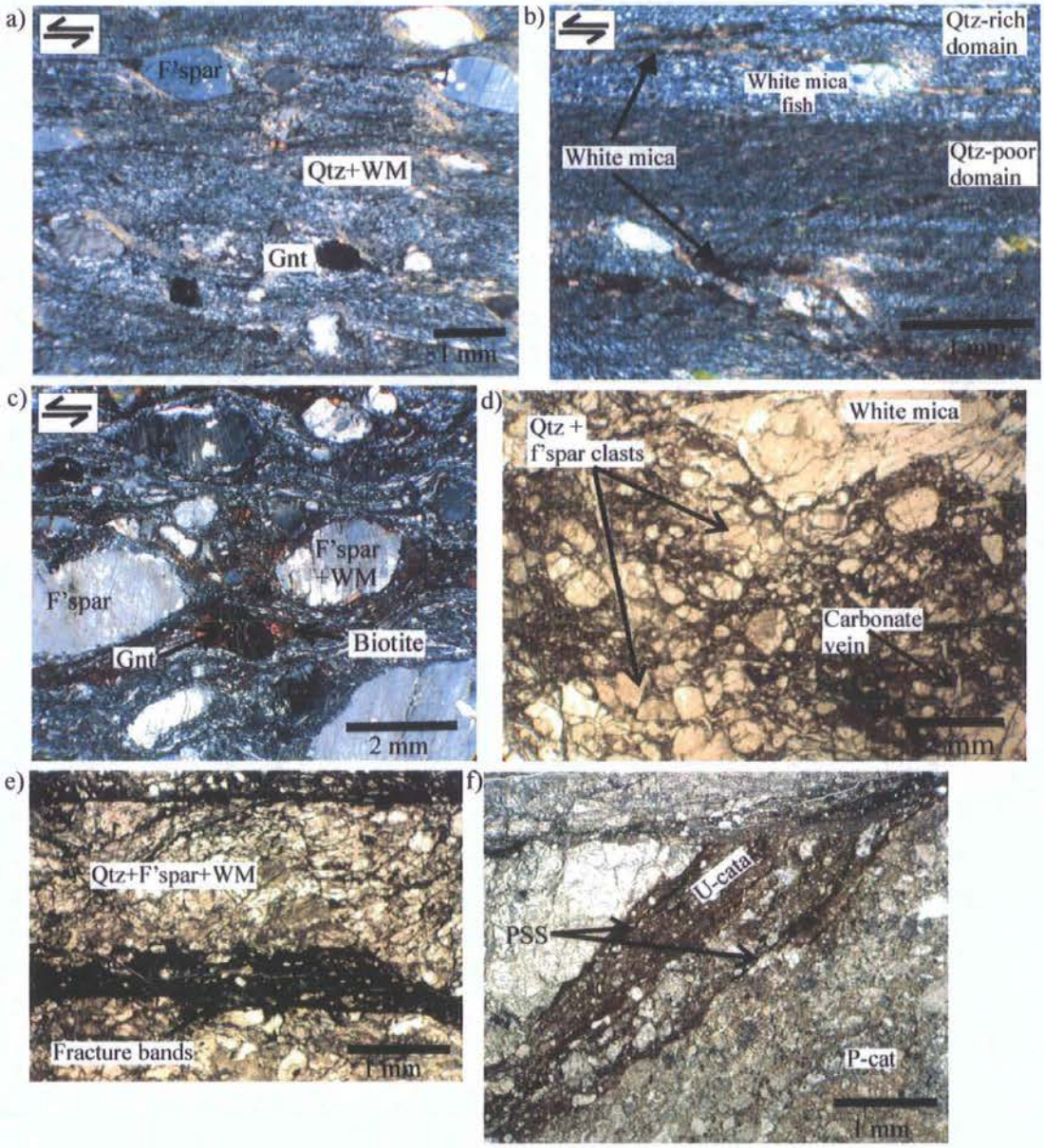

Figure 4.6. a) Ryoke mylonite derived from metamorphosed psammite and pelite. Thin section cross-polarised light view, feldspar (F'spar) and garnet (Gnt) porphyroclasts in fine-grained quartz (Qtz) + white mica (WM) matrix, b) thin section cross-polarised light view, shows white mica fish and the boundary between quartz-rich and quartz-poor domains, also shows slivers of finely comminuted white mica, c) cross polarised light thin section image of tonalitic mylonite clast within quartzo-feldspathic foliated cataclasite, d-f) Thin section plane polarised light images of quartzo-feldspathic cataclasite and foliated cataclasite, d) image of cataclasite showing angular quartz and altered feldspar clasts, e) image shows dense cluster of parallel to sub-parallel fractures lined with fine-grained ultra-cataclasite stained with Fe-oxide, f) Proto-cataclasite (P-cat) and foliated ultra-cataclasite (U-cat) seam with pressure solution seams (PSS) developed at the margins.

along compositional boundaries or the tails of wrapped porphyroclasts and mica fish (Fig. 4.6a-b). The quartz-feldspar deformation textures and stable mineralogy of quartz-albite-white mica-chlorite suggests that mylonitisation occurred under lower greenschist-facies metamorphic conditions.

The black coloured bands visible in outcrop are composed predominantly of very fine-grained (<0.05 mm) quartz (~60%) and mica (~40%), with no porphyroclasts present (Fig. 4.6b).

Greenschist-facies mylonitic fabrics are also well preserved in the central parts of the tonalite clasts that occur within the quartzo-feldspathic foliated cataclasite (Fig. 4.6c). Plagioclase and subordinate K-feldspar porphyroclasts up to 3 mm in length are undergoing limited crystal plastic deformation (undulose and sweeping extinction) and are breaking down to fine-grained aggregates of quartz and white mica. The mylonitic foliation wrapping around these porphyroclasts is defined by recrystallized quartz and biotite (often >0.05 mm). The quartz is undergoing sub-grain rotation and grain boundary migration recrystallization and in places quartz ribbons up to 1 mm in length have developed. Finely comminuted biotite is often localised within very thin (<0.1mm across) shear zones oriented sub-parallel or at low angles to the mylonitic foliation. Isolated examples of highly fractured garnet porphyroclasts (~0.7-1 mm in length) occur breaking down to biotite (Fig. 4.6c).

4.3.3.2. Quartzo-feldspathic cataclasite and foliated cataclasite

These rocks are predominantly proto-cataclasites composed of highly fractured clasts of quartz, albite, K-feldspar and calcite ~0.06-1.2 mm in length (e.g. Figs 4.6d and 4.6a-b). The feldspars are typically altered to white mica along cleavage and other fracture planes (Fig. 4.7b). The matrix represents ~25 % of the proto-cataclasite and is

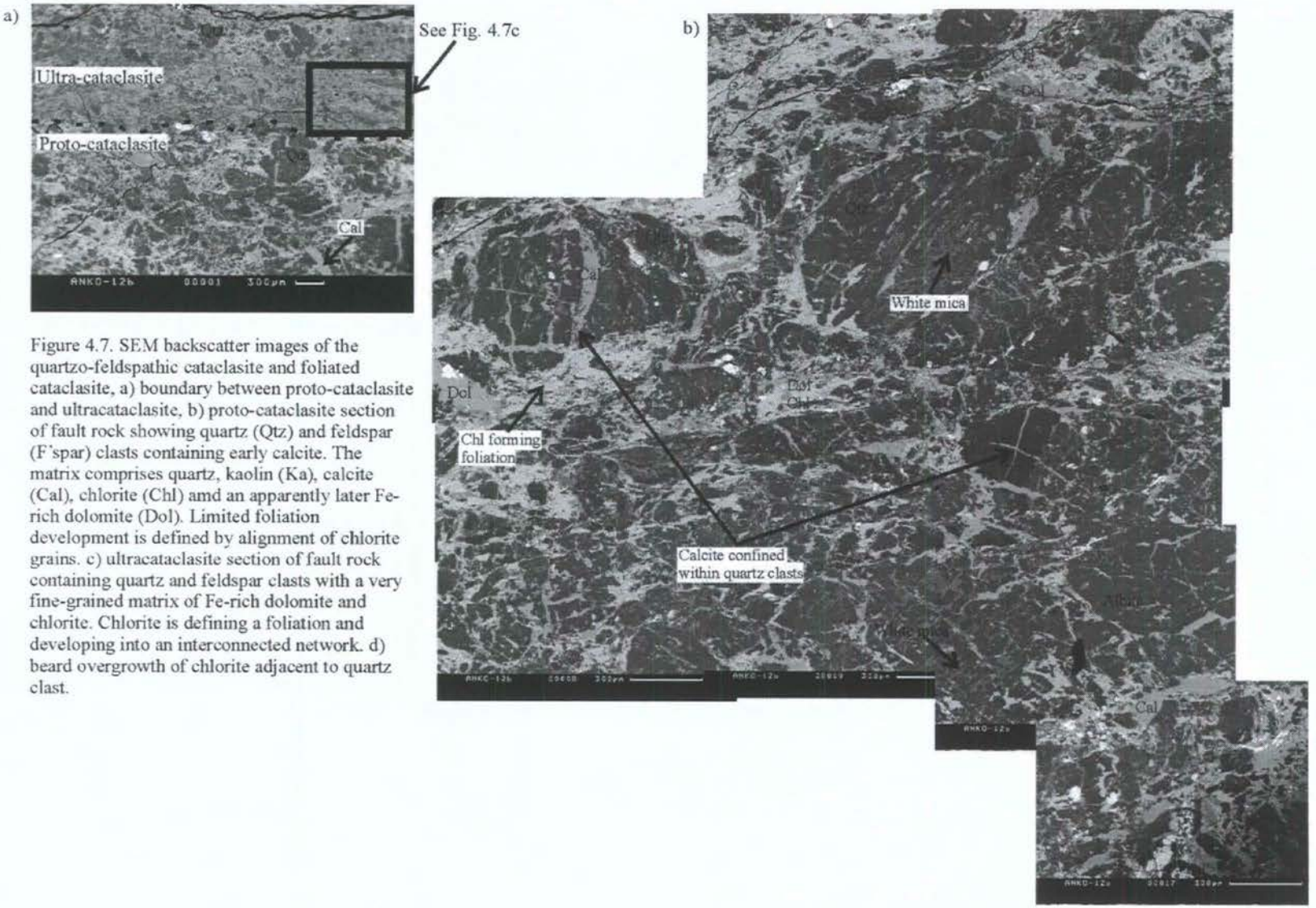

Figure 4.7. SEM backscatter images of the quartzo-feldspathic cataclasite and foliated cataclasite, a) boundary between proto-cataclasite and ultracataclasite, b) proto-cataclasite section of fault rock showing quartz (Qtz) and feldspar (F'spar) clasts containing early calcite. The matrix comprises quartz, kaolin (Ka), calcite (Cal), chlorite (Chl) amd an apparently later Fe-rich dolomite (Dol). Limited foliation development is defined by alignment of chlorite grains. c) ultracataclasite section of fault rock containing quartz and feldspar clasts with a very fine-grained matrix of Fe-rich dolomite and chlorite. Chlorite is defining a foliation and developing into an interconnected network. d) beard overgrowth of chlorite adjacent to quartz clast.


c)
Qtz
Qtz
Dol
Cal
Dol
Chl
Chl forming interconnected network
Calcite confined within quartz clast
d)
Dol
Qtz
Chl

made up of fine-grained (<0.5mm) quartz, kaolinite, calcite and chlorite plus a more Fe-rich dolomitic carbonate (Figs. 4.7a-b). Evidence for an early phase of calcite mineralization is preserved widely, with many clasts comprising fragments of albite or quartz net-veined with calcite (Fig. 4.7b). These may be reworked equivalents to the calcite veins observed cross-cutting the mylonites. There is only very limited development of a foliation defined by the weak alignment of chlorite grains.

Ultracataclasite (matrix ~5-10 μm with clasts <0.1 mm in length) bands up to 3 mm thick are defined in part by dense clusters of parallel to sub-parallel fractures lined with ultra-fine grained material stained with Fe-oxide (Fig. 4.6e). SEM images (Figs 4.7a, c and d) reveal that the ultra-cataclasites (85-90% matrix) comprise clasts of quartz, albite (highly altered to white mica) and calcite ranging between ~10-100 μm in length set in a very fine-grained (<5-10 μm) foliated matrix (Fig. 4.7c). The matrix is composed of chlorite (~10-15%) and apparently later Fe-rich dolomitic carbonate (70-75%), plus quartz, kaolin, white mica and Fe-oxide. The foliation is defined primarily by an interconnected network of aligned phyllosilicates (mainly chlorite, see Fig. 4.7c). The phyllosilicates defining this foliation are extremely fine-grained, e.g. chlorite grains are typically ~10 μm in length. They form an interconnected network only within the finest-grained sections of the ultra-cataclasite. Chlorite often forms beard-like overgrowths adjacent to angular clasts of quartz (Fig. 4.7d). Pressure solution seams are locally developed within the finest grained sections of the cataclasite, especially at the margins of foliated ultracataclasite seams (Fig.4.6f). Much of the carbonate mineralization is a Fe-rich dolomite variety that, together with chlorite makes up most of the ultra-cataclasite matrix (70-75%). Calcite vein material cutting clasts of quartz and feldspar (Fig. 4.7b) is clearly entrained as

clasts and its precipitation appears to predate that of the Fe-rich dolomite that surrounds these clasts.

4.3.3.3 Orange-black quartzose foliated cataclasite and gouge

Relict textures comparable to those found in the quartzo-feldspathic mylonites are locally preserved in the orange-coloured quartzose layers. Here, recrystallized quartz grains (~0.05-0.1 mm) wrap around the fractured relics of feldspar porphyroclasts (<1 mm) that are now mostly altered to fine-grained aggregates of white mica and kaolin (Fig. 4.8a). The rest of the cataclasite is composed of a matrix of quartz, kaolinite with flecks of white mica (~ 30 μm in length). The white mica flecks are aligned to define a weak foliation (Fig. 4.8b); a possible source for this white mica and kaolin is the breakdown of feldspar.

The injection veins of ultracataclasite observed in the field (e.g. Fig 4.5d) are predominantly composed of fine-grained (<10 μm) quartz, with minor Fe-oxide and carbonate with little or no feldspar preserved. When viewed in SEM, these accumulations show slight variations in colour due to crystallographic preferred orientation (CPO) contrasts. Clasts of the surrounding cataclasite up to ~0.1 mm in size are entrained within the quartz.

The bands that appear black in outcrop are composed of fine-grained (matrix ~5-10 μm) ultra-cataclasite and the foliation that is visible within these bands again appears to be defined by the parallel arrangement of fractures and associated fine-grained cataclasite material. Carbonate mineralisation is more extensive within these fine-grained cataclasite sections (Fig. 4.8c-e).

SEM and electron microprobe studies reveal that the orange-black foliated cataclasite contains three types of carbonate, calcite, Fe-rich dolomite and siderite

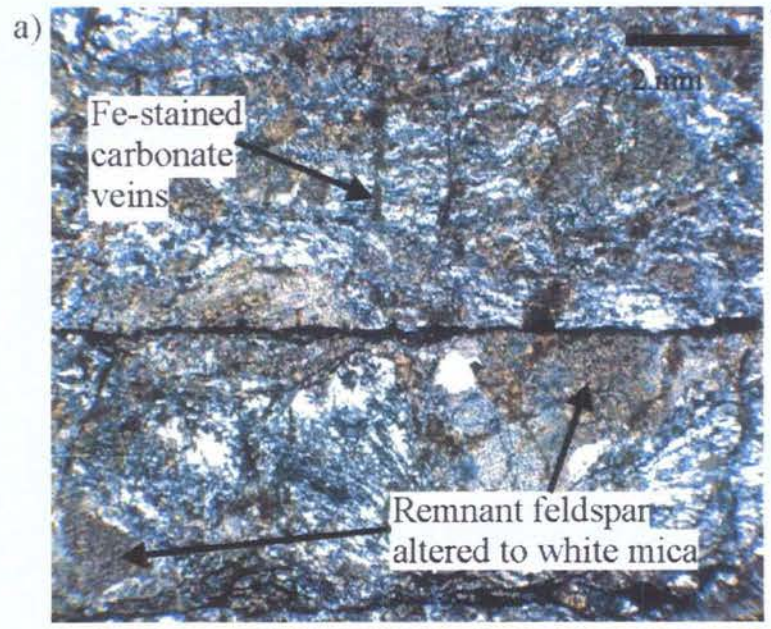

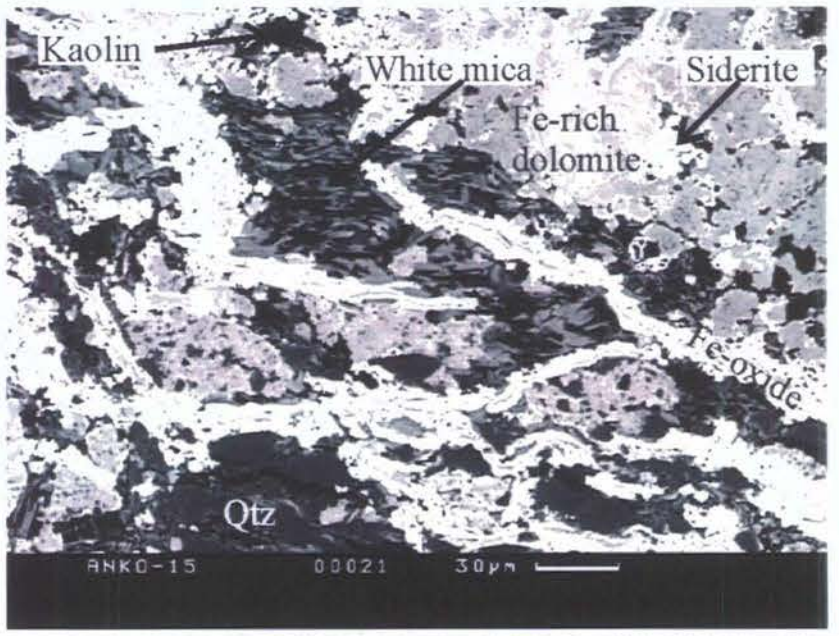

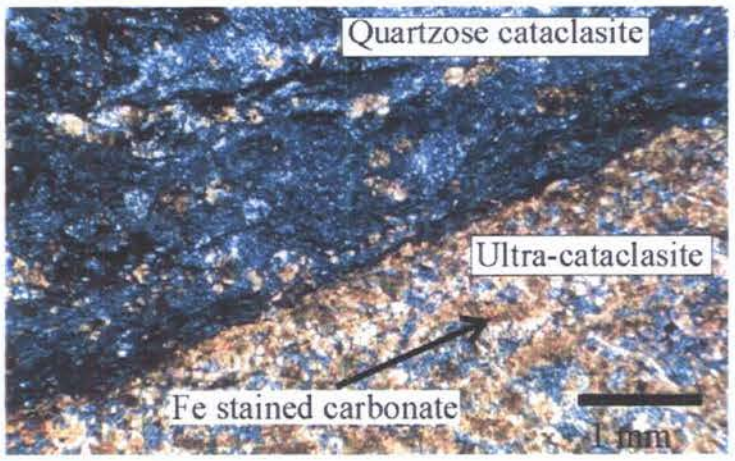

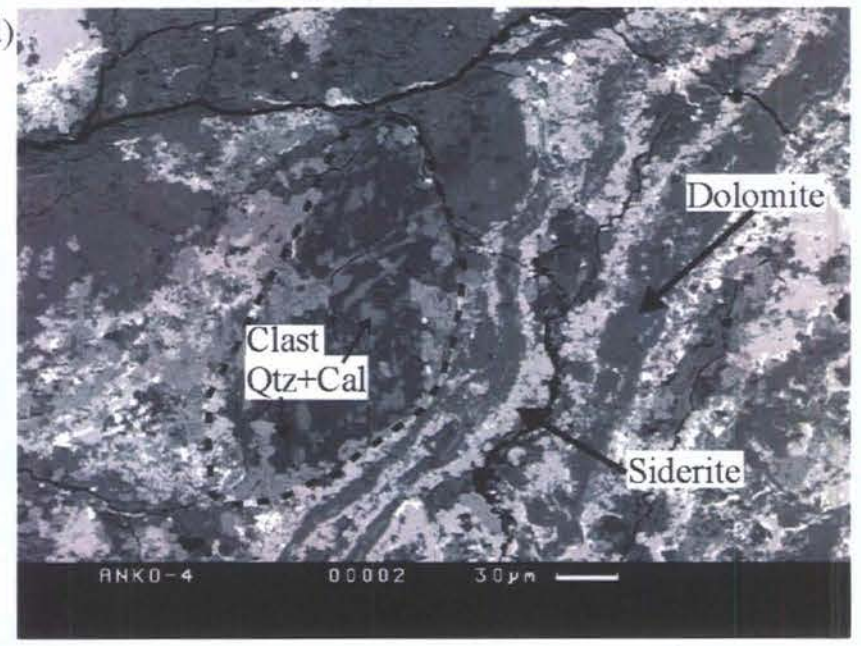

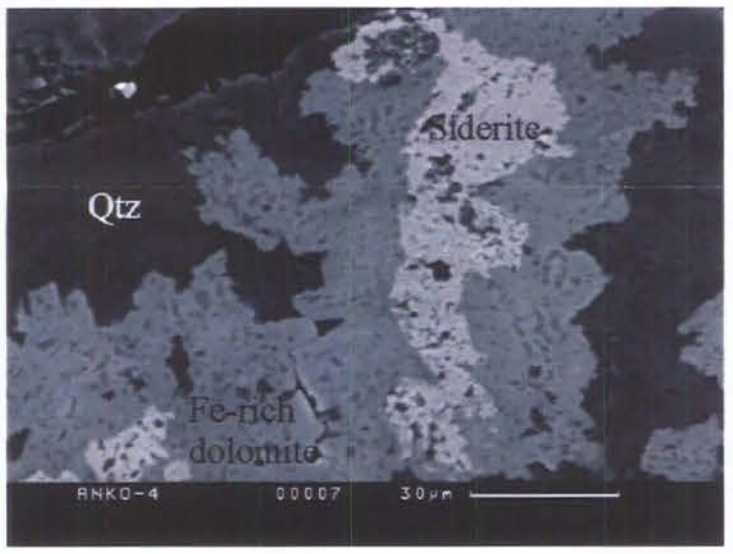

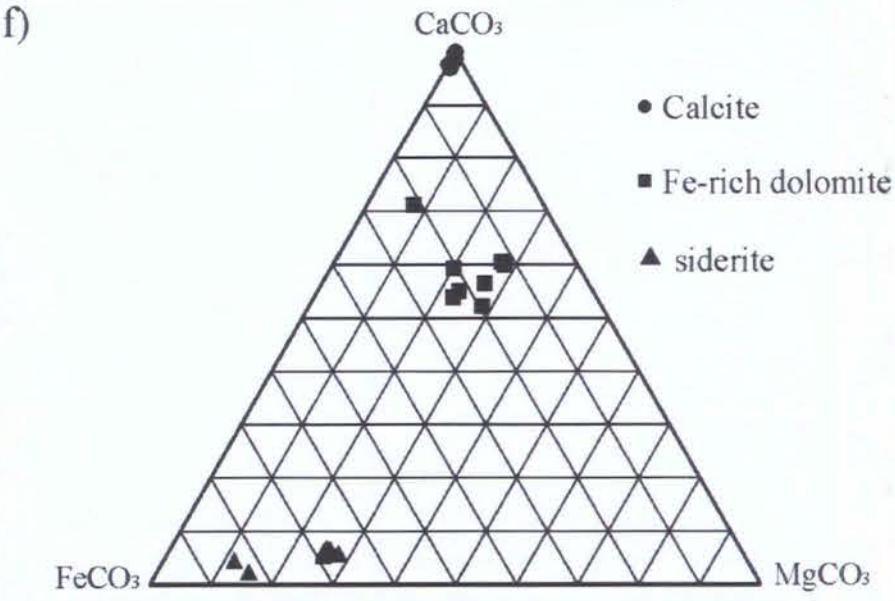

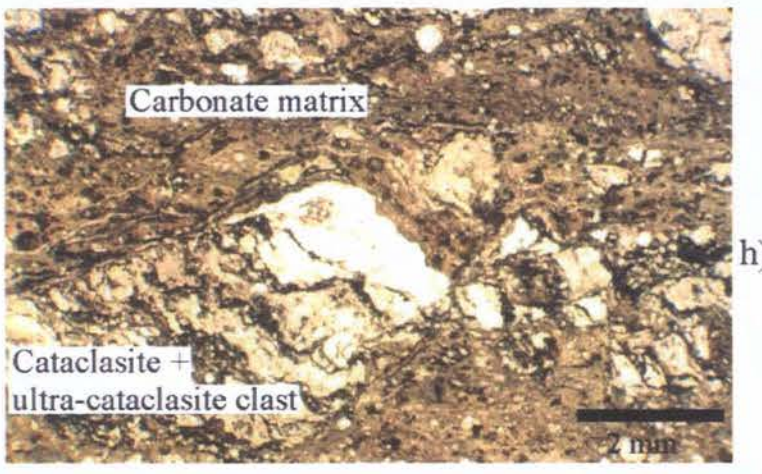

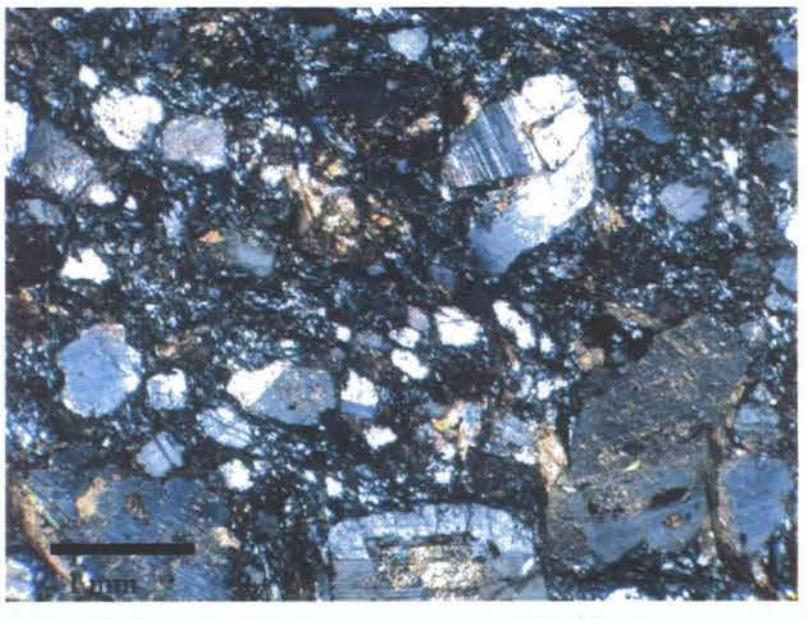

Figure 4.8. Microstructural observations of orange-black foliated cataclasite, a) plane polarised light thin section image showing relict mylonitic textures, b) SEM backscatter image showing aligned white mica and late net-veining Fe-oxide, c) cross polarised light thin section image showing weathering out of cataclasite, d) SEM backscatter image showing the three varieties of carbonate present, e) SEM backscatter image showing the rhombic and porous nature of late Fe-rich dolomite and siderite precipitation, f) Ternary diagram to show comparative CaCO3 - FeCO3 - MgCO3 content of carbonate within the orange-black foliated cataclasites. Data obtained from microprobe analyses,g) microstructural observations of orange-black foliated gouge, thin section plane polarised light view of cataclasite clasts within a predominantly Fe-rich carbonate matrix, h) thin section cross polarised light view of grey-green cataclasite showing highly fractured plagioclase and K-feldspar in afine-grained matrix of quartz, white mica, chlorite, calcite and opaques. Feldspar is breaking down to fine-grained white mica.

(Fig. 4.8f). Calcite appears to be the earliest phase occurring within clasts of quartz (Fig. 4.8d). Post-dating the calcite is extensive precipitation of a Fe-rich dolomite along fractures cutting through the cataclasite and within the cataclasite matrix (Figs 4.8b and d). Weathering out of the oxidised iron within these sections has resulted in Fe-staining and this gives the rock its distinctive orange colour (Figs 4.8a and c). A more Fe-rich sideritic carbonate is also often associated with the Fe-rich dolomite along fractures (Fig. 4.8d-e). SEM analysis reveals that the Fe-rich dolomite and siderite have a porous appearance, and the preservation of good rhombic crystal faces (Fig. 4.8e) implies that precipitation occurred into fluid filled cavities. This implies that the event was late in the fault rock development, although some minor brittle fracturing of carbonate occurred post-precipitation. The siderite typically occurs toward the centre of the mineralised fractures suggesting that it was slightly later than the Fe-rich dolomite. The final mineralisation event to occur involved the development of net-veined Fe-oxide that cuts across all observed cataclastic textures (Fig. 4.8b).

The orange-black foliated gouges adjacent to faults that dissect the section have an even higher carbonate content (~85% compared to ~70% in the orange and black foliated cataclasite). In thin section, clasts of cataclasite, including the parallel arranged fractures and ultra-cataclasite, sit within a predominantly carbonate matrix (Fig. 4.8g). Within the Fe-rich dolomite matrix angular clasts of quartz and albite up to 100 μm in length occur.

4.3.3.4. Grey-green and orange-stained cataclasites

The majority of clasts within the grey-green cataclasite are plagioclase and K-feldspar. Clasts are sub-angular to angular in shape and range from 0.1-0.6 mm in

length (Fig. 4.8h). The feldspar clasts are highly fractured, but show previous ductile deformation features (strained and sweeping extinction), and are breaking down to fine-grained white mica. The matrix grainsize is ~0.05 mm or less and it is composed of quartz, white mica, chlorite, calcite and opaques. White mica and calcite accumulations both form within the matrix. There is little foliation development except in thin (<0.1mm thick) isolated seams of dark ultracataclasite.

In thin section, few textural relationships are preserved in the orange-stained cataclasites as they are heavily altered to fine-grained alteration products such as white mica and clay minerals most likely derived from the breakdown of feldspar.

4.3.4 Major element geochemistry

XRF whole-rock major-element analyses were carried out to examine any changes in bulk geochemistry that occur across a suite of representative fault rock types collected from the Aokigawa River section (Fig. 4.9). The data show relatively little geochemical variation, which is consistent with the microstructural observations that apart from the carbonate and oxide mineralisation events, there are relatively limited mineralogical changes occurring across the suite of fault rock types. However, it also suggests either that the protoliths have similar major element compositions or that the sampled section is in a state of chemical equilibrium following extensive fluid fluxing through the fault zone. The lack of exposures of less deformed wall rock protoliths means that we are unable to reliably test these hypotheses and for this reason, we have not normalised the data relative to protolith compositions.

The more mobile elements (Mg, Ca, Na, K) show restricted variations most likely reflecting some small-scale remobilisation by circulating fluids. The most

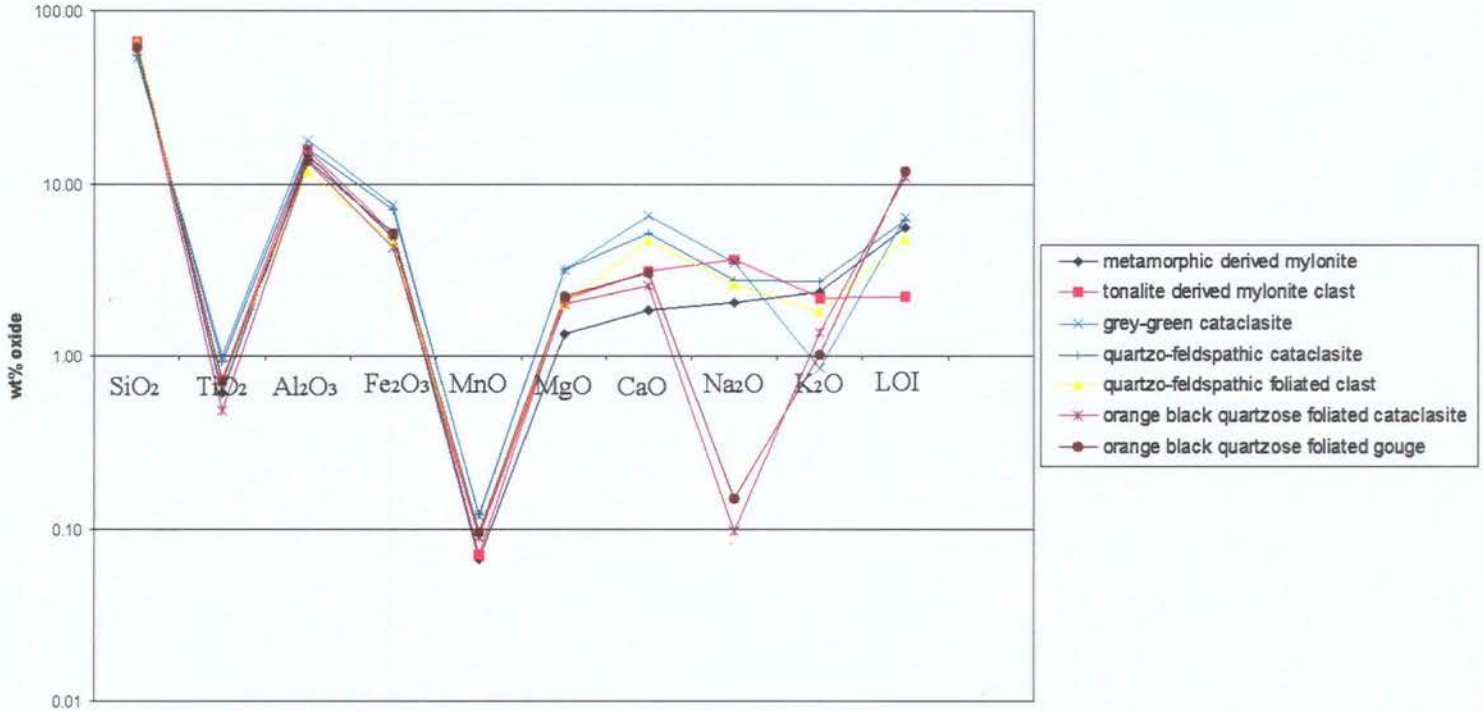

Figure 4.9. Plot showing XRF whole-rock major-element analyses for the main representative fault rock types from the MTL Anko section fault core. LOI = loss on ignition.

significant variations are observed in loss on ignition (LOI). The mylonitic clast within the quartzo-feldspathic foliated cataclasite, and the mylonite derived from a Ryoke metamorphic psammite-pelite show significantly lower LOI (2.2-6.4%) compared to the orange-black foliated cataclasite and gouge (10.9-11.9%). These changes likely reflect an increase of hydrous phases such as fine-grained white mica and chlorite developing at the expense of feldspar and biotite. However, as the loss on ignition value is related to both volatile and added compounds, for example O_2 (oxidation of FeO to Fe_2O_3) and also CO_2 (CaO to $CaCO_3$), so a higher oxide and carbonate content would produce a greater percentage LOI. Hence they may also reflect the higher amounts of carbonate and oxide mineralisation observed within the fine-grained ultra-cataclasites and gouges in the fault core.

4.4. Discussion

4.4.1. Brittle deformation, fluid flow and the development of foliated cataclasites

Table 4.1 presents a summary of the fault rock suites recognised in the core of the MTL in the Anko section and the interpreted deformation mechanism sequence and its relationship to fluid influx, mineralogical changes and rheological implications.

The fault rocks exposed in the Anko section suggest that the Ryoke metasedimentary and tonalitic protoliths became mylonitized during sinistral shear in a zone close to the MTL under greenschist-facies pressure-temperature conditions (see also Hayama et al., 1963; Hayama and Yamada, 1980; Takagi, 1986). Exhumation to shallower depths and lower temperatures occurred, possibly during the same prolonged phase of sinistral displacement, led to reworking of the mylonites in the MTL fault core by brittle fracturing and cataclasis. The development of pervasive

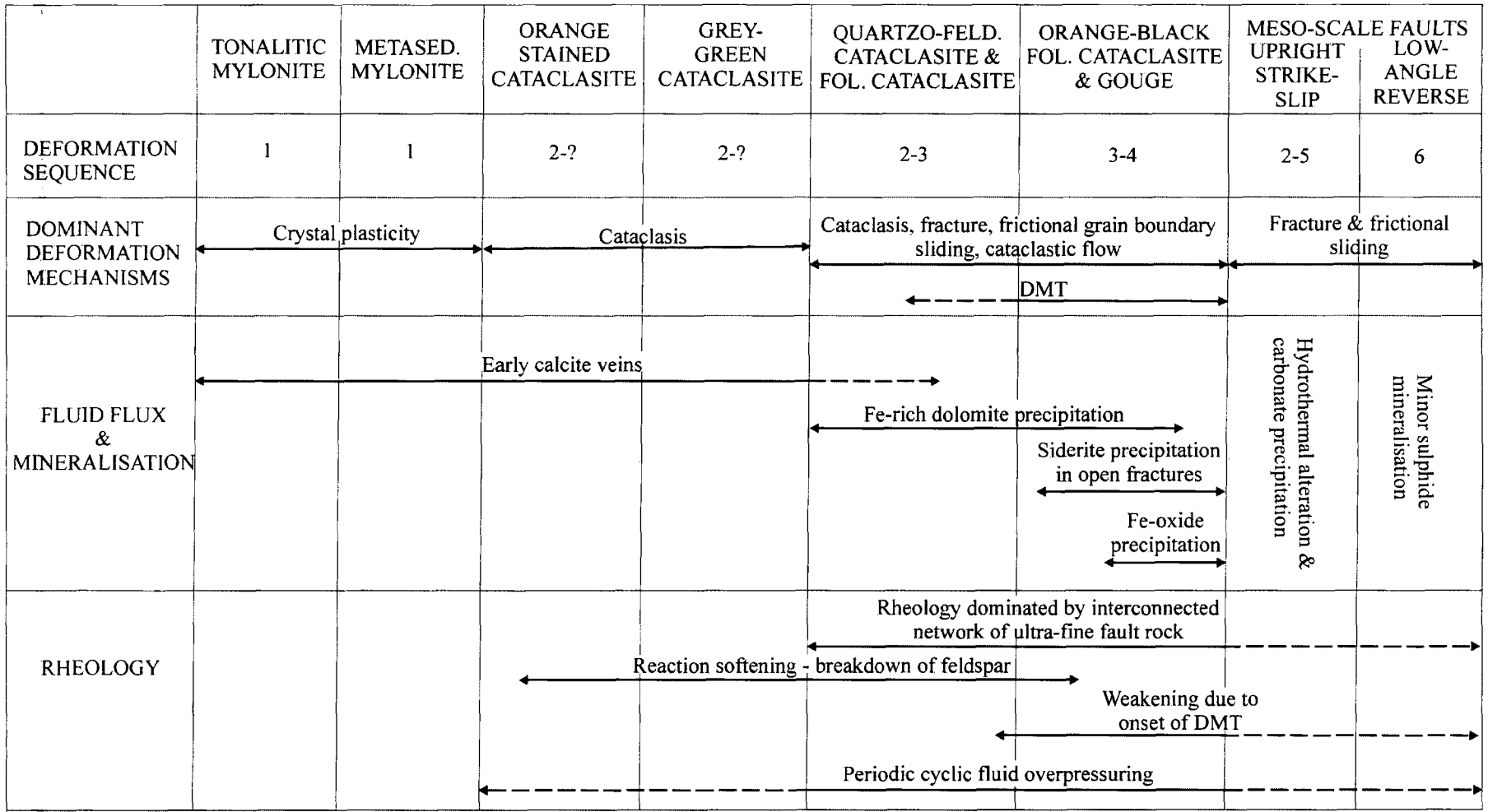

Table 4.1. Summary of the fault rock suites recognised in the core of the MTL in the Anko section and the interpreted deformation mechanism sequence and its relationship to fluid influx, mineralogical changes and rheological implications. METASED' = metasedimantary, FELD' = feldspathic, FOL' = foliated. DMT = diffusive mass transfer.

cm- to sub-mm-spaced fracture systems is a particularly striking feature and leads to the initial development of a crude mesoscale foliation oriented parallel to the MTL. These are associated with the cm-scale development of Riedel-type brittle shears oriented anticlockwise of the MTL at angles of up to 45°. Collectively, this fracture system imposes an initial architectural hierarchy that fundamentally influences the subsequent development of foliated cataclasite and gouge.

Once each initial fracture had formed, it appears that other fractures localised adjacent to the first break leading to the development of bands of densely spaced, sub-parallel fractures that eventually coalesce to form sub-mm-scale seams of dark ultracataclasite (i.e. Fig. 4.6e). These seams, which are found in all the foliated cataclasites, appear to broaden, presumably by the progressive abrasion of wall rocks, but rarely attain thicknesses of more than a few millimetres. The onset of brittle deformation appears to coincide with significant fluid influx presumably due to grain-scale dilatancy associated with cataclasis. The presence of an active fluid phase is indicated by: 1) the development of early calcite veins and mineralised breccias in fractured mylonite and proto-cataclasite; 2) the ubiquitous breakdown of feldspar, biotite and garnet to fine-grained aggregates of phyllosilicates (white mica, chlorite); and, 3) in the ultra-cataclasites, the precipitation of fibrous chlorite as aligned overgrowths on clasts and matrix grains. The latter process leads to the rapid development of a foliation in the ultracataclasite seams that is defined by an interconnected network of aligned phyllosilicate aggregates (see Fig. 4.7b-c). The preferential localisation of chlorite precipitation within the ultra-cataclasites is most likely initially favoured by their ultra-fine grainsize, which favours the operation of diffusive mass transfer on grain scales. There is also limited development of pressure solution seams in these fault rocks (e.g. Fig. 4.6f).

Thus the development of the initial fault network leads to the establishment of two quite distinct textural domains with very different inferred deformation behaviour in the foliated cataclasites of the MTL (Fig. 4.10a-b). The most intense deformation and, by inference, the largest displacements, are localised into a narrow, highly interconnected network of foliated ultra-cataclasites in which the grain-scale deformation mechanisms are likely to involve significant amounts of fluid-assisted diffusive mass transfer, including solution-assisted grain boundary sliding and lesser amounts of pressure solution (Fig. 4.10d). These narrow domains enclose tens-of-metre to mm-scale lenticular regions of less deformed proto-cataclasite (Fig. 4.10c) in which grain-scale processes are dominated by fracture, rigid rotation of grain fragments and limited frictional grain boundary sliding.

It is probably significant that a majority of the later carbonate and Fe-oxide mineralization is preferentially sited within regions of foliated ultra-cataclasite and foliated gouge, especially within the orange-black quartzose foliated cataclasites of the central MTL core. We propose that this occurs because fluid flow was increasingly focused into the foliated and fracture-bound network of ultra-cataclasites due to their likely effectiveness as fluid seals and also as a consequence of their connectivity in directions parallel to the MTL fault zone (Fig. 4.10a).

4.4.2. Rheological implications

During both frictional and viscous deformation, the rheology of polymineralic fault rocks depends very significantly upon the relative proportions of weak and strong phases and the connectivity of the weak phases (e.g. Handy, 1990, 1994). We assume here that the current textures of the proto-cataclasite regions (e.g. Fig. 4.10c) are representative of the fault zone as a whole immediately following exhumation and

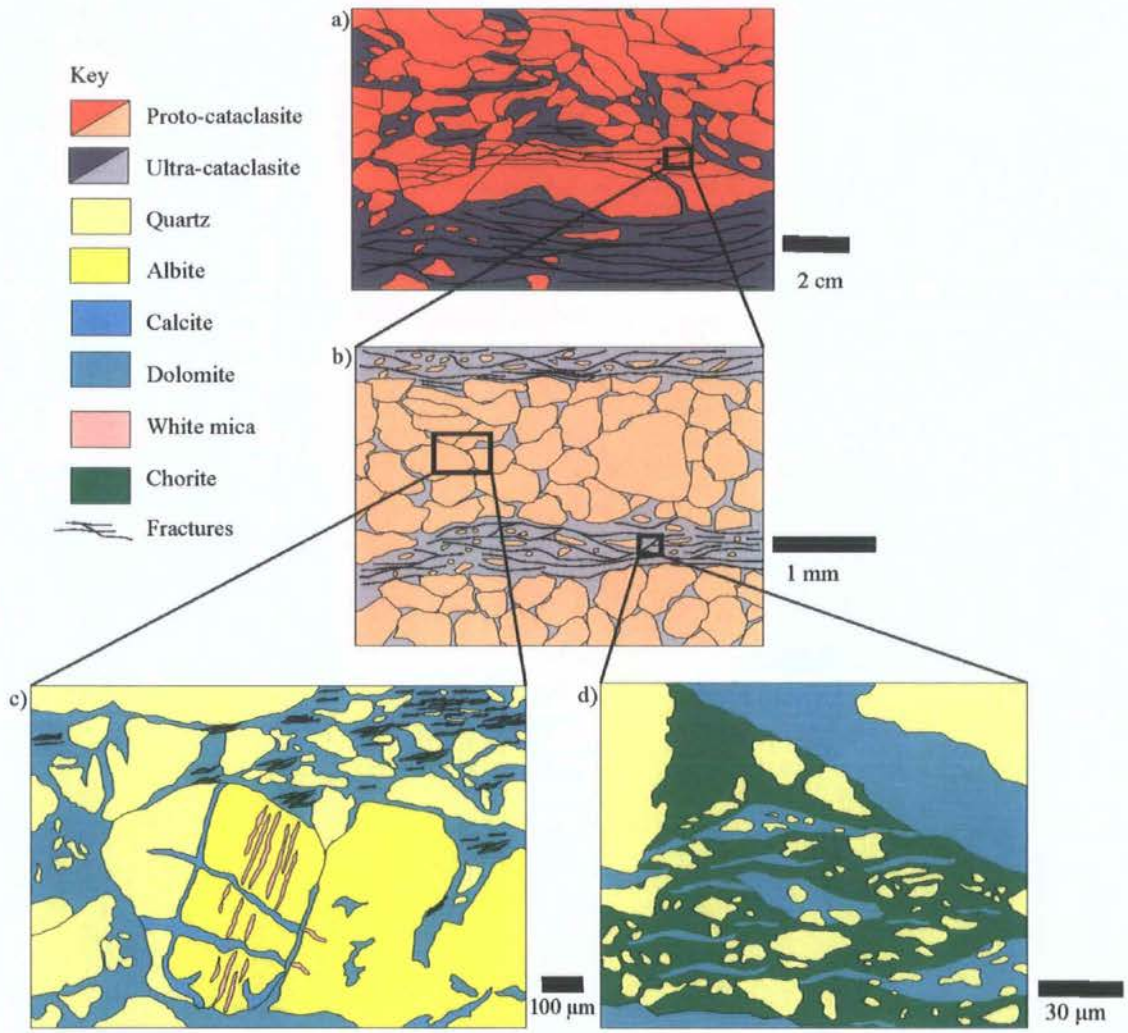

Figure 4.10. Schematic diagram depicting the principal features of the Anko foliated cataclasite on various scales. a) Hand specimen scale showing regions of orange coloured proto-cataclasite becoming broken down by sub-parallel fractures and regions of black coloured ultra-cataclasite showing the development of a crude foliation to give the overall cataclasite a banded appearance. See Fig. 4.5a-b. b) Thin section scale view showing narrow black bands are bands of closely spaced fractures around which ultra-cataclasite develops. Proto-cataclasitic portions are clast supported and within ultra-cataclasite sections fractures and associated fine-grained material create a interlinked network. See Fig. 4.6e. c) Micron-scale view of proto-cataclasite showing clasts of quartz and albite within a matrix of dolomite with isolated patches of aligned chlorite growth. See Fig. 4.7b. d) Micron-scale view of ultra-cataclasite. Aligned chlorite development is more pervasive with evidence for limited diffusive mass transfer, e.g. chlorite forming beard like overgrowths adjacent to clasts. Aligned chlorite grains form an interconnected layer throughout the ultra-cataclasite. Note that the interlinked nature of the foliated ultracataclasite on all scales makes it likely that the rheology of this fault rock dominated the overall behaviour of the fault zone.

the initial onset of brittle fracturing and cataclasis. Fractured clasts of earlier mylonite and calcite veins/mineral cements are randomly distributed and mostly lie in direct contact with each other forming a relatively strong load-bearing framework. However, the development of foliated ultra-cataclasites located along an interconnected network of brittle fractures aligned parallel to the MTL means that, if these ultra-fine grained fault rocks are weak, then their rheology will rapidly come to dominate the overall strength of the fault zone.

There are three compelling reasons to suppose that the development of foliated ultra-cataclasite has led to significant weakening. The first and most obvious observation is that once established, much of the subsequent deformation – and by inference displacement – has localised preferentially into the regions of foliated ultra-cataclasite. This ultimately leads to the development of flow-banded foliated gouges adjacent to major faulted boundaries (e.g. Figs 4.5c, f and g), including the main Ryoke-Sambagawa contacts. The local development of folds (Fig. 5e) and injection of mobilized units of ultracataclasite and gouge into adjacent rock units (Fig. 4.5h) is similarly consistent with weakening and the onset of cataclastic flow.

The second reason is that the foliated ultra-cataclasites display clear evidence for the operation of fluid assisted diffusive mass transfer mechanisms on grain scales, together with the development of an ultra-fine-grained interconnected network of strongly aligned phyllosilicates. There is now abundant evidence from both experimental studies (e.g. Mares and Kronenberg, 1993; Bos and Spiers, 2000, 2002; Bos et al., 2000 a & b) and studies of natural phyllosilicate-rich fault rocks (e.g. Wintsch et al. 1995; Stewart et al. 2000; Imber et al. 2001; Collettini and Holdsworth 2004; Jefferies et al., 2006) that the establishment of interconnected phyllosilicate layers coupled to the onset of diffusive mass transfer leads to profound long term

weakening. A more general reaction softening effect is also likely to be associated with the widely observed replacement of strong framework silicates by weak phyllosilicates. This leads to framework collapse and is well illustrated by the observed folding of crosscutting ultracataclasite seams within foliated cataclasites (e.g. Fig. 4.5d-e).

Finally, the persistent association observed at both outcrop and grain scales between cataclasis and (mainly carbonate) mineralization points to the periodic development of high pore fluid pressures in the fault core which would likely lead also to weakening, albeit on shorter timescales.

4.4.3. Comparison with other natural and experimental foliated cataclasites/gouges

The meso- and grain-scale character and development of the foliated cataclasites developed in the core region of the MTL are comparable to those observed in a number of other exhumed upper crustal faults, most notably examples from the San Andreas system in California (e.g. Chester and Logan, 1986; Chester et al., 1993; Evans and Chester, 1995). The development of a narrow central core region of foliated cataclasite and, within that core, the progressive localisation of slip into narrow seams of ultra-cataclasite and ultimately gouge represent the most obvious similarities. The key roles played by reaction softening, the development of fine-grained phyllosilicate-rich fault rocks and the focussing of mineralization processes are also recognised, emphasising the key role played by fluid-rock chemical interactions. Nevertheless, many of these studies essentially reiterate the contention that "cataclastic mechanisms of fracture, rigid rotation of grain fragments, and frictional sliding along grain boundaries were dominant" during the development of foliated cataclasites (Chester et al., 1983).

Our observations suggest that this view is an oversimplification. It is certainly true that brittle processes play a fundamental role through the development of the initial network of aligned fractures. However, based on our observations in the present study, we contend that the main grain-scale processes that lead to fault weakening and slip localisation are not cataclastic. These are the onset of diffusive mass transfer mechanisms, which facilitate frictional-viscous sliding along an interconnected network of fine-grained phyllosilicate foliae within the foliated ultra-cataclasites. The fracture network plays two key roles: firstly it determines where the initial shear localisation occurs that leads to the development of ultra-cataclasite seams, and secondly, it provides a highly interconnected network that transmits the grain-scale mechanical weakening upscale to affect the entire fault zone on a larger scale, despite the relatively modest volumes of foliated ultra-cataclasites and gouge present.

4.4.4. How are foliated cataclasites/gouges related to phyllonites?

Foliated cataclastic fault rocks are known to occur at a number of localities along the MTL (e.g. Tobe, Takagi et al., 1992; Hiruma, Takagi in Snoke et al., 1998; Tsukide, Wibberley and Shimamoto, 2003). Chapter 2 discusses the development of foliated cataclasites that overprint cataclastic fault rocks and suggest that ultimately this leads to the development of phyllonites. As in Anko, this sequence occurs because cataclasis in the vicinity of brittle fractures creates permeable pathways for the ingress of chemically active fluids into the fault zone. Once again, there is widespread evidence for the extensive operation of fluid assisted reactions where load-bearing phases such as feldspar are replaced by fine-grained, foliated aggregates of weaker phyllosilicate material (white mica, chlorite). However, at Miyamae, the extent of this alteration, and the precipitation of new chlorite is far more extensive

leading to the formation of a phyllonite band at least 15 m thick. There is also far more widespread evidence for the operation of fluid-assisted, grainsize-sensitive diffusive mass transfer mechanisms, in particular pressure solution, throughout the phyllonite. Once again, comparison was made with findings of recent experimental studies (notably Bos and Spiers, 2000, 2002) and, by applying the appropriate microphysical model, it was suggested that the development of phyllonite could have led to long-term weakening of the MTL and other crustal scale faults (Fig.4.11).

We propose that the absence of phyllonite in the Nagano section of the MTL may occur because this fault segment is less deeply exhumed compared to Miyamae and therefore that the two regions preserve fault rock assemblages that formed at different depths along the same fault at more or less the same time (Fig. 4.11). This suggestion is supported by the observation that the cataclastic rocks in both cases are associated with sinistral shearing events that overprint and rework pre-existing mylonite-ultramylonite sequences. The textural sequences and mineralogical development of the phyllosilicate-bearing fault rocks are similar, but the finer grain sizes of the phyllosilicates and the lesser development of pressure solution features at Anko is consistent with a shallower crustal location.

4.5. Conclusions

One example from the MTL fault core exposed at Anko shows that the development of an interconnected cm- to sub-mm scale network of coalescing fractures and associated ultra-fine grained cataclasite plays a major role in controlling the location where shear localisation occurs. Deformation mechanisms within the developing cataclasites and foliated cataclasites are dominated by fracture, frictional grain boundary sliding and cataclastic flow. Fluid influx initially occurred during the onset

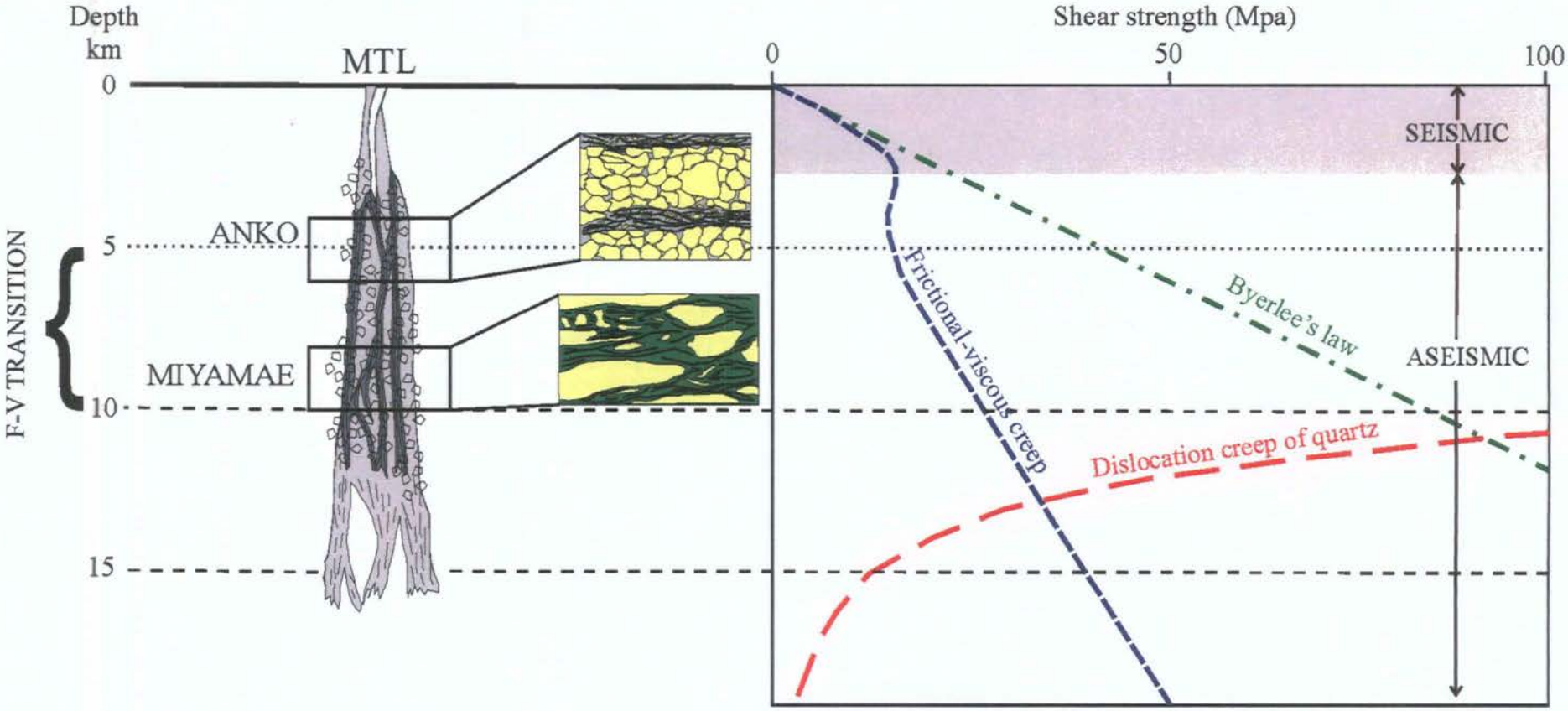

Figure 4.11. On the left, fault profile showing relative depths of formation and schematic textural diagrams of foliated cataclasite and gouge from Anko, Nagano Prefecture, and phyllonite fromMiyamae, Mie Prefecture. On the right, corresponding strength-depth profile for this section of the crust. Traditional crustal strength-depth profile is defined by Byerlee's law and dislocation creep of quartz, also shown is the profile produced by Bos and Spiers (2000; 2002) to show the resulting effect of the presence of foliated phyllosilicate-rich fault rocks within the core of a crustal-scale fault zone. For further explanation see text.

of cataclasis, and led to a switch in dominant deformation mechanism within the finest-grained sections of ultra-cataclasite formed around the pre-existing fracture network. Here, fluid assisted reaction softening and diffusive mass transfer processes are the most significant processes. DMT aided the development of a foliation defined by the alignment phyllosilicate (chlorite), with further chlorite growth leading to the creation of an interlinked network within the matrix and ultra-cataclastic sections of the foliated cataclasite. The pattern of initial fracture development provided the architecture for the creation of interlinked zones of fine-grained weak material throughout the fault core, and we suggest that this dramatically altered the rheology of the fault core. On textural and mineralogical grounds the development of foliated cataclasite and phyllonite are equivalent in both space (depth) and time (Fig.4.11). Conclusions from recent microphysical models (i.e. Bos and Spiers, 2000; 2002) suggest that the formation of foliated cataclasites and phyllonites within the core of large crustal-scale fault zones can dramatically reduce the fault zone strength effectively reducing the thickness of the seismogenic layer to <5 km (Fig. 4.11). On the shorter timescales, the fracture bound network of foliated ultra-cataclasite and gouge likely acted as very effective fluid seals leading to periodic overpressuring as evidenced by the widespread, mainly carbonate mineralisation, in the core of the MTL. These findings have important implications for the weakening of crustal scale faults in many tectonic settings worldwide.

Chapter 5
Conclusions and suggestions for further research.

5.1. Conclusions.

It is proposed that the formation of phyllosilicate-rich foliated cataclasites and phyllonites within the core of the MTL has led to long term weakening of the fault zone as a whole. Evidence from Miyamae suggests that the development of phyllonite from cataclasite is associated with the onset of two groups of processes by fluid influx facilitated by a strain-induced, brittle reduction in grain-size and associated increase in dilatency. Fluid influx led to widespread retrograde replacement of strong mineral phases (albite) by fine-grained, aligned weak aggregates of phyllosilicate (phengite and chlorite). In the transition from foliated cataclasite to phyllonite, the weak phyllosilicate minerals increasingly coalesce to form an interconnected network on all scales. This interconnected weak network controls the strength of the fault rock as a whole, ultimately leading to collapse of the load-bearing framework and development of a highly foliated phyllonite in the core of the MTL that results in weakening of the entire fault zone. The other group of grain-scale processes that lead to weakening and slip localisation are the grain size controlled onset of diffusive mass transfer mechanisms, which facilitate frictional-viscous sliding along an interconnected network of fine-grained phyllosilicate foliae. This is wholly consistent with the findings of recent experimental studies (e.g. Bos & Spiers, 2000; 2002; Bos et al., 2000 a and b; Niemeijer and Spiers, 2005) and field based evidence of strain focusing and localisation of later dextral reactivation to within the phyllonitic fault core at Miyamae.

The integrated geochemical and microstructural study of samples taken across the Miyamae and Tsukide transects highlight that crucial to the formation of

phyllonite is the ingress of fluid into the finest-grained sections of the fault core promoting phyllosilicate precipitation. Once such a foliation is well established within the MTL fault core it led to fluid focussing with a move from pervasive fluid flow across a broad damage zone of Ryoke variably fractured mylonites (e.g. Tsukide) to channellized flow within a narrow phyllonitic fault core adjacent to the central slip zone (e.g. Miyamae). Fluid-rock ratios – hence degree of fluid-rock interaction – are likely to have been higher at deeper crustal levels where fluid flow was strongly focused within weak phyllonitic shear zones (e.g. Miyamae). If permeability and porosity models such as those of Evans et al. (1997) and Géraud et al. (1995) are applicable to the MTL fault rocks, it is likely that the phyllonites provided effective conduits for large volumes of fault-parallel fluid flow whilst at the same time inhibiting transverse fluid flow. The convergence in the geochemical composition of the phyllosilicate-rich rocks within the fault core and those of the wall rock protoliths reflect this intensity of fluid channellization and volumetric throughput within the fault core compared with *apparently* more altered adjacent damage zone.

A key prerequisite to fluid influx and phyllonite development is a pre-existing brittle 'blueprint'. The study at Anko highlighted the fundamental role that brittle processes play in the development of the initial network of aligned fractures. The pattern of the initial fracture network firstly determines where initial shear localisation occurs providing the architecture for the creation of interlinked zones of fine-grained cataclastic material, dramatically altering the rheology of the fault core. Secondly, once weakening has occurred this highly connected network transmits the grain-scale mechanical effect upscale to affect the entire fault zone on a larger scale. Initial phyllosilicate growth localises along brittle structures within the finest-grained sections of the cataclastic fault core. The brittle structures effectively allow further

influx of fluid promoting further phyllosilicate growth and the operation of grain-size sensitive fluid-assisted diffusive mass transfer deformation mechanisms, ultimately leading to phyllonite formation and permanent fault zone weakening.

This project set out to investigate the problem of weak faults and through the study of some key sections of the MTL (Miyamae, Tsukide and Anko) exhuming fault rocks formed at depths down to the region of frictional-viscous transition. It has documented the presence of weak foliated phyllosilicate-rich fault rocks and has inferred that their initial formation can occur over a range of depths close to the central slip zone of the crustal-scale fault. This study has provided the first detailed investigation into the occurrence and formation of phyllosilicate-rich and phyllonitic fault rocks from Japan's largest strike-slip fault zone, the Median Tectonic Line. It has also highlighted a number of critical feedback mechanisms (Fig. 5.1) that occur between processes of strain focusing, brittle deformation, grain-size reduction, phyllosilicate mineral growth, the onset of diffusive mass transfer mechanisms and fluid influx within fault zones to provide the conditions and suitable environment for the formation of fault rocks that will be weak on long geological timescales. The presence of these rocks within the core of the fault zone are likely to have played a crucial role in the long-lived history or reactivation along the MTL, and as such the findings are likely to be applicable to other long-lived crustal-scale reactivated fault zones across the world.

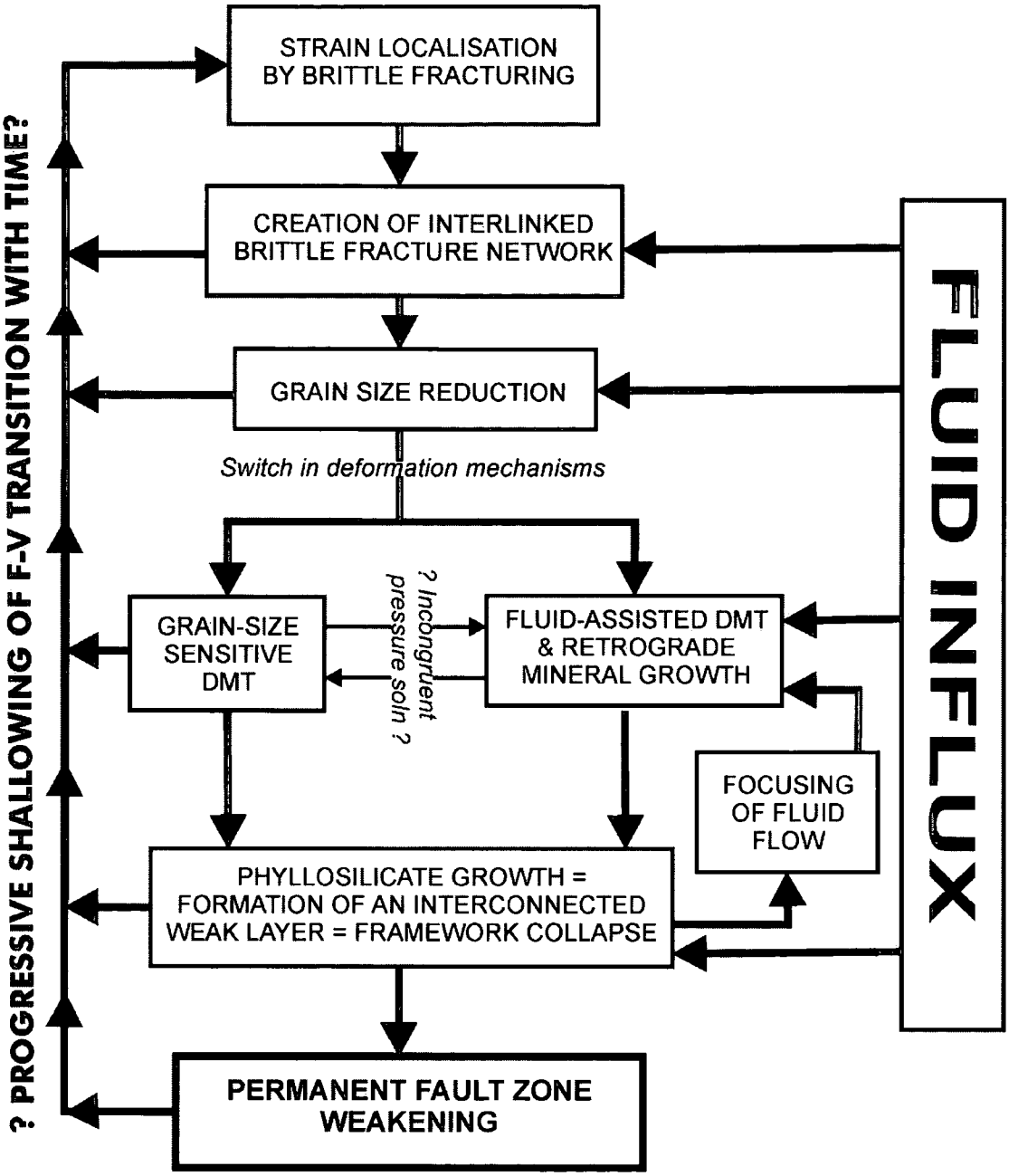

Figure 5.1a. Flow chart showing feedback between processes that lead to fault zone weakening. The sequence of mechanisms may result in a progressive shallowing of the frictional-viscous (F-V) transition over time, see Figure 5.1b.

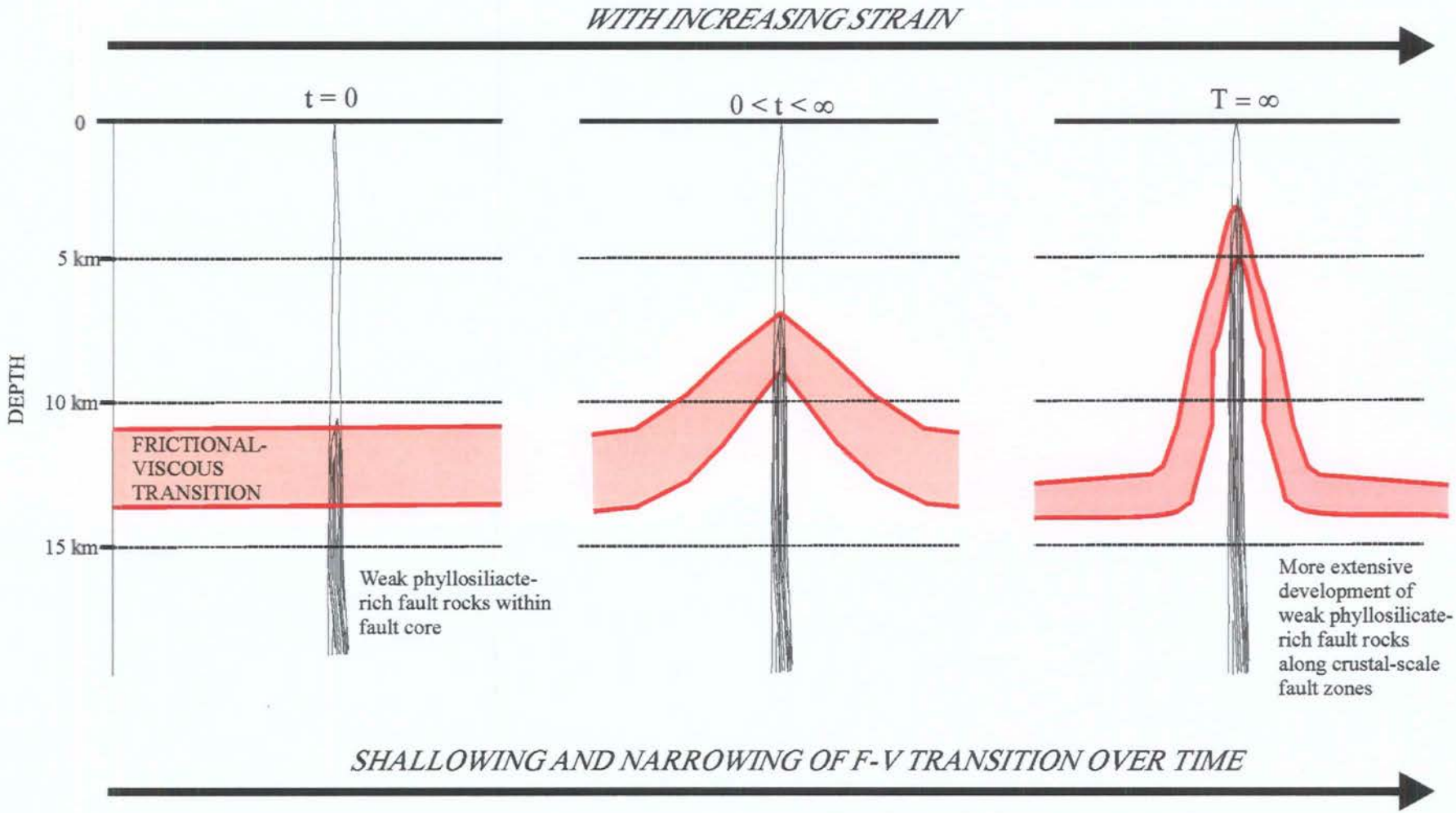

Figure 5.1b schematic shallowing and narrowing of the frictional-viscous (F-V) transition in the vicinity of large crustal-scale fault zone as a consequence of feedback mechanisms in Figure 5.1a (t = time).

5.2. Suggestions for further research.

The models presented in this thesis are based upon direct field, microstructural and geochemical observations, but none the less are theoretical. However, the study of the Median Tectonic Line in SW Japan, to date, has not been approached or thought of in these terms. Therefore, the hypotheses and models we have presented during this thesis hopefully will provide a platform for future work. A few brief ideas for future work are presented below.

The porosity network across MTL fault rocks.

A porosity study similar to that of Géraud et al., (1995) would give a valuable insight into the actual porosity network (cracks, tubes or a mixture of both, see section 3.8.2) existing within fault rocks across the MTL. Porosity and pore size can be estimated by measuring the volume of mercury injected into samples (so-called mercury injection porosimetry). The size, shape and distribution of pores viewed in oriented section cut parallel to the 3 axes of the strain ellipsoid can be observed by SEM. A rough estimate of permeability can be attempted based on the connected porosities and pore throat diameter. If such a study was carried out on the phyllonite from Miyamae, foliated cataclasites from Tsukide and Anko and variably fractured mylonites form Miyamae and Tsukide it could potentially provide valuable information to either support or allow us to modify the model of MTL fault zone porosity and permeability presented in Figure 3.16.

Stable isotope studies.

Oxygen isotope analysis is the most frequently used isotope during investigations of fault/shear zone alteration. By means of oxygen isotopic data the source, temperature and magnitude of the aqueous fluid reservoir can be assessed (Kerrich, 1986). Oxygen isotopic analysis of a selection of samples across the Miyamae and Tsukide transects and Anko will give a further insight into where the fluid in the MTL is coming from. In each study area is the fluid source the same? Does it vary between the damage zone and fault core at Miyamae and Tsukide? Is our theoretical fluid flow model (Fig. 3.17) correct? Have fluids evolved during the history of MTL reactivation and have fluid sources changed over time? An oxygen isotopic study would give a valuable insight into fluid flow and connected permeability of the MTL fault zone on the km-plus scale.

Thermobarometry.

A thermobarometry study of the pressure-temperature conditions during white mica and chlorite growth in the ultramylonite, foliated cataclasite and phyllonite within the fault core at Miyamae would enable us to track the changing conditions and possible depth changes (exhumation?) that occurred during phyllonite formation. If pressure and temperature conditions during the formation of foliated cataclasites at Tsukide and Anko were also determined it would allow us to present a more quantitative depth comparison for the formation of phyllonite and foliated than that of the model presented here (Fig. 4.11).

Appendix A: Geochemical data

X-ray fluorescence

XRF analysis was carried out at the Department of Geology, University of Leicester. Samples were crushed and powdered in an agate grinding mill. Pressed powder pellets are used to determine trace element concentrations in rocks by XRF. 46 mm diameter powder pellets are produced by mixing approx. 15g of rock sample powder into a small beaker with enough Moviol 88 solution (this is a solution of polyvinyl alcohol in a 1:6 mix of methanol and distilled deionised H_2O) to bind the powder together in small lumps, but not so much that the powder looks wet when thoroughly mixed. This mixture is then placed in the die, the surface smoothed, and then the top of the die and the plunger are replaced. The complete die is placed inside the hydraulic press. The final ram pressure is set to 15 tons.

Fusion beads are the best way of determining major element concentrations in rocks by XRF. Firstly 4-5g of the sample powder is put into a 10 ml glass vial. The rock powder is then dried over night in a drying oven at 110°C to remove low-temperature absorbed volatiles. These powders are then stored in a dessicator. Plastic snap tops are put on the vials once they have cooled to room temperature to avoid sample loss and cross contamination. The next step is to determine the weight loss during ignition, performed in fused Al_2O_3 (ALSINT) ceramic crucibles. The weight of the crucible (W1) and the weight of the crucible plus sample before (W2) and after ignition (W3) are recorded in order to determine the weight loss. The ignitions are performed in a furnace at 950°C for 1-1.5 hours. After ignition the samples are allowed to cool to room temperature in a dessicator before reweighing. After reweighing the samples are transferred to clean 10 ml glass vials with plastic snap

tops for storage prior to preparing fusion beads. The percentage weight loss (LOI) can then be determined using the following simple formula:

$$LOI = 100*(W2 - W3)/(W2 - W1)$$

On starting to make a batch of fusion beads a flux weight loss determination is made. Approx. 2-3g of cool, dried flux is weighed into a Pt/5% Au crucible and placed on the 'Spartan' gas burner for 5 minutes. It is then cooled to room temperature and the crucible and flux are reweighed and the weight loss determined. 5g plus the previously determined weight loss of dried flux is weighed into a Pt/Au crucible. Then 1g of ignited sample is weighed on top of the flux and mixed thoroughly together. The crucible and its contents are placed on the Spartan gas burner. During the fusion process the liquid must be agitated in order to remove particles of powder stuck to the crucible sides and to remove bubbles from the liquid. When the liquid is homogenised and no particles are left the fusion must be brought back up to temperature on the fusion burner. Heat the Pt/Au casting dish on the casting plate burner until it reaches operational temperature. The liquid is then poured into the casting dish, the resulting disc is left to cool for 3-4 minutes until it clearly parts from the casting dish and turned out.

Powder pellets and fusion beads were analysed using a Philips PW 1716 diffractometer with a current/voltage stabilised PW 1729 generator and a PW 1050/25 detector.

ICP-MS

Trace element and REE concentrations were determined using the ICP-MS at the Department of Earth Sciences, University of Durham. Samples were crushed, powdered in an agate grinding mill and dried, then fused to form glass discs. This procedure was designed to eliminate the possibility of accessory phases not dissolving during ICP-MS preparation. The discs were then powdered. After powdering and drying, 0.1g±0.001 of sample were transferred into a clean Teflon vial. 1 ml of Aristar HNO_3 were added to each sample and allowed to react with the sample. 4 ml of Aristar HF were then added to each sample. The vials were placed on a hot plate at 130-150° for 24 hours. The acid mixture refluxes within the vial dissolving the sample. After being allowed to cool, the vials were placed back on the hotplate at 130-150°C, without lids. The acid will evaporate and silica will be removed as SiF_4. The samples are removed from the hot plate prior to the sample oxidising and allowed to cool. Another 1 ml of Aristar HNO_3 was added to each sample and they were evaporated again as before. The process was repeated with a further 1 ml of HNO_3. After cooling, 2.5 ml of Aristar HNO_3 was added to each sample vial and topped up with 10-15 ml of de-ionised water. The vials were returned to the hotplate for 30 minutes at 130-150°C, and allowed to cool. 1.00 ml of internal standard was added to each sample. Each sample was transferred from Teflon vials to 50 ml polypropylene volumetric flasks and made up to 50 ml with de-ionised water. Each sample solution comprises the sample diluted to 50 ml in 3.5% HNO_3 with internal standards at 50 ppb.

Electron micro-probe analysis

Electron micro-probe analysis (EMPA) of selected minerals (chlorite, white mica, feldspar and carbonate) was carried out at the Department of Earth Sciences, University of Leeds, using a Cameca SX-50 microprobe fitted with three wavelength dispersive spectrometers and an Oxford Instruments energy dispersive system. Analysis is carried out on a small selected area of solid samples (carbon coated polished blocks), in which X-rays are excited by a focussed electron beam. The X-ray spectrum contains lines that are characteristic of elements present. By comparing the intensities of these lines with those emitted from standards it is possible to determine the concentrations of the elements. Accuracy ±1% is obtainable and detection limits are typically ~ 50 ppm.

XRF major and trace element analysis for Miyamae transect fault rocks																				
Pellet	L40231	L40232	L40233	L40234	L40235	L40236	L40237	L40239	L40238	L40240	L40241	L40243	L40242	L40244	L40245	L40246	L40247	L40248	L40249
Bead	LF19995	LF19996	LF19997	LF19998	LF19999	LF20000	LF20001	LF20003	LF20002	LF20004	LF20005	LF20007	LF20006	LF20008	LF20009	LF20010	LF20011	LF20012	LF20013
Sample	**MIS-17**	**MIS-15**	**MIS-14b**	**MIS-13**	**MIS-11**	**MIS-10**	**MI-29**	**MIS-05**	**MI-SM19**	**MI-SM14**	**MI-SM10**	**MI-SM09**	**MI-SM07**	**MI-SM05**	**MI-SM03**	**MI-09**	**MI-10**	**MI-GOUGE5**	**MI-GOUGE1**
SiO2	74.57	69.31	72.50	76.16	71.38	71.16	73.31	64.85	60.95	56.03	57.28	65.84	61.10	65.05	71.68	58.98	49.56	56.26	62.11
TiO2	0.12	0.42	0.27	0.13	0.30	0.35	0.23	0.57	0.74	0.61	0.61	0.67	0.68	0.50	0.28	1.48	0.59	0.56	0.63
Al2O3	12.71	14.74	13.67	13.04	14.26	14.53	11.91	14.02	14.31	13.52	14.57	14.77	14.69	13.98	12.85	13.75	10.69	14.03	14.43
Fe2O3	1.15	3.58	2.58	1.49	2.84	2.91	1.45	4.40	5.65	6.32	6.37	3.58	5.85	4.55	2.65	8.92	6.53	5.25	6.64
MnO	0.03	0.08	0.06	0.03	0.05	0.07	0.04	0.09	0.12	0.13	0.11	0.06	0.09	0.07	0.06	0.15	0.14	0.20	0.80
MgO	0.05	0.87	0.34	0.13	0.43	0.46	0.17	1.62	1.70	4.92	5.19	1.43	2.20	0.90	1.03	7.72	2.55	3.71	2.19
CaO	2.29	0.85	1.58	0.35	1.81	1.99	2.84	4.04	4.68	5.90	3.99	2.36	3.52	3.49	1.77	0.79	12.46	3.22	0.39
Na2O	3.36	4.70	3.97	3.87	4.09	4.01	5.16	3.86	3.32	2.20	2.40	4.18	3.22	4.36	3.28	0.12	1.64	2.05	1.54
K2O	4.77	3.46	3.77	4.32	3.51	3.09	1.36	1.99	2.22	1.88	2.26	2.46	2.29	2.05	2.27	0.49	1.04	2.87	2.60
LOI	0.70	1.25	0.89	0.79	1.01	1.42	3.09	4.21	5.84	7.71	6.54	3.59	5.25	4.33	3.24	7.00	13.85	10.61	8.18
Total	99.81	99.39	99.74	100.35	99.83	100.14	99.64	99.82	99.75	99.35	99.55	99.24	99.05	99.55	99.15	99.52	99.20	99.36	99.71
Sample	**MIS-17**	**MIS-15**	**MIS-14b**	**MIS-13**	**MIS-11**	**MIS-10**	**MI-29**	**MIS-05**	**MI-SM19**	**MI-SM14**	**MI-SM10**	**MI-SM09**	**MI-SM07**	**MI-SM05**	**MI-SM03**	**MI-09**	**MI-10**	**MI-GOUGE5**	**MI-GOUGE1**
Cu	3.04	0.34	1.06	0.55	-0.61	4.37	23.24	1.56	1.34	1.05	0.89	26.65	-0.48	20.84	-2.33	134.06	38.01	32	35.22
Ga	12.72	17.5	16.5	15.01	16.89	16.91	15.3	16.67	18.37	16.76	18.07	18.09	18.86	17.3	15.88	23.83	15.09	20.72	20.79
Nb	6.1	11.4	10.29	11.55	10.09	10.8	11.46	9.85	9.53	8.96	8.63	12.45	10.67	10.91	11.42	10.08	8.92	12	11.05
Ni	-0.35	0	-1.17	-0.88	-1.03	-0.29	-0.23	1.6	1.38	66.93	84.45	0.1	8.54	-0.49	9.5	764.58	287.98	28.57	40.11
Pb	28.23	17.04	25.6	29.69	22.38	21.27	22.96	11.07	12.42	6.53	5.25	7.94	12.09	9.63	4.3	6.26	12.5	15.41	17.04
Rb	134.89	134.07	111.36	144.11	94.29	81.29	51.41	86.78	90.63	84.63	115.31	104.44	98.32	86.51	102.83	40.86	51.89	125.93	125.07
Sr	111.14	334.68	272.71	174.91	306.5	339.13	284.08	259.54	239.05	315.08	204.58	206.99	243.96	299.75	157.53	97.14	432.56	262.75	109.19
Th	19.51	12.08	9.77	12.72	10.17	10.9	10.6	13.16	11.68	13.25	10.74	11.37	10.01	12.02	12.1	11.87	8.11	15.62	12.64
U	3.38	3.69	1.97	2.78	1.88	1.01	0.88	3.43	3.26	1.38	1.64	2.45	1.89	1.47	1.77	0.16	0.94	2.09	1.29
Y	9.5	22.99	23.58	18.55	25.88	21.62	36	27.15	28.19	25.21	22.44	32.86	27.28	30.31	30.1	47.97	18.45	23.73	20.85
Zn	16.92	56.48	49.83	25.4	47.45	61.66	39.44	63.81	64.91	127.08	92.13	139.58	86.09	53.92	17.75	107.7	76.26	84.34	84.02
Zr	67.64	118.93	159.87	108.88	163.54	198.33	214.47	137.9	129.56	143.97	138.84	189.58	173.14	189.83	210.01	138.58	103.25	143.79	122.3
Sample	**MIS-17**	**MIS-15**	**MIS-14b**	**MIS-13**	**MIS-11**	**MIS-10**	**MI-29**	**MIS-05**	**MI-SM19**	**MI-SM14**	**MI-SM10**	**MI-SM09**	**MI-SM07**	**MI-SM05**	**MI-SM03**				
DENSITY	2.78	2.58	2.37	2.8	2.83	2.85	2.41	2.77	2.68	2.53	2.54	2.6	2.94	2.87	2.89				

XRF major and trace element analysis for Tsukide transect fault rocks

Pellet	L40250	L40251	L40252	L40253	L40254	L40255	L40256	L40257	L40265	L40266	L40267	L40268	L40269	L40270	L40273	L40271	L40272	L40274	L40275	L40276
Bead	LF20014	LF20015	LF20016	LF20017	LF20018	LF20019	LF20020	LF20021	LF20022	LF20023	LF20024	LF20025	LF20026	LF20027	LF20030	LF20028	LF20029	LF20031	LF20032	LF20033
Sample	**TKR-09**	**TKR-12**	**TKR-07**	**TKR-23**	**TKR-26**	**TKR-16**	**TKR-18**	**TKS-10**	**TK-09**	**TKS-03**	**TKS-02**	**TKS-01**	**TKS-08**	**TK-06**	**TK-35**	**TK-38bi**	**TK-38bii**	**TK-GOUGE6**	**TK-GOUGE10**	**TKSS-02**
SiO2	72.35	73.46	70.58	77.65	73.54	71.49	74.22	62.23	66.45	66.59	57.08	62.95	75.22	58.97	70.39	49.33	60.36	64.92	67.79	70.03
TiO2	0.24	0.31	0.27	0.05	0.24	0.28	0.20	0.67	0.44	0.44	0.84	0.62	0.10	0.68	0.50	0.35	0.86	0.62	0.56	0.41
Al2O3	13.93	13.67	13.72	11.92	13.69	14.20	13.12	16.56	15.48	14.82	15.40	15.80	12.17	15.46	12.55	10.00	14.62	10.65	14.59	12.99
Fe2O3	2.43	2.17	2.76	0.58	2.41	2.73	2.11	4.42	3.23	3.11	6.04	4.33	0.89	5.25	3.60	6.80	4.23	4.70	4.39	2.37
MnO	0.039	0.045	0.054	0.013	0.052	0.056	0.056	0.064	0.057	0.060	0.116	0.068	0.014	0.091	0.091	0.136	0.059	0.124	0.168	0.054
MgO	0.30	0.44	0.43	-0.02	0.35	0.44	0.22	1.84	1.27	1.50	2.98	1.85	0.25	2.21	0.65	5.17	3.97	3.25	1.49	0.64
CaO	1.51	1.30	2.13	0.62	1.18	1.35	0.67	3.04	3.40	3.43	4.97	2.94	1.99	4.69	2.18	8.34	2.37	2.42	0.86	2.54
Na2O	4.62	4.07	5.01	4.21	4.71	4.88	4.31	3.92	4.98	5.03	3.03	4.46	5.11	4.11	2.34	1.99	1.04	0.31	2.37	4.19
K2O	2.659	3.806	2.888	3.936	2.633	2.779	3.620	2.313	1.145	1.175	2.044	1.827	1.033	1.637	2.601	2.013	1.966	1.246	2.796	2.888
LOI	1.19	1.01	1.14	0.49	1.10	1.11	1.02	4.11	2.98	3.78	6.53	4.23	1.92	5.80	4.32	11.88	9.69	11.55	5.44	2.65
Total	99.35	100.37	99.05	99.45	99.96	99.39	99.60	99.33	99.56	100.04	99.23	99.20	98.72	99.05	99.35	99.34	99.44	99.89	100.57	99.25

Sample	**TKR-09**	**TKR-12**	**TKR-07**	**TKR-23**	**TKR-26**	**TKR-16**	**TKR-18**	**TKS-10**	**TK-09**	**TKS-03**	**TKS-02**	**TKS-01**	**TKS-08**	**TK-06**	**TK-35**	**TK-38bi**	**TK-38bii**	**TK-GOUGE6**	**TK-GOUGE10**	**TKSS-02**
Cu	10.0	0.9	4.6	5.9	0.6	1.5	2.7	-0.7	-3.1	-0.4	3.8	1.3	-2.7	-0.8	15.7	11.9	44.9	30.6	28.4	5.0
Ga	15.7	15.5	15.8	14.8	15.8	17.6	16.6	21.8	17.2	15.7	19.5	17.9	14.0	19.0	17.5	16.4	19.0	16.2	20.1	16.1
Nb	8.5	11.9	8.7	9.0	8.2	9.4	12.9	8.1	8.4	6.7	9.4	8.0	8.0	9.7	11.9	9.9	11.0	8.9	12.1	9.9
Ni	-1.1	0.3	-0.5	0.4	-1.2	-1.1	-0.1	6.7	3.2	4.8	14.7	5.0	-0.9	14.7	15.0	19.6	331.5	297.9	23.8	5.6
Pb	19.4	29.8	18.4	24.9	19.9	19.9	20.7	4.3	10.1	11.8	13.7	13.8	32.3	15.9	79.7	14.4	19.2	12.6	17.6	14.3
Rb	75.7	121.6	81.6	117.5	71.1	74.3	140.6	74.2	36.5	39.0	76.4	58.8	33.1	63.8	107.1	109.6	164.5	47.0	129.1	108.3
Sr	334.7	230.1	275.9	127.9	330.3	312.6	165.3	276.3	568.7	423.3	293.0	413.2	344.5	408.5	121.5	371.5	239.2	522.7	147.3	211.3
Th	9.0	17.7	9.4	22.3	7.8	7.5	16.0	3.0	3.9	5.8	4.9	6.4	6.7	7.3	13.4	12.5	10.9	10.0	14.9	12.5
U	0.4	4.5	1.8	9.7	1.4	1.5	3.0	0.1	-0.5	0.8	1.6	0.2	0.2	1.8	2.1	1.9	1.4	1.7	1.9	2.3
Y	16.8	16.9	19.9	41.6	20.4	20.0	34.7	11.3	9.5	11.3	16.6	12.3	8.5	19.7	21.6	26.1	24.7	20.4	22.4	23.9
Zn	40.8	39.3	51.5	20.0	48.2	51.5	38.2	74.3	65.3	61.9	99.5	66.4	34.0	82.3	99.9	59.0	95.7	78.9	82.1	44.6
Zr	143.3	123.4	135.0	57.0	114.6	137.0	119.2	122.7	125.4	92.0	147.9	117.9	78.9	169.1	127.8	136.3	146.2	114.0	152.2	179.4

	TKR-09	**TKR-12**	**TKR-07**	**TKR-23**	**TKR-26**	**TKR-16**	**TKR-18**	**TKS-10**	**TK-09**	**TKS-03**	**TKS-02**	**TKS-01**	**TKS-08**	**TK-06**
DENSITY	3.0	1.6	2.4	2.3	2.8	2.8	2.3	1.8	3.2	3.0	2.8	2.8	2.4	2.8

XRF major and trace element analysis for Ryoke and Sambagawa protoliths

	RYOKE PROTOLITH				SAMBAGAWA PROTOLITH	
Sample	MIS-19	MIS-18	RYOKE AVERAGE	Sample	TKR-32	
SiO2	56.51	57.01	56.76	SiO2	69.71	
TiO2	0.82	0.80	0.81	TiO2	0.52	
Al2O3	17.45	17.19	17.32	Al2O3	13.97	
Fe2O3	7.47	7.10	7.28	Fe2O3	3.06	
MnO	0.142	0.124	0.13	MnO	0.06	
MgO	3.21	2.87	3.04	MgO	1.15	
CaO	6.64	6.96	6.80	CaO	0.69	
Na2O	3.36	3.59	3.48	Na2O	3.15	
K2O	1.737	1.331	1.53	K2O	2.98	
P2O5	0.153	0.167	0.16	P2O5	0.07	
SO3	0.060	0.032	0.05	SO3	0.19	
LOI	1.62	1.60	1.61	LOI	3.78	
Total	99.17	98.77	97.36	Total	95.53	

Sample	MIS-19	MIS-18	RYOKE AVERAGE	Sample	TKR-32	
Cu	35.4	5.8	20.6	Cu	13.3	
Ga	20.2	19.5	19.8	Ga	16.8	
Nb	10.2	8.9	9.5	Nb	11.0	
Ni	6.0	5.1	5.5	Ni	10.2	
Pb	9.3	9.6	9.5	Pb	18.4	
Rb	80.0	53.9	66.9	Rb	124.5	
Sr	376.6	389.5	383.0	Sr	104.6	
Th	6.5	8.1	7.3	Th	8.3	
U	2.9	1.4	2.2	U	2.4	
Y	39.5	26.2	32.9	Y	15.3	
Zn	92.4	88.8	90.6	Zn	52.4	
Zr	105.7	110.4	108.1	Zr	157.6	

	MIS-19	MIS-18	RYOKE AVERAGE		TKR-32	
DENSITY	2.75	2.87	2.81	DENSITY	2.775	

ICP-MS trace element analysis of a representive suite of fault rocks from the Miyamae transect, including Ryoke protolith MIS-18

Run Order		12	13	16	17	18	19	20	21	22	23	26	NORMALISATION FACTOR		
PPM		MIS-18	MIS-15	MIS-13	MIS-05	M1-SM-19	M1-SM-14	M1-SM-09	M1-SM-05	M1-SM-03	M1-10	M1-09	Boynton (1984): average chondritic value	Sun & McDonough (1989): C1 chondrite	Thompson (1982)
Sc	45	20.27	7.29	3.14	11.39	14.82	18.19	14.09	10.56	11.23	14.22	23.96			
Ti	49	0.78	0.42	0.12	0.49	0.69	0.58	0.61	0.47	0.26	0.60	1.22		445.00	620.00
V	51	125.40	31.45	5.02	59.66	77.69	91.15	43.61	31.61	17.70	98.94	234.58			
Cr	52	23.45	9.58	5.72	13.23	5.61	223.15	8.18	2.42	39.48	437.03	1262.69			
Cr	53	22.42	8.93	4.98	12.07	4.95	224.72	6.86	1.59	39.37	440.77	1284.09			
Mn	55	0.13	0.08	0.04	0.09	0.13	0.13	0.06	0.08	0.07	0.14	0.13			
Co	59	33.19	76.49	31.48	43.90	21.79	24.44	24.27	16.19	16.07	34.16	71.60			
Ni	60	7.77	1.92	0.70	3.83	2.31	68.37	2.78	3.04	11.14	303.59	661.68			
Cu	63	6.89	1.90	0.64	2.13	1.91	1.08	41.48	26.34	0.41	36.58	105.53			
Zn	66	81.70	48.24	19.80	52.15	63.40	105.76	110.44	50.45	16.03	61.42	96.76			
Ga	71	18.18	16.47	13.94	15.60	17.29	14.75	17.46	16.32	14.91	12.82	18.90			
Rb	85	49.80	125.13	135.11	82.03	86.71	78.98	98.35	80.79	99.20	47.58	33.00		2.32	0.35
Sr	88	363.44	307.72	166.54	249.83	229.18	304.93	195.95	284.41	152.73	409.46	75.91		7.26	11.80
Y	89	24.42	21.04	14.27	23.87	24.00	21.39	28.70	24.86	24.73	15.76	32.90		1.57	
Zr	90	13.29	25.86	40.11	31.60	46.81	59.54	68.51	47.05	64.38	76.12	91.31		3.87	6.84
Nb	93	8.26	11.27	9.32	9.00	8.47	8.18	11.04	9.92	10.06	7.89	6.87		0.25	0.35
Rh	103														
Cs	133	1.21	1.71	2.21	3.71	3.25	2.65	3.22	3.23	2.82	6.80	6.18		0.19	
Ba	137	333.97	483.79	501.44	489.68	308.24	327.21	506.93	588.61	414.78	273.63	106.94		2.41	6.90
La	139	21.52	27.19	14.22	24.30	23.09	25.20	27.69	28.57	33.00	17.23	23.72	0.31	0.24	0.33
Ce	140	44.85	53.77	37.69	48.02	46.59	52.48	55.58	57.42	66.15	35.40	25.42	0.81	0.61	0.87
Pr	141	5.59	6.09	3.57	5.69	5.68	6.54	6.67	6.80	7.92	4.25	5.87	0.12		
Nd	143	22.17	21.82	12.91	21.14	21.82	25.00	25.61	25.33	30.00	16.48	23.74	0.60	0.47	0.63
Sm	147+149 average	4.54	4.07	2.79	4.12	4.28	4.73	5.02	4.76	5.60	3.30	5.04	0.20	0.15	0.20
Eu	151	1.15	0.74	0.44	1.17	1.13	0.90	1.08	1.06	0.86	0.85	1.44	0.07		
Gd	157	4.59	3.80	2.66	4.09	4.25	4.37	5.06	4.69	5.14	3.23	5.70	0.26		
Tb	159	0.71	0.58	0.44	0.66	0.67	0.65	0.80	0.72	0.77	0.48	0.88	0.05		
Dy	161+163 average	4.05	3.34	2.56	3.79	3.97	3.69	4.73	4.20	4.42	2.77	5.17	0.32		
Ho	165	0.84	0.67	0.52	0.78	0.80	0.74	0.97	0.85	0.88	0.56	1.02	0.07		
Er	166+167 average	2.23	1.90	1.51	2.18	2.25	2.03	2.69	2.29	2.34	1.46	2.62	0.21		
Tm	169	0.35	0.32	0.28	0.36	0.36	0.32	0.44	0.38	0.37	0.23	0.39	0.03		0.034
Yb	172+174 average	2.19	2.18	1.85	2.31	2.29	2.02	2.80	2.27	2.25	1.42	2.29	0.21		0.22
Lu	175	0.35	0.35	0.31	0.37	0.37	0.33	0.44	0.36	0.35	0.23	0.35	0.03		
Hf	177+178 average	0.66	1.01	1.74	1.18	1.55	1.90	2.13	1.43	1.83	2.24	2.77			0.2
Ta	181	0.94	3.76	1.88	1.48	1.01	0.61	1.03	0.81	0.99	0.63	0.58		0.01	0.02
Re	187														
tot Pb	208	10.08	16.04	27.79	10.57	11.41	4.28	6.26	11.01	4.82	10.59	5.18		2.47	
Th	232	6.24	15.59	11.21	10.96	8.51	10.04	9.48	9.06	9.21	5.53	3.06		0.03	0.04
U	238	1.43	4.01	3.13	2.46	1.69	1.40	2.07	1.42	1.49	1.22	0.70		0.01	

ICP-MS trace element analysis of a representive suite of fault rocks from the Tsukide transect

									NORMALISATION FACTOR		
Run Order		27	37	38	39	40	41	42	Boynton (1984):	Sun & McDonough (1989):	Thompson (1982)
PPM		TKR-09	TKR-23	TKS-10	TK-09	TKS-02	TK-35 X	TK-38bi X	average chondritic value	C1 chondrite	
Sc	45	4.05	1.43	9.09	4.99	15.06	8.69	7.38			
Ti	49	0.22	0.04	0.65	0.39	0.78	0.45	0.35		445.00	620.00
V	51	8.78	2.40	47.05	22.52	71.31	55.92	45.33			
Cr	52	11.67	4.20	28.61	14.81	53.96	33.56	25.04			
Cr	53	10.72	3.44	27.03	13.53	53.19	32.58	23.92			
Mn	55	0.04	0.02	0.07	0.06	0.11	0.09	0.14			
Co	59	33.25	40.24	19.82	24.85	21.09	23.03	9.51			
Ni	60	1.20	0.46	8.85	4.81	16.90	18.11	25.07			
Cu	63	12.65	8.91	1.36	1.29	5.39	22.60	12.56			
Zn	66	36.35	14.81	62.52	54.79	83.61	81.09	49.68			
Ga	71	15.55	13.64	19.71	15.91	17.41	15.61	12.00			
Rb	85	71.81	115.31	67.12	34.87	66.92	100.92	91.88		2.32	0.35
Sr	88	319.52	128.13	263.70	543.39	268.17	118.46	353.68		7.26	11.80
Y	89	14.07	41.24	8.37	7.19	14.69	18.49	22.29		1.57	
Zr	90	12.66	37.04	24.91	33.73	58.96	68.85	80.59		3.87	6.84
Nb	93	6.77	9.80	7.34	7.20	8.73	11.26	7.63		0.25	0.35
Rh	103										
Cs	133	1.72	1.91	3.53	2.37	4.62	3.88	12.13		0.19	
Ba	137	870.41	240.14	563.78	540.96	440.42	291.80	221.34		2.41	6.90
La	139	38.18	5.55	10.89	16.08	16.27	23.60	20.53	0.31	0.24	0.33
Ce	140	68.88	13.07	22.02	29.90	34.74	50.61	43.21	0.81	0.61	0.87
Pr	141	7.72	2.03	2.77	3.47	4.40	5.92	5.13	0.12		
Nd	143	26.29	9.32	11.10	12.66	17.89	22.12	19.24	0.60	0.47	0.63
Sm	147+149 average	4.06	3.70	2.16	2.10	3.48	4.29	3.80	0.20	0.15	0.20
Eu	151	0.94	0.30	0.66	0.82	1.03	0.80	0.78	0.07		
Gd	157	3.37	4.99	2.01	1.86	3.33	3.96	3.83	0.26		
Tb	159	0.47	1.04	0.28	0.25	0.49	0.60	0.61	0.05		
Dy	161+163 average	2.45	6.68	1.55	1.36	2.70	3.27	3.61	0.32		
Ho	165	0.47	1.41	0.30	0.25	0.52	0.64	0.75	0.07		
Er	166+167 average	1.23	4.04	0.79	0.62	1.35	1.74	2.07	0.21		
Tm	169	0.20	0.66	0.12	0.09	0.21	0.27	0.33	0.03		0.034
Yb	172+174 average	1.17	4.14	0.75	0.57	1.30	1.68	2.03	0.21		0.22
Lu	175	0.18	0.65	0.12	0.09	0.21	0.27	0.33	0.03		
Hf	177+178 average	0.44	2.33	0.83	1.01	1.75	2.11	2.51			0.2
Ta	181	1.47	3.03	0.68	0.80	0.63	1.44	0.72		0.01	0.02
Re	187										
tot Pb	208	17.13	23.19	4.13	10.24	13.16	72.16	13.87		2.47	
Th	232	9.10	21.53	1.83	2.06	3.30	9.82	7.42		0.03	0.04
U	238	0.91	9.42	0.53	0.32	0.58	2.62	1.56		0.01	

ICP-MS REE analysis of a representative suite of fault rocks from the Miyamae transect, including Ryoke protolith MIS-18

Run Order		12	13	16	17	18	19	20	21	22	23	26	NORMALISATION FACTOR
PPM		MIS-18	MIS-15	MIS-13	MIS-05	M1-SM-19	M1-SM-14	M1-SM-09	M1-SM-05	M1-SM-03	M1-10	M1-09	Boynton (1984): average chondritic value
La	139	21.52	27.19	14.22	24.30	23.09	25.20	27.69	28.57	33.00	17.23	23.72	0.31
Ce	140	44.85	53.77	37.69	48.02	46.59	52.48	55.58	57.42	66.15	35.40	25.42	0.81
Pr	141	5.59	6.09	3.57	5.69	5.68	6.54	6.67	6.80	7.92	4.25	5.87	0.12
Nd	143	22.17	21.82	12.91	21.14	21.82	25.00	25.61	25.33	30.00	16.48	23.74	0.60
Pm		13.351	12.94	7.847	12.628	13.0475	14.8605	15.311	15.0445	17.7975	9.8905	14.389	
Sm	147+149 average	4.54	4.07	2.79	4.12	4.28	4.73	5.02	4.76	5.60	3.30	5.04	0.20
Eu	151	1.15	0.74	0.44	1.17	1.13	0.90	1.08	1.06	0.86	0.85	1.44	0.07
Gd	157	4.59	3.80	2.66	4.09	4.25	4.37	5.06	4.69	5.14	3.23	5.70	0.26
Tb	159	0.71	0.58	0.44	0.66	0.67	0.65	0.80	0.72	0.77	0.48	0.88	0.05
Dy	161+163 average	4.05	3.34	2.56	3.79	3.97	3.69	4.73	4.20	4.42	2.77	5.17	0.32
Ho	165	0.84	0.67	0.52	0.78	0.80	0.74	0.97	0.85	0.88	0.56	1.02	0.07
Er	166+167 average	2.23	1.90	1.51	2.18	2.25	2.03	2.69	2.29	2.34	1.46	2.62	0.21
Tm	169	0.35	0.32	0.28	0.36	0.36	0.32	0.44	0.38	0.37	0.23	0.39	0.03
Yb	172+174 average	2.19	2.18	1.85	2.31	2.29	2.02	2.80	2.27	2.25	1.42	2.29	0.21
Lu	175	0.35	0.35	0.31	0.37	0.37	0.33	0.44	0.36	0.35	0.23	0.35	0.03

ICP-MS REE analysis of a representive suite of fault rocks from the Tsukide transect																
Run Order		**12**	**27**	**37**	**38**	**39**	**40**	**41**	**42**		**NORMALISATION FACTOR**					
PPM		**MIS-18**	**TKR-09**	**TKR-23**	**TKS-10**	**TK-09**	**TKS-02**	**TK-35**	**TK-38bi**		**Boynton (1984): average chondritic value**					
La	139	21.52	38.18	5.55	10.89	16.08	16.27	23.60	20.53		0.31					
Ce	140	44.85	68.88	13.07	22.02	29.90	34.74	50.61	43.21		0.81					
Pr	141	5.59	7.72	2.03	2.77	3.47	4.40	5.92	5.13		0.12					
Nd	143	22.17	26.29	9.32	11.10	12.66	17.89	22.12	19.24		0.60					
Pm		13.351	15.175	6.5075	6.6295	7.379	10.686	13.205	11.516							
Sm	147+149 average	4.54	4.06	3.70	2.16	2.10	3.48	4.29	3.80		0.20					
Eu	151	1.15	0.94	0.30	0.66	0.82	1.03	0.80	0.78		0.07					
Gd	157	4.59	3.37	4.99	2.01	1.86	3.33	3.96	3.83		0.26					
Tb	159	0.71	0.47	1.04	0.28	0.25	0.49	0.60	0.61		0.05					
Dy	161+163 average	4.05	2.45	6.68	1.55	1.36	2.70	3.27	3.61		0.32					
Ho	165	0.84	0.47	1.41	0.30	0.25	0.52	0.64	0.75		0.07					
Er	166+167 average	2.23	1.23	4.04	0.79	0.62	1.35	1.74	2.07		0.21					
Tm	169	0.35	0.20	0.66	0.12	0.09	0.21	0.27	0.33		0.03					
Yb	172+174 average	2.19	1.17	4.14	0.75	0.57	1.30	1.68	2.03		0.21					
Lu	175	0.35	0.18	0.65	0.12	0.09	0.21	0.27	0.33		0.03					

Electron Microprobe Analysis of chlorite												
	Oxide wt%, O by stoichiometry											
	SiO2	TiO2	Al2O3	FeO	MnO	MgO	CaO	Na2O	K2O	H2O	total	
MIS 06: chlorite/1	24.072	0.145	20.743	36.504	0.537	6.528	0.082	0.022	0.026	10.782	99.441	
MIS 06: chlorite/2	24.078	0.098	20.858	36.934	0.521	5.809	0.165	0.024	0.029	10.740	99.256	
MIS 06: chlorite/3	27.040	0.120	21.544	34.491	0.445	7.229	0.044	0.133	0.307	11.369	102.722	
MIS 06: chlorite/3 rpt	24.669	0.169	20.950	34.772	0.408	7.200	0.038	0.084	0.198	10.882	99.370	
MIS 06: chlorite/4	25.105	0.072	20.900	35.665	0.392	5.666	0.110	0.039	0.173	10.805	98.927	
MIS 06: chlorite/5	24.463	0.095	20.704	36.211	0.636	6.092	0.191	0.045	0.000	10.778	99.215	
MIS 06: chlorite/6	23.910	0.113	21.951	39.019	0.361	3.601	0.076	0.030	0.000	10.726	99.787	
MIS 06: chlorite/6a	24.026	0.120	20.988	38.288	0.411	4.284	0.065	0.036	0.002	10.639	98.859	
MIS 06: chlorite/7	19.070	0.100	17.262	31.979	0.486	3.493	12.504	0.020	0.000	9.816	94.730	
MIS 06: chlorite/8	24.061	0.098	21.590	38.779	0.362	3.954	0.074	0.012	0.000	10.721	99.651	
MIS 06: chlorite/9	24.471	0.159	20.806	39.155	0.448	3.995	0.211	0.038	0.004	10.734	100.021	
MIS 06: chlorite/10	24.978	0.109	20.588	36.076	0.543	6.276	0.087	0.061	0.036	10.851	99.605	
MIS 06: chlorite/11	24.386	0.068	20.492	39.035	0.410	3.836	0.060	0.026	0.137	10.621	99.071	
MIS 06: chlorite/12	24.803	0.074	20.830	35.902	0.598	6.126	0.102	0.028	0.049	10.825	99.337	
MIS 06: chlorite/13	24.205	0.139	20.833	34.957	0.496	7.727	0.033	0.023	0.000	10.851	99.264	
MIS 06: chlorite/14	26.627	0.250	21.656	32.046	0.514	6.810	0.043	0.029	1.508	11.165	100.648	
MIS 06: chlorite/15	28.238	0.280	21.826	28.577	0.441	6.754	0.058	0.022	1.837	11.228	99.261	
MIS 06: chlorite/16	24.466	0.124	20.730	35.447	0.664	6.283	0.066	0.028	0.000	10.745	98.553	
MIS 06: chlorite/16a	24.378	0.122	20.820	35.067	0.753	6.385	0.045	0.027	0.010	10.734	98.341	
MIS 06: chlorite/17	24.202	0.113	21.492	38.501	0.340	4.333	0.223	0.008	0.034	10.775	100.021	
MI-SM05: chlorite/1	24.532	0.026	20.774	34.541	0.637	7.430	0.000	0.045	0.038	10.827	98.850	
MI-SM05: chlorite/2	24.478	0.053	20.419	35.320	0.772	6.828	0.115	0.061	0.022	10.768	98.836	
MI-SM05: chlorite/3	23.986	0.073	21.133	34.702	0.451	7.074	0.017	0.041	0.031	10.748	98.256	
MI-SM05: chlorite/4	24.103	0.113	21.129	35.739	0.423	6.583	0.016	0.051	0.035	10.783	98.975	
MI-SM05: chlorite/5	28.042	0.133	19.738	31.901	0.300	6.610	0.058	0.142	0.172	10.988	98.084	
MI-SM05: chlorite/6	24.006	0.134	21.064	33.204	0.628	7.763	0.330	0.037	0.028	10.770	97.964	
MI-SM05: chlorite/7	24.495	0.100	20.627	33.995	0.808	7.100	0.029	0.027	0.030	10.740	97.951	
MI-SM05: chlorite/8	24.381	0.060	20.558	35.725	0.270	6.245	0.088	0.043	0.039	10.688	98.097	
MI-SM05: chlorite/9	24.619	0.045	20.955	34.360	0.430	7.022	0.001	0.066	0.034	10.794	98.326	
MI-SM05: chlorite/9a	24.701	0.037	20.807	34.263	0.621	7.057	0.062	0.039	0.036	10.799	98.422	
MI-SM05: chlorite/9b	24.422	0.074	21.016	34.067	0.326	7.544	0.017	0.045	0.029	10.811	98.351	
MI-SM05: chlorite/9c	24.034	0.100	21.338	34.401	0.374	7.870	0.000	0.027	0.035	10.862	99.041	
MI-SM05: chlorite/10	24.380	0.045	20.443	35.674	0.701	6.321	0.010	0.022	0.050	10.697	98.343	
MISM14 -chlorite/1	28.332	0.094	21.417	23.001	0.377	15.770	0.037	0.130	0.312	11.830	101.300	
MISM14 -chlorite/2	27.380	0.057	21.350	23.112	0.434	15.996	0.008	0.013	0.533	11.692	100.575	
MISM14 -chlorite/3	26.988	0.026	20.400	23.132	0.231	16.459	0.062	0.032	0.010	11.501	98.841	
MISM14 -chlorite/4	26.699	0.068	20.500	23.420	0.134	16.633	0.205	0.038	0.024	11.522	99.243	
MISM14 -chlorite/5	26.237	0.014	21.179	24.140	0.258	15.962	0.031	0.007	0.085	11.499	99.412	
MISM14 -chlorite/6	26.271	0.144	21.355	24.109	0.428	16.068	0.014	0.018	0.020	11.567	99.994	
MISM14 -chlorite/7	26.435	0.064	21.301	23.344	0.236	16.170	0.008	0.029	0.241	11.534	99.362	
MISM14 -chlorite/8	28.828	0.065	20.157	20.943	0.402	17.175	0.066	0.028	0.555	11.761	99.980	
MISM14 -chlorite/9	27.351	0.086	20.708	22.411	0.231	16.771	0.131	0.029	0.209	11.623	99.550	
MISM14 -chlorite/10	26.770	0.015	20.746	22.737	0.254	17.481	0.021	0.020	0.000	11.613	99.657	
MISM14 -chlorite/11	30.503	0.000	0.060	0.831	0.710	0.530	43.640	0.016	0.112	9.426	85.828	
ANKO15-chlorite/1	10.460	0.067	5.115	41.805	0.589	11.335	0.910	0.068	1.232	7.217	78.798	

Electron Microprobe Analysis of chlorite												
	Cations to 36 O, OH											
	Si	Ti	Al	Fe2	Mn	Mg	Ca	Na	K	OH	total	
MIS 06: chlorite/1	5.355	0.024	5.438	6.791	0.101	2.165	0.020	0.009	0.007	16.000	35.910	
MIS 06: chlorite/2	5.377	0.016	5.490	6.898	0.099	1.934	0.039	0.010	0.008	16.000	35.871	
MIS 06: chlorite/3	5.705	0.019	5.357	6.085	0.080	2.274	0.010	0.054	0.083	16.000	35.666	
MIS 06: chlorite/3 rp	5.437	0.028	5.442	6.409	0.076	2.366	0.009	0.036	0.056	16.000	35.859	
MIS 06: chlorite/4	5.573	0.012	5.468	6.621	0.074	1.875	0.026	0.017	0.049	16.000	35.714	
MIS 06: chlorite/5	5.444	0.016	5.430	6.739	0.120	2.021	0.046	0.019	0.000	16.000	35.835	
MIS 06: chlorite/6	5.347	0.019	5.785	7.297	0.068	1.201	0.018	0.013	0.000	16.000	35.748	
MIS 06: chlorite/6a	5.417	0.020	5.577	7.219	0.078	1.440	0.016	0.016	0.001	16.000	35.783	
MIS 06: chlorite/7	4.660	0.018	4.971	6.535	0.101	1.273	3.274	0.009	0.000	16.000	36.841	
MIS 06: chlorite/8	5.383	0.016	5.692	7.255	0.069	1.319	0.018	0.005	0.000	16.000	35.757	
MIS 06: chlorite/9	5.468	0.027	5.479	7.317	0.085	1.331	0.051	0.016	0.001	16.000	35.775	
MIS 06: chlorite/10	5.521	0.018	5.363	6.668	0.102	2.068	0.021	0.026	0.010	16.000	35.797	
MIS 06: chlorite/11	5.507	0.012	5.454	7.372	0.078	1.292	0.015	0.011	0.039	16.000	35.780	
MIS 06: chlorite/12	5.496	0.012	5.439	6.652	0.112	2.024	0.024	0.012	0.014	16.000	35.786	
MIS 06: chlorite/13	5.350	0.023	5.427	6.462	0.093	2.546	0.008	0.010	0.000	16.000	35.918	
MIS 06: chlorite/14	5.720	0.040	5.483	5.757	0.094	2.181	0.010	0.012	0.413	16.000	35.711	
MIS 06: chlorite/15	6.032	0.045	5.495	5.105	0.080	2.151	0.013	0.009	0.501	16.000	35.431	
MIS 06: chlorite/16	5.461	0.021	5.454	6.617	0.126	2.091	0.016	0.012	0.000	16.000	35.797	
MIS 06: chlorite/16a	5.447	0.021	5.483	6.553	0.143	2.127	0.011	0.012	0.003	16.000	35.798	
MIS 06: chlorite/17	5.388	0.019	5.639	7.167	0.064	1.438	0.053	0.003	0.010	16.000	35.781	
MI-SM05: chlorite/1	5.434	0.004	5.424	6.399	0.120	2.454	0.000	0.019	0.011	16.000	35.865	
MI-SM05: chlorite/2	5.453	0.009	5.360	6.580	0.146	2.268	0.027	0.026	0.006	16.000	35.875	
MI-SM05: chlorite/3	5.353	0.012	5.558	6.476	0.085	2.354	0.004	0.018	0.009	16.000	35.869	
MI-SM05: chlorite/4	5.361	0.019	5.539	6.648	0.080	2.183	0.004	0.022	0.010	16.000	35.866	
MI-SM05: chlorite/5	6.121	0.022	5.078	5.823	0.055	2.151	0.014	0.060	0.048	16.000	35.372	
MI-SM05: chlorite/6	5.346	0.022	5.528	6.184	0.118	2.577	0.079	0.016	0.008	16.000	35.879	
MI-SM05: chlorite/7	5.470	0.017	5.429	6.349	0.153	2.364	0.007	0.012	0.009	16.000	35.809	
MI-SM05: chlorite/8	5.471	0.010	5.437	6.704	0.051	2.089	0.021	0.019	0.011	16.000	35.815	
MI-SM05: chlorite/9	5.471	0.008	5.488	6.385	0.081	2.326	0.000	0.028	0.010	16.000	35.797	
MI-SM05: chlorite/9a	5.486	0.006	5.446	6.364	0.117	2.337	0.015	0.017	0.010	16.000	35.798	
MI-SM05: chlorite/9b	5.418	0.012	5.495	6.321	0.061	2.495	0.004	0.019	0.008	16.000	35.835	
MI-SM05: chlorite/9c	5.307	0.017	5.553	6.352	0.070	2.591	0.000	0.012	0.010	16.000	35.911	
MI-SM05: chlorite/10	5.466	0.008	5.402	6.689	0.133	2.113	0.002	0.010	0.014	16.000	35.837	
MISM14 -chlorite/1	5.744	0.014	5.118	3.900	0.065	4.767	0.008	0.051	0.081	16.000	35.748	
MISM14 -chlorite/2	5.617	0.009	5.162	3.965	0.075	4.892	0.002	0.005	0.140	16.000	35.866	
MISM14 -chlorite/3	5.628	0.004	5.014	4.034	0.041	5.118	0.014	0.013	0.003	16.000	35.869	
MISM14 -chlorite/4	5.558	0.011	5.029	4.077	0.024	5.162	0.046	0.015	0.006	16.000	35.928	
MISM14 -chlorite/5	5.473	0.002	5.207	4.211	0.046	4.964	0.007	0.003	0.023	16.000	35.934	
MISM14 -chlorite/6	5.447	0.022	5.219	4.181	0.075	4.967	0.003	0.007	0.005	16.000	35.927	
MISM14 -chlorite/7	5.497	0.010	5.221	4.060	0.042	5.013	0.002	0.012	0.064	16.000	35.920	
MISM14 -chlorite/8	5.879	0.010	4.845	3.572	0.069	5.222	0.014	0.011	0.144	16.000	35.766	
MISM14 -chlorite/9	5.644	0.013	5.036	3.868	0.040	5.160	0.029	0.012	0.055	16.000	35.858	
MISM14 -chlorite/10	5.529	0.002	5.050	3.927	0.044	5.383	0.005	0.008	0.000	16.000	35.948	
MISM14 -chlorite/11	7.761	0.000	0.018	0.177	0.153	0.201	11.897	0.008	0.036	16.000	36.252	
ANKO15-chlorite/1	3.476	0.017	2.003	11.619	0.166	5.617	0.324	0.044	0.522	16.000	39.788	

Electron Microprobe Analysis of chlorite										
	Cation ratios etc.									
	[1]Mg#	Si[iv]	Al[iv]	Al[vi]	Fe2	Mn	Mg	6-Sum[vi]	Fe2/SumR2+	
MIS 06: chlorite/1	23.90	2.68	1.32	1.41	3.40	0.05	1.09	0.05	0.75	
MIS 06: chlorite/2	21.66	2.70	1.30	1.45	3.46	0.05	0.97	0.07	0.77	
MIS 06: chlorite/3	26.95	2.86	1.14	1.55	3.06	0.04	1.14	0.21	0.72	
MIS 06: chlorite/3 rpt	26.73	2.73	1.27	1.46	3.22	0.04	1.19	0.10	0.72	
MIS 06: chlorite/4	21.88	2.79	1.21	1.54	3.32	0.04	0.94	0.17	0.77	
MIS 06: chlorite/5	22.76	2.73	1.27	1.45	3.38	0.06	1.01	0.09	0.76	
MIS 06: chlorite/6	14.02	2.68	1.32	1.58	3.66	0.03	0.60	0.13	0.85	
MIS 06: chlorite/6a	16.48	2.71	1.29	1.51	3.62	0.04	0.72	0.11	0.83	
MIS 06: chlorite/7	16.09	2.64	1.36	1.46	3.71	0.06	0.72	0.05	0.83	
MIS 06: chlorite/8	15.26	2.70	1.30	1.55	3.63	0.03	0.66	0.12	0.84	
MIS 06: chlorite/9	15.24	2.75	1.25	1.50	3.67	0.04	0.67	0.12	0.84	
MIS 06: chlorite/10	23.40	2.77	1.23	1.46	3.34	0.05	1.04	0.11	0.75	
MIS 06: chlorite/11	14.77	2.76	1.24	1.49	3.69	0.04	0.65	0.13	0.84	
MIS 06: chlorite/12	23.03	2.75	1.25	1.48	3.33	0.06	1.01	0.12	0.76	
MIS 06: chlorite/13	27.98	2.68	1.32	1.40	3.24	0.05	1.28	0.04	0.71	
MIS 06: chlorite/14	27.16	2.89	1.11	1.66	2.91	0.05	1.10	0.28	0.72	
MIS 06: chlorite/15	29.32	3.06	0.94	1.84	2.59	0.04	1.09	0.45	0.70	
MIS 06: chlorite/16	23.67	2.74	1.26	1.47	3.32	0.06	1.05	0.10	0.75	
MIS 06: chlorite/16a	24.11	2.73	1.27	1.48	3.28	0.07	1.07	0.10	0.74	
MIS 06: chlorite/17	16.59	2.70	1.30	1.53	3.60	0.03	0.72	0.12	0.83	
MI-SM05: chlorite/1	27.35	2.72	1.28	1.43	3.20	0.06	1.23	0.08	0.71	
MI-SM05: chlorite/2	25.22	2.73	1.27	1.42	3.30	0.07	1.14	0.08	0.73	
MI-SM05: chlorite/3	26.40	2.68	1.32	1.46	3.24	0.04	1.18	0.07	0.73	
MI-SM05: chlorite/4	24.50	2.69	1.31	1.46	3.33	0.04	1.09	0.07	0.75	
MI-SM05: chlorite/5	26.79	3.07	0.93	1.62	2.92	0.03	1.08	0.35	0.73	
MI-SM05: chlorite/6	29.03	2.69	1.31	1.46	3.11	0.06	1.30	0.07	0.70	
MI-SM05: chlorite/7	26.66	2.74	1.26	1.46	3.18	0.08	1.18	0.10	0.72	
MI-SM05: chlorite/8	23.62	2.74	1.26	1.47	3.36	0.03	1.05	0.10	0.76	
MI-SM05: chlorite/9	26.46	2.74	1.26	1.49	3.20	0.04	1.16	0.11	0.73	
MI-SM05: chlorite/9a	26.50	2.75	1.25	1.47	3.19	0.06	1.17	0.11	0.72	
MI-SM05: chlorite/9b	28.11	2.71	1.29	1.47	3.17	0.03	1.25	0.09	0.71	
MI-SM05: chlorite/9c	28.75	2.66	1.34	1.44	3.18	0.04	1.30	0.05	0.70	
MI-SM05: chlorite/10	23.65	2.74	1.26	1.44	3.35	0.07	1.06	0.09	0.75	
MISM14 -chlorite/1	54.59	2.88	1.12	1.45	1.96	0.03	2.39	0.17	0.45	
MISM14 -chlorite/2	54.77	2.82	1.18	1.41	1.99	0.04	2.45	0.11	0.44	
MISM14 -chlorite/3	55.67	2.82	1.18	1.33	2.02	0.02	2.56	0.07	0.44	
MISM14 -chlorite/4	55.73	2.79	1.21	1.31	2.04	0.01	2.59	0.05	0.44	
MISM14 -chlorite/5	53.84	2.74	1.26	1.34	2.11	0.02	2.48	0.04	0.46	
MISM14 -chlorite/6	53.86	2.73	1.27	1.34	2.09	0.04	2.49	0.04	0.45	
MISM14 -chlorite/7	55.00	2.75	1.25	1.37	2.03	0.02	2.51	0.06	0.45	
MISM14 -chlorite/8	58.92	2.95	1.05	1.38	1.79	0.03	2.62	0.17	0.40	
MISM14 -chlorite/9	56.90	2.83	1.17	1.36	1.94	0.02	2.59	0.09	0.43	
MISM14 -chlorite/10	57.54	2.77	1.23	1.29	1.96	0.02	2.69	0.03	0.42	
MISM14 -chlorite/11	37.87	6.76	0.00	0.02	0.15	0.13	0.18	5.52	0.33	
ANKO15-chlorite/1	32.28	1.78	2.22	-1.20	5.95	0.08	2.87	0.00	0.67	

Electron Microprobe Analysis of white mica														
	Oxide wt%, O by stoichiometry													
	SiO2	TiO2	Al2O3	Fe2O3	MnO	MgO	CaO	Na2O	K2O	BaO	H2O	total	Fe2O3+MgO	
MIS 06: white mica/1	47.722	0.318	31.608	3.902	0.088	1.414	0.000	0.110	10.508	0.148	4.504	100.322	5.316	
MIS 06: white mica/2	48.102	0.270	30.351	4.076	0.054	1.433	0.000	0.145	10.451	0.195	4.468	99.545	5.509	
MIS 06: white mica/3	48.136	0.375	30.974	3.720	0.028	1.483	0.000	0.162	10.423	0.211	4.495	100.007	5.203	
MIS 06: white mica/4	49.778	0.313	30.188	3.395	0.003	1.599	0.000	0.229	10.048	0.306	4.534	100.394	4.994	
MIS 06: white mica/5	48.746	0.272	30.852	3.358	0.045	1.554	0.000	0.157	10.450	0.227	4.511	100.171	4.912	
MIS 06: white mica/6	47.168	0.293	31.532	4.244	0.063	1.526	0.000	0.192	10.501	0.274	4.487	100.281	5.770	
MIS 06: white mica/7	48.861	0.407	30.645	4.100	0.037	1.551	0.019	0.138	9.753	0.306	4.524	100.341	5.651	
MIS 06: white mica/8	47.466	0.192	32.855	3.185	0.003	1.213	0.000	0.132	10.121	0.201	4.507	99.876	4.398	
MIS 06: white mica/9	47.904	0.232	31.552	3.600	0.045	1.446	0.000	0.142	10.353	0.290	4.498	100.062	5.046	
MIS 06: white mica/10	47.321	0.294	31.240	4.382	0.097	1.555	0.000	0.125	10.093	0.142	4.477	99.727	5.937	
MIS 06: white mica/11	52.883	0.236	28.704	4.680	0.028	1.549	0.009	0.117	9.355	0.215	4.651	102.428	6.229	
MIS 06: white mica/12	48.104	1.016	30.813	4.180	0.105	1.408	0.570	0.129	10.346	0.326	4.540	101.537	5.588	
MIS 06: white mica/13	48.229	0.384	30.281	5.129	0.080	1.633	0.011	0.523	9.875	0.258	4.518	100.922	6.762	
MIS 06: white mica/14	49.470	0.345	30.094	3.648	0.000	1.512	0.023	0.104	10.151	0.280	4.517	100.144	5.160	
MIS 06: white mica/15	50.540	0.245	30.563	3.484	0.037	1.575	0.056	0.058	9.850	0.269	4.587	101.264	5.059	
MI-SM05: white mica/1	52.600	0.000	28.837	2.223	0.029	1.030	0.182	1.398	8.110	0.387	4.555	99.351	3.253	
MI-SM05: white mica/2	48.879	0.168	30.345	2.644	0.055	1.622	0.041	0.193	9.759	0.270	4.461	98.437	4.266	
MI-SM05: white mica/3	48.731	0.184	30.029	4.259	0.115	1.904	0.066	0.032	9.287	0.169	4.488	99.264	6.163	
MISM14 -white mica/1	49.075	0.514	31.169	2.055	0.000	1.805	0.157	0.095	10.238	0.070	4.521	99.699	3.860	
MISM14 -white mica/2	48.738	0.854	29.815	3.203	0.036	2.800	0.088	0.089	10.519	0.145	4.531	100.818	6.003	
MISM14 -white mica/3	49.184	0.275	31.801	1.857	0.000	1.752	0.019	0.068	10.341	0.124	4.536	99.958	3.609	
MISM14 -white mica/4	49.176	0.348	29.702	3.054	0.000	2.619	0.015	0.114	10.208	0.129	4.509	99.874	5.673	
MISM14 -white mica/5	47.811	0.258	31.357	2.670	0.010	2.377	0.097	0.183	10.571	0.123	4.500	99.956	5.047	
MISM14 -white mica/6	49.302	0.113	30.951	2.075	0.000	1.914	0.189	0.120	10.354	0.102	4.515	99.635	3.989	
MISM14 -white mica/7	49.218	0.695	30.943	2.202	0.045	1.835	0.039	0.077	10.029	0.091	4.524	99.698	4.037	
MISM14 -white mica/8	50.834	0.110	31.139	1.934	0.044	1.512	0.000	1.041	9.642	0.129	4.594	100.979	3.446	
MISM14 -white mica/9	48.589	0.167	31.477	2.329	0.000	1.850	0.011	0.190	10.608	0.070	4.510	99.801	4.179	
ANKO15-white mica/1	26.296	0.021	21.909	8.282	0.278	4.639	14.715	0.133	5.830	0.327	3.478	85.908		
ANKO15-white mica/2	48.025	0.436	33.038	1.983	0.038	1.237	0.000	0.144	10.056	0.177	4.520	99.654		
ANKO15-white mica/3	48.315	0.056	33.169	2.071	0.030	1.203	0.000	0.072	10.137	0.210	4.528	99.790		
ANKO15-white mica/4	48.238	0.040	35.272	1.893	0.056	0.424	0.079	0.079	9.574	0.059	4.579	100.293		
ANKO15-white mica/5	49.505	0.706	31.286	2.990	0.030	1.968	0.019	0.170	9.136	0.113	4.573	100.495		
ANKO15-white mica/6	48.908	0.007	35.596	0.912	0.012	0.426	0.000	0.160	9.036	0.043	4.589	99.689		
ANKO15-white mica/7	48.118	0.048	36.120	0.992	0.030	0.619	0.000	0.100	8.689	0.032	4.576	99.324		
ANKO15-white mica/8	49.498	0.046	36.060	0.755	0.012	0.302	0.007	0.164	8.725	0.038	4.630	100.237		
ANKO15-white mica/9	47.860	0.531	31.081	3.345	0.012	1.599	0.000	0.158	10.340	0.091	4.481	99.499		
ANKO15-white mica/10	48.443	0.062	33.304	1.865	0.038	1.204	0.025	0.158	9.727	0.296	4.532	99.654		
ANKO15-white mica/11	41.674	0.434	26.465	10.693	0.169	3.686	0.681	0.184	7.381	0.011	4.201	95.578		

Electron Microprobe Analysis of white mica												
	Cations to 24 O, OH											
	Si	Ti	Al	Fe3	Mn	Mg	Ca	Na	K	Ba	OH	total
MIS 06: white mica/1	6.353	0.032	4.959	0.391	0.010	0.281	0.000	0.028	1.785	0.008	4.000	17.847
MIS 06: white mica/2	6.455	0.027	4.800	0.412	0.006	0.287	0.000	0.038	1.790	0.010	4.000	17.825
MIS 06: white mica/3	6.421	0.038	4.870	0.373	0.003	0.295	0.000	0.042	1.774	0.011	4.000	17.827
MIS 06: white mica/4	6.583	0.031	4.705	0.338	0.000	0.315	0.000	0.059	1.695	0.016	4.000	17.742
MIS 06: white mica/5	6.480	0.027	4.834	0.336	0.005	0.308	0.000	0.040	1.773	0.012	4.000	17.815
MIS 06: white mica/6	6.303	0.029	4.966	0.427	0.007	0.304	0.000	0.050	1.791	0.014	4.000	17.891
MIS 06: white mica/7	6.476	0.041	4.787	0.409	0.004	0.307	0.003	0.035	1.650	0.016	4.000	17.727
MIS 06: white mica/8	6.315	0.019	5.151	0.319	0.000	0.241	0.000	0.034	1.718	0.010	4.000	17.807
MIS 06: white mica/9	6.385	0.023	4.957	0.361	0.005	0.287	0.000	0.037	1.761	0.015	4.000	17.831
MIS 06: white mica/10	6.337	0.030	4.931	0.442	0.011	0.310	0.000	0.032	1.725	0.007	4.000	17.826
MIS 06: white mica/11	6.817	0.023	4.361	0.454	0.003	0.298	0.001	0.029	1.539	0.011	4.000	17.536
MIS 06: white mica/12	6.353	0.101	4.796	0.415	0.012	0.277	0.081	0.033	1.744	0.017	4.000	17.829
MIS 06: white mica/13	6.400	0.038	4.736	0.512	0.009	0.323	0.002	0.135	1.672	0.013	4.000	17.841
MIS 06: white mica/14	6.566	0.034	4.708	0.364	0.000	0.299	0.003	0.027	1.719	0.015	4.000	17.736
MIS 06: white mica/15	6.607	0.024	4.709	0.343	0.004	0.307	0.008	0.015	1.643	0.014	4.000	17.672
MI-SM05: white mica/1	6.924	0.000	4.474	0.220	0.003	0.202	0.026	0.357	1.362	0.020	4.000	17.588
MI-SM05: white mica/2	6.570	0.017	4.807	0.267	0.006	0.325	0.006	0.050	1.674	0.014	4.000	17.737
MI-SM05: white mica/3	6.511	0.018	4.728	0.428	0.013	0.379	0.009	0.008	1.583	0.009	4.000	17.688
MISM14 -white mica/1	6.510	0.051	4.873	0.205	0.000	0.357	0.022	0.024	1.733	0.004	4.000	17.779
MISM14 -white mica/2	6.450	0.085	4.650	0.319	0.004	0.552	0.012	0.023	1.776	0.008	4.000	17.880
MISM14 -white mica/3	6.501	0.027	4.954	0.185	0.000	0.345	0.003	0.017	1.744	0.006	4.000	17.783
MISM14 -white mica/4	6.540	0.035	4.655	0.306	0.000	0.519	0.002	0.029	1.732	0.007	4.000	17.826
MISM14 -white mica/5	6.372	0.026	4.925	0.268	0.001	0.472	0.014	0.047	1.798	0.006	4.000	17.929
MISM14 -white mica/6	6.548	0.011	4.845	0.207	0.000	0.379	0.027	0.031	1.755	0.005	4.000	17.808
MISM14 -white mica/7	6.523	0.069	4.833	0.220	0.005	0.363	0.006	0.020	1.696	0.005	4.000	17.739
MISM14 -white mica/8	6.634	0.011	4.790	0.190	0.005	0.294	0.000	0.263	1.606	0.007	4.000	17.800
MISM14 -white mica/9	6.461	0.017	4.933	0.233	0.000	0.367	0.002	0.049	1.800	0.004	4.000	17.864
ANKO15-white mica/1	4.534	0.003	4.452	1.075	0.041	1.193	2.718	0.044	1.283	0.022	4.000	19.364
ANKO15-white mica/2	6.370	0.044	5.165	0.198	0.004	0.245	0.000	0.037	1.702	0.009	4.000	17.774
ANKO15-white mica/3	6.398	0.006	5.177	0.206	0.003	0.238	0.000	0.018	1.713	0.011	4.000	17.770
ANKO15-white mica/4	6.317	0.004	5.444	0.187	0.006	0.083	0.011	0.020	1.600	0.003	4.000	17.674
ANKO15-white mica/5	6.492	0.070	4.835	0.295	0.003	0.385	0.003	0.043	1.529	0.006	4.000	17.660
ANKO15-white mica/6	6.391	0.001	5.482	0.090	0.001	0.083	0.000	0.041	1.507	0.002	4.000	17.597
ANKO15-white mica/7	6.306	0.005	5.578	0.098	0.003	0.121	0.000	0.025	1.453	0.002	4.000	17.591
ANKO15-white mica/8	6.410	0.004	5.504	0.074	0.001	0.058	0.001	0.041	1.442	0.002	4.000	17.538
ANKO15-white mica/9	6.404	0.053	4.901	0.337	0.001	0.319	0.000	0.041	1.765	0.005	4.000	17.827
ANKO15-white mica/10	6.409	0.006	5.193	0.186	0.004	0.237	0.004	0.041	1.642	0.015	4.000	17.737
ANKO15-white mica/11	5.949	0.047	4.452	1.149	0.020	0.784	0.104	0.051	1.344	0.001	4.000	17.902

Electron Microprobe Analysis of albite

	Oxide wt%, O by stoichiometry										Cations to 8 O									
	SiO2	TiO2	Al2O3	Fe2O3	MnO	MgO	CaO	Na2O	K2O	total	Si	Ti	Al	Fe3	Mn	Mg	Ca	Na	K	total
MIS 06: albite/1	71.579	0.018	21.406	0.563	0	0.061	0.455	7.186	0.171	101.439	3.024735	5.72E-04	1.06607	1.79E-02	0	3.84E-03	0.0206	0.588743	9.22E-03	4.731688
MIS 06: albite/1a	66.609	0.043	22.157	0.403	0	0.041	0.559	9.804	1.089	100.705	2.899727	1.41E-03	1.136799	1.32E-02	0	2.66E-03	2.61E-02	0.827493	6.05E-02	4.967857
MIS 06: albite/2	68.772	0.043	19.76	0.269	0	0.009	0.457	11.333	0.055	100.698	2.984102	1.40E-03	1.010503	8.78E-03	0	5.82E-04	2.12E-02	0.953418	3.05E-03	4.983083
MIS 06: albite/3	69.376	0.053	20.365	0.52	0	0.026	0.439	11.653	0.218	102.65	2.962172	1.70E-03	1.024788	1.67E-02	0	1.66E-03	2.01E-02	0.964662	0.0118771	5.003647
MIS 06: albite/4	70.761	0.067	20.874	0.269	0	0.016	0.318	9.822	0.366	102.493	2.996004	2.13E-03	1.041604	8.57E-03	0	1.01E-03	1.44E-02	0.806278	1.98E-02	4.8898
MIS 06: albite/5	82.76	0.064	13.409	0.497	0	0.028	0.124	8.241	0.065	105.188	3.342369	1.94E-03	0.638233	1.51E-02	0	1.69E-03	5.37E-03	0.645283	3.35E-03	4.653335
MI-SM05: albite/1	65.201	0.083	23.074	1.289	0	0.473	0.13	7.810999	2.871	100.932	2.849991	2.73E-03	1.188668	4.24E-02	0	3.08E-02	6.09E-03	0.661961	0.160131	4.942792
MI-SM05: albite/2	68.327	0.01	19.652	0.076	0	0.021	0.145	11.676	0.082	99.98901	2.986092	3.29E-04	1.0122	2.50E-03	0	1.37E-03	6.79E-03	0.989331	4.57E-03	5.003181
MI-SM05: albite/3	69.325	0	20.245	0.135	0	0.02	0.087	11.842	0.225	101.879	2.976306	0	1.024363	4.36E-03	0	1.28E-03	4.00E-03	0.98571	1.23E-02	5.008349
MI-SM05: albite/4	74.292	0.048	18.662	0.118	0	0.01	0.332	10.043	0.173	103.678	3.095542	1.50E-03	0.916435	3.70E-03	0	6.21E-04	1.48E-02	0.811325	9.20E-03	4.853147

	Cation ratios etc.																			
	Ca[1]	Na	K	Ba	Sr															
MIS 06: albite/1	3.927202	94.59138	1.481416	0	0															
MIS 06: albite/1a	3.134444	90.2667	6.598856	0	0															
MIS 06: albite/2	2.231237	97.45748	0.311279	0	0															
MIS 06: albite/3	2.177522	96.63271	1.18976	0	0															
MIS 06: albite/4	1.834308	95.81587	2.349823	0	0															
MIS 06: albite/5	1.075434	98.4137	0.510864	0	0															
MI-SM05: albite/1	4.29722	77.06133	18.64145	0	0															
MI-SM05: albite/2	0.814096	98.72957	0.456335	0	0															
MI-SM05: albite/3	0.526457	98.24501	1.228526	0	0															
MI-SM05: albite/4	1.847271	97.05244	1.100286	0	0															

	Oxide wt%, O by stoichiometry										Cations to 8 O									
	SiO2	TiO2	Al2O3	Fe2O3	MnO	MgO	CaO	Na2O	K2O	total	Si	Ti	Al	Fe3	Mn	Mg	Ca	Na	K	total
MISM14 -albite/1	68.538	0.033	20.494	0.101	0.048	0.02	0.372	11.622	0.061	101.289	2.959903	1.07E-03	1.043089	3.28E-03	1.76E-03	1.29E-03	1.72E-02	0.973113	3.36E-03	5.004077
MISM14 -albite/2	68.563	0.06	20.179	0.357	0.059	0.039	0.142	11.631	0.173	101.203	2.965879	1.95E-03	1.028755	1.16E-02	2.16E-03	2.52E-03	6.58E-03	0.975478	9.55E-03	5.004494
MISM14 -albite/3	68.333	0.044	20.558	0.264	0.019	0.024	0.641	11.219	0.165	101.267	2.953458	1.43E-03	1.0472	8.59E-03	6.96E-04	1.55E-03	2.97E-02	0.940136	9.10E-03	4.991837
MISM14 -albite/4	69.306	5.60E-02	20.709	0.398	0.053	0.032	0.36	11.356	0.098	102.368	2.960136	1.80E-03	1.042434	1.28E-02	1.92E-03	2.04E-03	1.65E-02	0.940379	5.34E-03	4.98331
MISM14 -albite/5	69.405	0.013	20.736	0.264	0.03	0.014	0.306	11.692	0.09	102.55	2.960473	4.17E-04	1.042423	8.47E-03	1.08E-03	8.90E-04	1.40E-02	0.966932	4.90E-03	4.999577
MISM14 -albite/6	71.023	0.024	18.519	0.136	0.042	0.008	0.094	10.687	0.053	100.586	3.062721	7.79E-04	0.941184	4.41E-03	1.53E-03	5.14E-04	4.34E-03	0.893513	2.92E-03	4.911917
ANKO15-albite/1	68.265	0	20.136	0	0	0	0.701	11.211	0.025	100.338	2.971887	0	1.033133	0	0	0	3.27E-02	0.94627	1.39E-03	4.985375

	Cation ratios etc.							
	Ca[1]	Na	K[2]	An(si)	An(al+fe3)	An(ca)[1]	An(na)[3]	AvAn
MISM14 -albite/1	2.032248	97.6305	0.337249	4.009724	4.637122	2.025604	2.35253	3.256245
MISM14 -albite/2	1.130024	97.9115	0.958472	3.412056	4.037607	1.125826	1.497346	2.518209
MISM14 -albite/3	3.253841	95.8187	0.927463	4.654241	5.578673	3.192545	5.076366	4.625456
MISM14 -albite/4	2.114485	97.33271	0.55281	3.986359	5.522633	2.042907	5.428028	4.244982
MISM14 -albite/5	1.615598	97.8885	0.495909	3.95267	5.089724	1.59587	2.816981	3.363811
MISM14 -albite/6	0.707942	98.96903	0.323025	0	0	0.639145	10.3571	2.749061
ANKO15-albite/1	3.335206	96.52313	0.141659	2.811265	3.313255	3.269688	5.23411	3.65708

Electron Microprobe Analysis of calcite

	Carbonate weight percent, CO2 by stoichiometry					Cations normalised to 2 CO2					Normalised wt%				
	FeCO3	MnCO3	CaCO3	MgCO3	total	Fe	Mn	Ca	Mg	total	FeCO3	MnCO3	CaCO3	MgCO3	total
ANKO-15: test calcite/1	0.211	0.204	100.493	0.000	100.908	0.004	0.004	1.993	0.000	2.000	0.209	0.202	99.589	0.000	100
ANKO-15: test calcite/2	0.641	0.433	98.812	0.664	100.550	0.011	0.008	1.966	0.016	2.000	0.637	0.431	98.272	0.660	100
ANKO-15: calcite/1	0.154	0.190	102.782	0.000	103.126	0.003	0.003	1.994	0.000	2.000	0.149	0.184	99.666	0.000	100
ANKO-15: calcite/2	0.110	0.233	101.106	0.000	101.449	0.002	0.004	1.994	0.000	2.000	0.108	0.230	99.662	0.000	100
ANKO-15: calcite/3	1.844	0.147	100.604	0.434	103.029	0.031	0.002	1.957	0.010	2.000	1.790	0.143	97.646	0.421	100
ANKO-15: calcite/4	0.000	0.104	99.292	0.000	99.396	0.000	0.002	1.998	0.000	2.000	0.000	0.105	99.895	0.000	100
ANKO-15: calcite/5	0.383	0.162	100.301	0.000	100.846	0.007	0.003	1.991	0.000	2.000	0.380	0.161	99.460	0.000	100
ANKO-15: calcite/6	2.045	0.447	99.581	0.652	102.725	0.034	0.008	1.943	0.015	2.000	1.991	0.435	96.939	0.635	100
ANKO-15: calcite/7	2.316	0.375	94.220	0.621	97.532	0.041	0.007	1.937	0.015	2.000	2.375	0.384	96.604	0.637	100
ANKO-15: calcite/8	0.297	0.204	100.198	0.000	100.699	0.005	0.004	1.991	0.000	2.000	0.295	0.203	99.502	0.000	100
ANKO-15: calcite/9	0.182	0.419	102.459	0.000	103.060	0.003	0.007	1.990	0.000	2.000	0.177	0.407	99.417	0.000	100
ANKO-15: calcite/10	0.024	0.376	99.739	0.000	100.139	0.000	0.007	1.993	0.000	2.000	0.024	0.375	99.601	0.000	100
ANKO-15: calcite/11	0.000	0.433	100.915	0.000	101.348	0.000	0.007	1.993	0.000	2.000	0.000	0.427	99.573	0.000	100
MISM14: calcite/1	0.812	1.654	101.064	0.690	104.220	0.013	0.028	1.943	0.016	2.000	0.779	1.587	96.972	0.662	100
MISM14: calcite/2	0.541	0.856	99.916	0.052	101.365	0.009	0.015	1.975	0.001	2.000	0.534	0.844	98.571	0.051	100
MISM14: calcite/3	0.454	1.656	98.966	0.196	101.272	0.008	0.029	1.959	0.005	2.000	0.448	1.635	97.723	0.194	100
MISM14: calcite/4	1.085	1.384	97.006	0.806	100.281	0.019	0.024	1.938	0.019	2.000	1.082	1.380	96.734	0.804	100
MISM14: calcite/5	0.211	1.142	98.873	0.196	100.422	0.004	0.020	1.972	0.005	2.000	0.210	1.137	98.458	0.195	100
MISM14: calcite/6	0.440	1.156	96.726	0.238	98.560	0.008	0.020	1.966	0.006	2.000	0.446	1.173	98.139	0.241	100
MISM14: calcite/7	0.240	0.742	103.545	0.000	104.527	0.004	0.012	1.984	0.000	2.000	0.230	0.710	99.061	0.000	100
MISM14: calcite/8	0.541	1.385	97.459	0.315	99.700	0.009	0.024	1.959	0.008	2.000	0.543	1.389	97.752	0.316	100
MISM14: calcite/9	0.096	1.100	98.582	0.203	99.981	0.002	0.019	1.974	0.005	2.000	0.096	1.100	98.601	0.203	100
MISM14: calcite/10	0.168	1.499	102.531	0.217	104.415	0.003	0.025	1.967	0.005	2.000	0.161	1.436	98.196	0.208	100
MISM14: calcite/11	1.901	1.311	96.200	0.779	100.191	0.033	0.023	1.926	0.019	2.000	1.897	1.309	96.017	0.778	100
MISM14: calcite/12	0.000	0.628	98.988	0.122	99.738	0.000	0.011	1.986	0.003	2.000	0.000	0.630	99.248	0.122	100
MISM14: calcite/13	0.000	0.299	99.656	0.024	99.979	0.000	0.005	1.994	0.001	2.000	0.000	0.299	99.677	0.024	100
MISM14: calcite/14	0.813	1.085	97.426	0.627	99.951	0.014	0.019	1.952	0.015	2.000	0.813	1.086	97.474	0.627	100
MISM05: calcite/1	0.699	1.028	95.680	0.116	97.523	0.012	0.018	1.966	0.003	2.000	0.717	1.054	98.110	0.119	100
MISM05: calcite/2	1.301	0.970	97.322	0.172	99.765	0.023	0.017	1.956	0.004	2.000	1.304	0.972	97.551	0.172	100
MISM05: calcite/3	0.813	1.370	98.185	0.172	100.540	0.014	0.024	1.958	0.004	2.000	0.809	1.363	97.658	0.171	100
MISM05: calcite/4	0.000	0.099	98.591	0.000	98.690	0.000	0.002	1.998	0.000	2.000	0.000	0.100	99.900	0.000	100
MISM05: calcite/5	0.168	0.814	98.821	0.010	99.813	0.003	0.014	1.983	0.000	2.000	0.168	0.816	99.006	0.010	100
MISM05: calcite/6	0.785	0.985	96.392	0.137	98.299	0.014	0.017	1.965	0.003	2.000	0.799	1.002	98.060	0.139	100
MISM05: calcite/7	0.900	1.242	97.341	0.161	99.644	0.016	0.022	1.959	0.004	2.000	0.903	1.246	97.689	0.162	100
MISM05: calcite/8	0.469	1.186	98.655	0.067	100.377	0.008	0.021	1.970	0.002	2.000	0.467	1.182	98.284	0.067	100
MISM05: calcite/9	1.087	0.957	95.466	0.522	98.032	0.019	0.017	1.951	0.013	2.000	1.109	0.976	97.382	0.532	100
MISM05: calcite/10	0.499	0.084	99.009	0.014	99.606	0.009	0.001	1.990	0.000	2.000	0.501	0.084	99.401	0.014	100
MIS06: calcite/1	0.125	0.943	100.328	0.049	101.445	0.002	0.016	1.981	0.001	2.000	0.123	0.930	98.899	0.048	100
MIS06: calcite/2	0.628	0.428	96.558	0.179	97.793	0.011	0.008	1.977	0.004	2.000	0.642	0.438	98.737	0.183	100
MIS06: calcite/3	0.254	0.815	101.070	0.031	102.170	0.004	0.014	1.981	0.001	2.000	0.249	0.798	98.923	0.030	100
MIS06: calcite/4	0.757	1.129	97.151	0.060	99.097	0.013	0.020	1.965	0.001	2.000	0.764	1.139	98.036	0.061	100
MIS06: calcite/5	0.096	0.844	101.864	0.000	102.804	0.002	0.014	1.984	0.000	2.000	0.093	0.821	99.086	0.000	100
MIS06: calcite/6	1.059	0.557	99.512	0.165	101.293	0.018	0.010	1.968	0.004	2.000	1.045	0.550	98.242	0.163	100
MIS06: calcite/7	1.359	1.243	97.031	0.063	99.696	0.024	0.022	1.953	0.002	2.000	1.363	1.247	97.327	0.063	100
MIS06: calcite/8	0.369	0.486	98.659	0.000	99.514	0.006	0.009	1.985	0.000	2.000	0.371	0.488	99.141	0.000	100

Electron Microprobe Analysis of dolomite																
	Carbonate weight percent, CO2 by stoichiometry						Cations normalised to 2 CO2						Normalised wt%				
	FeCO3	MnCO3	CaCO3	MgCO3	total		Fe	Mn	Ca	Mg	total		FeCO3	MnCO3	CaCO3	MgCO3	total
ANKO-15: dolomite/1	22.446	0.655	51.693	21.731	96.525		0.398	0.012	1.061	0.530	2.000		23.254	0.679	53.554	22.513	100
ANKO-15: dolomite/2	64.357	0.909	6.256	25.194	96.716		1.201	0.017	0.135	0.647	2.000		66.542	0.940	6.468	26.049	100
ANKO-15: dolomite/3	21.181	0.377	53.350	22.348	97.256		0.371	0.007	1.083	0.539	2.000		21.779	0.388	54.855	22.979	100
ANKO-15: dolomite/4	11.682	0.537	58.484	27.272	97.975		0.199	0.009	1.153	0.639	2.000		11.923	0.548	59.693	27.836	100
ANKO-15: dolomite/5	67.661	1.051	5.302	25.328	99.342		1.234	0.019	0.112	0.635	2.000		68.109	1.058	5.337	25.496	100
ANKO-15: dolomite/6	11.867	0.423	59.015	26.615	97.920		0.202	0.007	1.166	0.624	2.000		12.119	0.432	60.269	27.180	100
ANKO-15: dolomite/7	63.501	0.961	6.317	24.040	94.819		1.211	0.018	0.140	0.631	2.000		66.971	1.014	6.662	25.354	100
ANKO-15: dolomite/8	16.450	0.506	54.773	25.787	97.516		0.284	0.009	1.095	0.612	2.000		16.869	0.519	56.168	26.444	100
ANKO-15: dolomite/9	64.714	0.791	5.625	27.383	98.513		1.180	0.015	0.119	0.687	2.000		65.691	0.803	5.710	27.796	100
ANKO-15: dolomite/10	19.917	0.630	57.296	19.467	97.310		0.350	0.011	1.167	0.471	2.000		20.468	0.647	58.880	20.005	100
ANKO-15: dolomite/11	63.994	1.013	5.671	23.737	94.415		1.228	0.020	0.126	0.626	2.000		67.779	1.073	6.006	25.141	100
ANKO-15: dolomite/12	18.337	0.504	49.095	26.607	94.543		0.327	0.009	1.013	0.652	2.000		19.395	0.533	51.929	28.143	100
ANKO-15: dolomite/13	85.269	1.535	4.579	11.772	103.155		1.575	0.029	0.098	0.299	2.000		82.661	1.488	4.439	11.412	100
ANKO-15: dolomite/14	19.866	1.245	66.159	7.038	94.308		0.370	0.023	1.427	0.180	2.000		21.065	1.320	70.152	7.463	100
ANKO-15: dolomite/15	83.074	1.588	2.362	15.168	102.192		1.535	0.030	0.051	0.385	2.000		81.292	1.554	2.311	14.843	100

References.

Albers, M., 2005. Microscale kinematics and deformation mechanisms in phyllonitic mylonites and implications for the strength of continental fault zones. Drs/MSc research thesis. University of Utrecht, Faculty of Geosciences.

Beach, A., 1979. Pressure solution as a metamorphic process in deformed terrigenous sedimentary rocks. Lithis 12, 51-58.

Beeler, N.M., Tullis, T.E., 1997. The roles of time and displacement in velocity-dependant volumetric strain of fault zones. Journal of Geophysical Research, 102, 22595-22609.

Bos, B., Peach, C.J., Spiers, C.J. 2000a. Slip behaviour of simulated gouge-bearing faults under conditions favouring pressure solution. Journal of Geophysical Research 105, 16699-16717.

Bos, B., Peach, C.J., Spiers, C.J. 2000b. Frictional-viscous flow of simulated fault gouge caused by the combined effects of phyllosilicates and pressure solution. Tectonophysics 327, 173-194.

Bos, B., Spiers, C.J. 2000. Effect of phyllosilicates on fluid-assisted healing of gouge-bearing faults. Earth and Planetary Science Letters 184, 199-210.

Bos, B., Spiers, C.J. 2002. Frictional-viscous flow of phyllosilicate-bearing fault rock: Microphysical model and implications for crustal strength profiles. Journal of Geophysical Research 107, no. B2, 2028.

Boynton, W.R., 1984. Geochemistry of the rare earth elements: meteorite studies. In: Henderson, P. (ed) Rare earth element geochemistry. Elsevier, Amsterdam. 63-114.

Brimhall, G.H., Dietrich, W.E., 1987. Constitutive mass balance relations between chemical composition, volume, density, porosity and strain in metasomatic hydrochemical systems. Geochimica et Cosmochimica Acta, 51, 567-587.

Brodie, K., Rutter, E.H., 1985. On the relationship between deformation and metamorphism with special reference to the behaviour of basic rocks. In: Thompson, A.B., Rubie, D. (eds). Kinetics, Textures and Deformation, Advanced Physical Chemistry 4, 138-179.

Byerlee, J., 1990. Friction, overpressure and fault normal compression. Geophysical Research Letters 17, 2109-2112.

Caine, J.S., Evans, J.P., Forster, C.B., 1996. Fault zone architecture and permeability structure. Geology, 24, 1025-1028.

Cathelineau, M., 1988. cation siite occupancy in chlorites and illites as a function of temperature. Clay Minerals 23, 471-485.

Chester, F.M., 1995. A rheologic model for wet crust applied to strike-slip faults. Journal of Geophysical Research, 100, 13033-13044.

Chester, F.M., Evans, J.P., Biegel, R.L., 1993. Internal structure and weakening mechanisms of the San Andreas fault. Journal of Geophysical Research 98, 771-786.

Chester, F.M., Friedman, M., Logan, J.M., 1985. Foliated cataclasites. Tectonophysics 111, 139-146.

Chester, F.M., Logan, J.M., 1986.Implications for mechanical properties of brittle faults from observations of the Punchbowl Fault Zone, California. Pure and Applied Geophysics, 124, 79-106.

Collettini, C., Holdsworth, R.E., 2004. Fault zone weakening and character of slip along low-angle normal faults: insights from the Zuccale Fault, Elba, Italy. Journal of the Geological Society, London 161, 1039-1051.

Dallmeyer, R.D., Takasu, A., Yamaguchi, K., 1995. Mesozoic tectonothermal development of the Sambagawa, Mikabu and Chichibu belts, south-west Japan: evidence from ^{40}Ar-^{39}Ar whole-rock phyllite ages. Journal of Metamorphic Geology 13, 217-286.

Dewey, J.F., Hempton, M.R., Kidd, W.S.F., Saroglu, F., Sengor, A.M.C., 1986. Shortening of continental lithosphere: the Neotectonics of Eastern Anatolia – a young collision zone. In: Coward, M.P., Ries, A.C. (eds). Collision Tectonics. Geological Society of London Special Publication 19, 3-37.

Drury, M.R., Urai, J.L., 1990. Deformation-related recrystallization processes. Tectonophysics 172, 235-253.

Enami, M., Wallis, S.R., Banno, Y., 1994. Paragenesis of sodic pyroxene-bearing quartz schists: Implications for the P-T history of the Sambagawa belt. Contributions to Mineralogy and Petrology 116, 182-198.

Engelder, T., 1984. The role of pore water circulation during the deformation of foreland fold and thrust belts. Journal of Geophysical Research 89, 4319-4325.

Etheridge, M.A., 1983. Differential stress magnitudes during regional deformation and metamorphism: upper bound imposed by tensile fracturing. Geology 11, 231-234.

Etheridge, M.A., Wall, V.J., Vernon, R.H., 1983. The role of the fluid phase during regional metamorphism and deformation. Journal of Metamorphic Geology 1, 205-226.

Evans, B., Goetze, C., 1979. The temperature variation of hardness of olivine and its implications for polycrystalline yield stress. Journal of Geophysical Research 84(B10), 5505-5524.

Evans, J.P., Chester, F.M., 1995. Fluid-rock interaction in faults of the San Andreas System; Inferences from San Gabriel fault rock geochemistry and microstructures. Journal of Geophysical Research, 100, 13007-13020.

Evans, J.P., Forster, C.B., Goddard, J.V., 1997. Permeability of fault-related rocks, and implications for hydraulic structure of fault zones. Journal of Structural Geology, 19, 1393-1404.

Ferry, J.M., 1992. Regional metamorphism of the Waits River Formation, Eastern Vermot: delineation of a new type of giant hydrothermal system. Journal of petrology 33, 45-94.

Forster, C.B., Evans, J.P., 1991. Fluid flow in thrust faults and crystalline thrust sheets: Results of combined field and modelling studies. Geophysical Research Letters 18, 979-982.

Géraud, Y., Caron, J., Faure, P., 1995. Porosity network of a ductile shear zone. Journal of Structural Geology, 17, 1757-1769.

Goodwin, L.B., Wenk, H.R., 1995. Development of phyllonite from Granodiorite: Mechanisms of grain-size reduction in the Santa Rosa mylonite zone, California. Journal of Structural Geology 17, 689-707.

Grant, J.A., 1986. The isochon diagram – a simple solution to Gresen's equation for metasomatic alteration. Economic Geology, 81, 1976-1982.

Grauch, R.I., 1989. Rare Earth Elements in Metamorphic Rocks. In: Lipin, B.R., McKay, G.A. (eds). Geochemistry and Mineralogy of Rare Earth Elements. Rieviews in Mineralogy, 21, 147-167.

Gresens, R.L., 1967. Composition-volume relationships of metasomatism. Chemical Geology, 2, 47-65.

Gueydan, F., Leroy, Y.M., Jolivet, L., Agard, P., 2003. Analysis of continental midcrustal strain localisation induced by microfracturing and reaction-softening. Journal of Geophysical Research, 107(B): doi: 10.1029/2001JB000611.

Handy, M.R., 1989. Deformation Regimes and Rheological Evolution of Fault Zones in the Lithosphere – the Effects of Pressure, Temperature, Grainsize and Time. Tectonophysics 163, 119-152.

Handy, M.R., 1990. The solid-state flow of polymineralic rocks. Journal of Geophysical Research 95, No. B6, 8647-8661.

Handy, M.R., 1994. Flow laws for rocks containing two non-linear viscous phases, a phenomenological approach. Journal of Structural Geology, 16, 287-301.

Hara, I., Shyoji, K., Sakurai, Y., Yokoyama, S., Hide, K., 1980. Origin of the Median Tectonic Line and its initial shape. Memoirs of the Geological Society of Japan 18, 27-49.

Hayama, Y., Miyagawa, K., Nakajima, W., Yamada, T., 1963. The Kashio Tectonic Zone, Urakawa to Wada Area, Central Japan. Earth Sciences (Chikyu Kagaku) 66, 23-31 (in Japanese with English abstract).

Hayama, Y., Yamada, T., 1980. Median Tectonic Line at the stage of its origin in relation to plutonism and mylonitisation in the Ryoke Belt. Memoirs of the Geological Society, Japan 18, 5-26.

Hellmann, R., Dran, J.C., Della Mea, G., 1997. The albite-water system: Part III. Characterization of leached and hydrogen-enriched layers formed at 300 deg. C using MeV ion beam techniques. Geochim. Cosmochim. Acta 61, 1575-1594.

Hemley, J.J., Jones, W.R., 1964. Chemical aspects of hydrothermal alteration with emphasis on hydrogen metasomatism. Economic Geology, 59, 538-567.

Hickman, S., Sibson, R., Bruhn, R., 1995. Mechanical involvement off fluids in faulting. Journal of Geophysical Research 100, 12831-12840.

Hippertt, J.F., 1998. Breakdown of feldspar, volume gain and lateral mass transfer during mylonitisation of granitoids in a low metamorphic grade shear zone. Journal of Structural Geology 20, 175-193.

Hirth, G., Kohlstedt, D.L. 1996. Water in the oceanic upper mantle: Implications for rheology, melt extraction and the evolution of the lithosphere. Earth and Planetary Science Letters 144, 93-108.

Holdsworth, R.E., 1994. Structural Evolution of the Gander Avalon Terrane Boundary – a Reactivated Transpression Zone in the NE Newfoundland Appalachians. Journal of the Geological Society 151, 629-646.

Holdsworth, R.E., 2004. Weak faults – rotten cores. Science 303, 181-182.

Holdsworth, R.E., Butler, C.A., Roberts, A.M., 1997. The recognition of reactivation during continental deformation. Journal of Geological Society 154, 73-78.

Holdsworth, R.E., Stewart, M., Imber, J., Strachan, R.A., 2001. The structure and rheological evolution of reactivated continental fault zones: A review and case study. In: Miller, J.A., Holdsworth, R.E., Buick, I.S., Hand, M. Continental Reactivation and Reworking. Geological Society, London, Special Publication 184, 115-137.

Humphries, S.E., 1984. The mobility of the rare earth elements in the crust. In: Hendersom, P. (ed) Rare earth element geochemistry. Elsevier, Amsterdam. 315-341.

Ichikawa, K., 1980. Geohistory of the Median Tectonic Line of Southwest Japan. Memoir of the Geological Survey of Japan 18, 187-212.

Imber, J., 1998. Deformation and fluid-rock interaction along the reactivated Outer Hebrides Fault Zone, Scotland. Unpublished PhD thesis, University of Durham.

Imber, J., Holdsworth, R.E., Butler, C.A., Lloyd, G.E., 1997. Fault-zone weakening processes along the reactivated Outer Hebrides Fault Zone, Scotland. Journal of the Geological Society London, 154, 105-109.

Imber, J., Holdsworth, R.E., Butler, C.A., Strachan, R.A., 2001. A reappraisal of the Sibson-Scholz fault zone model: The nature of the frictional to viscous ("brittle-ductile") transition along a long-lived, crustal-scale fault, Outer Hebrides, Scotland. Tectonics 20 (No. 5), 601-624.

Ito, M., 1978. Granitic rocks and mylonitisation in the Kayumi district Mie Prefecture. MTL 3, 99-101.

Ito, T., Ikawa, T., Yamakita, S., Maeda, T., 1996. Gently north-dipping Median Tectonic Line (MTL) revealed by recent seismic reflection studies, southwest Japan. Tectonophysics, 264, 51-63.

Jackson, J., 2002. Strength of the continental lithosphere: Time to abandon the jelly sandwich? GSA Today 12 (No. 9), 4-10.

Janecke, S.U., Evans, J.P., 1988. Feldspar-influenced rock rheologies. Geology 16, 1064-1067.

Jefferies, S.P., Holdsworth, R.E., Wibberley, C., Shimamoto, T., Niemeijer, A., Spiers, C., 2006. The nature and rheological consequences of phyllonite development in the cores of crustal-scale faults: an example from the Median Tectonic Line. Journal of Structural Geology, In press.

Jordan, P.G., 1987. The deformation behaviour of bimineralic limestone-halite aggregates. Tectonophysics 135, 185-197.

Kerrich, R., 1986. Fluid infiltration into fault zones; chemical, isotopic and mechanical effects. Pure and Applied Geophysics 124, 225-268.

Knipe, R.J., 1989. Deformation mechanisms – recognition from natural tectonites. Journal of Structural Geology 11, 127-146.

Kronenberg, A.K., Segall, P., Wolf, G.H., 1990. Hydrolytic weakening and penetrative deformation within a natural shear zone. In: Duba, A.G., Durham, W.B., Handin, J.W., Wang, H.F. (Eds). The brittle-ductile transition in rocks, Geophysical Monograph 56, 21-36.

Lachenbruch, A.H., Sass, J.H., 1980. Heat flow and energetics of the San Andreas fault zone. Journal of Geophysical Research 85, 6185-6223.

Law, R.D., 1990. Crystallographic fabrics: a selective review of their applications to research in structural geology. In: Knipe, R.J., Rutter, E.H. (eds). Deformation Mechanisms, Rheology and Tectonics. Geological Society of London Special Publication 54, 335-352.

Lloyd, G.E., Knipe, R.J., 1992. Deformation mechanisms accommodating faulting of quartzite under upper crustal conditions. Journal of Structural Geology 14, 127-143.

Mackwell, S.J., Zimmerman, M.E., Kohlstedt, D.L., 1998. High-temperature deformation of dry diabase with application to tectonics on Venus. Journal of Geophysical Research 103, 975-984.

Maggi, A., Jackson, J.A., Priestley, K., Baker, C., 2000a. A reassessment of focal depth distributions in southern Iran, the Tien Shan and northern India: Do earthquakes really occur in the continental mantle? Geophysical Journal International 143, 629-661.

Maggi, A., Jackson, J.A., McKenzie, D., Priestley, K., 2000b. Earthquake focal depths, effective elastic thickness and the strength of the continental lithosphere. Geology 28, 495-498.

Magloughlin, J.F., 1992. Microstructural and chemical changes associated with cataclasis and frictional melting at shallow crustal levels: the cataclasite-pseudotachylyte connection. Tectonophysics 204, 243-260.

Mares, U.M., Kronenberg, A.K., 1993. Experimental deformation of muscovite. Journal of structural geology, 15, 1061-1075.

McCaig, A.M., 1988. Deep fluid circulation in fault zones. Geology 16, 867-870/

McCaig, A.M., 1997. The geochemistry of volatile fluid flow in shear zones. In: Holness, M.B. (ed) Deformation-enhanced Fluid Transport in the Earth's crust and Mantle. Chapman & Hall, London. 227-266.

McCaig, A.M., Knipe, R.J., 1990. Mass-transport mechanisms in deforming rocks: Recognition using microstructural and microchemical criteria. Geology 18, 824-827.

Michibayashi, K., Masuda, T., 1993. Shearing during progressive retrogression in granitoids: abrupt grain size reduction of quartz at the pplastic-brittle transition for feldspar. Journal of Structural Geology 222, 151-164.

Morrow, C., Radney, B., Byerlee, J.D., 1992. Frictional strength and the effective pressure law of montmorillonite and illite clays. Fault mechanics and transport properties of rocks, 69-88pp. Academic Press, San Diego, CA, United States.

Niemeijer, A.R., & Spiers, C.J. 2005. Influence of phyllosilicates on fault strength in the brittle-ductile transition: Insights from rock analogue experiments. In: D.

Bruhn & L. Burlini (Eds.), Microstructural Evolution and Physical Properties in High Strain Zones. Geological Society London, Special Publication, In Press.

O'Hara, K., 1988. Fluid flow and volume loss during mylonitisation: an origin for phyllonite in an overthrust setting, North Carolina, U.S.A. Tectonophysics, 156, 21-36.

Ohtomo, Y., 1993. Origin of the Median Tectonic Line. Journal of Science of the Hiroshima University 9, 611-669.

Okada, A., 1980. Quaternary faulting along the Median Tectonic Line of Southwest Japan. Memoirs of the Geological Society of Japan 18, 79-108.

Okano, K., Kimura, S., 1996. Crustal movements in and around Shikoku, southwest Japan associated with great Nankai earthquakes. Journal of the Seismological Society, Japan 49, 361-374 (in Japanese).

Oliver, N.H.S., 1996. Review and classification of structural controls on fluid flow during regional metamorphism. Journal of Metamorphic Geology 14, 477-492.

Oliver, H.H.S., Valenta, R.K., Wall, V.J., 1990. The effect of heterogeneous stress and strain on metamorphic fluid flow, Mary Kathleen, Australia, and a model for large-scale fluid circulation. Journal of Metamorphic Geology 8, 311-331.

Onoue, K., Hoso, Y., Fujita, Y., Doi, H., Tanaka, T. 2002. Electro-optical measurements on Median Tectonic Line. Annals of Disaster Prevention Research Institute, Kyoto University 45B, 525-533.

Passchier, C.W., Trouw, R.A.J., 1996. Micro-tectonics. Springer-Verlag, Berlin.

Pearce, J.A., 1983. Role of the sub-continental lithosphere in magma genesis at active continental margins. In: Hawkesworth, C.J., Norry, M.J. (eds) Continental basalts and mantle xenoliths. Shiva, Nantwich. 230-249.

Reynolds, S.J., Lister, G.S., 1987. Structural aspects of fluid-rock interactions in detachment zones. Geology 15, 362-366.

Rice, J.R., 1992. Fault stress states, pore pressure distributions, and the weakness of the San Andreas Fault. In: Evans, B., Wong, T.-F. (Ed.) Fault Mechanics and Transport Properties in Rocks. Academic Press Ltd. London, 475-503.

Rubie, D. C., 1990. Mechanisms of reaction-enhanced deformability in rocks. In: Barber, D.J., Meredith, P.G. (eds). Deformation processes in minerals, ceramics and rocks. Cambridge University Press, 262-294.

Rutter, E.H., 1983. Pressure solution in nature, theory and experiment. Journal of the Geological Society 140, 725-740.

Rutter, E.H., Holdsworth, R.E., Knipe, R.J., 2001. The nature and tectonic significance of fault zone weakening: an introduction. In: Holdsworth, R.E., Strachan, R.A., Magloughlin, J.F., Knipe, R.J. (Ed.), The Nature and Tectonic Significance of Fault Zone Weakening. Geological Society Special Publication 186, 1-12.

Ryoke Research Group, 1972. The mutual relations of the granitic rocks of the Ryoke belt in central Japan. Earth Sciences (Chikyu Kagaku) 26, 205-216 (in Japanese with English abstract).

Sakakibara, N., 1995. Structural evolution of multiple ductile shear zone system in the Ryoke belt, Kinki Province. Journal of Science of the Hiroshima University 10, 267-332.

Sakakibara, N., Ohtomo, Y., Hara, I., 1989. Deformation of granitic rocks in the Ryoke belt (I) Deformation styles of quartz. DELP publication 28, 47-51.

Schmid, S.M., Handy, M.R., 1991. Towards a genetic classification of fault rocks: Geological usage and tectonophysical implications. In: Müller, D.W.,

McKenzie, J.A., Weissert, H. (Eds.), Controversies in Modern Geology. Academic Press, London, 339-361.

Scholz, C.H., 2000. Evidence for a strong San Andreas fault. Geology 28, 163-166.

Selverstone, J., Morteani, G., Staude, J.M., 1991. Fluid channelling during ductile shearing: transformation of Granodiorite into aluminous schist in the Tauern Window, Eastern Alps. Journal of Metamorphic Geology, 9, 419-431.

Shea, W.T., Kronenberg, A.K., 1992. Rheology and deformation mechanisms of isotropic mica schist. Journal of Geophysical Research 97, 15201-15237.

Shea, W.T., Kronenberg, A.K., 1993. Strength and anisotropy of foliated rocks with varied mica contents. Journal of Structural Geology 15, 1097-1121.

Shimada, K., Takagi, H., Osawa, H., 1998. Geotectonic evolution in transpressional regime: time and space relationships between mylonitisation and folding in the southern Ryoke belt, eastern Kii Peninsula, southwest Japan. Journal of the Geological Society of Japan 104, 825-844 (in Japanese with English abstract).

Shimada, K., Takagi, H., Suwa, K., Hayashida, M., 1999. The Median Tectonic Line and deformation of Ryoke Belt, Kii Peninsula. Field excursion guide (in Japanese), contact: Koji Shimada, Division of Geology, Graduate School of Science and Engineering, Waseda University, Shinjuku, Tokyo 169-8050, Japan.

Sibson, R.H., 1977. Fault rocks and fault mechanisms. Journal of the Geological Society, London 133, 191-213.

Sibson, R.H., 1981. Fluid flow accompanying faulting: Field evidence and models. In: Simpson, D.W., Richards, P.G. (eds). Earthquake Prediction: an International Review. American Geophysical Union, Maurice Ewing Series 4, 593-607.

Sibson, R.H., 1983. Continental fault structure and the shallow earthquake source. Journal of the Geological Society 140, 741-767.

Sibson, R.H., 1985. Stopping of earthquake ruptures at dilational fault jogs. Nature 316, 248-251.

Sibson, R.H., 1990. Conditions for fault-valve behaviour. In: Knipe, R.J., Rutter, E.H. (eds) Deformation mechanisms, Rheology and Tectonics. Geological Society of London Special Publication 54, 15-28.

Sibson, R.H., 1986. Brecciation processes in fault zones: inferences from earthquake rupturing. Pure and Applied Geophysics 124, 159-175.

Sibson, R.H., Moore, J.M., Rankin, A.H., 1975. Seismic pumping – a hydrothermal fluid transport mechanism. Journal of the Geological Society 131, 653-659.

Simpson, C., Wintsch, R.P., 1989. Evidence for deformation-induced K-feldspar replacement by myrmekite. Journal of Metamorphic Geology, 7, 261-275.

Snoke, A.W., Tullis, J., Todd, V.R., 1998. Fault-related rocks: a photographic atlas, 613 pp. Princeton University Press, Princeton, NJ.

Spray, J.G., 1995. Pseudotachylyte Controversy – Fact or Fiction. Geology 23, 1119-1122.

Stewart, M., 1997. Kinematic evolution of the Great Glen Fault Zone, Scotland. Unpublished PhD thesis, Oxford Brookes University.

Stewart, M., Strachan, R.A., Holdsworth, R.E., 1999. Structure and early kinematic history of the Great Glen Fault Zone: Late Caledonian reactivation of a regional basement structure? Journal of the Geological Society 154, 135-139.

Stewart, M., Holdsworth, R.E., Strachan, R.A., 2000. Deformation processes and weakening mechanisms within the frictional-viscous transition zone of major

crustal-scale faults: insights from the Great Glen Fault Zone, Scotland. Journal of Structural Geology 22, 543-560.

Streit, J.E., Cox, S.F., 1998. Fluid infiltration and volume change during mid-crustal mylonitisation of Proterozoic granite, King Island, Tasmania. Journal of Metamorphic Geology 16, 197-212.

Sugiyama, Y., 1992. Neotectonics of the forearc zone and the Setouchi Province in southwest Japan. Memoirs of the Geological Society of Japan 40, 219-223 (Japanese with English Abstract).

Sun, S.S., McDonough, W.F., 1989. Chemical and isotopic systematics of oceanic basalts: implications for mantle composition and processes. In: Saunders, A.D., Norry, M.J. (eds) Magmatism in ocean basins. Special Publication of Geological Society of London 42, 313-345.

Sutton, J., Watson, J.V., 1986. Architecture of the continental lithosphere. Philosophical Transactions of the Royal Society, London A317, 5-12.

Takagi, H., 1985. Mylonitic rocks along the Median Tectonic Line in Takato-Ichinose area, Nagano Prefecture. Journal of Geological Society, Japan 91, 637-651.

Takagi, H., 1986. Implications of mylonitic microstructures for the geotectonic evolution of the Median Tectonic Line, central Japan. Journal of Structural Geology 8, 3-14.

Takagi, H., Shibata, K., Sugiyama, Y., Uchiumi, S., Matsumoto, A., 1989. Isotopic ages of rocks along the Median Tectonic Line in the Kayumi area, Mie Prefecture. Journal of Petrology, Mineralogy and Economic Geology 84, 74-88 (in Japanese with English abstract).

Takagi, H., Takeshita, T., Uchiumi, S., Inoue, M., 1992. Middle Miocene normal faulting along the Tobe thrust in western Shikoku. Journal of the Geological Society of Japan, 98, 1069-1072.

Tanaka, K., Nozawa, T. (Eds.) 1977. Geology and Mineral Resources of Japan (3rd Edn.). Geological Survey of Japan.

Tanaka, H., Takagi, H., Inoue, M., 1996. Mode of cataclastic deformation and hydrothermal alteration of the fault rocks and history of fault activity along the Median Tectonic Line, central Japan. Journal of Tectonic Research Group of Japan 41, 31-44.

Thompson, R.N., 1982. British Tertiary Volcanic Province. Scottish Journal of Geology 18, 49-107.

Thompson, R.N., Morrison, M.A., Hendry, G.L., Parry, S.J., 1984. An assessment of the relative roles of crust and mantle in magma genesis: an elemental approach. Philosophical Transactions of the Royal Society, A310, 549-550.

Van Staal, C.R., Rogers, N., Taylor, B.E. 2001. Formation of low-temperature mylonites and phyllonites by alkali-metasomatism weakening of felsic volcanic rocks during progressive, subduction-related deformation. Journal of Structural Geology 23, 903-921.

Vocke, R.D., Hanson, G.N., Grunenfelder, M., 1987. Rare earth element mobility in the Roffna Gneiss. Contributions to Mineralogy and Petrology, 95, 145-154.

Wallis, S., Banno, S., Radvanec, M., 1992. Kinematics, structure and relationship to metamorphism of east-west flow in the Sambagawa belt, southwest Japan. The Island Arc 1, 176-185.

Walsh, J.B., 1965. The effect of crack on the compressibility of rocks. Journal of Geophysical Research, 70, 381-389.

Wang, C.-Y., 1984. On the constitution of the San Andreas fault zone in central California. Journal of Geophysical Research 89, 5858-5866.

Wheeler, J., 1987. The significance of grain-scale stresses in the kinetics of metamorphism. Contributions to Mineralogy and Petrology 17, 397-404.

White, S.H., Burrows, S.E., Carreras, J., Shaw, N.D., Humphreys, F.J., 1980. On mylonites in ductile shear zones. Journal of Structural Geology 2, 165-187.

White, S.H., Breton, P.G., Rutter, E.H., 1986. Fault-zone Reactivation: Kinematics and Mechanisms. Philosophical Transactions of the Royal Society of London 317(1539), 81-97.

Wibberley, C.A.J., 1999. Are feldspar-to-mica reactions necessarily reaction-softening processes in fault zones? Journal of Structural Geology, 21, 1219-1227.

Wibberley, C.A.J., 2005. Initiation of basement thrust detachments by fault-zone reaction weakening. In: Bruhn, D. & Burlini, L. (Eds.), High Strain Zones: Structure and Physical Properties, Geological Society Special Publication 245, 347-372.

Wibberley, C.A.J., Shimamoto, T., 2003. Internal structure and permeability of major-slip fault zones: the Median Tectonic Line in Mie Prefecture, Southwest Japan. Journal of Structural Geology 25, 59-78.

Williams, P.F., Goodwin, L.B., Ralser, S., 1994. In: Continental Deformation. Hancock, P.L. (ed). Ductile Deformation Processes. Pergamon Press, Oxford, 1-27.

Wintsch, R.P., Christofferson, R., Kronenberg, A.K., 1995. Fluid-rock reaction weakening of fault zones. Journal of Geophysical Research 100, 13021-13032.

Yamamoto, H., 1994. Kinematics of mylonitic rocks along the Median Tectonic Line, Akaishi Range, central Japan. Journal of Structural Geology 16, 61-70.

Yamamoto, H., Masuda, T., 1987. Horizontal ductile shearing in mylonites of the Ryoke Belt in the Misakubo district, northwest Shizuoka Prefecture. Abstract 94th Annual Meeting Geological Society, Japan, 452.

Yund, R.A, Blanpied, M.L., Tullis, T.E., Weeks, J.D., 1990. Amorphous material in high strain experimental fault gouges. Journal of Geophysical Research, 95, 15589-15062.

Zoback, M.D., 2000. Strength of the San Andreas. Nature 405, 31-32.

Zoback, M.D., Zoback, M.L., Mount, V.S. & ten others. 1987. New evidence on the state of stress on the San Andreas fault system. Science 238, 1105-1111.